Ludwig-Maximilians-Universität

Sigillum Universitatis Ludovici Maximiliani

Made-to-measure particle models
of intermediate-luminosity elliptical galaxies:
regularization, parameter estimation,
and the dark halo of NGC 4494

Dissertation der Fakultät für Physik
DISSERTATION OF THE FACULTY OF PHYSICS / DISSERTAZIONE DELLA FACOLTÀ DI FISICA

der Ludwig-Maximilians-Universität München
AT THE LUDWIG MAXIMILIAN UNIVERSITY OF MUNICH / DELL'UNIVERSITÀ LUDWIG MAXIMILIAN DI MONACO

für den Grad des
FOR THE DEGREE OF / PER IL TITOLO DI

Doctor rerum naturalium

vorgelegt von Lucia Morganti
PRESENTED BY / PRESENTATA DA

aus Castel del Piano, GR (Italien)
FROM / DA

München, 27.07.2012

Sigillum Universitatis Ludovici Maximiliani

1. Gutachter: Prof. Dr. Ortwin Gerhard

<small>REFEREE: / RELATORE:</small>

2. Gutachter: Prof. Dr. Ralf Bender

<small>REFEREE: / RELATORE:</small>

Tag der mündlichen Prüfung: 28.09.2012

<small>DATE OF THE ORAL EXAM / DATA DELL'ESAME ORALE</small>

CURRICULUM VITAE ET STUDIORUM

<div align="right">Lucia Morganti</div>

First name: Lucia
Last name: Morganti
Date of birth: May 7th, 1984
Place of birth: Castel del Piano, Grosseto, Italy
Citizenship: Italian

Education

2008 – 2012:   **Ph. D. rer. nat. Ludwig-Maximilians-Universität München**
Max-Planck-Institut für extraterrestrische Physik (Garching b. München)

2006 – 2008:   **Master in Astrophysics and Cosmology.**
Alma Mater Studiorum – University of Bologna, Italy
Final results: 110/110 with honours.
Thesis: *Two component galaxy models: the effect of density profile at large radii on phase-space consistency*
Supervisor: Prof. Dr. Luca Ciotti (University of Bologna)

2003 – 2006:   **Bachelor of Astronomy.**
Alma Mater Studiorum – University of Bologna, Italy
Final results: 110/110 with honours.
Thesis: *Hydrostatic equilibrium and dark matter halos in elliptical galaxies*
Supervisor: Prof. Dr. Luca Ciotti (University of Bologna)

1998 – 2003 :   **Science High School.**
Diploma results: 100/100.
Liceo Scientifico Enrico Fermi, Castel del Piano, Grosseto, Italy

Publications

Morganti, L., Gerhard, O., Coccato, L., Martinez-Valpuesta, I., Arnaboldi, M., "Elliptical galaxies with rapidly decreasing velocity dispersion profiles: NMAGIC models and dark halo parameter estimates for NGC 4494", submitted to *Montly Notices of the Royal Astronomical Society* (2012).

Morganti, L., & Gerhard, O., "Regularizing made-to-measure particle models of galaxies", 2012, *Montly Notices of the Royal Astronomical Society*, **422**, 1571.

Morganti, L., & Gerhard, O., "NMAGIC made-to-measure particle models of galaxies", 2011, "Advances in Computational Astrophysics: methods, tools and outcomes", *ASP Conference Series*, R. Capuzzo-Dolcetta, M. Limongi and A. Tornambè eds.

Ciotti, L., & **Morganti, L.**, "How general is the global density slope-anisotropy inequality?", 2010, *Montly Notices of the Royal Astronomical Society*, **408**, 107.

Ciotti, L., & **Morganti, L.**, "Consistency criteria for generalized Cuddeford systems", 2010, *Montly Notices of the Royal Astronomical Society*, **401**, 109.

Saglia, R.P., Fabricius, M., Bender, R., Montalto, M., Lee, C.H., Riffeser, A., Seitz, S., **Morganti, L.**, Gerhard, O., Hopp, U., "The old and heavy bulge of M31. I. Kinematics and stellar populations", 2010, *Astronomy & Astrophysics*, **509**, 61.

Ciotti, L., & **Morganti, L.**, "On the global density slope-anisotropy inequality", 2009, Proceedings of the international symposium "Plasmas in the laboratory and in the universe: interactions, patterns, and turbulence".

Ciotti, L., **Morganti, L.**, & de Zeeuw, P.T., "Two-component galaxies with flat rotation curve", 2009, *Montly Notices of the Royal Astronomical Society*, **393**, 491.

Ciotti, L., & **Morganti, L.**, "Two-component galaxies models: the effect of density profile at large radii on the phase-space consistency", 2009, *Montly Notices of the Royal Astronomical Society*, **393**, 179.

Lucia Morganti

E QUINDI USCIMMO A RIVEDER LE STELLE.

Dante Alighieri

Zusammenfassung

Dynamische Modelle sind wichtige Hilfsmittel, um aus projizierten Beobachtungsdaten auf die Massenverteilung und die Phasenraumstruktur von Galaxien zu schließen, und dabei ihre Entstehungs- und Entwicklungsprozesse zu verstehen. Eine relativ neue und vielversprechende Technik, dynamische Modelle zu konstruieren, ist die "made-to-measure" Methode, bei der ein System von Teilchen sukzessive einer beobachteten Lichtverteilung und gemessenen projizierten stellaren Kinematik angeglichen wird. Da die intrinsische, dreidimensionale Struktur der Modelle dann bekannt ist, können sie verwendet werden, um die Massenverteilung und Bahnstruktur der Galaxie zu verstehen. In dieser Arbeit verwenden wir den "made-to-measure particle" Code NMAGIC, um die spezielle Klasse der schwach im Röntgenbereich strahlenden elliptischen Galaxien von mittlerer Leuchtkraft zu erforschen, deren Geschwindigkeitsdispersionsprofile stark mit dem Radius abfallen, was auf sehr diffuse dunkle Materie Halos hindeutet, die möglicherweise in Konflikt zu Vorhersagen von Galaxienentstehungsmodellen stehen.

Im ersten Teil der Arbeit führen wir eine "moving prior" Regularisierungsmethode in NMAGIC ein, welche eine korrekte und von systematischen Fehlern freie Rekonstruktion der dynamischen Struktur der beobachteten Galaxie ermöglicht. Im sphärischen Fall, in welchem theoretisch eine eindeutige Invertierung der Daten möglich ist, zeigen wir, dass NMAGIC mit der neuen Regularisierungsmethode die Verteilungsfunktion und intrinsische Kinematik einer Zielgalaxie (mit idealen Daten) mit hoher Genauigkeit reproduziert, unabhängig von der ursprünglich als Startmodell gewählten Teilchenverteilung. Weiterhin untersuchen wir, wie sich unvollständige und verrauschte kinematische Daten auswirken, und kommen zu dem Schluss, dass die Zuverläßigkeit der Modelle auf Gebiete mit guten Beobachtungsdaten beschränkt

ist. Schließlich werden mit einer Version der moving-prior Regularisierung für axialsymmetrische Systeme die am besten passenden NMAGIC Modelle der zwei elliptischen, mittelstark leuchtenden Galaxien NGC 4697 und NGC 3379 aus früheren Arbeiten rekonstruiert, um einen glatteren Fit an die Beobachtungsdaten zu erhalten.

Im zweiten Teil der Arbeit untersuchen wir die rätselhafte elliptische Galaxie NGC 4494 mittlerer Leuchtkraft. Wir konstruieren axialsymmetrische NMAGIC Modelle mit unterschiedlichen dunkle Materie Halos und Inklinationen, um etwas über ihre Massenverteilung und Bahnstruktur zu erfahren. Die Modelle werden eingegrenzt durch Radialgeschwindigkeiten von planetarischen Nebeln und kinematischen Absorptionsliniendaten in "slitlets", was uns ermöglicht, zu erforschen, bei welchen Radien die dunkle Materie anfängt zu dominieren bzw. Spuren des Entstehungsmechanismus sichtbar werden. Mit geeigneten Monte-Carlo-Simulationen bestimmen wir mit NMAGIC die $\Delta\chi^2$ Werte verschiedener Konfidenzniveaus für die Schätzung der Parameter der dunklen Halos und finden andere Werte, als in der Literatur über dynamische Modellierung normalerweise verwendet. Unsere best-fit NMAGIC Modelle für NGC 4494 innerhalb dieser Konfidenzniveaus schließen einen diffusen dunklen Halo aus; sie haben einen Anteil dunkler Materie von ungefähr $0,6 \pm 0,1$ bei 5 Effektivradien und eine näherungsweise flache (konstante) totale Kreisgeschwindigkeit von ~ 220 km/s außerhalb des Effektivradius. Die Anisotropie der Sternbahnen ist mässig radial. Diese Ergebnisse sind unabhängig von der angenommenen Inklination der Galaxie, aber edge-on Modelle werden bevorzugt.

Schließlich vergleichen wir die dunklen und stellaren Halos von den bisher modellierten elliptischen Galaxien mittlerer Leuchtkraft und folgern, dass ihre Kreisgeschwindigkeiten ähnlich sind. Die genaue Wechselwirkung zwischen dunkler und leuchtender Materie war während der Entstehung jeder Galaxie wahrscheinlich unterschiedlich – und NGC 4494 zeigt einen besonders hohen Anteil an dunkler Materie, speziell im Zentrum, was vielleicht das Ergebniss vergangener Verschmelzungsereignisse sein könnte.

Abstract

Dynamical models are an important tool to infer the mass distribution and phase-space structure of galaxies from projected observational data, and thereby learn about the processes driving their formation and evolution. A recent and promising technique to build dynamical models is through made-to-measure particle methods, in which a system of particles is trained to match the observed light distribution and projected stellar kinematics of a galaxy. Because the intrinsic, three-dimensional structure of such models is then known, they can be used to understand the mass distribution and orbital structure of the galaxy. In this thesis we use the made-to-measure particle code NMAGIC to investigate the particular class of X-ray-faint, intermediate-luminosity elliptical galaxies, whose velocity dispersion profiles decline strongly with radius, suggesting very diffuse dark matter halos in possible tension with the predictions of galaxy formation models.

In the first part of the work, we introduce a moving prior regularization method in NMAGIC which facilitates a correct and unbiased recovery of the dynamical structure of the observed galaxy. In the spherical case in which theoretically a unique inversion of (idealized) data exists, we show that NMAGIC with the new regularization method recovers the distribution function and intrinsic kinematics of the target galaxy with high accuracy, independent of the initial particle model. We then investigate the effects of less complete and noisier kinematic data, and conclude that the reliability of the models is limited to those regions in which good observational constraints exist. A version of the moving prior regularization suited for axisymmetric systems is then used to reconstruct the best-fitting NMAGIC models determined in previous works for the two intermediate-luminosity elliptical galaxies NGC 4697 and NGC 3379, obtaining smoother fits to the observational data.

In the second part of the work, we explore the enigmatic intermediate-luminosity elliptical galaxy NGC 4494. We construct axisymmetric NMAGIC models with different dark matter halos and inclinations, in order to learn about its mass distribution and orbital structure. The kinematic constraints include radial velocities of Planetary Nebulae and absorption line kinematics data in slitlets, and allow us to probe those radii where dark matter starts to dominate and the imprint of formation mechanisms becomes apparent. Using suitable Monte Carlo simulations, we determine the $\Delta\chi^2$ values of various confidence levels for the estimation of the dark halo parameters with NMAGIC, and find that these are different from the values usually employed in the dynamical modeling literature. Our best-fitting NMAGIC models for NGC 4494 within these confidence levels rule out a diffuse dark halo; they have a dark matter fraction of about 0.6 ± 0.1 at 5 effective radii, and an approximately flat total circular velocity ~ 220 km/s outside 1 effective radius. The orbital anisotropy of the stars is moderately radial. These results are independent on the assumed inclination of the galaxy, but edge-on models are preferred.

Finally, we compare the dark and stellar halos of the intermediate-luminosity ellipticals modeled so far, and conclude that their circular velocity curves are similar. The detailed interaction between dark and luminous matter during galaxy formation was probably different for each galaxy, and NGC 4494 shows a particularly high dark matter fraction, especially in the center, which might be a reminiscence of merger events.

Contents

1

Introduction

Elliptical galaxies have become the focus of a vast number of observational and theoretical studies during recent years. Understanding their dynamical structure is one way of learning how these galaxies formed and evolved. In this respect, dynamical models represent an important tool to infer the gravitational potential, mass distribution, dark matter content, and stellar orbits of galaxies from observational data.

This Introduction provides the reader with the basic background about galaxies. First, the observational classification of galaxies is described, and their formation in the cosmological context is sketched. Then, we focus on ellipticals, discussing their observational properties and dynamics, with particular care to their dark and stellar halos. Finally, we outline the main issues that will be addressed in the thesis.

1.1   Galaxies - an overview

Astronomy is probably the oldest of all sciences. The charming beauty of the night sky has always fascinated people, originating legends and myths of any sort. The word "galaxy" itself derives from a Greek term for milk, since in one of these legends the swathe of light in the sky - our own Galaxy, the Milky Way - is nothing less than a river of milk flowing from the breast of Hera, wife of Zeus in the Olympian pantheon.

Already thousands years ago, galaxies could be spotted by eye in the night sky as small clouds or "nebulae", but it was only in the XVII century that Galileo realized, with the help of the first telescope, that our Milky Way is actually made of many stars, and it was
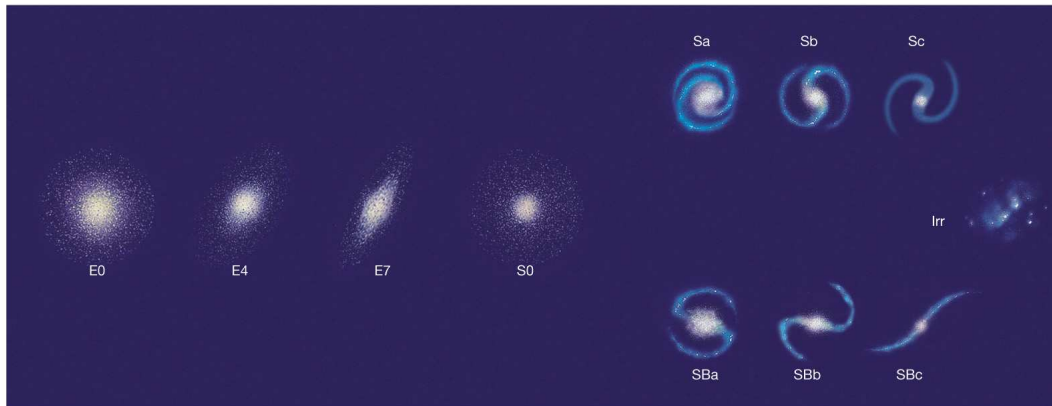
Figure 1.1: The Hubble-Sandage classification scheme for galaxies, from Chaisson and McMillan (2004). For the alternative de Vaucouleurs' classification scheme, see Kormendy (1982).

only in the XVIII century that Thomas Wright speculated (correctly) that some of these nebulae were separate Milky Ways - "island universes", as Immanuel Kant called them. Whether the nebulae were actually independent galaxies was a long-standing issue, culminated in the so called Great Debate held in the 20's between Harlow Shapley and Heber Curtis (see *e.g.* Trimble, 1995). Eventually, their extragalactic nature was uncovered by Edwin Hubble, who was able to resolve the outer parts of M31 - the Andromeda galaxy - as a collection of stars, and observed some Cepheid variables there. Cepheids are pulsating stars that obey a well-defined relation between luminosity and pulsation period, which allows to measure their distance. In this way, Hubble could prove that M31 lies well beyond the boundaries of our Milky Way.

After spending many years surveying thousands of galaxies, Hubble noticed a remarkable trend: galaxies could be grouped according to their morphology at optical wavelengths[1] in a diagram which is still widely used (Hubble, 1936).

The diagram, shown in Fig. 1.1, classifies galaxies into a small number of "natural groups" that share common structural features. It is characterized by a tuning-fork: to the left of the bifurcation are ellipticals, called early-type galaxies, to the right are spirals and irregulars, called late-type galaxies. This notation originates from the incorrect thought that the sequence, from left to right, is an evolutionary one.

Elliptical galaxies are among the brightest objects in our Universe. The isophotes, i.e. contours of constant surface brightness (light per unit area), on their images are

---

[1] Galaxies can be also classified at alternative wavelengths, for instance using their near-infrared morphology (*e.g.* Jarrett, 2000).

describable as concentric ellipses (see Section 1.3.1). The ellipticity increases along the sequence, from E0 (circular image on the sky) to E7 (elongated image). The number n in the label En quantifies the degree of ellipticity, with $n = 10(1 - q)$, where $q = b/a$ is the apparent axis-ratio, a the projected long axis, and b the short one. The sequence E0→E7 is not a sequence of anything fundamental, but rather one of apparent flattening (Tremaine, 1987). Galaxies can be flattened for at least two reasons, rotation and orbital anisotropy[2] (*e.g.* Illingworth, 1977; Binney, 1978; Davies, 1981), and ellipticals are mainly flattened by orbital anisotropy. However, they span only a moderate range of true flattenings (*e.g.* Sandage et al., 1970), and their apparent flattening mostly depend on the inclination at which the galaxy is observed (Binney and de Vaucouleurs, 1981). The absence of elliptical galaxies flatter than about E7 can be explained with a firehose instability (Merritt and Hernquist, 1991; Merritt and Sellwood, 1994).

Spiral galaxies contain a bulge and a prominent disk, which exhibits spiral arms. Whilst "classical bulges" are similar to small ellipticals residing in the center of disks, some bulges, the so called "pseudo-bulges", are really more like disks (Kormendy, 1993). These pseudo-bulges show photometric and kinematic evidence for disk-like dynamics, and are thought to be built secularly out of disk material (Kormendy and Kennicutt, 2004). Pure (thin) disk galaxies, i.e. bulgeless systems, are also observed (*e.g.* Goad and Roberts, 1981; Matthews et al., 1999; Kormendy et al., 2010). Hubble's diagram breaks up spirals according to the presence or absence of a bar-like structure. More than half of all spirals are barred, whereas ellipticals do not have bars. Spiral galaxies belong to a sequence Sa→Sd of *(i)* decreasing bulge to total luminosity, *(ii)* less tightly wound arms, *(iii)* increasing clumpiness. The gas mass also increases along such sequence.

Lenticular (S0) galaxies constitute a hybrid class between ellipticals and spirals: they have disk-like dynamics, but resemble ellipticals in the lack of cool gas, young stars, and spiral arms. Recently, the kinematic analysis of a large sample of nearby early-type galaxies (ellipticals and lenticulars) from the ATLAS-3D survey showed that only one third of the morphologically classified ellipticals are genuinely elliptical-like objects, while the rest are misclassified lenticular-like systems (Cappellari et al., 2011). Over the years, alternative classifications for S0s have been proposed in which lenticular galaxies parallel the sequence Sa→Sc of spirals (van den Bergh, 1976; Cappellari et al., 2011; Krajnović et al., 2011;

---

[2] This refers to the shape of the velocity dispersion tensor (see Section 1.4).

Kormendy and Bender, 2012).

Ellipticals and S0s make up for about the 40% of the total mass of galaxies in the local universe (Bernardi et al., 2010).

Finally, the less luminous and less defined objects on the right of the diagram are named "irregulars", and there is no galaxy so unusual that it cannot be fit into this group.

Even if a proper definition of a "galaxy" is still matter of debate (*e.g.* Willman and Strader, 2012), roughly speaking galaxies are complex systems made up of different components - dust, gas, stars, dark matter - held together by gravity. Their stellar mass[3] increases from irregular galaxies ($\sim 10^8 M_\odot$) to ellipticals ($\sim 10^{12} M_\odot$). Elliptical galaxies are surrounded by atmospheres of hot gas, which constitutes a few percent of their baryonic mass, and they do not contain cold gas. The content of cold gas increases along the Hubble sequence, contributing up to 90% of the luminous mass in the most gas-rich irregular galaxies.

Hubble's original division between the two classes of ellipticals and spirals stood the test of time, and such *bimodality* has been recently confirmed by several large statistical surveys of the local galaxy population, such as the Sloan Digital Sky Survey and the two-degree Field survey (*e.g.* Bell et al., 2003; Kauffmann et al., 2003; Baldry et al., 2004). In most cases, the morphology of a galaxy matches its colour, presumably because of different populations of stars, either old or newly formed, that dominate its light (see *e.g.* the review by Roberts and Haynes, 1994). In particular, spiral galaxies appear blue because they are actively forming hot young stars, while elliptical galaxies are red, with an old stellar population. The morphology of galaxies is closely linked to the environment, with elliptical galaxies preferentially clustering in overdense regions of the Universe, such as the inner parts of galaxy clusters (*e.g.* Baldry et al., 2006).

Significant revisions of the Hubble sequence have been proposed by Kormendy and Bender (1996), who ordered ellipticals by isophote shape as an indicator of velocity anisotropy (see Section 1.3.1), and by Cappellari et al. (2011), who separated early-type galaxies into fast and slow rotators, instead of lenticular and elliptical galaxies, in a way that is nearly insensitive to projection effects (see Section 1.3.2).

After this observational overview of the kind of galaxies that populate our Universe, we now turn to describe how these stellar systems formed and evolved in the cosmological

---

[3] The solar mass $M_\odot = (1.98892 \pm 0.00025) \times 10^{33}$ g is a standard unit of mass in Astronomy.

framework. In this context, as originally proved by Slipher's and Hubble's observations of galaxies receding from us, galaxies are the building blocks, the fundamental units of an expanding Universe.

1.2 Galaxy formation in the cosmological scenario

THE STUDY OF ORIGINS IS THE ART
OF DRAWING SUFFICIENT CONCLUSIONS
FROM INSUFFICIENT EVIDENCE.
Allan Sandage

The basic picture of modern cosmology is that of a Universe which began from a hot and homogeneous state, then expanded, cooled down, and ultimately assembled the structures that we appreciate today - galaxies, galaxy clusters, and superclusters (*e.g.* Weinberg, 1972; Peacock, 1999).

The expansion of the Universe is most often described by the scale factor $a(t)$, which is set to unity today, and by the expansion rate or Hubble function $H(t) = \dot{a}/a$, which regulates the proportionality between the distance and recession velocity of galaxies. The current expansion rate is the Hubble constant $H_0 = 100h$ km/s/Mpc, with $h \sim 0.7$ (Komatsu et al., 2011)[4]. The equations of Einstein's General Relativity, together with the equations of state of the different components of the Universe, determine the evolution of the scale factor.

Nowadays, many independent and complementary observations[5] support the evidence that the expansion of the Universe is presently accelerated.

The most economical framework to describe the currently available observational data is the so called ΛCDM paradigm, in which the Universe has a flat space-time geometry, and its energy budget is dominated by a cosmological constant, which is the simplest version of an unknown form of dark (or vacuum) energy responsible for the accelerated expansion (Efstathiou et al., 1990). Typically, the densities of the different components of the Universe are expressed via the ratio Ω_i of the density of the i-component to the critical density, i.e. the density of a flat Universe. As shown in Fig. 1.2, the ΛCDM concordance model has cosmological parameters $\Omega_M = 0.27$ for the matter density, contributed by

---

[4] For reference, 1 parsec (pc) is abut 3.26 light-years.

[5] Observational evidence of the presently accelerated expansion of the Universe includes and combines the analysis of distant Supernovae of Type Ia (Riess et al., 1998; Schmidt et al., 1998; Perlmutter et al., 1999), temperature fluctuations in the Cosmic Microwave Background radiation (Komatsu et al., 2011), Baryon Acoustic Oscillations (Percival et al., 2010; Sanchez et al., 2012), large-scale clustering of galaxies (Maddox et al., 1990; Reid et al., 2010), integrated Sachs-Wolfe effect (Giannantonio et al., 2008), and weak lensing tomography (Schrabback et al., 2010).
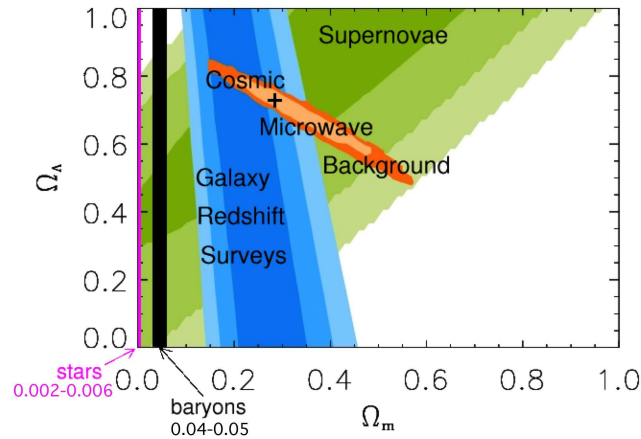
Figure 1.2: Constraints on the energy budget of our "dark" Universe from different observational data (Gondolo, 2004). A Universe characterized by $\Omega_M = 0.27$ and $\Omega_\Lambda = 0.73$ is almost 14 billion years old.

baryons plus considerable non-baryonic cold dark matter, and $\Omega_\Lambda = 0.73$ for the density of dark energy (Komatsu et al., 2011). Cold Dark Matter (CDM) is assumed to consist of non-relativistic and collisionless particles, interacting only through gravity.

According to the current picture of theoretical cosmology, quantum fluctuations in the early Universe were exponentially amplified during an accelerating phase of expansion which is referred to as inflation (Guth, 1981), and transformed into classical density perturbations. Dark matter density fluctuations were the first to collapse by gravitational instability (Jeans, 1902) right after the epoch of *equivalence*, when the Universe switched from being radiation-dominated to being matter-dominated. These dark matter fluctuations originated the potential wells in which later the baryonic material was accreted, and the first structures assembled. This happened only after *recombination*, i.e. the epoch when the Universe had cooled down enough for the protons to capture electrons and form hydrogen atoms. Once recombination occurred, the photons could travel freely (*decoupling*), and so the Universe became transparent.

The most investigated model of structure formation, which is supported by strong observational evidence, is the so called *bottom-up scenario*: structures grow hierarchically, with small dark matter structures forming first, and then assembling into larger systems (Doroshkevich and Zeldovich, 1975; Peebles, 1984; White et al., 1987).

While the linear regime of structure formation can be described analytically, this is not true for the non-linear regime, and numerical simulations have become the major tool

to investigate the evolution of dark matter halos at every scale - from galaxy clusters down to dwarf galaxies. Indeed, since cold dark matter behaves as a collisionless fluid, N-body simulations provide a simple way to sample its phase-space distribution with a set of N particles evolving under self-gravity. Cosmological N-body simulations, from the pioneering work of Einasto et al. (1974); White and Rees (1978) to the latest high-resolution simulations (*e.g.* Springel et al., 2005b, 2008), show that the structures are embedded in extended dark matter halos, and that these dark halos share a universal mass density profile (Navarro et al., 1996, 2010). With proper scaling, a dwarf galaxy halo is almost indistinguishable from a galaxy cluster halo.

Unfortunately, dark matter-only simulations do not provide any information about the baryons which astronomers directly observe. The build-up of the stellar content of galaxies is actually very complicated, and many different physical processes are involved, which are strongly non-linear, deeply intertwined, and poorly understood: gas cooling and heating, star formation, feedback from Active Galactic Nuclei (AGN) and stellar evolution, galaxy interactions and mergers. In practice, two strategies have been developed to tackle the problem: *(i)* full cosmological simulations model gas dynamics directly, adopting a Lagrangian (Smoothed Particle Hydrodynamics, *e.g.* Monaghan, 1992) or Eulerian (Adaptive Mesh Refinement, *e.g.* Berger and Colella, 1989) approach, and specific prescriptions for star formation and feedback (*e.g.* Springel et al., 2001; Norman et al., 2007; Springel, 2010); *(ii)* semi-analytic models use precise recipes, which are both physically and observationally motivated, to include baryonic physics in the output of N-body simulations (*e.g.* White and Rees, 1978; Kauffmann et al., 1993; Springel et al., 2001; Guo and White, 2008).

The basic process leading to galaxy formation is the cooling of gas, and its descent into the potential well of dark matter halos. This collapse increases the density and temperature of the gas, which generally reduces the cooling time more rapidly than it reduces the collapse time, so that the original gas cloud fragments into small, high-density clouds that eventually form the first stars in the young galaxies (Binney, 1977; Rees and Ostriker, 1977; Silk, 1977).

At one extreme, the process of galaxy formation can be treated as totally dissipational with respect to energy, with the accreted gas that dissipates into thermal energy the kinetic energy it acquires while descending in the potential well (*e.g.* Lackner and Ostriker,

2010). According to the "classical" picture of the monolithic collapse, elliptical galaxies assembled their mass in a rapid burst of "in-situ" star formation at early times, and then passively evolved to present day (Eggen et al., 1962; Larson, 1975; Jimenez et al., 1999). Investigations of the dynamical implications of this scenario with numerical simulations have shown density profiles and orbital structures similar to those of real ellipticals (*e.g.* van Albada, 1982).

At the opposite extreme, a purely dissipationless model for the assembly of the stellar component predicts that stars are formed in smaller systems far from the ultimate galaxy, i.e. "ex-situ", and then assembled through minor or major mergers[6], which are more naturally rooted in a hierarchical scenario of structure formation (White and Frenk, 1991). When compared to the characteristic structures of a monolithic collapse, mergers can reproduce a wider diversity of dynamical systems.

The idea that elliptical galaxies can originate from mergers of disk galaxies, i.e. the so called "merger hypothesis" (Toomre, 1977), is especially consistent with the observed "morphology-density relation" by which the number of ellipticals increases with increasing density of the environment, contrary to the number of spirals (Dressler, 1980; Postman and Geller, 1984). Indeed, early numerical simulations showed that mergers could lead to something resembling elliptical galaxies (*e.g.* Fall, 1979; Gerhard, 1981; Negroponte and White, 1983; Blumenthal et al., 1984). Moreover, direct observations of recent merger remnants (*e.g.* Schweizer, 1982; Lake and Dressler, 1986; Doyon et al., 1994; Genzel et al., 2001; Rothberg and Joseph, 2004; Cooper et al., 2012) and of faint shells and tidal features around elliptical galaxies (*e.g.* Malin and Carter, 1983) support the idea of mergers as drivers for galaxy evolution at high and low redshift[7].

Of course, major mergers have a more dramatic effect. However, the current view is that the bulk of the stars in present day ellipticals cannot originate from major mergers of present day disk galaxies, or major mergers of their progenitors (Naab et al., 2009). Minor mergers, instead, are much more frequent, and dominate the assembly history of elliptical galaxies (Bell et al., 2006; Khochfar and Silk, 2006; Genel et al., 2008; Lotz et al., 2011; Hirschmann et al., 2012; Gabor and Davé, 2012). Simulations (Hilz et al.,

---

[6] The relative sizes of the merging galaxies determine whether a merger is major (roughly equal-sized galaxies) or minor (one galaxy is significantly smaller than the other).

[7] In this context, redshift indicates the cosmological redshift z, i.e. the stretching of light due to the expansion of the Universe, and provides a distance measurement for those galaxies which are far away enough that their peculiar motions can be ignored.

2012) show that different dynamical processes dominate the evolution of dissipationless major and minor mergers, respectively violent relaxation (Lynden-Bell, 1967; Spergel and Hernquist, 1992) and tidal stripping.

The presence of gas during the merger event also plays an important role in shaping the final kinematic structure of the merger remnant: gas rich (wet) mergers produce galaxies dominated by rotation, whereas the remnants of gas-poor (dry) mergers are dominated by random motions (*e.g.* Barnes and Hernquist, 1996; Bournaud et al., 2005; Cox et al., 2006; Naab et al., 2006; Ciotti et al., 2007). As shown by Hernquist et al. (1993), wet mergers represent a way to solve one strong problem with the "merger hypothesis", namely the fact that the stellar phase-space densities at the centers of ellipticals far exceed the maximum densities in observed spirals (Carlberg, 1986; Kormendy, 1989). An important consequence of wet mergers is that the gas flows to the center and forms new stars in a compact starburst, thus modifying the inner profiles of the remnant (Mihos and Hernquist, 1994; Springel, 2000; Springel et al., 2005a; Hopkins et al., 2008, 2009). Such process may account for the extra light at small radii observed in low-luminosity ellipticals (*e.g.* Kormendy, 1999; Kormendy et al., 2009).

The picture of galaxy formation has become more complex - and more exciting - with the recently established phenomenon of *archaeological downsizing* (Cowie et al., 1996): older stellar ages are observed in more massive galaxies, suggesting that the stellar mass is assembled first and faster in massive galaxies rather than in smaller ones, in an anti-hierarchical fashion with respect to a naive reading of the hierarchical growth of structures. Interestingly, the observed downsizing does not contradict a hierarchical structure formation scenario, and cosmological simulations of galaxy formation seem to do a good job in reproducing the observations by including appropriate feedback from AGN and/or stellar evolution (*e.g.* Springel et al., 2005a; Scannapieco et al., 2005; Oser et al., 2012). The reason resides in the difference between *formation time* and *assembly time*: the most massive galaxies do harbor the oldest stars, which formed early on in smaller structures; the galaxies themselves were assembled later (see *e.g.* De Lucia et al., 2006).

Recent cosmological simulations for the build-up of elliptical galaxies provide a useful interpretation for the interplay of different processes during galaxy formation in terms of a *two-phase formation scenario* (*e.g.* Naab et al., 2007; Oser et al., 2010; Johansson et al.,

2012; Lackner et al., 2012). According to these numerical works, galaxies experience two regimes of growth: a hierarchical regime at high redshift, when baryons follow the growth of dark halos, and an anti-hierarchical quenching of star formation and accretion episodes at later epochs. The first rapid "in-situ" phase is dominated by accretion of gas and strong and dissipational star formation, whereas the subsequent dissipationless "ex-situ" phase is more extended in time, and it is dominated by stellar mergers and re-arrangement of stars that have formed outside the galaxy itself. In this *inside-out* hierarchical growth scenario, elliptical galaxies assembled their dense core until redshift $z \sim 1-2$, and then slowly built their outer envelope until present day by accreting smaller systems, whose star formation history was truncated at early times. The phenomenon of accretion is particularly prominent in more massive systems (Hirschmann et al., 2012; Gabor and Davé, 2012; Lackner et al., 2012).

In general, simulations reproduce a whole body of observational findings on size evolution (ellipticals were more compact and denser in the past, *e.g.* Trujillo et al. (2006); van Dokkum et al. (2010); Szomoru et al. (2012)), stellar kinematics (*e.g.* Saglia et al., 2010a; Arnold et al., 2011; Coccato et al., 2011), and metallicity (*e.g.* Mehlert et al., 2003; Forbes et al., 2011; Greene et al., 2012) in nearby elliptical galaxies. Both theoretical and observational studies (*e.g.* Bender et al., 1992; Ciotti and van Albada, 2001; Robertson et al., 2006; Scarlata et al., 2007; Faber et al., 2007) have argued that a combination of dissipational and dissipationless processes is needed to match the observed properties of elliptical galaxies. Higher quality of observational data, together with improvements and refinements of the modeling techniques, undoubtedly represent the keys to unveil the formation pathways of ellipticals.

1.3 Observational properties of elliptical galaxies

<div align="right">

Thinking is more interesting than knowing,
but less interesting than looking.
Johann Wolfgang von Goethe

</div>

Elliptical galaxies have long been regarded as boring "red and dead" objects, populated by old stars and passively evolving over cosmic time (*e.g.* Dunlop et al., 1989).

For quite a long time, it has been erroneously thought that these systems were dynamically simple, flattened by rotation, structureless, and depleted of gas. However, since the mid-1970s it became clear that these stellar systems are far from being boring (*e.g.* de Zeeuw

and Franx, 1991). Though smaller ellipticals can be flattened by rotation, ellipticals in general rotate too slowly (*e.g.* Bertola and Capaccioli, 1975; Illingworth, 1977), and rather are flattened by orbital anisotropy (*e.g.* Binney, 1978; Davies, 1981). In this respect, they are dynamically *hot systems* in which most of the support against gravitational collapse comes from random motions, opposed to cold systems, like spiral galaxies, in which ordered rotation contributes most of the internal kinetic energy. Consequently, stars in elliptical galaxies move along orbits which are much more intricate than those in spirals, and this makes it harder to understand their dynamics and formation mechanisms. Furthermore, the launch of X-ray satellites revealed that most of these galaxies do contain *gas*, contributing up to 10% of their total mass (*e.g.* Sarazin, 1990). Their interstellar medium is at high temperatures $\sim 10^7$K, and notable Bremsstrahlung emission can be observed at X-ray wavelengths (*e.g.* Forman et al., 1979).

Over the years, a rich variety of *sub-structures* have been identified in elliptical galaxies in the various forms of shells, ripples, stellar disks, rings, kinematically decoupled components, and younger stellar components (*e.g.* Malin and Carter, 1983; Franx and Illingworth, 1988; Bender, 1988a; Krajnović et al., 2011).

Nowadays, every elliptical is also thought to harbor a central *supermassive black hole* whose mass correlates with the properties of the host galaxy, suggesting an intimate connection between the processes of black hole growth and galaxy evolution (Magorrian et al., 1998; Ferrarese and Merritt, 2000; Gebhardt et al., 2000).

This Section summarizes the main observed properties of nearby elliptical galaxies in terms of photometry and kinematics. The modeling of photometric and kinematic observational data provides significant insights into the global structure of these galaxies, as will be shown in this thesis.

1.3.1 Optical photometry

The isophotes of elliptical galaxies are concentric ellipses within the photometric errors (Kent, 1984; Lauer, 1985; Jedrzejewski, 1987; Peletier et al., 1990).

Stark (1977) proved that elliptical galaxies whose isophotes are similar ellipses have volume brightness distributions which are constant on similar ellipsoids. Thus, the intrinsic shape of elliptical galaxies can be spherical, axisymmetric oblate (flattened), axisymmetric prolate (elongated), or triaxial (fully ellipsoidal).

Accurate CCD photometry shows that the isophotes are not perfect ellipses, and deviations from pure ellipses are usually quantified by the amplitude a_4 of the $\cos(4\vartheta)$ term in a Fourier expansion of the isophote radius in polar coordinates (Carter, 1978; Bender and Moellenhoff, 1987). The sign of the a_4 parameter discriminates between disky (elongated along the major axis, $a_4 > 0$) and boxy (rectangular, $a_4 < 0$) isophotes. As discussed by Kormendy and Bender (1996), isophote shape is an indicator of velocity anisotropy. In particular, all disky ellipticals rotate rapidly, and in general are isotropic, while boxy ellipticals tend to rotate slowly and are anisotropic. Being the orbital anisotropy a fundamental dynamical property of galaxies, Kormendy and Bender (1996) proposed a revised version of the Hubble's sequence based on the a_4 parameter, which measures velocity anisotropy, rather than on the apparent ellipticity. Such new gradation from boxiness to diskiness is illustrated in Fig. 1.3.
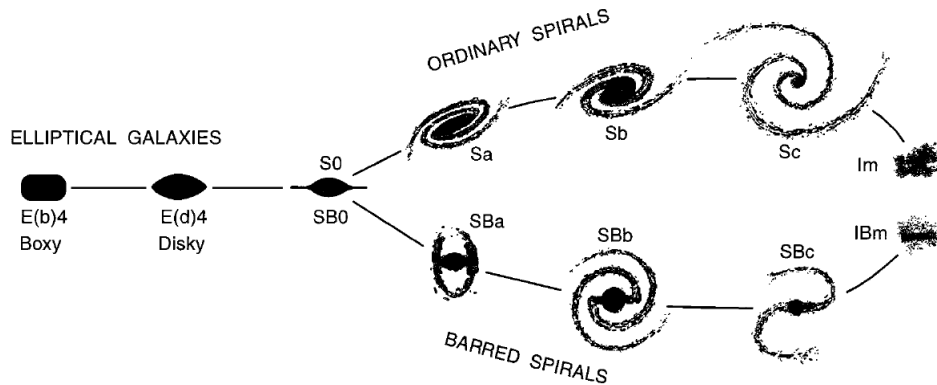
Figure 1.3: Morphological classification of galaxies proposed by Kormendy and Bender (1996). Elliptical galaxies are illustrated edge-on and at ellipticity $\epsilon \sim 0.4$.

It has been variously suggested that many physical properties of elliptical galaxies correlate with the two kinds of deviations of the isophote shape, implying an intrinsic *dichotomy*: normal and fainter ellipticals, which are typically radio and X-ray quiet, are disky, rapidly rotating, and generally axisymmetric, whereas giant ellipticals, which are usually X-ray and radio loud, tend to be boxy and slowly rotating, and may be moderately triaxial and anisotropic (Bender et al., 1988; Bender, 1988b; Kormendy and Djorgovski, 1989; Kormendy and Bender, 1996; Faber et al., 1997; Trujillo et al., 2004b; Kormendy et al., 2009). The two families of ellipticals also exhibit a different behaviour of the surface brightness profile in the central galactic regions: fainter elliptical galaxies are coreless and have central extra light, while brighter ellipticals have cores, i.e. central missing light

(*e.g.* Nieto et al., 1991; Kormendy et al., 2009). It is very likely that the structural and physical differences between these two families reflect different formation mechanisms. Recent simulations of galaxy formation show that massive boxy ellipticals may originate from equal-mass mergers of disk galaxies or early-type galaxies, while low-luminosity disky ellipticals may be produced by minor mergers or late infall of gas (Naab and Burkert, 2003; Khochfar and Burkert, 2005). Bekki and Shioya (1997) found that the isophotal shapes are strongly affected by the rapidity of gas consumption by star formation in wet mergers, and that mergers with gradual star formation are more likely to form disky ellipticals. In general, dissipational remnants tend to be disky whereas dissipationless remnants tend to be boxy (Cox et al., 2006). The extra light at the centers of the fainter, disky ellipticals may be a signature of dissipational starburst in wet mergers (*e.g.* Nieto and Bender, 1989; Springel, 2000; Hopkins et al., 2009; Kormendy et al., 2009), whereas central cores may be indicative of dry mergers, or scouring by binary massive black holes[8] after the last major merger.

The orientation of the isophotes may change going from the galactic center outwards: isophote twists have been observed since long time ago (*e.g.* Liller, 1960; King, 1978), and they can be interpreted as a projection effect of a triaxial galaxy in which the ellipticity changes with radius (Stark, 1977; Kormendy, 1982), or as an intrinsic misalignment of the major axis at different radii in a merger remnant (Gerhard, 1983b,a).

In general, ellipticals have bright nuclei and faint outer envelopes. Their surface brightness can be well fitted by several empirical formulae, of which the most well-known is the generalization of the de Vaucouleurs ($R^{1/4}$) law proposed by Sersic (1968):

$$I(R) = I_\mathrm{e} \exp(-7.67[(R/R_\mathrm{e})^{1/n} - 1]) \tag{1.1}$$

(Bertin, 2000), where I is the surface brightness at projected radius R, R_e is the effective radius that contains half of the projected light, I_e is the surface brightness at R_e, and n the Sersic index, which correlates with the luminosity (Ciotti and Bertin, 1999).

The intrinsic luminosity density of an elliptical galaxy can be obtained by deprojecting its surface brightness, if one assumes a certain shape and inclination (Magorrian et al., 1998; Kronawitter et al., 2000). However, the deprojection is unique only for spherical

---

[8] If more than one of the merging galaxies contains a massive black hole, then galaxy mergers imply the formation of bound systems of massive black holes (Begelman et al., 1980) which can influence the stellar distribution on larger spatial scales than single supermassive black holes (Milosavljević and Merritt, 2003), and leave a "mass deficit" imprint in the galactic nucleus (Merritt, 2006).

systems, or axisymmetric systems viewed edge-on, i.e. for a viewing direction in the plane normal to the axis of symmetry (Rybicki, 1987; Gerhard and Binney, 1996). In principle, the stellar mass profile can then be inferred from the luminosity density, if the stellar mass-to-light ratio is known from stellar population or dynamical models.

1.3.2 Kinematics of ellipticals

The motions, or kinematics, of stars in elliptical galaxies contain fundamental information on the orbital structure and mass distribution of these systems, and can be measured from the absorption lines generated by the atmospheres of giant stars in the galaxy spectra. These absorption lines are broadened and shifted by the motion of stars along the line-of-sight. The line-of-sight velocity distribution (LOSVD) can be extracted from such broadening (Bender, 1990; Rix and White, 1992), and fitted by a Gaussian with mean V equal to the bulk motion of the stars, and width equal to the dispersion σ in the velocities of the stars along the line-of-sight. Deviations of the line profile from a Gaussian are commonly parameterised by Gauss-Hermite coefficients h_n, with odd/even Gauss-Hermite moments measuring skewed/symmetric deviations (van der Marel and Franx, 1993; Gerhard, 1993). Higher-order terms are of the greatest importance to constrain the anisotropy and mass distribution of ellipticals (Gerhard, 1993; Merritt, 1993).

Typical results from measuring the line profiles by fitting (V, σ, h_3, h_4) report velocity rotation curves which tend to rise in the very central galactic regions and then flatten out, and dispersion profiles that either stay flat or fall in the outer regions (Bender et al., 1994; Gerhard et al., 1999; Rix et al., 1999; Saglia et al., 2010b; Pu et al., 2010; Spolaor et al., 2010).

In recent years, the development of integral field units such as SAURON (Bacon et al., 2001), VIRUS-P (Hill et al., 2008), and DEIMOS (Proctor et al., 2009), has literally added a new dimension to the observations of nearby ellipticals, providing two-dimensional maps of the LOSVD moments typically out to $1R_e$ (*e.g.* Emsellem et al., 2004, 2011). Based on the huge amount of new kinematic data obtained with the survey ATLAS-3D conducted with SAURON, an alternative classification for early-type galaxies (ETGs) has been proposed by Cappellari et al. (2011), as shown in Fig. 1.4.

In this new framework, ETGs are divided into slow and fast rotators according to the stellar angular momentum λ_R that they possess per unit mass (Emsellem et al., 2007). The
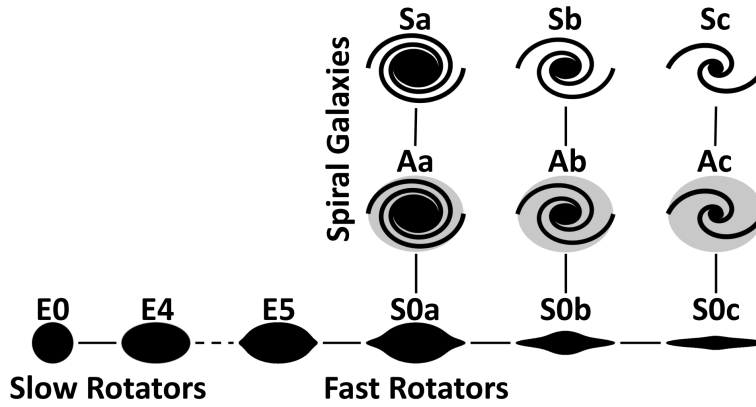
Figure 1.4: Classification of nearby galaxies from the ATLAS-3D sample (Cappellari et al., 2011). The ETGs are classified according to the absence of spiral arms or extended dust lanes.

two classes appear to have different dynamical properties: slow rotators are more massive and nearly round, with some triaxiality highlighted by significant kinematic misalignment (see Section 1.4.1), while fast rotators are rather flattened, nearly axisymmetric, and span a larger range of orbital anisotropies. Most ETGs (85%) are fast rotators (Emsellem et al., 2011). Different formation mechanisms have been proposed to explain the origin of fast and slow rotators (see Burkert et al., 2008, and references therein). In particular, it is believed that slow rotators accrete a lot of mass (50%-90%) and undergo up to three major mergers (Naab et al., 2006; Bois et al., 2011), while fast rotators accrete less than 50% of their mass, and experience less than one major merger during their life (Khochfar et al., 2011).

For many elliptical galaxies, kinematics have been accurately measured within $1 - 2R_e$, with only a few studies reaching out to $3 - 4R_e$ (*e.g.* Mehlert et al., 2000; Spolaor et al., 2010; Coccato et al., 2010), into the very interesting region where dark matter starts to dominate and the orbital timescales become long, so that one would expect that the signatures of formation processes are preserved longer. Lately, the effort of pushing kinematic observations towards the galactic halos has been undertaken measuring stellar LOSVDs from deep multi-object spectroscopic observations out to $3.5R_e$ (Proctor et al., 2009; Foster et al., 2011).

As will be shown in this thesis, the spatial coverage of the data, together with their quality, plays a fundamental role in limiting the degeneracies involved in the dynamical modeling of galaxies.

1.3.3   Kinematics from discrete tracers

Probing the mass distribution and kinematics of the outer halos of ellipticals is a task which is strongly thwarted by the rapid fall-off of the stellar surface brightness, which hinders measurements of the absorption line kinematics. A way to overcome such limitation is provided by the so called discrete tracers, i.e. populations of objects, such as planetary nebulae (PNe) or globular clusters (GCs), that can be used as test particles to trace the kinematics. The velocities of these discrete tracers can be measured even when the surface brightness is low.

PNe occur as a brief stage of stellar evolution, when stars with masses between $0.8 - 8M_{\odot}$ leave the asymptotic giant branch, and set forth to the white dwarf stage. In this rapid phase, stars are surrounded by an envelope of gas which converts up to 15% of their ultraviolet radiation energy in a bright [OIII] emission line (Dopita et al., 1992). At this wavelength, these little stars are incredibly brighter than anything else around them. This allows spectroscopic identification of PNe, and measurement of their line-of-sight velocities from Doppler shift. Thus, kinematics can be measured out to several effective radii of the galaxies, where the stellar density is too faint, and optical spectroscopy suffers from low signal-to-noise ratio. Indeed, the use of PNe allowed to measure two-dimensional velocity and velocity dispersion out to $6 - 9R_{\rm e}$ in nearby elliptical galaxies (*e.g.* Ciardullo et al., 1993; Hui et al., 1995; Arnaboldi et al., 1996; Méndez et al., 2001; Douglas et al., 2002; Teodorescu et al., 2005; Coccato et al., 2009).

GCs, instead, are near-spherical clusters of old stars which move as test particles in the galaxy potential (Harris, 1991), and they appear in large number in almost all elliptical galaxies. At the distance of ellipticals, these objects are nearly point-like sources, though very bright. Hence, after photometric identification, the absorption line kinematics in integrated spectra can be measured, even in the outer regions of galaxies. Being the ages of GCs comparable to the age of the Universe, these objects are valuable tools to investigate the earliest star formation episodes of their host galaxy. However, the observed colour bimodality of GC systems, commonly interpreted as a metallicity bimodality (Brodie and Strader, 2006), complicates the study of their kinematics (*e.g.* Côté et al., 2003; Strader et al., 2011). In particular, while the density and kinematics of PNe are generally in good agreement with those of the stars, there are indications that the (metal-poor) GCs may

not be in equilibrium with the bulk of the stellar population (*e.g.* Peng et al., 2004; Romanowsky et al., 2009; Das et al., 2011).

In order to place significant constraints on the mass distribution of galaxies, a sample of roughly $100 - 200$ radial velocities is needed, provided that some information on the stellar kinematics within the central galactic regions is available (Saglia et al., 2000; Romanowsky and Kochanek, 2001; Gerhard, 2006). Since typical samples of discrete tracers consist of a few hundred objects, only the mean velocity and velocity dispersion moments of the LOSVD can be accurately determined (but see Napolitano et al., 2009; Amorisco and Evans, 2012).

Whilst random errors in absorption line kinematics are dominated by the signal-to-noise (which depends on exposure time, wavelength range, and spectral resolution), random errors in kinematics from discrete tracers are typically dominated by the small numbers statistics, and attention must be paid to systematics, selection, and completeness of the sample of indicators.
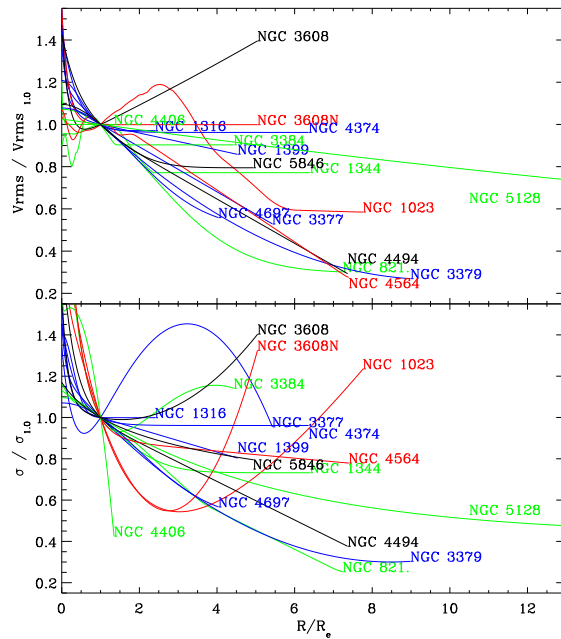
Figure 1.5: Mean RMS velocity (*top*) and velocity dispersion (*bottom*) profiles as a function of radius for the sample of elliptical galaxies studied in Coccato et al. (2009).

Combining absorption line kinematics and PNe velocities, Coccato et al. (2009) investigated the outer-halo kinematics of a sample of 16 early-type galaxies. An intriguing outcome of their study is shown in Fig. 1.5: galaxies fall into two groups, with either *slowly decreasing* or *steeply falling* mean RMS velocity profile $V_{\rm rms}^2 = \sigma^2 + V^2$. The few

ellipticals with rapidly falling velocity profiles, which suggest diffuse dark matter halos in some tension with the predictions of galaxy formation models (see Section 1.5.1), are the subject of this work.

Interestingly, Coccato et al. (2009) showed that the outer halo kinematics are correlated with other galaxy properties: brighter ellipticals, which are preferentially boxy in shape and have smaller values of V/σ (see Section 1.3.1), tend to have flatter mean RMS velocity profile. These galaxies are brighter both in B-magnitude and X-ray, and the reason for the correlation between the flat velocity profile and the X-ray emission is presumably that a massive halo is needed to keep the X-ray emitting gas. Ellipticals with declining RMS velocity profiles, instead, are generally less massive, and come in a wider range of shapes and V/σ ratios.

In general, galactic halos are characterized by more complex radial profiles of the specific angular momentum parameter λ_{R} than the ones observed within $1R_{\mathrm{e}}$ (see also Proctor et al., 2009). However, slow rotators have on average flatter mean RMS velocity profiles, whereas galaxies with steeply declining profiles are fast rotators.

1.3.4 Scaling relations

Elliptical galaxies are an amazing combination of complexity and regularity. Despite the complicated mechanisms behind their origins, and the observed dichotomy, they are characterized by several fundamental relations between the observed photometric and kinematic properties. These scaling relations have long been thought to contain important clues about the physical processes that shaped their formation and evolution (see *e.g.* the review by Renzini, 2006).

Scaling laws of ellipticals have been known since de Vaucouleurs (1948), who showed the similarity of their surface brightness profiles, and Fish (1964), who found a relation between potential energy and mass. Sandage (1972) discovered a color-magnitude relation obeyed by the elliptical galaxies belonging to Virgo and Coma clusters: the integrated colours of elliptical galaxies become bluer and bluer towards fainter magnitudes (see also Baum, 1959; Visvanathan and Sandage, 1977). A similar scaling law was found to hold for Local Group and cluster ellipticals (Faber, 1973), and it has been confirmed by many successive investigations (*e.g.* Bower et al., 1992). More massive ellipticals have older stellar populations and higher metallicity, which would both result in redder colours.

However, there are compelling evidences in favour of the metallicity origin for the color-magnitude relation (Kodama and Arimoto, 1997).

Faber and Jackson (1976) identified a relation between the magnitude and the velocity dispersion of elliptical galaxies, which encouraged them to propose that these systems belong to a one-parameter family, the mass being the parameter. The Faber-Jackson relation states that the total blue luminosity increases with velocity dispersion approximately as $L_{\rm B} \propto \sigma^4$ (see the analog for spiral galaxies by Tully and Fisher, 1977). Similarly, the Mg_2 absorption line index increases with velocity dispersion, and both the colour-magnitude and the $\text{Mg}_2 - \sigma$ relations are primarily sequences in galaxy stellar mass. At increasing stellar mass, as traced by either luminosity or velocity dispersion, the redder colour and Mg-absorption line strength along the relations reflect an increase in both total metallicity and α/Fe ratio[9] (*e.g.* Thomas et al., 2005a; Gallazzi et al., 2006). Furthermore, Kormendy (1977) showed that the surface brightnesses and effective radii of ellipticals correlate with luminosity and with one another. In particular, the more luminous galaxies are larger but have lower surface brightnesses.

As a matter of fact, both the Faber-Jackson and the Kormendy relation are important projections of a much tighter correlation which implies that elliptical galaxies lie on the so called Fundamental Plane in the three-dimensional space of $[\log(R_{\rm e}), \log(\sigma_0), I_{\rm e}]$ (Dressler et al., 1987; Djorgovski and Davis, 1987; Bender et al., 1992). The Fundamental Plane relation is a useful indicator of the distances of elliptical galaxies, as it allows to estimate $R_{\rm e}$ in physical units from the two distance-independent quantities σ and $I_{\rm e}$. Since the original formulation of this relation, the size and quality of early-type galaxy samples have been constantly improving (*e.g.* Bernardi et al., 2003; Gargiulo et al., 2009; Hyde and Bernardi, 2009; La Barbera et al., 2010; Graves and Faber, 2010; Saglia et al., 2010b) in the effort of understanding its intrinsic scatter (thickness) and its tilt relative to the two-dimensional surface defined by virial equilibrium. In particular, the tilt of the Fundamental Plane can result from either a non-homology of early-type galaxies, or a systematic variation of their mass-to-light ratio with mass, due to differing stellar populations and/or dark matter fractions (*e.g.* Ciotti et al., 1996; Busarello et al., 1997; Nipoti et al., 2003; Trujillo et al., 2004a; Bolton et al., 2007; Tortora et al., 2009).

---

[9] The α-elements are O, Ne, Mg, Si, S, Ar, Ca, and Ti, i.e. those that are built up by nuclear fusion reactions that consume α-particles nuclei. The α-Fe ratio quantifies the relative importance of Supernovae of Type Ia and II, and hence is used to constrain formation timescales (Greggio and Renzini, 1983; Matteucci and Greggio, 1986).

Finally, another remarkable correlation between the intrinsic properties of elliptical galaxies has been discovered more recently, and it relates the masses of supermassive black holes, which are present in the center of most galaxies (Kormendy & Richstone 1995), with the luminosity and even better with the velocity dispersion of their hosts (Magorrian et al. 1998; Ferrarese & Merritt 2000; Gebhardt et al. 2000; Tremaine et al. 2002; Graham & Driver 2007). The existence of such correlations provides strong evidence that the black hole growth and the evolution of its host galaxy directly influence one another (see *e.g.* Ciotti, 2009).

1.4 Dynamics of elliptical galaxies

PHILOSOPHY IS WRITTEN IN THAT GREAT BOOK
WHICH EVER LIES BEFORE OUR EYES - I MEAN THE UNIVERSE -
BUT WE CANNOT UNDERSTAND IT IF WE DO NOT FIRST LEARN THE LANGUAGE
AND GRASP THE SYMBOLS IN WHICH IT IS WRITTEN.
IT IS WRITTEN IN THE MATHEMATICAL LANGUAGE,
AND THE CHARACTERS ARE TRIANGLES, CIRCLES AND OTHER GEOMETRIC FIGURES,
WITHOUT WHOSE HELP IT IS IMPOSSIBLE TO COMPREHEND A SINGLE WORD OF IT;
WITHOUT THESE CHARACTERS ONE WANDERS THROUGH A DARK LABYRINTH IN VAIN.
Galileo Galilei

Elliptical galaxies contain up to hundreds of billions of stars which move according to Newton's laws of motion and Newton's law of gravity. Hence, a statistical approach can be profitably adopted in stellar dynamics, similar to that employed in classical statistical mechanics. However, there are some fundamental differences between stellar systems and other N-body systems like gases or plasmas, and they reside in the nature of the gravitational force, which is a *long-range interaction*, and which is always *attractive*.

The long-range nature of gravity implies that stars in galaxies rarely undergo physical collisions, unless they move in unusually crowed regions like galactic nuclei. Moreover, the graininess in these stellar systems can be neglected, since nearby stars have an unimportant perturbing effect on the gravitational force felt by any individual star. As a result, the gravitational force on any star does not change rapidly and unevenly as the star orbits, so that each star moves in the smooth average field generated by the galaxy as a whole - stars, gas, dust, and dark matter.

The lack of gravitational charges of opposite sign, instead, entails that stellar systems tend to form strongly inhomogeneous equilibria where in macroscopic terms gravity is balanced by a stellar-dynamic "pressure", or orbital anisotropy, as described below.

This Section summarizes the basic ideas on how the dynamics of stars in elliptical galaxies can be described and how dynamical models of observational data can be constructed.

1.4.1 Stellar orbits in elliptical galaxies

The dynamics of ellipticals are related to the trajectories, or orbits, of their stars. These are much more complicated in ellipticals than in disk galaxies, and range from highly eccentric, near-radial to tangential, near-circular orbits. The orbital distribution is defined *isotropic* if it consists of a balanced combination of orbits such that the local velocity dispersions in all directions are equal, and *anisotropic* otherwise. A wide range of anisotropies is possible, but systems with very strong radial anisotropy are unstable to the formation of a bar, and this instability limits the amount of radial anisotropy in the central galactic regions (Fridman and Poliachenko, 1984).

Most notably, the orbits of stars are distinguished according to the symmetry of the gravitational potential. Generally, they do not have a simple shape, and they are not closed, the two only exceptions being the point-mass Kepler potential and the homogeneous sphere harmonic potential.

Regular orbits in $2n$-phase-space possess n isolating integrals of motion[10] which shape their orbits. They can be formally decomposed into n independent periodic motions, and they lie on an n-dimensional manifold which is topologically equivalent to an n-torus. This is not true for irregular (stochastic) orbits, which may wander anywhere permitted by conservation of energy, with a complicated structure. It is generally believed that regular orbits provide a skeleton for the mass distribution that produces the gravitational potential, but stochastic orbits exist that populate phase-space regions avoided by regular orbits (de Zeeuw, 1985). Even if such stochastic orbits typically exhibit substantial variability on short timescales, it is still possible to characterize some statistical properties of ensembles of these orbits (*e.g.* Merritt and Fridman, 1996).

In any *spherically-symmetric potential*, all stars move on regular orbits, and have four isolating integrals: energy and angular momentum vector. The trajectories of stars are confined to a plane perpendicular to their angular momentum vector, and they consist of a combination of two periodic motions, in the radial and azimuthal direction, which can be represented as a path on a 2-torus. Stars typically move on rosette orbits, that

---

[10] An integral of motion $I(\mathbf{x}, \mathbf{v})$ is a function of the phase-space coordinates that stays constant along the orbit of a star. It is called isolating if it restricts motion to subspaces of phase-space.

is precessing ellipses confined between an inner pericentre radius and an outer apocentre radius in the orbital plane.

In any *axisymmetric potential*, there are two integrals of motion: energy and angular momentum component along the symmetry axis. In the plane perpendicular to the symmetry axis, in which the gravitational force is central, axisymmetric potentials are indistinguishable from spherical ones. Instead, the motion of stars beyond the equatorial plane can be reduced to the motion in a non-uniformly rotating meridional plane. For realistic galactic potentials, it is often found that most of the stellar orbits are regular, and that they respect an effective third integral of motion, for which in general there is no analytic expression (Contopoulos, 1963; Binney and Tremaine, 2008). In these systems a few stochastic orbits exist, which respect only the two classical integrals. However, in the general case the third integral does not exist. Stellar orbits can be grouped into topologically distinct families: in oblate axisymmetric potentials the main family is represented by the short-axis tube (or loop) orbits, whereas in prolate potentials the inner and outer long-axis tube orbits dominate.

Non-axisymmetric (triaxial) potentials admit an even richer and more intricate orbital structure (Statler, 1987), the only integral of motion being the energy. Long-axis and short-axis tube orbits still exist in non-rotating triaxial potentials, and by superposing them it is possible to arrange for intrinsic rotation field whose angular momentum vector can be aligned with any axis. This is a unique property of triaxial systems, and indeed represents a kinematic signature of triaxiality. Furthermore, a new orbital family dominates the backbone of these systems, the one of box orbits, which resemble Lissajous figures, carry stars arbitrarily close to the galactic center, and have an alternating sense of rotation.

1.4.2 Dynamical equilibria of ellipticals

Being the 2-body timescale, i.e. the time over which 2-body encounters significantly change stellar orbits, longer than the age of the Universe[11], elliptical galaxies are normally assumed to be collisionless. Since the dark halos of galaxies are believed to be composed of particles for which the collision-times are even longer, they can be described as collisionless fluids in phase-space as well.

---

[11] This may not be true in the central nuclei of ellipticals.

For a collisionless systems, the discreteness effects can be ignored, and the dynamics of any population of stars can be fully described by the so called distribution function (hereafter DF) or phase-space density $f(\mathbf{x}, \mathbf{v}, t)$, which represents the probability density of finding some stars in the small phase-space volume $d^3\mathbf{x}\, d^3\mathbf{v}$ centered on $(\mathbf{x}, \mathbf{v})$ at time t. In a statistical sense, f is the density of stars expected over an ensemble of equivalent systems sharing the same global (macroscopic) properties but having different detailed positions and velocities of the individual stars.

The motion of the phase-space fluid must conserve mass, that means particles are neither created nor destroyed. This is enough to derive the Vlasov (or collisionless Boltzmann) equation $Df/Dt = 0$, which, together with the Poisson's equation, are the fundamental equations of collisionless stellar dynamics (Henon, 1982; Binney and Tremaine, 2008).

The dynamical evolution of the DF is governed by the mean-field gravitational potential, and it is generally time-dependent. However, the smooth appearance and regular shapes of ellipticals suggest that they rest in a (nearly) steady-state equilibrium, so we can focus on describing equilibrium states of elliptical galaxies, i.e. time-independent solutions to the Vlasov equation. These equilibrium solutions are valid for timescales shorter than the evolutionary time.

Assuming that ellipticals are collisionless systems in steady state, their DF can depend on the phase-space coordinates only through the integrals of motion of the gravitational potential by Jeans' theorem. Only the isolating integrals are relevant (Lynden-Bell, 1962), and correspond to the action integrals on the orbital tori (Binney and Tremaine, 2008).

Jeans' theorem is commonly assumed in building equilibrium models of elliptical galaxies. Its global nature implies that different parts of a stellar system are dynamically coupled, so that the target galaxy should be modelled globally. Moreover, the global nature of the the integrals implies that knowing the density at one point on the torus means knowing it everywhere on it. This is why it is possible to construct a dynamical model from observations which are known only in a subspace of phase-space.

Two basic techniques have been devised to construct galaxy models: that from the DF f to the spatial density ρ, and that from ρ to f (Dejonghe, 1986; Bertin, 2000; Binney and Tremaine, 2008). The distribution function priority method (from f to ρ) proceeds choosing a physically-based DF, and then obtaining the density distribution via

the equation

$$\rho(\mathbf{x}) = \int f(\mathbf{x}, \mathbf{v}) d^3 \mathbf{v}. \tag{1.2}$$

In the self-consistent case in which the density determines the gravitational potential through Poisson's equation, the potential can also be obtained. Solving the so called Jeans' problem (from ρ to f) requires instead an inversion of the integral equation above for a specific potential-density pair. Since the distribution function is generally not known a priori, modelers normally adopt the second approach, but more than ρ is used nowadays to constrain f, and dynamical models need to be capable of matching an increasing amount of observational data of diverse kind.

In particular, observance of the full LOSVD allows to reconstruct the DF in the case in which the potential is known (Dejonghe and Merritt, 1992), or to put constraints on both the DF and the gravitational potential in the more general case in which the latter is not known in advance (Merritt and Saha, 1993; Gerhard, 1993).

In any case, the solution to the Jeans' inversion problem does not always exist, since some consistency requirements ($f > 0$) should be imposed (*e.g.* Ciotti and Morganti, 2009, 2010a). Also, the solution is generally not unique, and many DFs might exist that reproduce the data. In fact, the hot nature of elliptical galaxies gives them great freedom in the way stellar orbits can be arranged. Unfortunately, this means that velocity dispersion profiles alone (plus streaming velocity profile, in the case in which the galaxy has some rotation) are not enough to determine the mass distribution, due to a inherent degeneracy with orbital anisotropy (Binney and Mamon, 1982). Such degeneracy is amplified further by the uncertainties related to the actual shape of elliptical galaxies and our viewing geometry, so that many solutions can be found that are equally compatible with the observational data, and assumptions are necessary in order to obtain a unique answer.

Different methods to construct dynamical models which match the observational data are available, as discussed below.

1.4.3 Dynamical models

The modeling of photometric and kinematic observational data is of the greatest importance to infer the intrinsic properties of elliptical galaxies, and ultimately understand their origin and evolution. Dynamical models are an essential tool to determine the mass,

gravitational potential, orbital structure, and phase-space DF from the observed data. First, a measurement of the total mass and of the mass profile of stellar systems is a key element to constrain the mass-to-light ratio of the stars, equivalent to the stellar initial mass function, and the amount and radial distribution of dark matter, in order to compare real galaxies with the predictions of numerical models of galaxy formation. Second, a measurement of the total gravitational potential, which plays a fundamental role in shaping the orbital structure, can only be done indirectly via dynamical models, a part from the cases of X-ray bright elliptical galaxies (see the review by Buote and Humphrey, 2012), or early-type lens galaxies (*e.g.* Treu and Koopmans, 2004). Finally, the orbital structure, and the 6-coordinates DF of the stellar populations and sub-populations, can only be constrained or recovered via dynamical modeling.

Different techniques to create models which reproduce the observational data have been devised, and we now briefly describe each one of them in turn. Even if it is not clear whether the usual modeling assumptions, *e.g.* dynamical equilibrium, gravitational potential, symmetry, anisotropy, are fully justified, in principle dynamical models can also be used to test the validity of these assumptions.

Moment-based (Jeans) models   Rather than undertaking the venture of solving the Vlasov equation, one can consider a set of moment equations (Dejonghe, 1986; Binney and Tremaine, 2008). The system of moment equations is often not closed, but there are important cases in which it can be closed and solved, and in these cases one can gain valuable insights.

For instance, in spherical stellar systems, combining the first two equations of the hierarchy results in the first-order Jeans equations, which read simply

$$\frac{d(\rho\sigma_{\rm r}^2)}{dr} + \frac{2\beta\rho\sigma_{\rm r}^2}{r} = -\rho\frac{d\phi}{dr}, \tag{1.3}$$

where ϕ is the total gravitational potential, and ρ and $\sigma_{\rm r}$ are the density and the radial velocity dispersion of any tracer population which moves in the potential. The anisotropy parameter

$$\beta(r) \equiv 1 - \frac{\sigma_{\rm t}^2}{2\sigma_{\rm r}^2} \tag{1.4}$$

(Binney and Mamon, 1982), where $\sigma_{\rm t} = \sqrt{(\sigma_\vartheta^2 + \sigma_\phi^2)/2}$ is the tangential velocity dispersion, quantifies the anisotropic pressure of stellar motions. $\beta = 0$ identifies an

isotropic orbital distribution, whereas $\beta \to 1$ and $\beta \to -\infty$ describe radial and tangential departures from orbital isotropy, respectively. If the DF depends only on energy, then the velocity distribution is isotropic everywhere ($\beta = 0$). Instead, values of $\beta \neq 0$ are determined by the way in which the DF depends on the angular momentum. In consistent stellar systems, i.e. systems whose DF is non-negative, the value of the anisotropy parameter is linked to the slope of the density profile (An and Evans, 2006; Ciotti and Morganti, 2010b).

Assuming that the system is isotropic, i.e. $\beta = 0$, the equation above can be simply integrated based on inverted ρ and σ_r, which are derived from the actual measured quantities (surface brightness and line-of-sight velocity dispersion). Instead, the typical way to solve the Jeans equations for anisotropic models is to assume a specific functional form for $\beta(r)$ and then treat equation (1.3) as a first-order linear differential equation for $\rho\sigma_r^2$. Different choices of $\beta(r)$ yield different predictions for the line-of-sight velocity dispersion profile, and the anisotropy parameter can then be constrained optimizing the fit to the observations.

Jeans equations have been extended to the axisymmetric case, assuming a constant mass-to-light ratio and a velocity ellipsoid that is aligned with cylindrical coordinates (*e.g.* Cappellari, 2008), and also to triaxial galaxies (van de Ven et al., 2003) with separable potentials (de Zeeuw, 1985).

Since the Jeans equations relate quantities which are observationally accessible, such as the surface density and the velocity dispersion profile, they constitute a valuable tool to model galaxies. The technique is very simple, and it has proven to be extremely useful in a large variety of applications (*e.g.* Young, 1980; Binney and Mamon, 1982; Binney et al., 1990; Magorrian and Binney, 1994; Lokas, 2002; Williams et al., 2009; Cappellari et al., 2009a). Among the drawbacks of these moment-based methods are the need for assumptions to close the system of equations, the lack of any guarantee on the positivity of the underlying DF (consistency requirements), and the difficulties in modeling higher order information such as the LOSVD (but see Lokas and Mamon, 2003).

Models with distribution functions Jeans' theorem naturally brings up the idea of representing galaxies as a superposition of functions of the integrals of motion, and fit the observations with combinations of parametrized functions of the integrals of motion or of

the action integrals of orbits.

Such DF-based methods have been explored in spherical or integrable systems (*e.g.* Dejonghe, 1986; Dejonghe and de Zeeuw, 1988; Gerhard, 1991; Hunter and de Zeeuw, 1992; Carollo et al., 1995; Kronawitter et al., 2000), axisymmetric models (see *e.g.* Hunter and Qian, 1993; Dehnen and Gerhard, 1994; Kuijken, 1995; Magorrian, 1995; Merritt, 1996), and nearly integrable potentials (*e.g.* Dehnen and Gerhard, 1993; Matthias and Gerhard, 1999; Binney, 2010).

The main advantage of these techniques is that they obviously access the full phase-space DF directly, although generally requiring assumptions on the symmetry of the target galaxy.

Schwarzschild models The integrals of motion define a torus in phase-space, which is traced out by the orbits of stars. Therefore, by Jeans' theorem, the DF can be regarded as a function of the orbits, and the problem can be handled with numerical orbit integration, desisting from the analytic approach.

This is the basic idea behind the Schwarzschild method (Schwarzschild, 1979, 1993), which is essentially a way to solve an optimization problem: a trial potential is assumed, a large library of orbits in that potential is computed, and finally the contribution of each orbit is adjusted so to reproduce the observed photometry and kinematics. A sequence of trial potentials can be explored, and $\Delta\chi^2$ analysis can be used to infer confidence levels on the best-fitting model (Press et al., 1992).

Orbit-based models do not place any assumption on the orbital anisotropy, and they can use any kind of kinematic information, including higher order moments of the LOSVD, and discrete kinematic tracers (*e.g.* Chanamé et al., 2008). Of course, the orbit library needs to be constructed so as to provide a good sampling of phase-space (see *e.g.* Thomas et al., 2004; van den Bosch et al., 2008).

Schwarzschild modeling is very powerful, and it has been extensively used (*e.g.* Richstone and Tremaine, 1985; Rix et al., 1997; van der Marel et al., 1998; Cretton et al., 1999; Cappellari et al., 2012; Gebhardt et al., 2003; Valluri et al., 2004; Thomas et al., 2005b; van den Bosch and de Zeeuw, 2010), although applications are mostly restricted to axisymmetric systems. A shortcoming of the method is that it requires the computation of a large and representative orbit library for every new trial potential.

Made-to-measure particle models A yet different numerical approach to the problem consists of representing the target galaxy with a N-body particle system. Provided particles explore the available phase-space reasonably well, then the DF (or at least mass distribution function) can be mapped out in a statistical sense by following the particles along their orbits, in analogy with the Schwarzschild technique.

Particle-based methods work by slowly correcting the individual weights of particles as they are evolved in the gravitational potential, following the idea of Syer and Tremaine (1996). The correction of the particle weights aims at finding a satisfactory compromise between the goodness of the fit to the observational data, and some degree of smoothness (regularization) of the underlying particle model. Density and kinematic observables are used simultaneously in the weight correction by minimizing χ^2-deviations between data and particle model (de Lorenzi et al., 2007), as will be explained in Chapter 2. A new regularization method for spherical and axisymmetric made-to-measure particle models will be presented in this thesis, that facilitates recovering both a smoother and more accurate DF (Morganti and Gerhard, 2012).

The particle-method was first applied to the Milky Way's bulge and disk in Bissantz et al. (2004). Then, a version modified to model observational data with errors was implemented in the parallel code NMAGIC by de Lorenzi et al. (2007). So far, NMAGIC has been used to investigate the dynamics of the outer halos of two intermediate-luminosity elliptical galaxies, NGC 4697 and NGC 3379 (de Lorenzi et al., 2008, 2009), and of a massive elliptical galaxy, NGC 4649 (Das et al., 2010a).

Recent implementations of the particle method can be found in Dehnen (2009), who proposed a different technique for the weight adaptation, and Long and Mao (2010), who modelled a sample of SAURON elliptical and lenticular galaxies (Long and Mao, 2012) with a technique similar to NMAGIC. A related particle method but with a different way of adjusting to the observational constraints is the iterative technique of Rodionov et al. (2009).

Among the main strengths of the particle technique are its geometric flexibility, the fact that the potential can be evolved self-consistently from the particles, and that there is no need to specify integrals of motion or stellar orbits a priori. Several relevant issues are still open regarding made-to-measure particle models, and particularly the recovery of the unique solution, and the way in which we fit models to data and draw inferences

from these fits. We will come back to these issues in the next chapters.

1.5   The outer halos of elliptical galaxies

<div align="right">
There is no dark side of the moon, really.
As a matter of fact, it's all dark.
Pink Floyd
</div>

1.5.1   Dark halos

The structures in our Universe, at both small and large scales, are not constituted by the luminous matter alone. Instead, some sort of dark component, whose exact nature is still unknown[12], makes up for the dominant fraction of their mass.

At the largest scales of galaxy clusters, there is overwhelming evidence of dark matter from the mass profiles derived applying virial theorem arguments to the velocities of galaxies (*e.g.* Zwicky, 1937), hydrostatic equilibrium to the X-ray emitting intracluster medium (*e.g.* Sarazin, 1988), and gravitational lensing techniques (*e.g.* Mellier et al., 1993; Schindler et al., 1995).

At smaller scales, dark matter manifested much earlier in spiral galaxies than in ellipticals, due to the presence of an ideal diagnostic like the neutral hydrogen HI in the disk (*e.g.* van Albada and Sancisi, 1986; Persic et al., 1996). The remarkable flatness of the rotation curve of the extended disk of cold gas provides convincing evidence that the luminous matter alone is not enough to explain the total gravitational potential, unless alternative theories of gravitation, such as the Modified Newtonian Gravity (Milgrom, 1983), are considered. Accordingly, spiral galaxies are believed to reside in extended dark matter halos.

Dark matter in dwarf galaxies was first suggested by Faber and Lin (1983), and measurements of stellar velocity dispersions indicate that dwarf galaxies possess the highest mass-to-light ratios of any known galactic systems. (*e.g.* Koch et al., 2007; Mateo et al., 2008; Walker and Peñarrubia, 2011). It is still much debated whether flat cores, rather than the cusps predicted by dissipationless cold dark-matter models, exist in the central regions of dwarf galaxy halos. In particular, observations of central cores

---

[12] Baryons as candidate for dark matter are ruled out by astrophysical and cosmological evidence (Gaitskell, 2004). Non-baryonic candidates are classified as hot and cold dark matter depending on their kinematical state (relativistic/non-relativistic) in the early universe, at the time of decoupling of light and matter. Hot dark matter is ruled out by measurements of the Cosmic Microwave Background and the clustering of galaxies (*e.g.* Tegmark et al., 2004; Cole et al., 2005; Seljak et al., 2006). An intermediate state called warm dark matter is also a viable possibility (*e.g.* Bode et al., 2001; Avila-Reese et al., 2001).

(*e.g.* Carignan and Beaulieu, 1989; de Blok et al., 2001; Lokas, 2002; de Blok et al., 2008) have also been interpreted as evidence for warm dark matter (*e.g.* Moore, 1994).

A crucial prediction of the hierarchical scenario for galaxy formation (see Section 1.2) is that every galaxy, ellipticals included, should be embedded in a dark matter halo. Indeed, dark matter is also inferred in elliptical galaxies, as detailed below.

Knowing the dark matter distribution in galaxies is of the greatest importance not only to verify the predictions of galaxy formation theories, but also to constrain their major-assembly epoch, which, due to the collisionless nature of dark matter, is related to the halo concentration (*e.g.* Navarro et al., 1996; Wechsler et al., 2002).

The evidence of dark matter in ellipticals is much more challenging than in spiral galaxies, because of a lack of an ubiquitous kinematic tracer of immediate interpretation such as the cold gas. In fact, only rarely ellipticals harbor extended gas disks or rings that can be used as direct tracers of the total potential (*e.g.* Bertola et al., 1993; Franx et al., 1994; Oosterloo et al., 2002; Weijmans et al., 2008). In general, the presence of dark matter in elliptical galaxies is inferred from modelling the dynamics of stars, from hydrostatic equilibrium of their X-ray emitting gas, and from gravitational lensing.

The first stellar dynamical evidence of dark matter halos came from the measurements of a slowly decreasing velocity dispersion profile in the three elliptical galaxies NGC 4472, IC 4296, and NGC 7144 (Saglia et al., 1993). Subsequently, considerable improvement of the quality of spectroscopic data allowed an accurate modeling of the observed LOSVD (including higher order moments), and eventually ascertained the presence of dark halos around ellipticals in nearby groups of galaxies, as well as in the Virgo, Fornax, and Coma galaxy clusters (*e.g.* Kronawitter et al., 2000; Gerhard et al., 2001; Cappellari et al., 2006; Thomas et al., 2007b, 2009b; Tortora et al., 2009). Kinematic information from discrete tracers such as PNe and GCs represents a key element to probe the mass distribution and orbital structure of elliptical galaxies well beyond $2R_{\mathrm{e}}$, out in the halo (*e.g.* Méndez et al., 2001; Douglas et al., 2002; Peng et al., 2004; de Lorenzi et al., 2008, 2009; Napolitano et al., 2009; Das et al., 2011; Napolitano et al., 2011; Deason et al., 2012). As explained in Section 1.4, dynamical evidence of dark halos is complicated by the fact that the stellar orbits are not known a priory, and different orbital distribution may give the same distribution of light. Also, while the total mass of a galaxy can be inferred via dynamical modeling, assessing the relative contribution of the stellar and dark matter components

is much harder (*e.g.* Thomas et al., 2007b; Deason et al., 2012).

The best-fitting dynamical models are generally consistent with a total flat circular velocity curve (see *e.g.* Ciotti et al., 2009) similar to the rotation curves measured in spirals. These models have dark matter fractions of $10\% - 50\%$ of the total mass within $1R_e$, and higher values at $4R_e$ (Thomas et al., 2007b; Weijmans et al., 2009). There are indications that such dark matter fractions are lower for fast rotators than for slow rotators (Cappellari et al., 2006).

So far, the greatest evidence for dark matter is confined to the bright giant elliptical galaxies, for which it is possible to map the mass distribution using X-ray emission of hot gas (*e.g.* Loewenstein and White, 1999; Mathews and Brighenti, 2003; Fukazawa et al., 2006; Humphrey et al., 2006; Nagino and Matsushita, 2009; Das et al., 2010b) or strong gravitational lensing techniques combined with stellar dynamics (*e.g.* Maoz and Rix, 1993; Keeton, 2001; Treu and Koopmans, 2004; Auger et al., 2010a). On the whole, these studies agree that, at least for the more massive ellipticals (and lenticulars), dark matter halos are generally present, and the total mass density profile is consistent with being isothermal, i.e. the potential is logarithmic, similar to disk galaxies (*e.g.* Gavazzi et al., 2007; Bolton et al., 2008; Koopmans et al., 2009; Churazov et al., 2010; Grillo, 2012).

Unfortunately, this kind of analysis are feasible for only a fraction of ellipticals (Pellegrini et al., 2007), and the situation with less-luminous, X-ray faint, intermediate-mass elliptical galaxies is much more challenging. Originally, the observations of surprisingly low PNe radial velocities in the outskirts of ordinary ellipticals have been interpreted as an odd signature of "naked" halos, characterized by very low dark matter fractions (Ciardullo et al., 1993; Méndez et al., 2001; Romanowsky et al., 2003; Douglas et al., 2007). However, advanced dynamical models, using NMAGIC, have shown that the observational data of two of these galaxies, NGC 4697 and NGC 3379, are consistent with dark matter halos and radially anisotropic stellar distributions (de Lorenzi et al., 2008, 2009). These halos are typically more diffuse than those found for the X-ray bright galaxies. Radial orbits may mask the dark matter distribution, and projection effects when viewing a triaxial elliptical may also produce lower line-of-sight velocity dispersions (Dekel et al., 2005).

The combined modeling of kinematics from absorption line spectra plus radial velocities of discrete tracers is roughly consistent with the simple picture where less-luminous

ellipticals are also embedded in dark matter halos, with dark matter fractions $\sim 50\%$ at $5R_{\rm e}$ (Napolitano et al., 2009; Deason et al., 2012).

Results from stellar dynamical models, which for massive systems are confirmed by X-ray and lensing studies, are broadly consistent with the predictions of high-resolution simulations of galaxy formation (*e.g.* Dekel et al., 2005; Mamon and Lokas, 2005; Naab et al., 2007; Oñorbe et al., 2007). It is anyway important to keep in mind that the simulations are still quite sensitive to the specific implementations of baryonic physics.

1.5.2 Stellar halos and constraints on galaxy formation

The mechanisms responsible for the build-up of elliptical galaxies have been an open issue in astrophysics for a long time. The smooth morphology and dynamically hot nature of these galaxies, together with their long ages and old stellar populations, and with the relatively short star formation timescales implied by the α-enrichment, suggest that they are the result of a formation episode far back in time, characterized by violent relaxation in phase-space (Lynden-Bell, 1967; Spergel and Hernquist, 1992). This is also consistent with the observations of massive elliptical galaxies at high redshift (*e.g.* Franx et al., 2003; Daddi et al., 2004; Glazebrook et al., 2004), and with the tightness of the observed scaling relations and their slow evolution with redshift (*e.g.* van Dokkum et al., 2000; Blakeslee et al., 2003). Meanwhile, many pieces of evidence favour the merging hypothesis (*e.g.* van Dokkum, 2005, and references therein). Most likely, galaxy formation is a combination of dissipative and dissipationless processes.

Elliptical galaxies today are collisionless to a very good approximation, hence they retain a wealth of information about their formation pathways in the present-day orbital structure. These relics of their formation history are especially preserved in the galactic halos, due to longer dynamical timescales.

For instance, a dynamically violent assembly process results in a well mixed distribution of orbits, without strong gradients in the phase-space density. By contrast, dissipational evolution, *e.g.* through wet mergers, ends up more likely in disky remnants, with phase-space density peaks on orbits with high angular momentum (*e.g.* Dehnen and Gerhard, 1994; Thomas et al., 2009a).

Hence it is clear that the recovery of the dynamical structure of elliptical galaxies gives valuable information about the history of these systems.

Typical results of spherical models fitting the observational data show that the orbital structure of ellipticals is radially biased, a part from the very central regions (Rix et al., 1997; Gerhard et al., 1998; Kronawitter et al., 2000; Gerhard et al., 2001; Magorrian and Ballantyne, 2001; Houghton et al., 2006). Some mild radial anisotropy is also found using gravitational lensing techniques (*e.g.* Koopmans et al., 2009). A gradual change from central isotropy to strong outer radial anisotropy is the fingerprint of the classical "monolithic collapse" in the orbital structure (van Albada, 1982). Also, a radially anisotropic orbital composition can be seen as a result of accretion processes during galaxy formation. Axisymmetric dynamical models of elliptical galaxies have found a variety of orbital distributions (*e.g.* Matthias and Gerhard, 1999; Emsellem et al., 1999; Cretton et al., 2000; Verolme et al., 2002; Gebhardt et al., 2003; Copin et al., 2004; Cappellari et al., 2006; Thomas et al., 2009b), and this might also be a consequence of the fact that spherical models are typically constructed for the more massive round galaxies, whose formation is characterized by significant accretion, whereas axisymmetric models for the smaller disky ellipticals. A large variety of orbital configurations can be naturally interpreted as a consequence of different initial conditions in the specific merging configuration.

In this respect, a very promising avenue of research is represented by the comparison of the orbital structure derived from dynamical models of observed galaxies with that of simulated galaxies (*e.g.* Sáiz et al., 2004; Jesseit et al., 2005; Burkert and Naab, 2005; Burkert et al., 2008; Thomas et al., 2009a). In the literature, simulated merger remnants rotate slowly, and have radially anisotropic velocity distributions, due to the accretion of smaller sub-units onto the central object (Abadi et al., 2006; Naab et al., 2009). Dissipational processes in wet mergers may decrease the level of radial anisotropy (*e.g.* Naab et al., 2006; Thomas et al., 2009b) and explain many of the features observed in real ellipticals, including counter-rotating disks and kinematically decoupled components (*e.g.* Cox et al., 2006; Jesseit et al., 2007; Hoffman et al., 2010).

1.6 Aims and structure of this thesis

> It would be so nice
> if something made sense
> for a change.
> *Lewis Carroll*

The goal of the present thesis is to improve our knowledge about the mass distribution

and dynamical structure of the intermediate-luminosity elliptical galaxies, and also about the made-to-measure modelling technique. In particular, we present significant improvements to the made-to-measure particle method, which is relatively unexplored but highly promising, since in principle it is simpler to use, and more general, than the Schwarzschild method. The class of intermediate-luminosity elliptical galaxies with rapidly decreasing velocity dispersion profiles represents a particularly interesting target for dynamical modeling, as their surprisingly fast-decreasing velocity profiles have cast doubts on the presence of dark matter (*e.g.* Romanowsky et al., 2003; Douglas et al., 2007).

The first, "methodological" part of this thesis is devoted to answer to some questions which are important to address in order to draw robust conclusions from made-to-measure particle models of galaxies:

- How reliable are made-to-measure particle models of the observational data? To which level of accuracy can particle models recover the phase-space distribution function and intrinsic properties of a target galaxy?

- For a given set of observational data, how much does the final particle model depend on the initial one? How worse does the situation get with incomplete or noisy data?

- Given a realistic data set, how well can the characteristic parameters of the dark matter halo of galaxies be recovered with made-to-measure methods? Which is the uncertainty, or the level of accuracy, for dark halo parameter estimates?

As we will see in Chapter 2, the issue of an efficient regularization method for particle models arises naturally from the first two questions above. Therefore, we will introduce an alternative technique to regularize made-to-measure particle models, which enforces a correct and unbiased recovery of the target galaxy from noisy observational data.

Then, in the second part of this thesis we will apply our improved made-to-measure particle method to study the dynamics of the intermediate-luminosity elliptical galaxy NGC 4494 (Chapter 3). The main goal of this part of the work is to constrain the dark matter halo of NGC 4494; in particular, our axisymmetric NMAGIC models explore a sequence of dark matter halos, and different inclinations, and fit photometric and kinematic observational data which extend beyond $3R_{\rm e}$, and include PNe radial velocities and - for the very first time - new absorption line kinematics data in slitlets placed all

around the galaxy. The questions that we would like to answer with our dynamical models are:

- What is the mass distribution, and dark matter fraction of NGC 4494? Do the observational data require dark matter, or are they rather consistent with the picture of a "naked" galaxy?

- What is the orbital structure of the stars in NGC 4494, and which formation channels are suggested for this intermediate-luminosity elliptical?

- Are the halos of the three intermediate-luminosity ellipticals with rapidly falling velocity dispersion profiles modelled so far with NMAGIC (NGC 4697, NGC 3379, NGC 4494) similar, or do they differ? And what about their orbital structure?

Finally, the thesis will close in Chapter 4 with a summary and an outlook of future directions of research.

2

Regularizing made-to-measure particle models of galaxies

Made-to-measure methods such as the parallel code NMAGIC are powerful tools to build galaxy models reproducing observational data. They work by adapting the particle weights in an N-body system until the target observables are well matched. In this Chapter we introduce a moving prior regularization (MPR) method for such particle models. It is based on determining from the particles a distribution of priors in phase-space, which are updated in parallel with the weight adaptation. This method allows one to construct smooth models from noisy data without erasing global phase-space gradients. We first apply MPR to a spherical system for which the distribution function can in theory be uniquely recovered from idealized data. We show that NMAGIC with MPR indeed converges to the true solution with very good accuracy, independent of the initial particle model. Compared to the standard weight entropy regularization, biases in the anisotropy structure are removed and local fluctuations in the intrinsic distribution function are reduced. We then investigate how the uncertainties in the inferred dynamical structure

increase with less complete and noisier kinematic data, and how the dependence on the initial particle model also increases. Finally, we apply the MPR technique to the two intermediate-luminosity elliptical galaxies NGC 4697 and NGC 3379, obtaining smoother dynamical models in luminous and dark matter potentials.

2.1   Introduction

In galactic dynamics, the modelling of photometric and kinematic observations is of great importance to infer intrinsic properties of galaxies such as their orbital structure, total gravitational potential, and phase-space distribution function (DF). As detailed in Chapter 1, different techniques to create made-to-measure systems reproducing the observational data have been devised, and can be broadly grouped in DF-based, moment-based, orbit-based, and particle-based methods [see also Syer and Tremaine (1996, hereafter ST96)].

DF-based methods fit observations with parametrized functions of the integrals of motion or of the action integrals of orbits. Applications include spherical or integrable systems (*e.g.* Dejonghe, 1986; Dejonghe and de Zeeuw, 1988; Gerhard, 1991; Hunter and de Zeeuw, 1992; Carollo et al., 1995; Kronawitter et al., 2000), axisymmetric models (see *e.g.* Hunter and Qian, 1993; Dehnen and Gerhard, 1994; Kuijken, 1995; Magorrian, 1995; Merritt, 1996), and nearly integrable potentials (*e.g.* Dehnen and Gerhard, 1993; Matthias and Gerhard, 1999; Binney, 2010). The main advantage of these methods is that they provide the phase-space DF directly, although they generally require assumptions on the symmetry of the target galaxy.

Moment-based methods find solutions of the Jeans equations that best reproduce observed quantities such as surface density and velocity dispersion (*e.g.* Young, 1980; Binney and Mamon, 1982; Binney et al., 1990; Magorrian and Binney, 1994; Lokas, 2002; Cappellari, 2008; Williams et al., 2009; Cappellari et al., 2009a). Among the drawbacks of these methods are the need for assumptions to close the system of equations, the lack of any guarantee on the positivity of the underlying DF, and the difficulties in modelling higher order information such as the line-of-sight velocity distribution (LOSVD).

Orbit-based methods (Schwarzschild, 1979, 1993) compute a large library of orbits in a fixed potential, and then adjust the weight of each orbit until the photometry and

kinematics of the target galaxy are well matched (*e.g.* Richstone and Tremaine, 1985; Rix et al., 1997; van der Marel et al., 1998; Cretton et al., 1999; Cappellari et al., 2002, 2006; Gebhardt et al., 2003; Valluri et al., 2004; Thomas et al., 2005b; van den Bosch and de Zeeuw, 2010). Schwarzschild modelling is widely used, *e.g.* to infer the masses of black holes at the centers of galaxies, but applications are mostly restricted to axisymmetric systems. Moreover, the technique requires the computation of a large and representative orbit library for every new trial potential.

Particle-based methods for the most part work by slowly correcting individual weights of particles as they are evolved in the gravitational potential (ST96), until the N-body system reproduces the observational data. Kinematic and density observables can be used simultaneously in the weight correction by minimizing χ^2-deviations between data and particle model (de Lorenzi et al., 2007, hereafter DL07). Among the main strengths of this so-called made-to-measure (M2M) technique are its geometric flexibility, the fact that the potential can be evolved self-consistently from the particles, and that there is no need to store an orbit library.

The M2M method was first applied to the Milky Way's bulge and disk in Bissantz et al. (2004). A version modified to model observational data with errors (χ^2M2M) was implemented in the parallel code NMAGIC by DL07. This has been used to investigate the dynamics of the outer halos of the two intermediate-luminosity elliptical galaxies NGC 4697 and NGC 3379 (de Lorenzi et al., 2008, 2009, hereafter DL08; DL09), and of the massive elliptical galaxy NGC 4649 (Das et al., 2010a). More recent implementations of the M2M method can be found in Dehnen (2009), who proposed a different technique for the weight adaptation, and Long and Mao (2010). A related particle method but with a different way of adjusting to the observational constraints is the iterative technique of Rodionov et al. (2009).

M2M techniques are very promising, but relatively unexplored. It is therefore a natural question whether these particle methods can actually recover the phase-space DF of a target galaxy if the data uniquely specify it. For a given set of data, how much does the final particle model depend on the initial one? And how is this dependence influenced by incomplete or noisy data? Furthermore, given that a system of N particles is trained to match a much smaller number of observational constraints, the problem arises of reducing model degeneracies and preventing the method from fitting the noise in the data.

The above issues are related and are connected to the concept of regularization. In standard χ^2M2M practice, a weight entropy is used to regularize the particle model: through the entropy function all particle weights are biased towards a smooth distribution of predefined priors, which are specified together with the initial model, and thus implicitly contain assumptions about the dynamical structure of the target galaxy. Therefore, unless the dynamical structure of the galaxy is known beforehand, smoothing with weight entropy makes it difficult to construct models with strong phase-space gradients, *e.g.* between near-radial and near-circular orbits. This is discussed further in Section 2.2 below. A similar effect arises in Schwarzschild models regularized using maximum-entropy constraints (Richstone and Tremaine, 1988), which tend to isotropize the final DF (*e.g.* Thomas et al., 2005b).

In this Chapter we describe a new Moving Prior entropy Regularization (MPR) method based on the idea of a distribution of particle priors, which are computed according to phase-space occupation and which evolve together with the adaptation of the particle weights. The new method minimizes the dependence of the solution on the adopted initial particle model, and facilitates recovering both a smoother and more accurate DF, reducing local fluctuations without erasing global phase-space gradients.

The Chapter is organized as follows. In Section 2.2 the basics of the χ^2M2M method are laid out, the main concerns related to the traditional regularization are explained, and our implementation of MPR is developed. In Section 2.3 a series of spherical target models is constructed for testing the M2M method with MPR. Then, in Section 2.4 and 2.5 we investigate the different roles played by regularization, initial particle model, and data quality for recovering the correct galaxy model, and we show that the true solution can indeed be recovered from sufficiently good data. Finally, two astrophysical applications are presented in Section 2.6, where we reconstruct regularized NMAGIC models for the two intermediate-luminosity elliptical galaxies NGC 4697 and NGC 3379 in their dark matter halos.

2.2   Regularization of particle models

In this Section we outline the χ^2M2M method, and discuss some issues related to its standard (weight entropy) regularization. An alternative method to regularize M2M

particle models is then presented.

2.2.1 The χ^2M2M technique to model observational data

The goal of the χ^2M2M method (DL07) is to evolve an N-body system of particles orbiting in a potential to make it reproduce the observables of a target galaxy. The potential can be either fixed and known *a priori*, or time-varying and self-consistently computed from the particles.

Each particle is characterized by its phase-space coordinates $\mathbf{z}_i = (\mathbf{r}_i, \mathbf{v}_i)$ and by a weight w_i. The particles should be interpreted in a probabilistic sense: they do not represent single stars but rather phase-space fluid elements (*e.g.* Hernquist and Ostriker, 1992). If M is the total stellar mass of the system, then individual particles have masses $m_i = w_i M / \sum_{i=1}^{N} w_i$.

An observable of a target galaxy characterized by a distribution function $f(\mathbf{z})$ is defined as

$$Y_j = \int K_j(\mathbf{z}) f(\mathbf{z}) \, \mathrm{d}^6 z, \tag{2.1}$$

where K_j is an appropriate kernel and $\mathbf{z} = (\mathbf{r}, \mathbf{v})$ are the phase-space coordinates.

Given a set of observables Y_j, $j = 1, ..., J$, including *e.g.* photometry and kinematics, the particle weights w_i of the N-body system are evolved until the model observables

$$y_j(t) = \sum_{i=1}^{N} w_i K_j \left[\mathbf{z}_i(t)\right] \tag{2.2}$$

agree with the target observables Y_j. Here, the kernel includes a selection function which ensures that only particles with a direct effect on the observable y_j contribute to it. Commonly, the model observables are replaced by their time-averaged values

$$\widetilde{y}_j(t) = \alpha \int_0^{\infty} y_j \left(t - \tau\right) e^{-\alpha\tau} \, \mathrm{d}\tau \tag{2.3}$$

to increase the effective number of particles contributing to them, and to reduce temporal fluctuations.

The task of adapting individual weights of orbiting particles until the target and the model observables match is accomplished by solving the set of differential equations referred to as "force-of-change":

$$\frac{\mathrm{d}w_i(t)}{\mathrm{d}t} = \varepsilon w_i(t) \left(\mu \frac{\partial S}{\partial w_i} - \sum_j \frac{K_j \left[\mathbf{z}_i(t)\right]}{\sigma(Y_j)} \Delta_j(t) \right), \tag{2.4}$$

where ε is a small positive constant, and the meaning of the other variables is clarified below.

Equation (2.4) maximizes the merit function

$$F = -\frac{1}{2}\chi^2 + \mu S \tag{2.5}$$

with respect to the particle weights w_i. Here

$$\chi^2 = \sum_{j=1}^{J} \Delta_j^2 \tag{2.6}$$

is a statistical measurement of the goodness of the fit in terms of deviations

$$\Delta_j(t) = \frac{\widetilde{y}_j - Y_j}{\sigma(Y_j)} \tag{2.7}$$

between target and model observables, taking the error $\sigma(Y_j)$ of the target observable into account.

For the regularization functional, the weight entropy

$$S = -\sum_{i=1}^{N} w_i \log(w_i/\hat{w}_i) \tag{2.8}$$

is a common choice. S is a measure of the plausibility of the model in terms of the smoothness of the weight distribution and thus, indirectly, of the resulting DF, and it serves the purpose of regularization by pushing the particle weights towards some smooth predetermined weights $\hat{w}_i$, called priors. In typical applications the number of particles is much higher than the number of data constraints on the particle model; this intrinsic ill-conditioning of the problem translates into a large freedom in the weight adaptation, and results in models fitting the noise in the data. That is why a simple minimization of χ^2 is not a well-defined procedure to determine the model uniquely, and a certain degree of regularization is necessary.

The balance between regularization and fit to observational constraints in equation (2.5) is controlled by the constant μ, so that generally models with smaller μ aim for better fits to the data, but models with larger μ have smoother DFs. In practice, the best choice of μ is case-dependent (see *e.g.* Gerhard et al., 1998; Thomas et al., 2005b, DL08, DL09), hinging on the specific properties of the observational data to be modelled (error bars, scatter, spatial coverage), the phase-space structure of the galaxy, and possibly also the adopted initial particle model.

As we will see in the next Chapter, a likelihood term can also be added to the merit function (2.5) to account for the constraints from a sample of discrete velocities.

2.2.2 Issues with standard weight entropy regularization

In the framework of the χ^2M2M method summarized above, individual particle weights are slowly adjusted according to a compromise between χ^2, which pushes them to match the target observables, and entropy S, which instead penalizes against deviations of the weights from the preassigned set $\{\hat{w}_i\}$ of priors; more precisely, from $\{\hat{w}_i/\mathrm{e}\}$ (see equations [2.5] and [2.8]).

Even though no rule on the choice of the priors exists, they are traditionally set to $\hat{w}_i = w_0 = 1/N$ (the "uninformative" or "flat" priors in Bayesian statistics), and the same is done for the individual weights of the initial particle model. Through the weight adaptation (2.4), then, the standard Global Weight entropy Regularization (hereafter GWR) encourages a dynamical structure in the particle model which is similar to that of the initial particle system. Of course, this bias is stronger for larger values of μ, and wherever the constraining power of the data is smaller, *e.g.* in the outer galactic regions. In practice, smoothing the weights globally towards a set of preassigned, flat priors through the entropy (2.8) makes it difficult to reproduce strong phase-space gradients of the target galaxy, *e.g.* strongly anisotropic velocity distributions, unless either the right orbital structure is already in place in the initial particle model, i.e. its dynamics is known beforehand, or a very small value of μ is adopted at the expense of smoothness of the underlying DF. This was noticed both in DL08 (see their Fig. 10) and DL09, where under-smoothed models proved necessary to recover strong radial anisotropy in their elliptical galaxy models.

However, under-smoothed particle models do not represent a proper solution. Indeed, sufficient regularization is needed not only to prevent the model from fitting the noise in the data, but also to oppose fluctuations of the particle weights caused by the noise in the data, and to ensure that the weight distribution on neighbouring phase-space tori remains continuous, as intuitively expected for a relaxed stellar system.

In what follows we present a new regularization method which alleviates the main issues of the standard global weight entropy smoothing, and permits smooth M2M particle models to be obtained that reproduce the phase-space gradients of the target galaxies

independently of initial conditions.

2.2.3   Alternative regularization based on moving priors

The logical step forward to ease the issues with the GWR is to abandon the idea of constant priors defined along with the initial particle distribution. Instead we will determine a smooth distribution of particle priors which follows the phase-space structures traced by the weight distribution, as the weight distribution evolves to match the observational data. Then we will use the weight entropy to bias particle weights towards such moving priors.

This procedure, which we will denote as Moving Prior entropy Regularization (MPR) should facilitate a smooth DF without erasing larger-scale phase-space gradients. In terms of orbits, this means that the new regularization should assign the same prior to particles belonging to the same orbit, similar priors to particles on nearby orbits, and different priors to particles moving on very different orbits, as required in the presence of strong velocity anisotropy.

Assignment of new local priors

Therefore, based on Jeans' theorem (see Section 1.4.2), the assignment of new individual priors which mirror the underlying evolving DF is best based on the integrals of motion, respectively orbits, of the particles. This is particularly simple in the spherical case, where the integrals of motion are known and can be easily found from the particle model. As already pointed out by DL09, the need for regularization is also strongest for spherical models, due to their larger number of independent orbits with respect to less symmetric systems. The aim of the present study is to show that this method works, and how well it works, in the spherical case. A simple axisymmetric scheme is shown in Section 2.6, and generalizations to more complicated geometries are sketched out in Section 2.7.

For assigning priors in the spherical case, in practice we sort the particles according to their energy E and total angular momentum into a rectangular (E, x) grid, where the so called circularity integral $x = L/L_c$ is the ratio between the actual angular momentum and the angular momentum L_c which a circular orbit would have at the given energy E. Once particles are binned in a grid of $n_E \times n_x$ energy and circularity cells, we compute the average weight $\hat{w}_{kl}(k = 1, \ldots, n_E, l = 1, \ldots, n_x)$ contained in each cell, and then we

assign it as a new prior to all the particles belonging to that cell.

Provided the (E, x) grid correctly resolves the relevant phase-space properties of the target, such new priors ensure an orbit-based regularization which acts locally, homogenizing the weights of particles moving on the same and on neighbouring orbits, but at the same time tolerates global differences among particles on different orbits.

Smoothing of the grid of particle priors

We will see that the priors computed in this way can be quite noisy. To avoid coarseness in the distribution of priors, and so ensure the global smoothness of the underlying model DF represented by the (E, x) grid, we implement a two-dimensional spline fit of the gridded priors. The technique (Press et al., 1992) is well known and widely used, also in an astrophysical context (*e.g.* Merritt, 1993; Gerhard et al., 1998; Das et al., 2010b): a thin-plate spline function for the new priors on the grid is searched, that minimizes the penalized least square function

$$\Delta^2 \equiv \sum_{k,l} \xi^2 + \lambda \sum_{k,l} \Lambda(\hat{W})_{kl}, \tag{2.9}$$

having defined a function $\hat{W}(E, x)$ which equals the values of the priors on the (E, x) grid. In the equation above, ξ^2 measures the deviation between the original value of the prior and its spline value in each (k, l)-cell, and

$$\Lambda(\hat{W})_{kl} = \left[\left(\frac{\partial^2 \hat{W}}{\partial E^2} \right)^2 + 2 \left(\frac{\partial^2 \hat{W}}{\partial E \partial x} \right)^2 + \left(\frac{\partial^2 \hat{W}}{\partial x^2} \right)^2 \right]_{\substack{E=E_k \\ x=x_l}} \tag{2.10}$$

quantifies the complexity of the fitting spline in terms of the second derivatives, which are numerically computed via finite differences.

The regularization parameter λ determines which of a family of splines, ranging from a plane for $\lambda \to \infty$ to an interpolating cubic spline surface for $\lambda \to 0$, is fitted to the grid of priors. Obviously, the optimal λ is that which resolves the relevant structures in the underlying prior distribution, but at the same time damps strong and presumably spurious variations among nearby priors.

In principle, λ can be calibrated with a sequence of experiments on the (E, x) grid. However, since particle weights evolve in time, and so does the grid of priors, we decided to implement the General Cross Validation technique (GCV, G. Wahba, 1990) to determine

automatically the optimal value of λ each time a new grid of priors is computed. GCV is based on the principle of sequentially omitting each data point, re-fitting the spline, and predicting the value of the point from the spline. The technique singles out the optimal value of λ for this to work best.

New definition of pseudo-entropy

The new moving priors substitute the traditional ones in the definition (2.8) of the pseudo-entropy, which we slightly modify in order to account for the normalization of the weights. As already noted, maximizing the standard entropy biases the weights towards $\hat{w}_i/\mathrm{e}$, so that oversmoothing (*e.g.* for high values of μ) causes an undesired global decrease of all weights which leads to a poor fit of the mass distribution (see *e.g.* Fig. 10 in DL08). In order to avoid such problems, we define a new weight entropy

$$ S = -\sum_{i=1}^{N} w_i \left[\log\left(\frac{w_i}{\hat{w}_i}\right) - 1 \right], \tag{2.11} $$

for which we can immediately check that (*i*) maximizing this quantity pushes the weights to the actual values of the priors, (*ii*) positive and negative corrections to the weights are now a priori equally likely, and (*iii*) the whole regularization scheme is neutral to mass, so that the only power to alter the total mass of the system is left to the data (see Section 2.3.2 below).

2.3   Target models and observables

In this Section we construct a series of spherical targets that we will then model with NMAGIC (Section 2.4 and 2.5) in order to address two issues, namely (*i*) testing the ability of the new regularization scheme to fit the target data with an intrinsically smooth and unbiased particle model, and (*ii*) exploring the extent to which the χ^2M2M technique can recover the target phase-space structure from a given data set independently of the initial particle model.

With these aims in mind, we first focus on a problem whose solution is theoretically known to be unique. As proved by Dejonghe and Merritt (1992) in the spherical non-rotating case, if the gravitational potential is known and complete information on the LOSVD at all radii is available, then the underlying DF can be uniquely recovered. Therefore, the

first target model we design has a known spherical potential and is truncated in radius, so that photometric and kinematic data can fully constrain it.

As a second target model, we build an untruncated (infinite) system whose outer regions remain unconstrained by data, similar to the case of modelling real galaxies.

For both target models, we use the 3D luminosity density together with the LOSVD along several long-slits as target data in the modelling, similar to DL08 and DL09. For each model, we generate both a set of idealized kinematic data, i.e. a large number of data points with small error bars, and a set of more realistic, i.e. sparser and noisier, data points. We use NMAGIC itself to construct our target dynamical equilibrium structures, and to determine their observables, as described in more detail below.

2.3.1 Spherical anisotropic Hernquist targets

Our target models are Hernquist (1990) spheres with a radially anisotropic orbital structure either of the Osipkov-Merritt kind (Osipkov, 1979; Merritt, 1985, hereafter OM), or of the more mildly anisotropic, quasi-separable kind (Gerhard, 1991). Generally speaking, they are isotropic in the central regions, and radially anisotropic for radii greater than a specified anisotropy radius.

The potential-density pair for Hernquist models is

$$\rho(r) = \frac{aM}{2\pi r(r+a)^3}, \qquad \varphi(r) = -\frac{GM}{r+a}, \tag{2.12}$$

where M is the total mass, G the gravitational constant and a the scale length. We set the scale length equal to 1 kpc, and we use characteristic values of the elliptical galaxy NGC 3379 for the total luminosity $L = 1.24 \times 10^{10} L_\odot$, the stellar mass-to-light ratio $\Upsilon = 5$, and the distance $D = 9.8$ Mpc. The projected effective radius of our target model is $R_e \approx 38.3'' = 1.82$ kpc.

With respect to the orbital anisotropy, we either fix the OM anisotropy radius $r_a = 2a$, or we use $\alpha = 2$ and $L_0 = 0.3\sqrt{GMa}$ in the prescription of Gerhard (1991) to generate moderately radially anisotropic models (see equations [2.2] and [3.14] therein).

Following the method described in Debattista and Sellwood (2000), we generate particle model realizations of the spherical targets. To construct a truncated target, we only retain particles with energies lower than $E_{\max} \equiv \varphi(r_{\max})$, with $r_{\max}$ equal to the model boundary.

Finally, we relax the particle models in the fixed Hernquist potential (note that the truncated target is therefore not a self-consistent system), and we compute the target observables from the final particle model using NMAGIC to integrate the particles, as detailed below.

2.3.2   Luminosity observables

We consider as density constraint a spherical harmonics expansion of the target luminosity density on a 1-D mesh of radii r_k. The expansion coefficients

$$a_{lm,k} = L \sum_i \gamma_{ki}^{CIC} Y_l^m(\theta_i, \varphi_i) w_i \qquad (2.13)$$

are computed from the particle realizations through NMAGIC, making use of the cloud-in-cell technique (see *e.g.* DL07, Binney and Tremaine, 2008) to distribute the weight of a particle between nearby grid points. In the definition above, L is the total luminosity of the target, Y_l^m are the standard spherical harmonic functions, and γ_{ki}^{CIC} is the selection function associated with the cloud-in-cell scheme. The radial grid has 60 points, quasi-logarithmically spaced between $r_{\min} = 0.01''$ and $r_{\max}$ equal to the model boundary (for the truncated target) or to $1500'' \sim 40 R_{\mathrm{e}}$ (for the infinite target).

Poissonian error bars, dependent on the number of particles in each shell, are assumed for the radial mass, while 50 Monte Carlo realizations of the density field of the target model allow errors to be assigned to the higher order mass moments (see DL07). Because the targets are spherical, all model $a_{lm,k}$ with $l \neq 0, m \neq 0$ are constrained to be zero within these errors, while the $a_{00,k}$ are constrained by their values for the known target luminosity distribution.

When comparing the target data with the model observables, we compute the latter in the exact same way from the particle model.

By fitting the $a_{lm,k}$ coefficients (2.13), the total luminosity of the model is adjusted to the target luminosity L. The sum of the weights, initially set to $\sum_{i=1}^N w_i = 1$, may therefore change if the luminosity of the initial model $L_{\mathrm{initial}} \neq L$. In this work, we set $L_{\mathrm{initial}} = L$, and we do not adjust the mass-to-light ratio, except in Section 2.6, so that the total mass is also constant throughout the evolution.
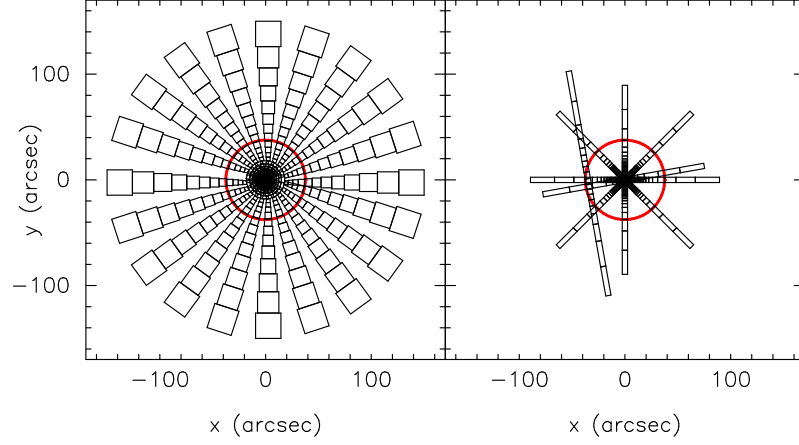
Figure 2.1: Geometry of the two different slit setups. The *red circle* corresponds to R_{e}. *Left panel: idealized* configuration of 10 slits covering the target; slit cells outside $R_{\mathrm{e}}/2$ are square (see Section 2.3.3). *Right panel: realistic* slit configuration, adapted from NGC 3379 (DL09).

2.3.3 Kinematic observables

As kinematic target observables, we use the luminosity-weighted Gauss-Hermite moments of the LOSVD (van der Marel and Franx, 1993; Gerhard, 1993) in various slit cells, computed from the particle realizations using NMAGIC, through

$$b_{n,p} \equiv l_p\, h_{n,p} = 2\sqrt{\pi} L \sum_i \delta_{pi} u_n(\nu_{pi}) w_i \tag{2.14}$$

(DL07). Here, l_p is the luminosity in slit cell $\mathcal{C}_p$, δ_{pi} selects only particles belonging to that cell, the dimensionless Gauss-Hermite functions are

$$u_n(\nu) = \left(2^{n+1}\pi n!\right)^{-1/2} H_n(\nu) \exp\left(-\nu^2/2\right), \tag{2.15}$$

where H_n denote the standard Hermite polynomials, and finally

$$\nu_{pi} = \left(v_{z,i} - V_p\right)/\sigma_p, \tag{2.16}$$

with $v_{z,i}$ the line-of-sight velocity of particle i, and V_p and σ_p the best-fitting Gaussian parameters of the target LOSVD in the given slit cell.

To compute V_p, σ_p, h_3, h_4 from the particle model, we adopt the following procedure. First, we compute the mean velocity and RMS velocity of particles in each slit cell, and use them to estimate the $b_{n,p}$ from the particles through equations (2.14). Next, we use the first order relations

$$\Delta h_1 = -\frac{1}{\sqrt{2}}\frac{\Delta V}{\sigma}; \quad \Delta h_2 = -\frac{1}{\sqrt{2}}\frac{\Delta \sigma}{\sigma} \tag{2.17}$$

(van der Marel and Franx, 1993; Rix et al., 1997) iteratively to correct V_p and σ_p, until h_1 and h_2 both converge to zero. Then, the new target moments $b_{n,p}$ are temporally smoothed to reduce fluctuations caused by particle noise, and this leads to values of h_1 and h_2 slightly different from zero. Finally, the resulting velocity profile is fitted by a Gauss-Hermite series (van der Marel and Franx, 1993) setting $h_1 = h_2 = 0$, and the $b_{n,p}$ are recomputed.

Two different slit configurations are considered, as shown in Fig. 2.1. There, the left panel illustrates a schematic view of an idealized slit data set-up, which consists of 10 slits covering the target and extending as far as $r_{\max} = 150'' \sim 4R_{\mathrm{e}}$. In order to increase spatial coverage in the outer regions, and so to decrease the effects of particle noise, slit cells outside $R_{\mathrm{e}}/2$ are enlarged and made square. Moreover, Gauss-Hermite coefficients up to h_6 are considered. To assign error bars to the target kinematic data, we compute averaged values of the final time-smoothed $b_{n,p}$ moments in the 10 different slits, and then we set the errors equal to $\sqrt{2}$ times the RMS deviation of the individual slit cell moments from the average[1]. To complete the generation of this slit data set, Gaussian random variates with 1σ equal to these errors are added to the average moments $b_{n,p}$. In the following, we refer to this kinematic data set as *idealized* data.

For the truncated model, these data are sufficiently close to the required "complete" data set that we would expect to be able to recover the theoretically unique underlying model with very good accuracy.

The right panel of Fig. 2.1 shows instead the 6 slits which were used by DL09 to model NGC 3379; for this second slit configuration, $r_{\max} = 100'' \sim 3R_{\mathrm{e}}$, only v, σ, h_3, h_4 are available, and observational errors for this galaxy are adopted. Finally, Gaussian random variates are added to the data with 1σ equal to the observational errors. Hereafter we refer to this latter kinematic data set as *realistic* data.

2.4 Convergence to a theoretically unique solution

We now construct NMAGIC models for the radially anisotropic target galaxy model described above. As constraints we use the luminosity density and the *idealized* kinematic data. We determine the optimal value of the regularization parameter, investigate whether

---

[1] The factor $\sqrt{2}$ in the error bars is necessary because, given this generation of kinematic data, the NMAGIC model will have an intrinsic particle noise similar to that of the data which it will try to match.

it is possible to converge to the theoretically unique solution, and see how well the target galaxy can be reproduced starting from different initial particle models.

Our NMAGIC models show for this case that if a unique inversion of data to recover the underlying target DF exists, then it can actually be found via χ^2M2M modelling from good enough data. The new regularization method proposed in this thesis significantly improves both the accuracy with which the target intrinsic properties are reproduced, and the convergence to the right solution independently of initial conditions.

2.4.1 Modelling procedure and diagnostic quantities

Starting from an initial particle model, the weights of all particles are evolved until the particle system matches the target. As initial particle system, we adopt an isotropic Hernquist sphere with the same luminosity but scale length $a = 1.5$ kpc. Different velocity distributions are also considered, as specified below. During the whole evolution, the potential is kept fixed to the target potential. The particles are integrated using a leap-frog scheme.

After a relaxation phase in which the particle system is advanced without weight correction, weights are updated according to the force-of-change in equation (2.4), i.e. subject to both data constraints and smoothing constraints, for $\sim 10^5$ correction time steps. We define the model to have converged if χ^2/J averaged over 50 steps is almost constant in the last 10^4 steps, with fluctuations which are typically of order 2%. The particle weights are then constant to a similar accuracy with MPR. Finally, the particles are freely evolved for another 10^4 steps without any further weight correction, to ensure that the final particle model is well phase-mixed. For reference, 10^4 correction time steps correspond to ~ 42 circular rotation periods at the target $R_{\rm e}$.

When using the new regularization scheme, individual priors are not kept constant in time but rather they are continuously updated while particle weights are changed to match the target observables, as detailed above. Particles are sorted according to their orbital integrals in a grid of $n_E = 30$ and $n_x = 10$ bins, chosen as a compromise between retaining good resolution for the orbit distribution and ensuring a sufficient number of particles in all grid cells. The average weight contained in each grid cell is computed, and then a GCV thin-plate smoothing spline is fitted to the distribution of average weights on the grid. The spline value in every grid cell is finally assigned as the new prior to all

particles belonging to the cell.

A typical outcome of the procedure early in the evolution is shown in Fig. 2.2, where the (E, x) grid of priors is plotted before (left) and after (right) smoothing, and similarly for a horizontal cut (fixed angular momentum) through the grid.
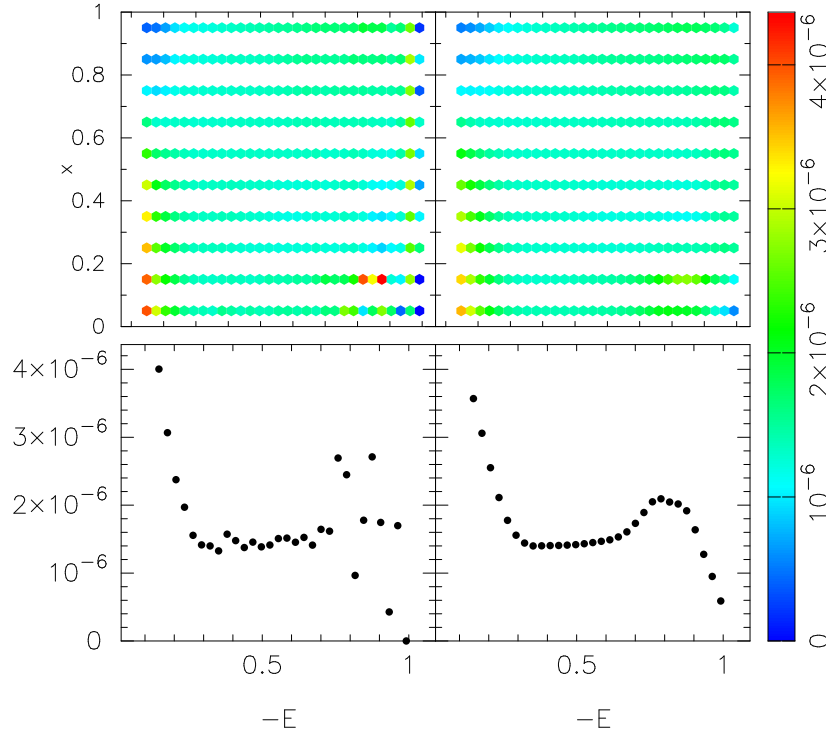

Figure 2.2: *Top*: unsmoothed (*left*) and smoothed (*right*) grid of individual particle priors after $\sim 10^3$ correction time steps (colour bar on the right). *Bottom*: a cut of the above grid for $x = 0.05$, showing unsmoothed (*left*) and smoothed (*right*) particle priors as a function of energy. Priors are smoothed among nearby cells with the GCV thin-plate smoothing spline described in Section 2.2.3.

The cut shows considerable noise before smoothing in the central grid cells, where even with a total $N \sim 10^6$ particles the number of particles per cell for a Hernquist model cusp is still small. In the tests presented here, new priors are computed frequently in the initial phase and every 10^4 correction time steps later in the run, which results in an efficient regularization at a minimum computational cost. When testing the new scheme for very large μ values, priors are computed and updated more often.

The quality of the final particle model of each run is assessed through three diagnostic quantities. The first is the goodness of the fit to the data in terms of χ^2/J, where J is the number of data points. Assuming the goodness of fit statistics follows a χ^2 probability distribution function, the mean of the χ^2 distribution is equal to the number of degrees

of freedom, i.e. the number of constraints (data points plus constraints introduced by the merit function) subtracted by the number of parameters (model parameters plus fitted weights), which are both difficult to quantify. However, if the number of degrees of freedom is approximately equal to the number of data points, then $\chi^2/J < 1$ means that we are fitting the data well.

The second is the level to which the known intrinsic kinematics of the target galaxy are recovered by NMAGIC, quantified by the RMS difference between the intrinsic velocity moments of the target galaxy and those of the final particle model realization. In the following, the internal kinematics (streaming velocity and velocity dispersions) of the particle model are computed by binning particles in spherical polar coordinates, using 21 radial shells quasi-logarithmically spaced between $r_{\mathrm{min}} = 0.01''$ and r_{max}, 12 bins in the azimuthal angle ϕ, and 21 equally spaced bins in $\cos\theta$, where θ is the polar angle.

Finally, we determine the degree to which the particle model reproduces the known phase-space structure of the spherical target. To quantify this we compute the mass-weighted relative RMS difference between model and target weights ($w_{kl,m}$ and $w_{kl,t}$, respectively) in the grid of energy and circularity (E, x) used also for the regularization:

$$\Delta_{\mathrm{grid}} = \sqrt{\sum_{k,l} w_{kl,t} \left(\frac{w_{kl,t} - w_{kl,m}}{w_{kl,t}} \right)^2 / \sum_{k,l} w_{kl,t}}. \tag{2.18}$$

2.4.2 Calibrating regularization

Following the same approach as Gerhard et al. (1998), Thomas et al. (2005b), DL08, and DL09, we construct NMAGIC models for the target galaxy which only differ in the adopted regularization scheme and the amount of regularization, i.e. the value of the parameter μ. Note that ε is kept constant between all models.

The results are summarized in Fig. 2.3, where the normalized goodness of fit χ^2/J, the mass-weighted RMS over the (E, x) grid, Δ_{grid}, and finally the RMS difference between the internal velocity moments of the target and final particle model, Δ_{kin}, are plotted as a function of μ, from unsmoothed models (small μ) to oversmoothed models (high μ). We first focus on the NMAGIC particle models obtained with the traditional GWR technique (crosses, Fig. 2.3). For a wide range of values of $\mu \leqslant 10^4$, NMAGIC is able to fit the data with $\chi^2/J \lesssim 1$. No clear minimum is present in the plotted RMS deviations in grid and
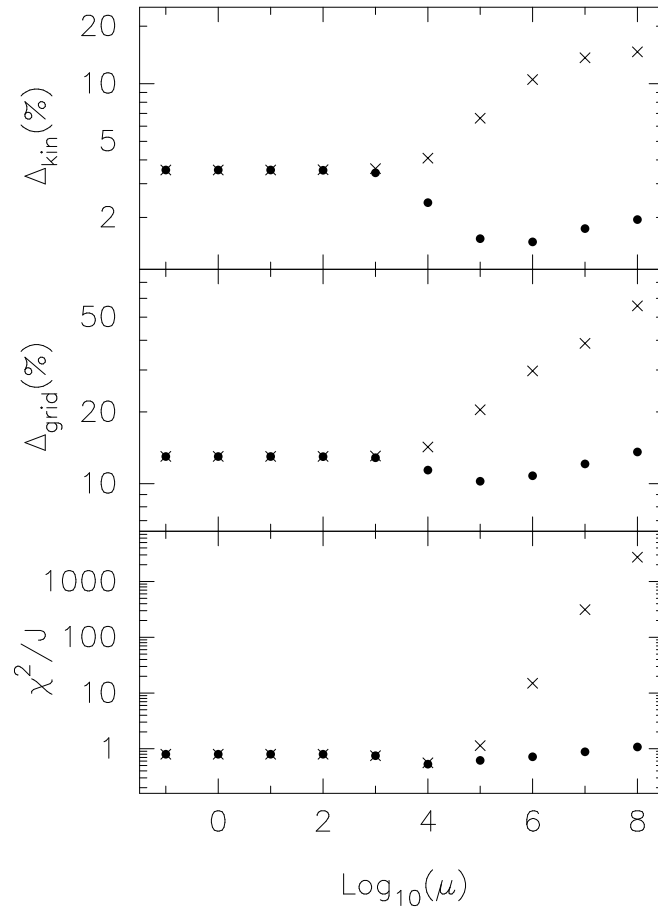
Figure 2.3: Quality of the final NMAGIC particle models as a function of the regularization parameter μ. *Top panel*: RMS deviation (%) of the final particle model from the target internal velocity moments. *Middle panel*: RMS deviation (%) between the occupation of the (E, x) grid of the target and of the final NMAGIC model. *Bottom panel*: goodness of the particle model fit to photometric and kinematic data. *Crosses* refer to models obtained with the traditional GWR scheme, *dots* to models obtained with the new MPR.

intrinsic kinematics as a function of μ: these quantities stay almost flat for a large range of μ, and then rapidly increase for $\mu \gtrsim 10^4$, when the increasing degree of smoothing upsets the fit to the data. By the time the smoothing becomes effective in damping fluctuations in the intrinsic quantities, the bias introduced by the global nature of the smoothing has already set in - hence no clear optimal value of μ is found. For GWR and this particular data set, $\mu = 10^4$ gives a good compromise between quality of the data fit and recovery of the target properties - but with little smoothing.

How well the intrinsic kinematics of the target galaxy can be recovered is shown in the left panel of Fig. 2.4, which compares the known target kinematics with the final NMAGIC models obtained with $\mu = 10^4, 10^5, 10^6, 10^7$. As expected, for higher values of μ the
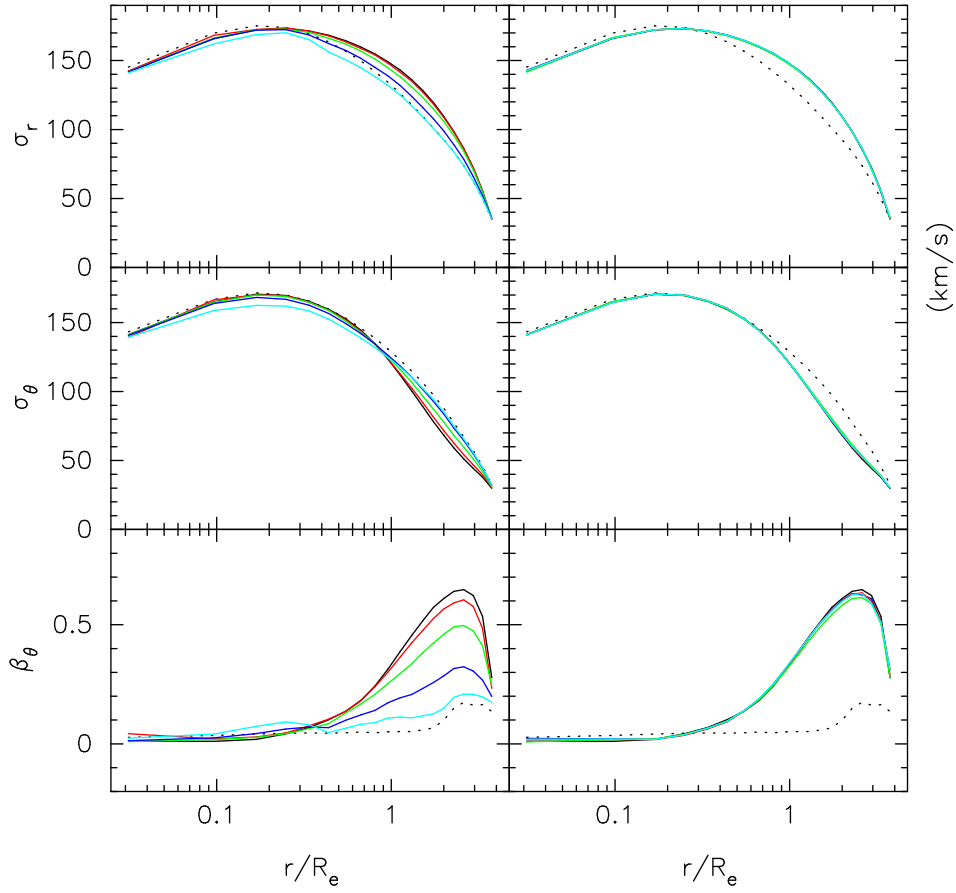
Figure 2.4: Intrinsic kinematics of the NMAGIC models obtained with the GWR (*left panel*), and with the new MPR method (*right panel*). *From top to bottom*: radial velocity dispersion profile, vertical velocity dispersion profile, and anisotropy parameter. The *dotted* and *full black lines* show the intrinsic kinematics of the initial near-isotropic particle model, and of the truncated target galaxy, respectively. *Red, green, blue,* and *light blue lines* correspond to $\mu = 10^4, 10^5, 10^6, 10^7$ adopted in the modelling.

internal moments remain closer to the initial isotropic moments.

Fig. 2.5 shows the level to which the known target DF can be recovered by NMAGIC for $\mu = 10^4, 10^6$: the distribution of total particle weights in the (E, x) grid is plotted for the initial particle model, the truncated target, and the models obtained with NMAGIC. We denote this by "mass distribution function", or MDF for brevity. Clearly, for $\mu = 10^4$ the main phase-space structures are well recovered, showing that NMAGIC is able to fit the data and to approximately find the underlying MDF, but the peak on high-E near-radial orbits is underestimated because of the global nature of GWR. For the more heavily smoothed case with $\mu = 10^6$, this peak is completely wiped out.

We now consider χ^2M2M models obtained by fitting the same target data with MPR. As can be seen in Fig. 2.3 (black dots), the new method works very well in reproducing
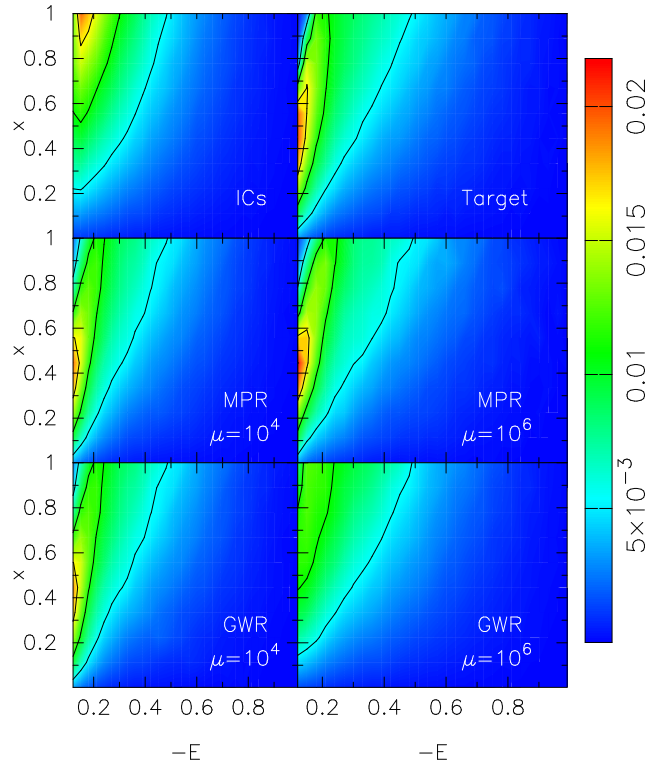
Figure 2.5: Mass distribution function (MDF) of particle weights in the (E, x) grid, for the initial particle model (*top left*), the truncated target galaxy (*top right*), the models obtained with the standard GWR (*bottom*) and with the MPR method (*middle*), for different values of μ. The colour scheme reflects the total weight contained in each grid cell, where $n_E = 30$, $n_x = 10$.

the target, and a series of NMAGIC models fitting the photometric and kinematics constraints of the galaxy within $\chi^2/J \lesssim 1$ can be generated for a wider range of μ values. Of these, models obtained for values of $\mu \lesssim 10^3$ are essentially driven by the χ^2 term alone. However, when regularization becomes significant, a minimum is reached both in the RMS deviation between intrinsic moments of the particle model and of the target, and in the RMS deviation of their (E, x) distributions (top and middle panels of Fig. 2.3, respectively). Remarkably, the minimum is well below that achievable with traditional weight entropy smoothing, indicating that the phase-space structure and the internal moments of the target can be recovered much better using MPR.

The right panel of Fig. 2.4 shows how close the internal kinematics of the final particle models for $\mu = 10^4, 10^5, 10^6, 10^7$ are to those of the target galaxy. Note that the residuals are so small that the trend with μ seen in Fig. 2.3 cannot be seen; the new scheme allows one to recover the target moments almost perfectly. The accuracy with which the MDF in (E, x) integral space is reproduced is shown in Fig. 2.5. Visually comparing this plot

with the corresponding ones for the truncated target and the best model obtained using standard GWR, shows that the target is now recovered much better. In particular at small energies, i.e. in the outer regions, the weight of particles on radial orbits is increased while that of particles on circular orbits is decreased more effectively with MPR, especially for the preferred $\mu = 10^6$.

We conclude that, for this particular data set-up, the best choice for μ with MPR is $\sim 10^6$. This value is considerably larger than the corresponding μ of the traditional GWR, showing that the new regularization succeeds better in reconciling the smoothness of the underlying model with orbital anisotropy.

It is instructive to compare the final distribution of particle weights for both regularization schemes. Fig. 2.6 shows that MPR results in a more compact and more structured weight distribution, which avoids extended tails of extremely increased or decreased weights, while still providing a good and less noisy fit the data (see below). A similar comparison in the context of Schwarzschild modelling can be found in Fig. 17 of Thomas et al. (2007b).
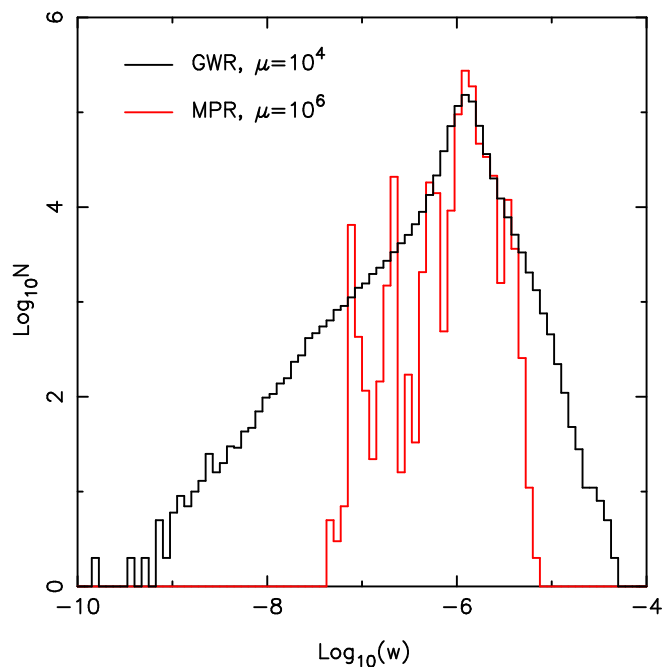

Figure 2.6: Distribution of particle weights for the final optimally smoothed NMAGIC models obtained with the traditional GWR (*black histograms*, $\mu = 10^4$) and with the MPR scheme (*red histograms*, $\mu = 10^6$). Particle weights were initialized to $w_0 = 1/750000 \sim 10^{-6}$.

Along with a more compact weight distribution, MPR also leads to a smoother particle
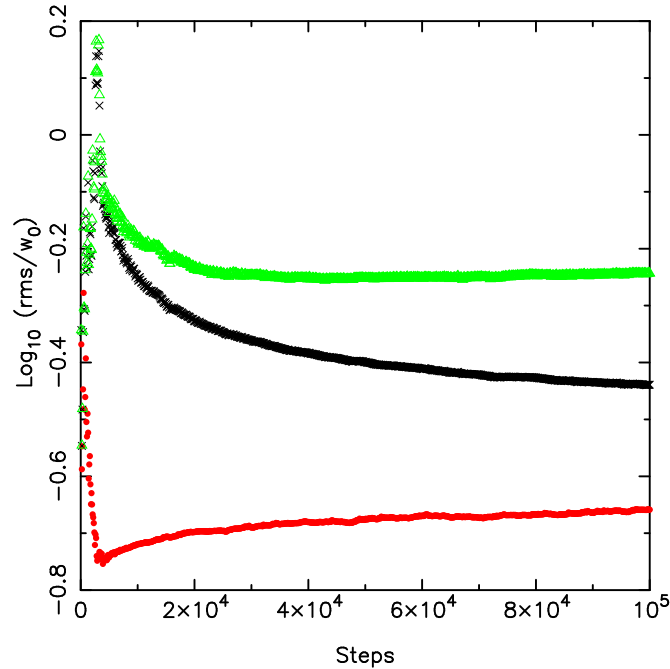
Figure 2.7: RMS fluctuations of particle weights around the mean value in each (E, x) cell for the optimally smoothed NMAGIC models obtained with GWR (*black crosses*, $\mu = 10^4$) and with MPR (*red dots*, $\mu = 10^6$), as a function of the number of NMAGIC correction time-steps. The top curve (*green triangles*) shows an essentially unsmoothed model ($\mu = 10^3$). $w_0 = 1/750000 \sim 10^{-6}$ is the value of the initial particle weights. The grid has $n_E = 30$ times $n_x = 10$ cells, and only those containing more than 50 particles are taken into account, to avoid particle noise effects in the computation of the residuals.

model. This can be quantified by computing the RMS fluctuations of particle weights around the mean value in all the cells of the (E, x) grid for the different kinds of regularization, as shown in Fig. 2.7.

Not unexpectedly, the fit to the data also looks smoother when adopting the new regularization, and the larger μ value permitted by this scheme opposes an overfitting of the data points, as can be appreciated for different observables in Section 2.6 below.

To summarize, we have tested the χ^2M2M method with a new Moving Prior Regularization scheme for a radially anisotropic truncated target model with *idealized* data, and have calibrated the best value of the regularization parameter μ. We have shown that the corresponding NMAGIC models match the target data well and recover the MDF for this model in its known potential. We have also seen that these models are much less sensitive to the value of μ than with the traditional weight entropy regularization, which can only reproduce the global anisotropy of this model essentially without smoothing. The new regularization scheme allows NMAGIC to recover a particle model that fits the

data well but is both intrinsically smoother and reproduces the properties of the target more accurately.

2.4.3 Varying the initial particle model

The results above already show that NMAGIC can recover the orbit distribution of our truncated spherical target galaxy from a set of data that specifies it essentially uniquely. In this experiment, we used an isotropic initial model, so now we investigate the natural question whether and how this result is dependent on the choice of initial particle model. In particular, we consider both the case in which the initial particle model has a radially anisotropic OM orbital structure (with anisotropy radius $r_a = 3a$, different from the target galaxy), and the case in which it is tangentially anisotropic according to the quasi-separable prescription of Gerhard (1991, with $\alpha = 2$, $L_0 = 0.3\sqrt{GMa}$, $c = 0.1$). For both initial particle models we checked that a minimum number of particles on radial and tangential orbits is present at each energy. By analogy with the experiment described in the previous Section, the initial particle models are Hernquist spheres with scale-length $a = 1.5$ kpc, larger than the target galaxy ($a = 1$ kpc). The same set-up of the NMAGIC run is adopted, together with the optimal μ values determined in Section 2.4.2 above for the two regularization methods.

With the new MPR scheme, the final NMAGIC models obtained for different initial orbital distributions differ remarkably little. Table 2.1 and Figs. 2.8-2.9 show how well the intrinsic kinematics and phase-space MDF match those of the known target galaxy. The MDF of the final particle model is very similar to that of the target galaxy, independent of the choice of initial conditions (Fig. 2.9). Typical fluctuations in the mass-weighted relative RMS difference between target and model MDF are 12%, while the intrinsic kinematics of the target is recovered almost perfectly, as shown in Fig. 2.8.

It is instructive to see how a similar result cannot be achieved with the traditional weight entropy: an inspection of Table 2.1, or Fig. 2.8 and Fig. 2.9 shows the poorer accuracy of the resulting particle models. Especially for the models with tangentially anisotropic initial conditions, the smaller number of particles on radial orbits together with GWR makes it more difficult to reproduce the radially anisotropic target.

We conclude that with the new regularization method NMAGIC converges to the (theoretically essentially unique) solution to a very good level of accuracy, independently
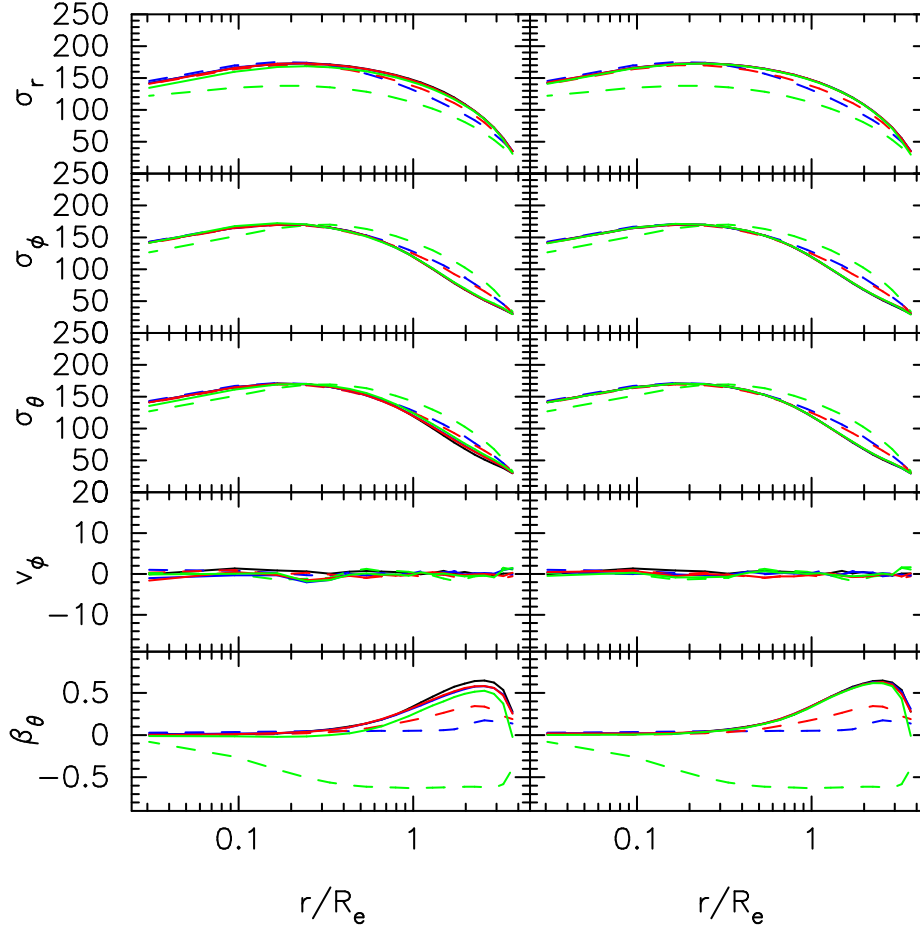
Figure 2.8: Truncated target with *idealized* data: recovery of the intrinsic kinematics with different initial particle models. *From top to bottom*: radial, azimuthal, and vertical velocity dispersion profiles, mean azimuthal streaming velocity, and anisotropy parameter of the NMAGIC models (*full lines*) for different initial conditions (*dashed lines*). The *black line* indicates the intrinsic moments of the target galaxy. *Blue, red,* and *green* colours correspond to isotropic, radially anisotropic and tangentially anisotropic initial conditions, respectively. GWR was adopted in the runs shown in the *left panel*, while MPR in the runs shown in the *right panel*.

		ICs	χ^2/J	$\Delta_{\text{kin}}(\%)$	$\Delta_{\text{grid}}(\%)$
Idealized	GWR	iso	0.57	4.07 *(14.67)*	14.24 *(43.98)*
data		rad	0.46	3.62 *(11.85)*	12.94 *(32.25)*
		tang	1.64	7.56 *(27.20)*	17.51 *(75.46)*
	MPR	iso	0.72	1.49 *(14.67)*	10.80 *(43.98)*
		rad	0.67	1.62 *(11.85)*	11.21 *(32.25)*
		tang	1.57	3.38 *(27.20)*	12.53 *(75.46)*
Realistic	GWR	iso	0.26	2.44 *(5.17)*	7.49 *(17.63)*
data		rad	0.20	3.25 *(3.85)*	12.68 *(15.79)*
		tang	0.29	7.42 *(16.14)*	20.85 *(56.44)*
	MPR	iso	0.37	1.32 *(5.17)*	7.39 *(17.63)*
		rad	0.38	3.13 *(3.85)*	10.27 *(15.79)*
		tang	0.38	2.35 *(16.14)*	11.09 *(56.44)*

Table 2.1: NMAGIC models for the truncated target galaxy. Different initial particle models are adopted. For the traditional weight entropy smoothing $\mu = 10^4$; for the new regularization scheme, $\mu = 10^6$. The goodness of fit χ^2/J, Δ_{kin} and Δ_{grid} are computed as described in Section 2.4.1. In brackets, the same Δ_{kin} and Δ_{grid} computed between the initial particle model and the target.
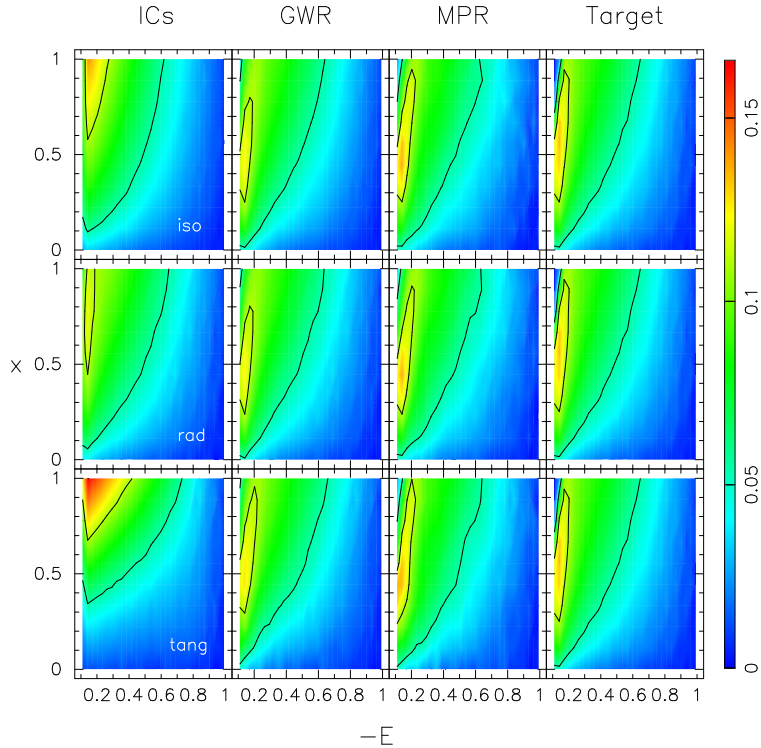

Figure 2.9: Recovery of the MDF of the truncated target (*last column on the right*) for different initial particle models from *idealized* kinematic constraints. The *first column* shows the distribution of particle weights in the (E, x) grid for the isotropic, radially and tangentially anisotropic initial particle models (*from top to bottom*). The *second column* corresponds to the final NMAGIC particle models obtained with traditional GWR; the *third column* to the models obtained using the new MPR. The colour scheme reflects the square root of the total weight contained in each grid cell, where we have adopted $n_E = 30, n_x = 10$.

of the choice of the initial particle model. In this respect, the new MPR method is a definite improvement over the traditional weight entropy scheme.

2.5   Effects of imperfect data

In astronomical applications, the data constraints are typically less stringent than in the idealized case considered so far. We therefore now investigate how the results change in more realistic circumstances.

The following tests represent a sequence of problems that are increasingly less determined by the data, starting from the truncated target covered by *realistic* data, and moving on to infinite stellar systems constrained by data with finite extent. This allows us to isolate the different roles played by the quality and completeness of data, the initial particle model, and the regularization scheme.

We find that it is still possible to get close to the target dynamical structure from different initial particle models with the help of the new regularization method, even though the lack and/or poor quality of data introduce degeneracies in the models.

2.5.1   Truncated target and realistic kinematic errors

First we construct NMAGIC models for a truncated target with the *realistic* kinematic data, with the goal to establish how well the target galaxy can then be reproduced from different initial particle systems.

The *realistic* data have larger error bars and smaller data coverage (see Section 2.3.3). For these models $r_{\mathrm{max}} = 100''$ is thus smaller than in the previous case. The different initial particle models have the same anisotropy structure as in Section 2.4.3, but are adapted to this r_{max} - hence they are more similar to the target.

We have repeated the analysis described in Section 2.4.2 to determine the optimal value of the smoothing parameter μ when these *realistic* data are adopted. Results do not change much, and suggest that we can keep the values of $\mu = 10^4$ for the GWR and $\mu = 10^6$ for MPR.

The results of these models are shown in Figs. 2.10 (top part) and 2.11, and more quantitatively in Table 2.1, for both regularization methods.

The top part of Fig. 2.10 shows the deviations of the models from the target, comparing the two cases in which *idealized* and *realistic* constraints are used. The three sub-panels
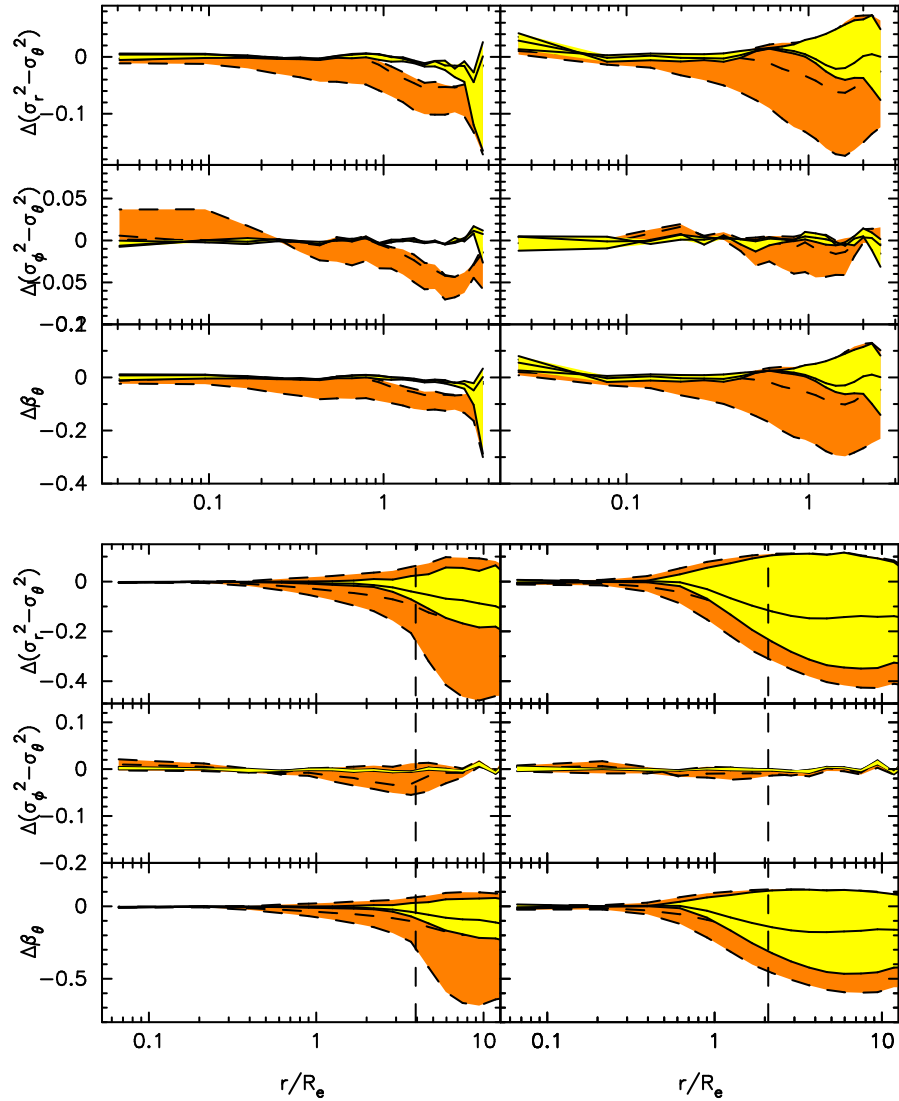
Figure 2.10: Recovery of the intrinsic kinematics for the truncated and infinite targets (*top* and *bottom* figure, respectively) with *idealized* and *realistic* data (*left* and *right columns*, respectively). The *vertical dashed line* corresponds to the radial extent of the data for the infinite target. The *shaded yellow* (*orange*) area shows the range of deviations for the MPR (GWR) method, when the specified range of initial conditions is adopted. *Full* (*dashed*) *lines* represent the deviations for the final NMAGIC models obtained with MPR (GWR) starting from different initial particle models. Plotted in each panel are, *from top to bottom*, deviations of normalized $\sigma_r^2 - \sigma_\vartheta^2$, $\sigma_\phi^2 - \sigma_\vartheta^2$, and anisotropy parameter β from the respective true value of the target.

show the deviations of $\sigma_r^2 - \sigma_\vartheta^2$ and $\sigma_\phi^2 - \sigma_\vartheta^2$ normalized by the sum of the two velocity dispersions, and the deviations of the velocity anisotropy β, as a function of radius. In this figure, the shaded regions correspond to the range of deviations obtained from modelling the data with the chosen initial particle systems.

As intuitively might be expected, these deviations increase (i) moving to larger radii, and (ii) when *realistic* data are considered. The effect of imperfect data on the final models is noticeable, in particular closer to the model boundary where poorer constraints from slit data worsen the recovery of the intrinsic kinematics.

However, we see that also for realistic data the new MPR works well in recovering the internal kinematics of the target galaxy independently of the initial particle model, and it is superior to the GWR, as deviations are considerably smaller.

The accuracy with which the phase-space mass distribution function of the target is matched by the NMAGIC models is shown in Fig. 2.11, where is clear that the traditional GWR works less well with these realistic data, especially when tangential initial conditions are adopted.

Because the realistic error bars are larger than those used in the experiments in Section 2.4, the particle weights undergo smaller changes until they match target observables in a χ^2 sense [see equations (2.6) and (2.7)]. For the same reason, the final normalized χ^2 between data and model observables turns out to be smaller (see Table 2.1).

To conclude, these experiments show that the new MPR method improves both the quality with which the intrinsic properties of the target galaxy can be recovered, and the independence of the final particle model from the adopted initial model. In fact, MPR makes it possible to recover the underlying dynamical structure of our radially anisotropic target galaxy with good accuracy ($\Delta\beta \sim \pm 0.1$ only at the outermost point) even when the quality of the data is not perfect. As already noticed, MPR allows the use of higher μ values, thus reducing mass fluctuations and enforcing the smoothness of the underlying model without spoiling the fit to the data.

2.5.2 Finite data for an infinite target

Real stellar systems are clearly not as sharply truncated in radius as the target galaxies studied so far, and their outer regions are usually not constrained by the available data. We now come to the more realistic case of modelling an infinite target galaxy using finite
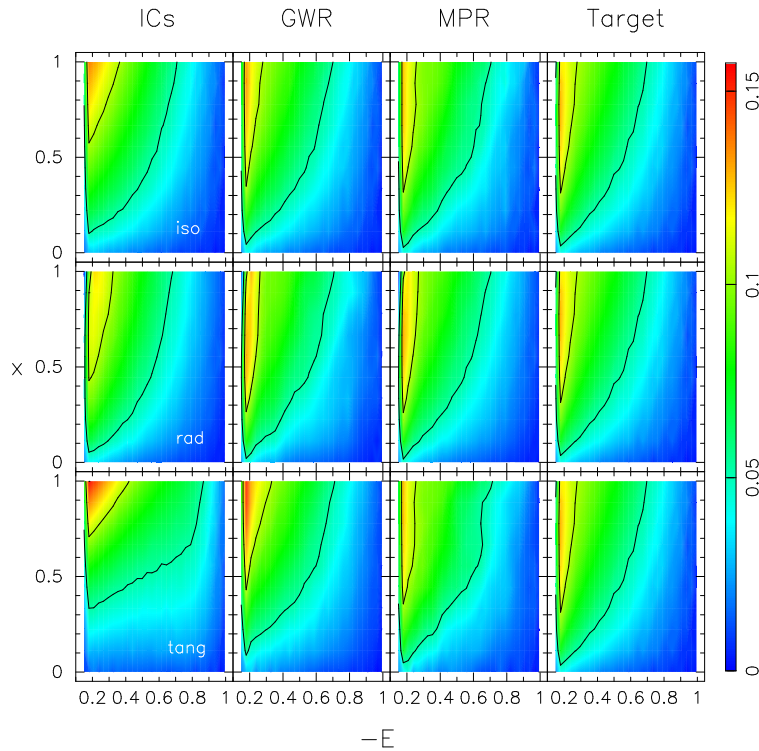
Figure 2.11: Recovery of the MDF of the truncated target (*last column on the right*) with *realistic* data for different initial particle models. As Fig. 2.9.

data, to explore the limitations that the modelling encounters in this case.

As target galaxy we consider our usual Hernquist sphere with scale length $a = 1$ kpc, but this time without truncation. Because of the extreme behavior of the OM radially anisotropic systems at large radii, we choose a milder anisotropy for our target galaxy, using the models of Gerhard (1991) with specified circularity function [equations (2.2) and (3.14) therein], which only depend on a constant parameter α, set equal to 2.

Following the same procedure as adopted above, we model the target starting from different initial particle models (isotropic, less radially anisotropic, and more radially anisotropic than the target) and using both regularization schemes. *Idealized* data and *realistic* data are considered in turn.

Infinite target with excellent but radially limited data

Our modelling of the infinite target with *idealized* but radially limited data confirms previous experiments (Thomas et al., 2004, DL08) in that the velocity dispersions, streaming rotation, and anisotropy parameter of the infinite target galaxy can be

		ICs	χ^2/J	$(\chi^2/J)_{A_{lm}}$	$(\chi^2/J)_{\rm slit}$
Idealized	GWR	iso	1.08	0.39	1.17
data		$\alpha = 1$	1.02	0.27	1.11
		$\alpha = 3$	0.89	0.21	0.98
	MPR	iso	0.92	0.45	0.98
		$\alpha = 1$	1.02	0.34	1.12
		$\alpha = 3$	0.78	0.34	0.86
Realistic	GWR	iso	0.54	0.27	0.67
data		$\alpha = 1$	0.46	0.19	0.59
		$\alpha = 3$	0.43	0.16	0.56
	MPR	iso	0.62	0.27	0.79
		$\alpha = 1$	0.58	0.25	0.74
		$\alpha = 3$	0.55	0.22	0.71

Table 2.2: NMAGIC models for the infinite target galaxy in its fixed potential. Different initial conditions and regularization schemes are adopted. χ^2 is the usual goodness of fit, normalized by the respective number of observables.

reproduced reliably only in the regions well inside the part of the galaxy covered by the data.

Quantitative results are reported in Table 2.2, while the bottom left panel of Fig. 2.10 shows the range of deviations of the final models from the target obtained for different initial particle systems. The vertical dashed line corresponds to the outermost data point. This panel shows that in the inner regions of the galaxy, where the data provide good constraints to the models, the intrinsic properties of the target galaxy are well recovered independently of the initial particle model, as already found for the truncated target galaxy. However, at larger radii, and close to the outermost data point, regularization plays a dominant role in the weight correction of particles, and in those external regions a bias towards the dynamical structure of the initial particle model cannot be avoided. Nevertheless, our experiments show that the new MPR considerably reduces such bias towards the dynamical structure of the initial particle model, as can be seen comparing the two shaded regions for MPR and GWR.

If we require $|\Delta\beta| \leqslant 0.1$ and compute how far out this is achieved for the range of models obtained starting from different initial conditions, we find that this radius is $1.4R_{\rm e}$ for GWR, while it shifts to $4.3R_{\rm e}$ when adopting MPR. Considering instead the radius $r(\Delta\beta = \pm 0.2)$, the standard GWR fails at $3.1R_{\rm e}$, while the new method at $8R_{\rm e}$.

When, as in this case, a range of dynamical models obtained from different initial particle models is compatible with the data, one could compare and rank models according to the usual goodness-of-fit basis (see *e.g.* Table 2.2), or additionally according to a plausibility

criterion that, *e.g.* , favours a constant or smooth outer anisotropy profile.

Infinite target with realistic and finite data

As a logical final step, we consider the case in which an infinite target like the one described above is constrained by realistic, rather than idealized, data.

We model this target starting again from different initial particle models, and show the accuracy of the final NMAGIC models in the bottom right panel of Fig. 2.10, and in Table 2.2.

The bottom part of Fig. 2.10 compares the deviations of the final models from the target for *idealized* and *realistic* data. Apparently, the realistic constraints on an infinite target galaxy make it really hard for NMAGIC to recover the true intrinsic kinematics of the target independently of the initial particle model, even though it is still true that the new MPR method is superior to the GWR.

To quantify how well the particle model reproduces the intrinsic kinematics of the target galaxy, we can compute $r(\Delta\beta = \pm 0.1)$, which is $0.6R_{\rm e}$ for the standard GWR, and $1R_{\rm e}$ when adopting the new regularization. Considering instead the radius $r(\Delta\beta = \pm 0.2)$, GWR fails at $0.9R_{\rm e}$, while MPR at $1.4R_{\rm e}$. Here the kinematic data extend to $\sim 2R_{\rm e}$.

Thus, the results previously obtained for the *idealized* data are confirmed: the new regularization scheme provides a better reconstruction of the target properties, and is more independent on the choice of the initial particle model. However, as soon as there is a lack of data to constrain the models, regularization becomes the dominant term in the force of change acting on particle weights, and the bias towards the initial particle model becomes evident.

The main conclusion from these tests is that the reliability of our dynamical models is limited to those regions in which good observational data exist, and that the better quality of the data is reflected in a better recovery of the intrinsic properties of the target galaxy.

2.6   Regularized particle models for NGC 4697 and NGC 3379

We now show our new regularization method at work on two real galaxies, and reconstruct the best-fitting NMAGIC models determined in DL08 and DL09 for the two intermediate-luminosity elliptical galaxies with rapidly falling velocity dispersion profiles NGC 4697 and NGC 3379, respectively.

DL08 and DL09 used NMAGIC to fit spherical and axisymmetric models of different inclinations to extensive data sets for these galaxies, including photometry, long-slit spectroscopy, integral-field data and PNe velocities. Different from the experiments of Sections 2.4 and 2.5, particles are evolved in a total gravitational potential

$$\phi = \phi_\star + \phi_D, \tag{2.19}$$

where $\phi_\star$ is estimated from the N-particle model for the light distribution via a spherical harmonic decomposition (Sellwood, 2003, DL07) assuming a constant mass-to-light ratio Υ, and ϕ_D is a dark matter halo potential with the logarithmic parametrization

$$\phi_D(R, z) = \frac{v_0^2}{2} \ln\left(r_0^2 + R^2 + \frac{z^2}{q^2}\right). \tag{2.20}$$

Moreover, the mass-to-light ratio is not a fixed parameter, but rather it is determined simultaneously with the modelling of the dynamical structure in the NMAGIC run.

For both galaxies, the slit data show clear rotation along the major axis on the sky. However, the regularization scheme as developed in Section 2.2.3 for spherical systems discourages any rotation in the particle model, as it biases individual weights towards the same prior regardless of the sense of rotation of the particles. Thus, in the following tests we adopt a modified set-up for the grid of priors, binning particles according to E and x, and also according to the sign of their L_z, and assigning individual priors that differ between particles with different sense of rotation. For an axisymmetric potential, this effectively uses the total angular momentum L as an approximate third integral, which may be expected to be a reasonable first approximation unless $L \simeq L_z \simeq 0$ (Gerhard and Saha, 1991).

2.6.1   The case of NGC 4697 and its halo

The intermediate-luminosity elliptical galaxy NGC 4697 is seen almost edge-on. Assuming that the observed nuclear dust-lane is settled in the equatorial plane, Dejonghe et al. (1996) derived an inclination $i = 78° \pm 5°$, which is consistent with the bulge-disk decomposition of Scorza et al. (1998) if the disk component has an intrinsic axis ratio $h/R \sim 0.2$. NGC 4697 has fitted Sersic model index $n = 3.5$, and an effective radius $R_{\rm e} \approx 66'' = 3.36$ kpc at an assumed distance $D = 10.5$ Mpc. Kinematic data show significant major axis rotation reaching ~ 100 km/s at $90''$.
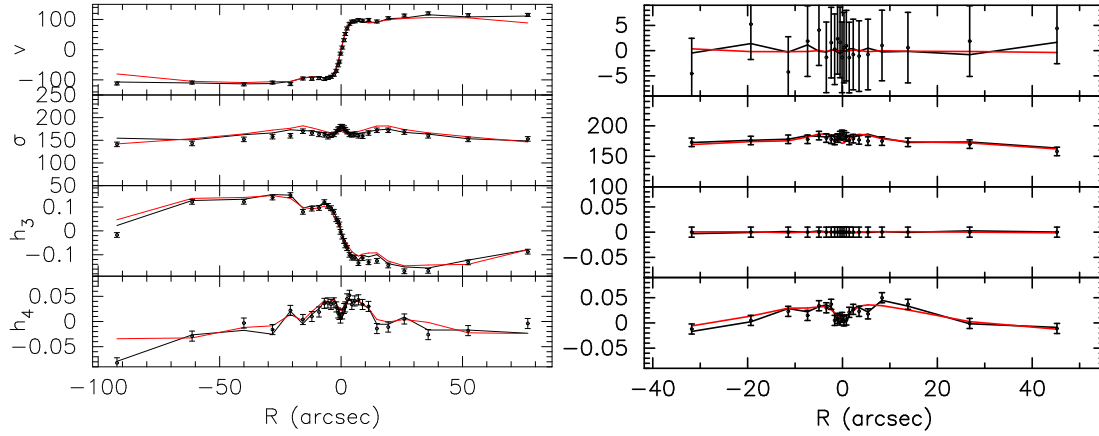
Figure 2.12: Particle model fits to the slit data of NGC 4697 along the major (*left*) and minor axis (*right*). The model data points are averages over the same slit cells as the target data, and are connected by straight line segments. The *black line* shows model J of DL08, while the *red line* shows the same model obtained using the new MPR.
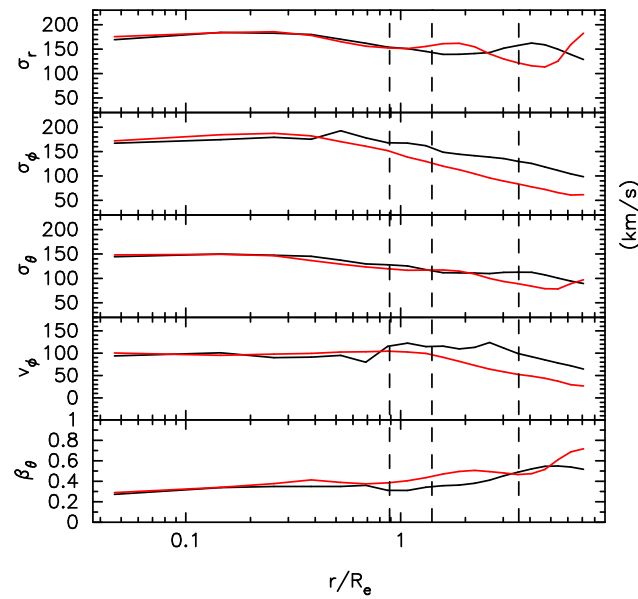

Figure 2.13: Internal velocity moments in the equatorial plane for model J of DL08 (*black line*) and the new regularized J model obtained here (*red line*), for NGC 4697. The *vertical dashed lines* indicate the radial extent of the minor axis slit data, major axis slit data, and PN data, *from left to right*.

NMAGIC axisymmetric particle models assuming an inclination $i = 80°$ were constructed for NGC 4697 (DL08) fitting simultaneously surface brightness photometry, long-slit absorption-line kinematics and hundreds of PNe velocities. A range of quasi-isothermal halos was found to be consistent with the observational constraints, and a massive halo with circular velocity $v_0 = 250$ km/s at $4.3R_e$, referred to as model J in the notation of DL08, fits the PN data best. This model is characterized by a moderately radially anisotropic orbit distribution, with the anisotropy parameter $\beta \sim 0.3$ at the center and increasingly higher in the outer regions.

These models were constructed using the traditional GWR, and the μ parameter was set to 100 to avoid strong biases to the initial conditions. This in turn led to some overfitting of the slit kinematics data, especially for the higher order kinematic moments (see DL08 for details).

Thus we now build a new regularized J model of NGC 4697, to see whether a similarly good but smoother particle model can be obtained with the help of the new MPR. We rerun that exact model with the code NMAGIC using the new regularization scheme, and $\mu = 10^5$, and using constraints from both photometric and kinematic data, including PNe. As specified above, we bin particles according to their integrals E, x, and L_z when adopting the new regularization method, to allow for the rotation seen in the slit data.

A comparison of the final particle models obtained by DL08 and with this new MPR is shown in Figs. 2.12 and 2.13. Fig. 2.12 shows the projected absorption line kinematics of the final particle models overplotted on the data points. As discussed in DL08, asymmetries between the left-hand side and right-hand side in the profiles do not imply deviations from axisymmetry or equilibrium, but rather they are due to averages over slightly different slit cells on both sides. As expected, these asymmetries decrease when using the new MPR, which allows a higher amount of regularization, and the model profiles are indeed smoother than for the DL08 model.

The intrinsic kinematics of the final particle models are compared in Fig 2.13: the velocity anisotropy increases from the center outwards when adopting either GWR or MPR, but MPR results in much smoother profiles in the regions constrained by data.
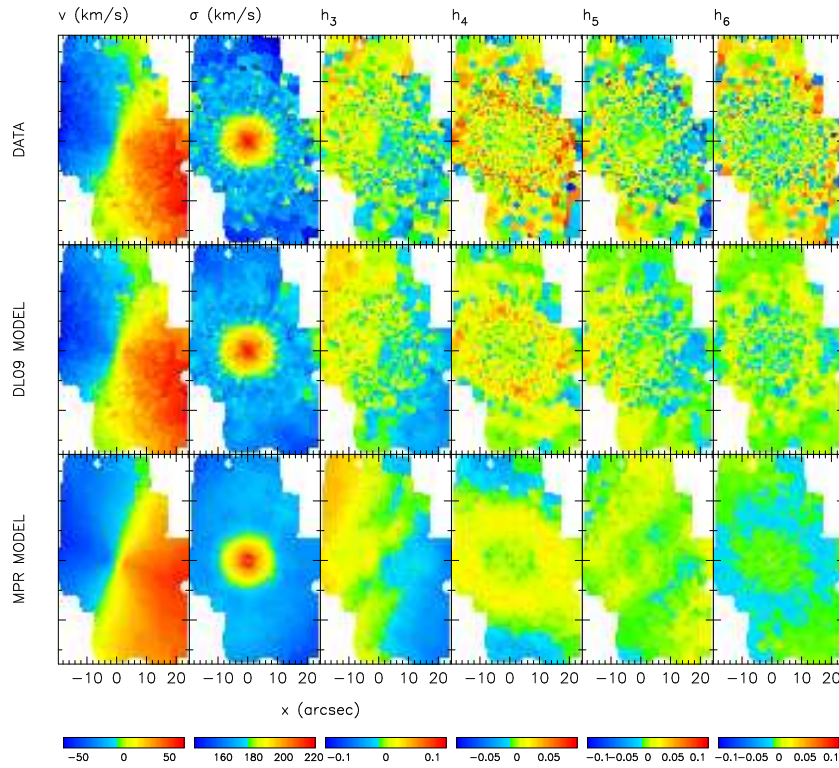
Figure 2.14: Particle model fits to the SAURON integral field kinematic data (Shapiro et al., 2006) for NGC 3379. *Top row*: symmetrized SAURON data. *Middle row*: best-fitting C model (DL09). *Bottom row*: new regularized C model. Mean velocity, velocity dispersion, and higher order Gauss-Hermite moments are shown in the panels *from left to right*.
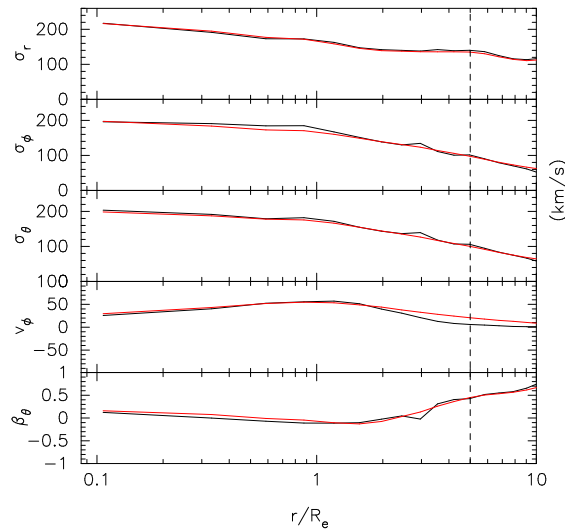

Figure 2.15: Internal velocity moments in the equatorial plane for model C of DL09 (*black*) and the new regularized C model obtained here (*red*), for NGC 3379. The *vertical dashed line* marks the last data point.

2.6.2   The case of NGC 3379 and its halo

In DL09 a sequence of spherical and axisymmetric NMAGIC models fitting an extensive data set (photometry, long-slit and SAURON absorption-line kinematics, PN velocity dispersion data) was constructed to investigate the mass distribution and orbital structure of the intermediate-luminosity E1 galaxy NGC 3379.

No independent information on the inclination is available for this galaxy, and values of $i > 40°$ are consistent with the photometry. The effective radius $R_e \approx 47'' = 2.23$ kpc at an assumed distance $D = 9.8$ Mpc. The combined kinematic data set shows major axis rotation reaching ~ 50 km/s at $20''$, with PNe indicating a further increase to ~ 70 km/s at $220''$.

DL09 explored a sequence of spherical and axisymmetric models, together with some triaxial test models. They found that their results were insensitive to the adopted geometry. Both strongly radially anisotropic models embedded in massive dark matter halos and nearly isotropic systems dominated by the stellar mass are consistent with the data. I.e., even the extensive data set used in the modelling was not sufficient to break the mass-anisotropy degeneracy (Binney and Mamon, 1982, see also Section 1.4.2) because of the rapidly decreasing velocity dispersion profile for NGC 3379. However, an analysis of the quality of the fit and of the likelihood of the observed PN velocity data for the spherical models slightly favoured a range of models centered around the radially anisotropic halo C, which was obtained for a quasi-isothermal potential in equation (2.20), with $r_0/R_e = 3$, $v_0 = 130$ km/s, and $q = 1$.

We now reconstruct that spherical C model with the new MPR method. Given the data set-up is very similar to the one adopted in the tests of Section 2.5, we set $\mu = 10^6$. We bin particles according to their integrals E, x, and L_z, because of the observed rotation in both the slit and SAURON data. For the energy grid we use a linear binning of the function $\exp(E)$, which provides a better sampling of the model DF in the outer regions for this potential.

Fig. 2.14 shows the fit to SAURON data for the final NMAGIC models obtained with GWR and MPR. Both particle models reproduce the observed rotation with great accuracy, and the MPR model is clearly smoother than the original (symmetrized) data. In particular, notice the ring-like structure in the h_4 plot. Even though the new model is

generated using a much higher value of μ, i.e. much stronger smoothing, it still does a good job in fitting the observational data, with $(\chi^2/J)_{\mathrm{sauron}} = 0.86$ (compared to 0.17 for the traditional GWR).

The intrinsic kinematics of the final NMAGIC models (Fig. 2.15) are similar, but using MPR the kinks in the profiles disappear. It can be seen that a strong radial anisotropy is required to match the PNe data in this dark matter halo.

2.7 Discussion and conclusions

Building on the work of ST96, successive investigations (DL07; DL08; DL09; Dehnen, 2009; Long and Mao, 2010) have shown the power of the χ^2M2M modelling technique to learn about the dynamics of galaxies. χ^2M2M methods work by adapting the weights of an N-body particle system until the observational data are well matched in a χ^2 sense, subject to additional regularization constraints. These constraints are needed to prevent the particle model from acquiring large fluctuations because of scatter and noise especially in the kinematic data.

Traditionally, a Global Weight entropy Regularization (GWR) is adopted to regularize the underlying particle system. However, through constant flat priors GWR introduces a bias in the particle model which makes it difficult to reproduce strong phase-space gradients of the target galaxy, *e.g.* anisotropic velocity distributions, unless its dynamical structure is known beforehand.

In this Chapter we have described a new Moving Prior Regularization (MPR) method, based on a prior distribution for the particles which evolves with the model. Individual particle priors are updated along with particle weights to keep track of the phase-space structures of the evolving weight distribution. The basic idea is to determine the priors such that they are similar for particles on neighbouring orbits, specified by orbital invariants or integrals of motion such as energy and angular momentum in the spherical case. The new priors are then used in a weight entropy function to ensure a regularization which smoothes locally in phase-space, without erasing global phase-space gradients.

We have then tested this MPR scheme, together with the χ^2M2M modelling technique, using a series of spherical target galaxies with both idealized and realistic data.

Our main conclusions are as follows:

- For a truncated spherical target galaxy with idealized data, for which in theory a unique inversion of the data exists, our NMAGIC models with MPR show that the target can be recovered accurately, and independent of the initial particle model.

- The new MPR generally improves both the accuracy with which the dynamical structure of the target galaxy is reproduced, and the convergence to the true solution independent of the initial particle model. Compared to GWR, biases in the anisotropy structure are removed, and local fluctuations in the intrinsic distribution function are reduced. Moreover, MPR allows a higher amount of smoothing than the weight entropy regularization, while the data are still fitted well.

- Lack or poorer quality of data introduce degeneracies in the dynamical modelling results and a dependence on the initial particle model, so that the reliability of the models is limited to those regions in which good observational data exist. Also in this case, the new MPR achieves a better reconstruction of the target properties and is less dependent on the choice of the initial particle model.

- Using the new MPR, we have reconstructed the best-fitting NMAGIC models determined in previous work by DL08 and DL09 for the two elliptical galaxies NGC 4697 and NGC 3379 in their dark matter halos. To this goal, we have extended the MPR method to the axisymmetric case, using the integrals E and L_z and the total angular momentum as an approximation to the third integral. The final models are intrinsically smoother and provide smoother fits to the available data.

There is clearly room for improving the current version of MPR: the method could be generalized to systems of lower symmetry using the invariants associated with orbits, *e.g.* the turning points, to assign moving priors in phase-space to the particles. Moreover, a cumulative grid-less variant of the method could also be implemented. Re-sampling of the N-body system from time to time during and after the adjustment of the weights (Dehnen, 2009) would enforce equal weight for particles orbiting the same torus, but it would not take care of smoothing between nearby tori with very different weights.

To conclude, the experiments described in this Chapter show that the moving prior regularization method improves the correct and unbiased recovery of the orbit structure of the target galaxy from noisy data. A similar regularization scheme could also be implemented in Schwarzschild orbit superposition models.

3

Elliptical galaxies with rapidly decreasing velocity dispersion profiles: NMAGIC models and dark halo parameter estimates for NGC 4494

This work has been submitted as Morganti et al. (2012) to MNRAS.

NGC 4494 is one of several intermediate-luminosity elliptical galaxies inferred to have an unusually diffuse dark matter halo. We use the χ^2-made-to-measure particle code NMAGIC to construct axisymmetric models of NGC 4494 from photometric and various kinematic data. The extended kinematics include light spectra in multiple slitlets out to $3.5R_{\rm e}$, and hundreds of planetary nebulae velocities out to $\simeq 7R_{\rm e}$, thus allowing us to probe the dark matter content and orbital structure in the halo.

We use Monte Carlo simulations to estimate confidence boundaries for the halo parameters, given our data and modelling set-up. We find that the true potential of the dark matter halo is recovered within $\Delta G(\text{merit function}) \lesssim 44$ ($\Delta\chi^2 \lesssim 101$) at 70% confidence (C.L.), and within $\Delta G \lesssim 59$ ($\Delta\chi^2 \lesssim 108$) at 90% C.L. These numbers are of the same order as fluctuations caused by variations of the data within errors, and only weakly dependent on regularization. They are much larger than the usually assumed $\Delta\chi^2 = 2.3(4.6)$ for 70% (90%) C.L. for two free parameters, perhaps case-dependent, but

calling into question the general validity of the standard assumptions used for halo and black hole mass determinations.

The best-fitting models for NGC 4494 have a dark matter fraction of about 0.6 ± 0.1 at $5R_{\mathrm{e}}$ (70% C.L.), and are embedded in a dark matter halo with circular velocity ~ 200 km/s. The total circular velocity curve (CVC) is slightly falling outwards from $v_{\mathrm{c}} = 220$ km/s. The orbital anisotropy of the stars is moderately radial, increasing slightly from the center outwards. These results are independent on the assumed inclination of the galaxy, and edge-on models are preferred.

Comparing with the halos of the intermediate-luminosity ellipticals NGC 3379 and NGC 4697, whose velocity dispersion profiles also decrease rapidly from the center outwards, the CVCs are quite similar. NGC 4494 shows a particularly high dark matter fraction, and a strong concentration of baryons in the center.

3.1   Introduction

The formation and evolution of elliptical galaxies have been an open issue in astrophysics since a long time. Being collisionless to a very good approximation, ellipticals retain relics of their formation history in the present-day orbital structure, especially in their halos due to the longer dynamical time scales. According to the currently favoured hierarchical formation scenario in a ΛCDM cosmology, these halos are dark matter dominated. The ambitious task of inferring both the orbital structure and mass distribution of ellipticals is commonly tackled by dynamical modelling of the observational data.

Unfortunately, the lack of an ubiquitous tracer such as HI gas in spiral galaxies (but see Bertola et al., 1993; Franx et al., 1994; Oosterloo et al., 2002) makes mass measurements in elliptical galaxies quite challenging, and the greatest evidence of dark halos is confined to the bright giant ellipticals whose mass distribution can be determined from X-ray emission of the hot gas (*e.g.* Loewenstein and White, 1999; Humphrey et al., 2006; Das et al., 2010b) or strong gravitational lensing techniques (*e.g.* Maoz and Rix, 1993; Keeton, 2001; Treu and Koopmans, 2004; Auger et al., 2010a). These studies are consistent with massive dark halos, and nearly isothermal total mass profiles (Ciotti et al., 2009). By contrast, the situation with less massive, X-ray faint ellipticals is more controversial. However, dynamical models, particularly when fitting higher order moments of the line-of-

sight velocity distribution (LOSVD) from stellar absorption lines, eventually ascertained the presence of dark matter halos around these intermediate-luminosity ellipticals and are generally consistent with flat circular velocity curves. Being LOSVD measurements limited by the rapid fall-off of the stellar surface brightness, the kinematics of discrete tracers such as planetary nebulae (PNe) and globular clusters (GCs) usually represent the only possibility to probe the mass distribution and orbital structure beyond $2R_{\mathrm{e}}$, in the realm of dark matter (*e.g.* Hui et al., 1995; Méndez et al., 2001; Douglas et al., 2002; Peng et al., 2004; de Lorenzi et al., 2008, 2009; Napolitano et al., 2009; Das et al., 2011; Napolitano et al., 2011; Deason et al., 2012).

Curiously, the PNe velocity dispersion profiles of some of the nearby intermediate-luminosity ellipticals show a strong decline with radius outside $1R_e$ (Coccato et al., 2009), suggesting very little (if any) dark matter (Romanowsky et al., 2003). The aim of the present analysis is to expand the sample of modelled intermediate luminosity ellipticals focussing on NGC 4494, and then compare the results with those which have been previously obtained for the other galaxies with strongly declining velocity dispersion profile, namely NGC 4697 (de Lorenzi et al., 2008, hereafter DL08) and NGC 3379 (de Lorenzi et al., 2009, hereafter DL09).

NGC 4494 is an E1-E2 elliptical galaxy (according to NED - the NASA/IPAC Extragalactic Database) in the outer regions of the Virgo cluster, with a smooth light profile and an intermediate stellar mass of about $10^{11}M_{\odot}$ (Foster et al., 2011, hereafter F11). It has been described as either a loose group member (Forbes et al., 1996) or an isolated galaxy (Lackner and Ostriker, 2010). Among the peculiarities of this galaxy, a sharp central ring of dust (Forbes et al., 1995; Lauer et al., 2005), a kinematically decoupled core (Bender et al., 1994; Krajnović et al., 2011), and significant rotation ~ 60 km/s out to $\sim 3R_{\mathrm{e}}$ (Proctor et al., 2009) have been reported. The latter features, when coupled, make it difficult to classify NGC 4494 as either a fast or slow rotator (Emsellem et al., 2007; Coccato et al., 2009; Krajnović et al., 2011). The velocity dispersion profile of NGC 4494 is rapidly decreasing, from about 160 km/s in the center to about 70 km/s at $\sim 7R_{\mathrm{e}}$ (Napolitano et al., 2009, hereafter N09), hinting to a deficiency in dark matter. Also, the X-ray flux of NGC 4494 is two hundred times fainter than that of other galaxies of the same optical luminosity, which in turn has been interpreted as the result of a recent interaction which has depleted the gas, or again the evidence of little dark matter

(O'Sullivan and Ponman, 2004; Fukazawa et al., 2006).

NGC 4494 has been recently modelled using spherical Jeans models (N09), and axisymmetric particle models constructed with the iterative method (Rodionov et al., 2009). The available observational data, which included PNe velocities out to $\sim 7R_{\rm e}$ (N09), were best fit by low concentration dark halos, with some uncertainties related to the adopted modelling assumptions, the small differences in the quality of the fits for different models (N09), and the number of explored models (Rodionov et al., 2009).

Lately, new observational data consisting of stellar absorption line kinematics in multiple slitlets out to $\sim 3.5R_{\rm e}$ became available for this galaxy (Proctor et al., 2009, F11). Moreover, NGC 4494 made a comeback in the work of Deason et al. (2012) as an outlier with curiously low dark matter fraction within $5R_{\rm e}$ with respect to model predictions assuming either a Salpeter or a Chabrier initial mass function. These facts prompt a further careful analysis of the dark matter content and orbital structure of NGC 4494, incorporating as many observational data as currently available and assessing the uncertainties in the recovery of dark halo parameters via dynamical models.

To this aim, we construct new dynamical models fitting all the available photometric and kinematic data with the flexible particle code NMAGIC (de Lorenzi et al., 2007, hereafter DL07), which implements a slight modification of the made-to-measure (M2M) technique proposed by Syer and Tremaine (1996), suited to the modelling of observational data with errors (χ^2M2M). NMAGIC works by slowly correcting the particle weights of an evolving N-body system until a satisfactory compromise is achieved between the goodness of the fit to the observational data, and some degree of regularization of the underlying particle model. More recent implementations of the method can be found in Dehnen (2009), who proposed a different technique for the weight adaptation and Long and Mao (2010). In the previous Chapter, we introduced a new Moving Prior Regularization method to generate smooth χ^2M2M particle models fitting noisy data without erasing the global phase-space structures. So far, the M2M technique has been used to investigate the dynamics of the Milky Way's bulge and disk (Bissantz et al., 2004), the mass distribution and orbital structure in the outer halos of elliptical galaxies (DL08; DL09; Das et al., 2011), and the dynamics of a sample of SAURON elliptical and lenticular galaxies (Long and Mao, 2012). In this Chapter, we construct axisymmetric NMAGIC models of the observational data, which include PNe (N09) and new stellar absorption line kinematics in slitlets (F11), for

different dark matter contributions to the total gravitational potential, and for different inclinations.

One of the key points in this work is the study of the accuracy with which the parameters of our models can be estimated given the observational data at hand. M2M particle methods, similarly to the more exploited Schwarzschild methods, work by weighting a system of particles (orbits) in order to achieve a good match to the data, and typically adjust many more weights than they have data constraints, hence the number of degrees of freedom[1] is likely much smaller than the number of data points (Cretton et al., 2000; Gebhardt et al., 2000). The relative differences $\Delta\chi^2 = \chi^2 - \chi^2_{min}$ are commonly used to measure which combinations of parameters provides an equally good fit as the one that achieves the minimum χ^2. On the assumption that the observational errors are Gaussian distributed (but see van der Marel et al., 2000), $\Delta\chi^2$ follows χ^2-statistics (*e.g.* Press et al., 1992). A large number of modelling studies so far assumed that the number of degrees of freedom is known, and estimated the 68% confidence level on 1 (2,3) free model parameter(s) based on $\Delta\chi^2 = 1(2.3, 3.5)$ (*e.g.* van der Marel et al., 1998; Cretton et al., 1999; Barth et al., 2001; Verolme et al., 2002; Cappellari et al., 2002; Gebhardt et al., 2003; Valluri et al., 2004; Shapiro et al., 2006; Chanamé et al., 2008; Cappellari et al., 2009b; van den Bosch and de Zeeuw, 2010; Murphy et al., 2011; Adams et al., 2012). However, it is hard to figure out the effective number of free parameters involved in the modelling. Hence, we follow a different approach and use Monte Carlo simulations of an NGC 4494-like reference galaxy to assign specific confidence intervals enclosing a certain probability of finding the true values of the parameters (*e.g.* Press et al., 1992; Thomas et al., 2005b).

The Chapter is organized as follows. In Section 3.2 we describe the observational data. In Section 3.3 we outline the modelling technique. In Section 3.4 we construct a NGC 4494-like target galaxy, together with its observables, and we use it to calibrate the optimal amount of regularization, and assess the confidence levels for parameter estimation with NMAGIC. Dynamical models of NGC 4494 for a range of dark matter halo potentials and inclinations are constructed in Section 3.5, and the main implications of our findings are discussed in a broader context in Section 3.6. Finally, the Chapter closes in Section 3.7.

---

[1] The number of degrees of freedom is defined as the number of constraints (data points plus constraints introduced by *e.g.* regularization) subtracted by the number of free parameters (model parameters plus fitted weights).
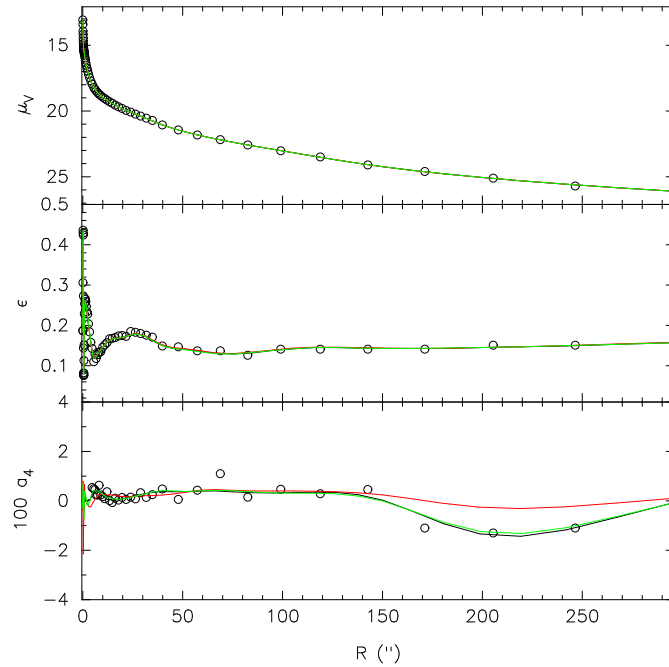
Figure 3.1: *From top to bottom*: V-band surface brightness, ellipticity, and fourth-order isophotal shape coefficient a_4 as a function of major-axis projected radius for NGC 4494. *Circles* are the measurements, *lines* represent the reprojected values from the axisymmetric deprojections, having assumed an inclination of 90°(*black*), 70°(*green*), and 45°(*red*).

3.2   Observational data

In this Section we describe the observational data that we will use for modelling the elliptical galaxy NGC 4494. We adopt a distance of 15.8 Mpc (Tonry et al., 2001), so that 1 kpc=13″, a systemic velocity $v = 1344$ km/s, from NED, and $R_e = 49'' \approx 3.77$ kpc (de Vaucouleurs et al., 1991).

3.2.1   Photometric data and deprojection

As photometric data, we use the V-band surface brightness profile, ellipticity and shape parameter a_4 values of N09. The photometric data extend to $273''$ along the major axis, and are a combination of *HST* data in the V and I bands inside $4.3''$ (Lauer et al., 2005), ground-based observations in BVI out to $32''$ (Goudfrooij et al., 1994), and Megacam data from the Sloan Digital Sky Survey g' filter (N09). The total extinction-corrected luminosity in the V-band is $2.6 \times 10^{10} L_{V,\odot}$ (N09).

A Sérsic fit to the surface brightness profile outside the central dust region $(R > 5.6'')$ gives $n = 3.30$ (N09). The observed ellipticity is $\epsilon = 0.15-0.20$ (axis ratio $q = 0.85-0.80$)

for $R < R_e/2$, outside of which NGC 4494 becomes rounder, with $\epsilon = 0.13 - 0.15$ ($q = 0.87 - 0.85$) for $1 - 1.5R_e$.

The radial profiles of surface brightness, ellipticity, and shape parameter a_4 are shown in Fig. 3.1.

In our NMAGIC models for the galaxy NGC 4494, we will not use the 2D surface brightness, but rather its 3D deprojected luminosity density. The deprojection of the surface brightness is unique only for spherical or edge-on axisymmetric systems (*e.g.* Gerhard and Binney, 1996). Here, we consider axisymmetric deprojections for inclinations $i = 90°, 70°, 45°$, which is very close to the minimum inclination allowed by the observed flattening of NGC 4494 (N09; F11). For each inclination angle, we use the maximum penalized likelihood scheme and program described in Magorrian (1999) to find a smooth axisymmetric density distribution consistent with the surface brightness profile. The method favours a power-law density profile in the radial region not constrained by photometric data.

The overall good agreement between the measured and reprojected surface brightness, ellipticity, and shape parameter a_4 is shown in Fig. 3.1.

3.2.2   Kinematic data

We combine three kinematic data sets in order to achieve the widest possible spatial coverage and probe the mass distribution and orbital structure far out in the halo of NGC 4494. In particular, we use long-slit absorption line kinematics extending out to $\sim 2R_e$ (Coccato et al., 2009), absorption line kinematics in slitlets out to $\sim 3.5R_e$ (F11), and PNe line-of-sight velocities reaching $\sim 7R_e$ (N09). The spatial coverage of the combined kinematic constraints can be appreciated in Fig. 3.2.

Stellar-absorption line slit data

Long-slit absorption line kinematics within $\sim 2R_e$ were presented in Coccato et al. (2009), and consist of line-of-sight velocity v, velocity dispersion σ, and higher-order Gauss-Hermite coefficients h_3 and h_4, along the major and minor axis of NGC 4494.

The original data are shown in Fig. 3.3 with black dots. They are consistent with small or zero rotation along the minor axis, and substantial major axis rotation, flattening beyond $20''$ at $V \sim 60$ km/s out to $120''$. In the inner $10''$ along the major axis, the signature of
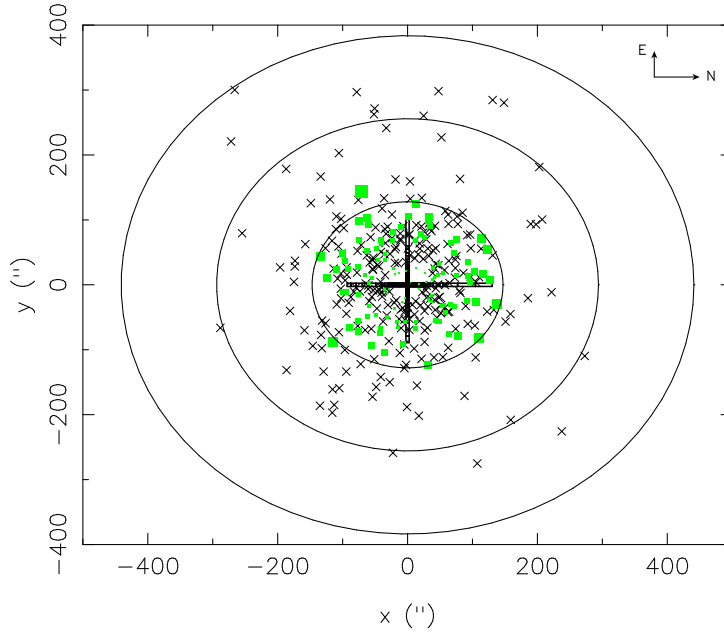
Figure 3.2: Spatial distribution of published kinematic data for NGC 4494. Long-slits along the major and minor axis are plotted, where the x-axis coincides with the major axis of the galaxy. The positions of PNe are marked by *black crosses*, those of the slitlets by *green squares*. *Ellipses* represent $3, 6$, and $9R_e$, for an axis ratio $q = 0.87$.

the decoupled core is apparent. The velocity dispersion decreases from about 160 km/s at the center to about 80 km/s at $\sim 100''$.

We noticed a systematic offset between the velocities and h_3 coefficients measured along the major and minor axes in the central arcsec. This leads us to suspect an offset of the minor axis slit in the South direction. The required offset (less than $1''$) is smaller than the slit width and the average seeing. Furthermore, the h_3 measurements along the minor axis are overall negative on both sides, which is unexpected even for a triaxial system with minor axis rotation. For the modelling, we therefore replace the measurements of v and h_3 along the minor axis with Gaussian random variates with zero mean and 1σ dispersion equal to the observational errors.

Inside $32''$ there are many nearby data points whose respective RMS deviations are larger than their error bars. In order to reduce their impact on the modelling, we run a central moving average over the data within $32''$, averaging over 7 data points (3 points on each side), and substituting each point with the value of the average.

Then, we minimize the impact of the feature at $\sim 20''$ along the major axis, which is due to contamination from a foreground star, by artificially increasing the error bars of those measurements.
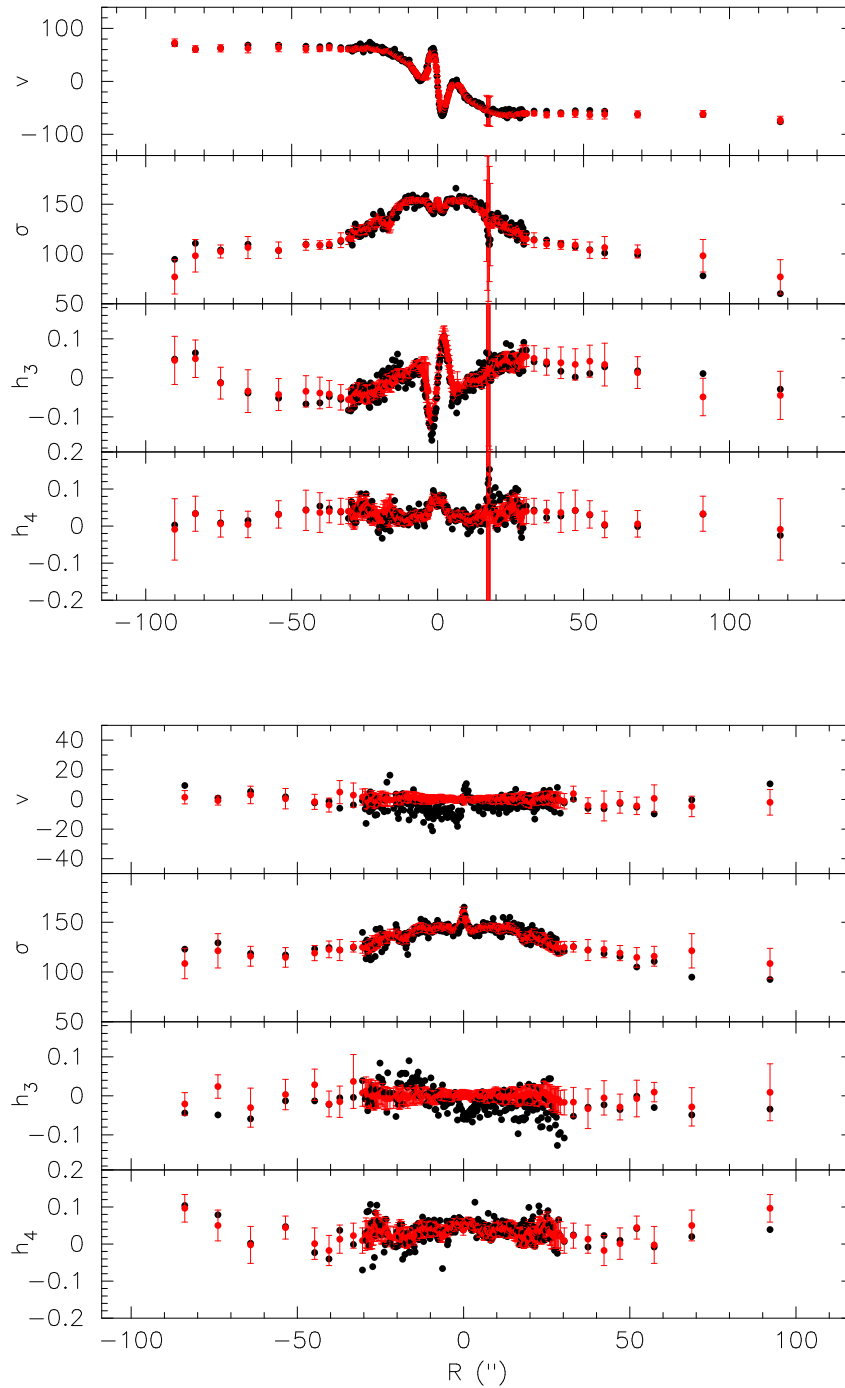
Figure 3.3: Long-slit kinematics along the major (*top*) and minor axis (*bottom*) of NGC 4494. *Black* and *red dots* represent the original data and the data used for the modelling, respectively. See Section 3.2.2 for details.

As we are interested in axisymmetric models of the data, we finally symmetrize the slit data set, as in DL09. In practice, we average the values of the measured kinematics at two similar radii (R_+, R_-) on both sides of the slit with respect to the center. Since the kinematic data show major axis rotation, we take into account the sign reversal of v and h_3 when symmetrizing the major axis slit data. Then, the new symmetrized data point is set equal to the weighted mean of the points on both sides, with weights proportional to the inverse square of the original errors. If σ_+ and σ_- are the errors on both sides, the new error σ on the symmetrized data points is set equal to the maximum of

$$\frac{2}{\sigma^2} = \frac{1}{\sigma_+^2} + \frac{1}{\sigma_-^2} \tag{3.1}$$

and half of the deviation between the original data points, which includes systematic errors between both sides of the galaxy.

The resulting data, with their respective error bars, are shown with red dots in Fig. 3.3, where they can be compared with the original measurements.

Stellar-absorption line slitlets data

We include in our kinematic constraints the measurements of v, σ, h_3, and h_4 in 115 galaxy light spectra in slitlets recently presented in F11, which extend out to $3.5R_{\rm e}$.

F11 discussed the generally good agreement between these data and the long-slit absorption line kinematics of Coccato et al. (2009). Also, they reported that their uncertainties are likely to be slightly underestimated.

On the whole, the absorption line kinematic data do not show significant evidence for minor axis rotation. Therefore, being interested in axisymmetric models of the data, we 4-fold the original sample of slitlets, taking into account the sign reversal of v and h_3, in order to decrease the impact of data asymmetries in our models.

Finally, we look for possible outliers in the 4-folded data set consisting of 460 data points. To this aim, we use the following procedure: for each slitlet, we compute the value of the average field of v, σ, h_3, and h_4 from its 20 nearest neighbours, excluding the slitlet itself. This average is worked out by excluding the lowest and highest 2 values in the neighbourhood, i.e. considering only the central 80% of the distribution. Moreover, the average is a weighted one, with weights equal to the inverse square of the larger of the individual observational error and the median of the observational errors in the
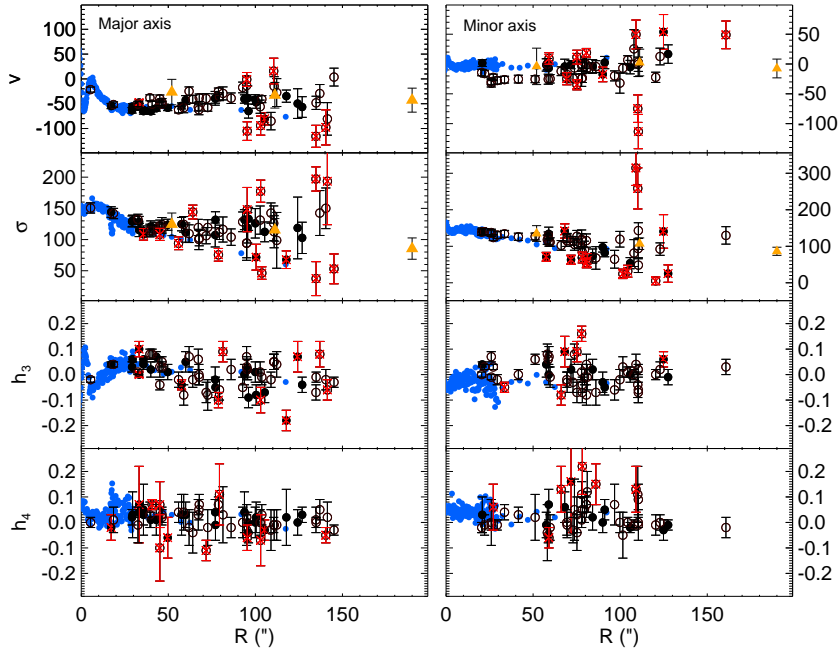
Figure 3.4: Slitlets kinematics in the 4-folded data set (*circles*), compared with long-slit (*blue dots*) and PNe data (*orange triangles*). Left and right column are for the measurements around the major and minor axis, respectively. *Filled circles* represent the data in a cone of $\pm 15°$ around the axis, while *empty circles* are the data points in cones $30° \pm 15°$, $60° \pm 15°$, respectively. Outliers determined by the method described in Section 3.2.2 are marked *red*.

central 80% of the distribution. In the same way, we calculate a weighted RMS σ in each neighbourhood. Then, we flag as outlier any point deviating by more than 2σ from the weighted mean of its neighbours.

With this procedure, 158 data points are flagged as outliers in velocity and/or velocity dispersion, and removed from the 4-folded data set. Of the resulting data set consisting of 302 slitlets, 68 points are marked as outliers in h_3 or h_4, and therefore we only consider their velocity and velocity dispersion in the modelling below.

The slitlets data points, together with the outliers determined in this way, are shown in Fig. 3.4.

Planetary nebulae velocities

Our kinematic observables are completed by the 267 PNe line-of-sight velocities obtained by N09 with the Planetary Nebulae Spectrograph (PNS, Douglas et al., 2002). As illustrated in Fig. 3.2, PNe extend out to $\sim 7R_e$.

Fig. 3.4 shows the comparison of all kinematic data. In the region of overlap, the
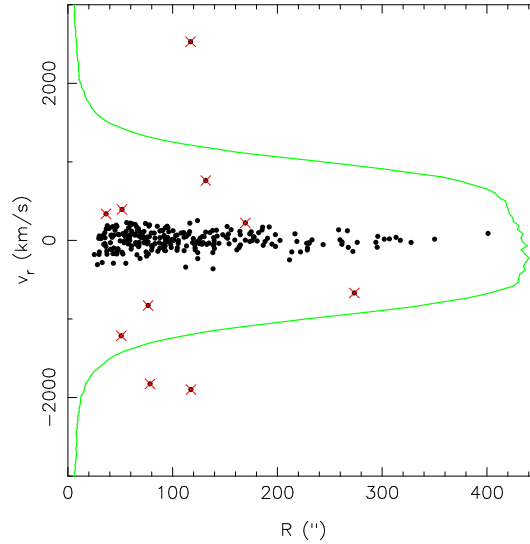
Figure 3.5: Distribution of the line-of-sight velocities of PNe as a function of projected radius. *Red crosses* mark the outliers identified by the friendless algorithm. The PNS filter band-pass is overplotted in *green*.

kinematics of PNe are consistent with those of the stars (see N09, Fig. 6 therein).

In order to look for possible outliers in the sample of PNe, we use the friendless algorithm presented in Merrett et al. (2003), which flags as outlier any object deviating by more than $n \times \sigma$ from the velocity distribution of its M nearest neighbours, where σ is the RMS computed in each neighbourhood. Adopting $n = 2.5$ and $M = 20$, we remove 10 outliers from the original sample of PNe. These outliers are highlighted in Fig. 3.5, which shows the projected phase-space distribution of PNe.

We are left with a catalogue of 257 PNe, whose size we double by applying point-symmetry, i.e. generating for every PN (x,y,v) the symmetric PN (-x,-y,-v). Such point-symmetric velocity fields are expected in axisymmetric (or triaxial) potentials. From previous experiments we know that increasing the number of PNe by a further factor of two does not improve the modelling significantly.

3.3 Modelling data with NMAGIC

In this Section we briefly recall the NMAGIC made-to-measure (M2M) modelling technique. We also explain how the initial particle model is set up, and how the photometric and kinematic target observables are preprocessed for the dynamical modelling.

3.3.1   NMAGIC

The parallel code NMAGIC (DL07) is an implementation of a particle-based method to create χ^2M2M models in agreement with observations of galaxies. The algorithm is a slight modification of the technique proposed by Syer and Tremaine (1996), designed to model observational data with errors.

The basic idea behind M2M particle methods is to train a system of $i = 1, \ldots, N$ particles to reproduce the observables of a target galaxy by maximizing the function

$$F = -\frac{1}{2}\chi^2 + \mu S + \mathcal{L} \tag{3.2}$$

with respect to the particle weights w_i. This maximization strikes a compromise between the goodness of the fit (χ^2) in terms of deviations between target and particle model observables, and a pseudo-entropy functional

$$S = -\sum_{i=1}^{N} w_i \left[\log\left(\frac{w_i}{\hat{w}_i}\right) - 1 \right] \tag{3.3}$$

which serves the purpose of regularization. The likelihood term $\mathcal{L}$ is added to equation (3.2) to account for the likelihood of a sample of PNe velocities (see DL08).

Since in typical applications the number of particles is much higher than the number of data constraints on the particle model, regularization is essential. In standard M2M technique, regularization is achieved by pushing the individual particle weights towards a smooth distribution of predetermined priors $\hat{w}_i$, which mirror the initial particle weight distribution and are kept constant during the modelling. As we showed in Chapter 2, such a Global Weight Entropy scheme makes it hard to reconcile smoothness and orbital anisotropies in the final particle model. Therefore, in this work we adopt the alternative Moving Prior Regularization method, and we determine priors which follow the smooth phase-space structures traced by the weight distribution, as the latter adapts to match the observational data. This method facilitates recovering both a smoother and more accurate mass distribution function from noisy data, smoothing over local fluctuations without erasing global phase-space gradients.

Maximizing the function (3.2) translates into a prescription, the so-called "force-of-change", for correcting the weights of the particles while these are evolved in the total gravitational potential.

3.3.2   The gravitational potential

The particle modelling technique allows to use both a fixed potential, known a priori, and a time-varying potential, self-consistently computed from the particle distribution. In our dynamical models, we assume that the total gravitational potential is generated by the luminous and dark matter distributions, i.e.

$$\phi = \phi_\star + \phi_D. \tag{3.4}$$

Following Sellwood (2003) and DL07, $\phi_\star$ is frequently computed from the N-particle model for the light distribution via a spherical harmonic decomposition, assuming a constant mass-to-light ratio Υ. The value of Υ is not a fixed parameter, but rather it is determined during the NMAGIC run, simultaneously with the modelling of the observational data (see DL08).

Instead, the dark matter halo potential ϕ_D is parametrized, and has the logarithmic form

$$\phi_D(R, z) = \frac{v_0^2}{2} \ln\left(r_0^2 + R^2\right), \tag{3.5}$$

(Binney and Tremaine, 2008), where v_0 and r_0 are a characteristic (constant) circular velocity and scale-length. This mass model has been widely and successfully used to fit galaxies (*e.g.* Fall and Efstathiou, 1980; Persic et al., 1996; Kronawitter et al., 2000; Thomas et al., 2007b, DL09).

Our dynamical models will explore a range of circular velocity curves, whose behaviour at large radii varies between the near-Keplerian decline (when stars dominate the total potential), and a nearly flat (quasi-isothermal) shape obtained for massive dark halos, as shown in Fig. 3.6.

3.3.3   The initial particle model

We set up initial models of $N = 750000$ particles extending to $30R_{\rm e}$, i.e. ~ 110 kpc at the distance of NGC 4494.

The density of these initial particle models is given by a spherical deprojection of the circularly-averaged surface brightness profile. We follow the method described in Gerhard (1991) to obtain an isotropic stellar velocity distribution in the total gravitational potential generated by the stars plus the different dark matter halos described above.
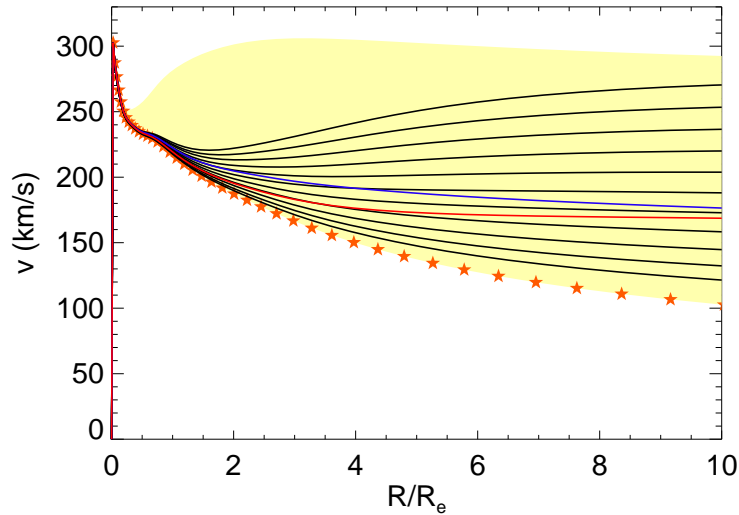
Figure 3.6: The *shaded area* shows the range of circular velocity curves corresponding to the total gravitational potentials used in the dynamical models. *Stars* represent the self-consistent case with constant M/L; *solid lines* correspond to models embedded in various spherical dark matter halos. *Black* lines correspond to dark halos with $r_0 = 4R_e$ and $v_0 = [70, ..., 270]$ km/s (from bottom to top). *Blue* and *red* lines correspond to $v_0 = 150$ km/s, and $r_0 = 3R_e$ and $5R_e$, respectively.

The particles' coordinates and velocities are drawn according to the complete distribution function applying the method of Debattista and Sellwood (2000), and particle weights are set equal to $1/N$.

Finally, following Kalnajs (1977) and DL08, we switch the sign of the velocity of a fraction of the retrograde particles, with probability

$$p(L_z) = p_0 \frac{L_z^2}{L_z^2 + L_0^2} \tag{3.6}$$

(where $p_0 = 0.3$, $L_0 = 0.02$), to introduce some angular momentum about the z-axis, while maintaining a smooth DF in equilibrium. This expedient makes it easier to reproduce the rotation velocity seen in the kinematic data.

3.3.4 Photometric and kinematic observables for the modelling

We now explain how the different photometric and kinematic observational data are processed in order to be used as constraints for the NMAGIC models.

For the photometric observables, the 3D luminosity density profile obtained from the deprojection of the surface brightness is expanded in spherical harmonic functions, and the expansion coefficients A_{lm} are used as luminosity constraints (*e.g.* DL07). These A_{lm} are

computed on a grid of 50 quasi-logarithmically spaced radial shells between $R_{\min} = 0.01''$ and $r_{\max} = 20R_{\mathrm{e}}$, and all the moments that would allow non-axisymmetry are set to zero. Poissonian errors are used for the mass in shells, whereas the errors for the higher-order mass moments are determined via Monte Carlo simulations of the density field of the target galaxy (see DL07).

For the long-slits and slitlets data, we use the luminosity-weighted kinematic observables for NMAGIC. Hence, we add to the target observables the luminosity in each slit cell or slitlet, obtained by integrating the surface brightness distribution with a Monte Carlo algorithm. For the slits, we assume that the slitwidth equals $5''$; for the slitlets, we set the slitwidth equal to the larger value between $1''$ and the diameter of a circle containing at least 250 particles of the initial particle model, so as to limit particle noise when computing model observables. Errors in these luminosities are set to 1% of the luminosity in each cell.

PNe data are modelled by maximizing the likelihood of the sample of discrete velocities and positions, as detailed in DL08. For computing the likelihood, the particles and PNe are binned in elliptical segments, assuming an average projected ellipticity of 0.2. We consider 3 radial and 4 equally-spaced angular bins, with the first angular bin centered on the major axis, as shown in Fig. 3.7. Each segment contains at least 30 PNe.

3.3.5 Modelling procedure

Starting from the initial particle model described in Section 3.3.3, the weights of all particles are evolved until the N-body system matches the target. During the whole evolution, the potential of the dark halo is kept fixed, but the stellar potential is frequently computed from the light distribution of the particle system. Particles are integrated in the total gravitational potential using a leapfrog scheme with adaptive time step.

After a relaxation phase of 1000 steps in which the initial particle model is advanced without any weight correction, particle weights are updated according to the force-of-change obtained maximizing equation (3.2), for $\sim 10^5$ correction time steps. Finally, the particles are freely evolved for another 10^4 steps without any further weight correction, to ensure that the final particle model is well phase-mixed. For reference, 10^4 correction time steps correspond to ~ 300 circular rotation periods at the target R_{e}. We define the model to have converged if χ^2 averaged over 50 steps stays almost constant in the last
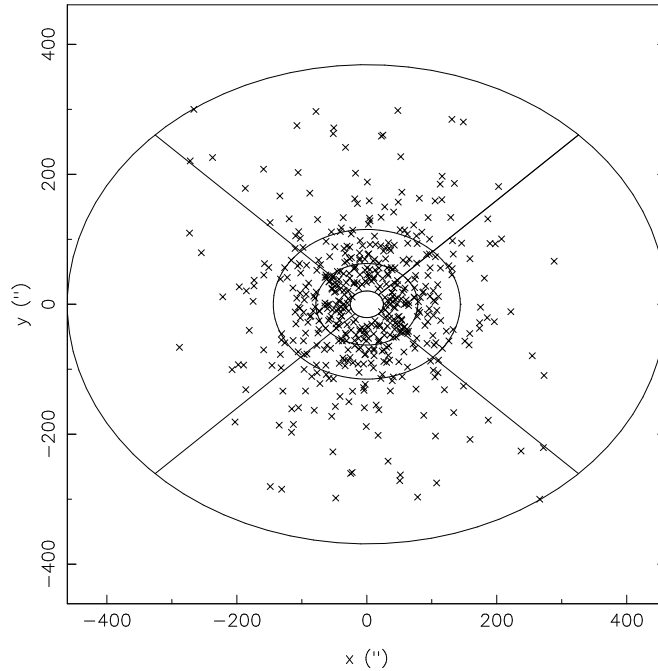
Figure 3.7: Segments in which the line-of-sight velocity distribution of particles is computed, for the likelihood method used to fit PNe with NMAGIC.

10^4 steps, with fluctuations which are typically of order 2%.

Since the errors are very small for the A_{lm} but much larger for the PNe, the A_{lm} term contributes more to the force-of-change equation, and changes made to the particle weights by the PNe data are small. In order to ensure that the halo is appropriately modelled, we thus increase the contribution of PNe to the force-of-change equation by a factor of 10.

Finally, to generate NMAGIC models we adopt the Moving Prior Regularization presented in Chapter 2. Hence, new priors are determined in phase-space by binning particles according to their orbital integrals. In particular, we grid particles according to energy (E), total circularity function x, and angular momentum with respect to the rotation axis L_z, in a grid of $n_E = 20$, $n_x = 4$, $n_z = 2$ bins, which at the same time resolves the relevant phase-space structures and ensures enough particles in each grid cell. The average weight contained in each cell is computed, and then a thin-plate smoothing spline is fitted to the grainy grid of priors, before assigning them to the particles. The optimal smoothing parameter for the thin-plate function is determined by Generalized Cross Validation (G. Wahba, 1990). The individual particle priors computed in this way are not kept constant in time but rather they are frequently updated while the particle weights are adapted to match the target observables.

3.4 Parameter estimation: how well can the dark matter halo be recovered?

In this study, we will fit the observational data of NGC 4494 with a sequence of NMAGIC models obtained for different dark matter halos and for different inclinations. We are not interested simply in dynamical models that look good on the data (the so-called "chi-by-eye" approach), but wish to quantify the uncertainties in the best-fit parameters from a statistical distribution appropriate for our data and modelling method. In this Section, we describe a simple Monte Carlo method to estimate such a distribution.

In the following, the best-fit parameters are defined as those for which a minimum is achieved in the merit function

$$G = \frac{1}{2}\chi^2 - \mathcal{L}, \tag{3.7}$$

which measures the agreement between the observational data and the final model in terms of the χ^2, that the χ^2M2M method tries to minimize, and of the log likelihood $\mathcal{L}$, that the method tries to maximize (note the difference with respect to equation [2.5]). In order to carry out a robust parameter estimation, we also need to quantify the uncertainties in these best-fit parameters.

Boundaries of the confidence regions for the estimated parameters will correspond to contours of constant ΔG relative to the best-fitting model in the sampled parameter space. In previous dynamical mass analysis (*e.g.* Gebhardt et al., 2003; Thomas et al., 2005b; Chanamé et al., 2008; Murphy et al., 2011), uncertainties in the model parameters are typically estimated by considering the parameter change necessary to increase χ^2 by 1 (or 2.3), and to decrease the log likelihood $\mathcal{L}$ (see DL08) by a factor of 0.5 (or 1.2) for 1 (or 2) fitted potential parameters (Press et al., 1992). As discussed in the Introduction, this is equivalent to assuming that all the fitted weight parameters minus the smoothing constraints are used completely to determine the DF from the data, and only the potential parameters are left to be determined by the remaining data constraints. We find empirically for our data set and modelling set-up that $\Delta\chi^2$ values are $\gg 1$, and therefore in this Section we compute confidence regions for parameter estimation via Monte Carlo experiments.

In Section 3.4.1, we build a mock target galaxy closely similar to the elliptical galaxy NGC 4494, which is embedded in a dark matter halo with scale radius and circular velocity

corresponding to the best-fitting model determined by N09 for NGC 4494. We generate photometric and kinematic observables for this mock galaxy with the same observational errors as for NGC 4494. In Section 3.4.2, we use the pseudo-data and known intrinsic parameters of this NGC 4494-like target galaxy to calibrate the regularization parameter appropriate for the modelling of NGC 4494. In Section 3.4.3, we use a sequence of NMAGIC models for the target galaxy to show how well the circular velocity and scale radius of its (known) dark halo, the total enclosed mass, and the mass-to-light ratio can be recovered, in a more rigorous way than in previous NMAGIC modelling (DL08; DL09 Das et al., 2011). Finally, in Section 3.4.4 we use Monte Carlo experiments to determine the appropriate ΔG to be used for confidence boundaries which allow us to quantify uncertainties in the dark halos parameters and to discriminate between different mass distributions in the modelling of the real data of NGC 4494.

3.4.1 An NGC 4494-like galaxy and its observables

Our chosen NGC 4494-like target galaxy has the luminosity distribution obtained by deprojecting the surface brightness of NGC 4494 for $i = 90°$, and it is embedded in a logarithmic dark matter halo (3.5), with $r_0/R_e = 4$ and $v_0 = 150$ km/s, as in the best-fitting Jeans model of N09 for NGC 4494. Similar to the orbital anisotropy predicted by some merger models in the current cosmological scenario (*e.g.* Dekel et al., 2005), the velocity distribution of this NGC 4494-like galaxy is isotropic in the center and increasingly radially anisotropic at larger radii. As for NGC 4494, we observe the target galaxy from a distance of 15.8 Mpc, and the projected effective radius $R_e \approx 49''$. We set its stellar mass-to-light ratio to 3.8.

Following the procedure outlined in Section 3.3.3, we generate a particle model realization for this target, using 750000 particles. To implement the orbital anisotropy of the target galaxy, we adopt the models with specified circularity function of Gerhard (1991). Furthermore, we add a certain amount of rotation to the particle model (see Section 3.3.3) so as to mimic the real NGC 4494.

As luminosity observables we use the coefficients A_{lm} of the spherical harmonic expansion of the 3D luminosity density, computed as described in Section 3.3.4. The kinematic observables are v, σ, h_3, h_4, projected onto both the long-slit set-up and the slitlets set-up used for the modelling of NGC 4494. These observables can be readily determined using
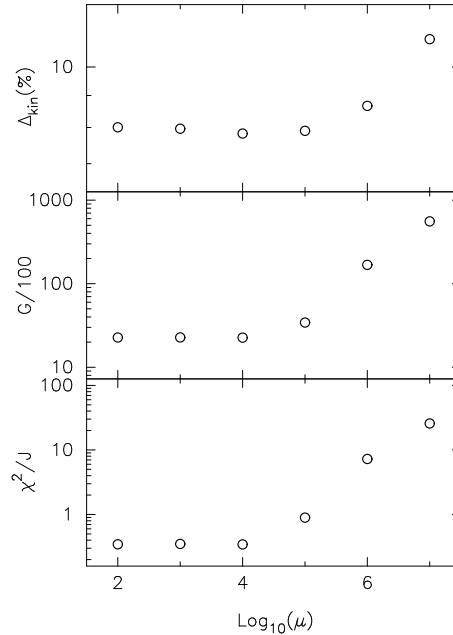
Figure 3.8: Quality of the final NMAGIC particle models as a function of the regularization parameter μ, from unsmoothed models (small values of μ) to oversmoothed models (high values of μ). *Top panel*: RMS deviation (%) of the internal velocity moments of the final particle model from the target, computed over the radial region constrained by the data. *Middle panel*: merit function G in equation (3.7). *Bottom panel*: χ^2/J of the particle model fit to the J photometric and absorption-line kinematic data points ($J = 4214$).

NMAGIC with weight correction turned off, integrating the particle model representing the target galaxy. After an initial relaxation phase in the fixed total gravitational potential, time-smoothed kinematic observables are computed directly from the particles, as described in the previous Chapter. Observational errors from NGC 4494 are adopted, and Gaussian random variates with 1σ equal to such errors are added to the kinematic observables computed in this way.

Finally, we generate a mock sample of PNe velocities similar to that described in Section 3.2.2. To this purpose, we again use NMAGIC to integrate the particle model which imitates NGC 4494, and in parallel compute the time-averaged velocity and velocity dispersion of the particles binned in radial and angular segments on the sky. We adopt the same 3 radial bins and 4 equally-spaced angular bins as in Section 3.3.4. Then, we consider the catalogue of PNe used for the modelling of NGC 4494, and assign a new velocity to every PN in the catalogue, according to a Gaussian distribution with velocity and velocity dispersion of the spatial segment the PN would belong to, given its position on the sky.

3.4.2 Calibrating regularization

The regularization parameter to be used when constructing dynamical models is case-dependent, and it is influenced by several factors, most notably the observational data to be modelled (error bars, scatter, spatial coverage) and the phase-space structure of the target galaxy (see *e.g.* Gerhard et al., 1998; Cretton et al., 1999; Thomas et al., 2005b, DL08; DL09).

To determine the optimal amount of smoothing given the data, we model the observational data of the NGC 4494-like galaxy using different values for the regularization parameter μ, which controls the balance between regularization and goodness-of-fit in equation (3.2). The Moving Prior Regularization method is used.

The results of our experiments are summarized in Fig. 3.8, which shows, for increasing values of μ, the reduced χ^2, the merit function G in equation (3.7), and the RMS difference (Δ_{kin}) between the internal velocity moments (see previous Chapter) of the target and of the final NMAGIC model.

The minimum in the Δ_{kin} plot determines the value of μ for which the model best recovers the internal moments of the input model. This occurs at $\mu \simeq 10^4$. In Fig. 3.8 we also see that for values of $\mu \geqslant 10^5$ a smooth model fitting the data points within errors can no longer be found.

Based on the results of these experiments, in the following we will adopt a value of $\mu = 10^4$ to regularize our NMAGIC models.

3.4.3 Recovery of the dark halo parameters of an NGC 4494-like galaxy

We now construct NMAGIC models that fit the data of the NGC 4494-like target galaxy for a range of assumed parameters of the dark halo potential in equation (3.5). The key question that we are interested in is: how well can NMAGIC recover the true parameters ($r_0 = 4R_e$, $v_0 = 150$ km/s) of the dark halo given the observational data at hand?

We follow the modelling procedure outlined in Section 3.3.5, starting from an isotropic initial particle model computed in each dark halo, as explained in Section 3.3.3. We use all available photometric and kinematic constraints, including PNe through the likelihood technique. Our NMAGIC models are regularized with the Moving Prior Regularization method, adopting the optimal value of $\mu = 10^4$ determined above.
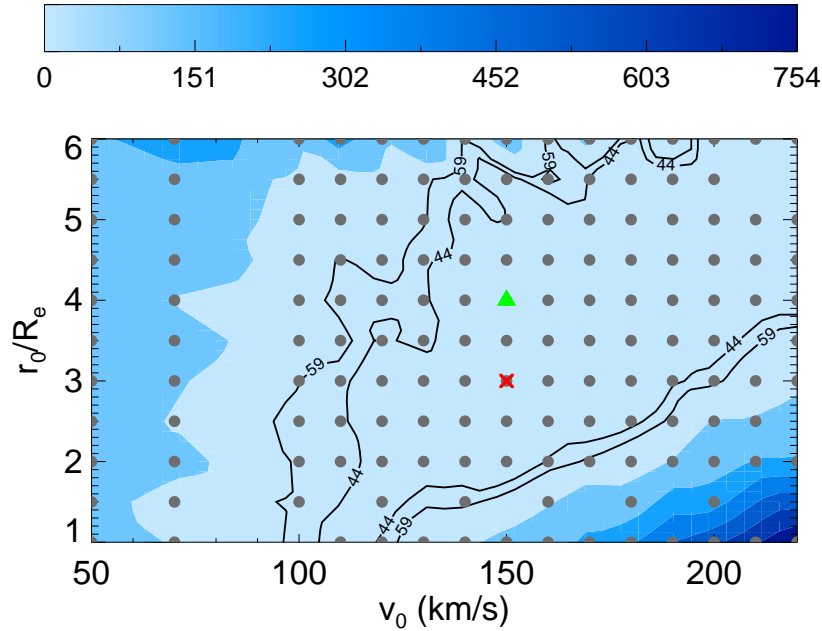
Figure 3.9: Recovering the halo parameters of an NGC 4494-like galaxy. Each *grey circle* represents a final NMAGIC model. The true dark halo has scale radius $r_0 = 4R_e$ and circular velocity $v_0 = 150$ km/s (*green triangle*). The colour scheme reflects the magnitude of the ΔG of each model relative to the overall best-fitting model, defined as that with the smallest G (*red cross*). The *black lines* correspond to 70% and 90% confidence contours, as derived from the simulations of Section 3.4.4.

We sample the halo parameters (r_0, v_0) on a grid of ~ 200 models. The results of these experiments are shown in Fig. 3.9 in terms of the ΔG of each NMAGIC model relative to the best-fitting model, which corresponds to the overall smallest G.

The shape of the contours of ΔG in Fig. 3.9 is regular, and there is an extended region for which the values of G are similar. Many models providing similarly good fits to the data, all with reduced $\chi^2/J \leqslant 1$, are obtained for different parameters of the dark halo (the number of data points $J = 4214$). The best-fitting model is found for values of the dark halo parameters $r_0 = 3R_e$ and $v_0 = 150$ km/s, and it has a reduced $\chi^2/J = 0.33$, log likelihood $\mathcal{L} = -1541.04$, and $G = 2228.45$. The scale radius of this best-fitting model is smaller than that of the true model, which achieves a reduced $\chi^2/J = 0.34$, log likelihood $\mathcal{L} = -1539.87$, and $G = 2265.08$. For comparison, the no-dark halo model, which provides the poorest fit to the available observational data, has a final reduced $\chi^2/J = 0.48$, log likelihood $\mathcal{L} = -1564.33$, and $G = 2566.35$.

Surprisingly, the values of ΔG are large ($\gg 1$). For instance, the model obtained for the true parameters of the (known) dark matter halo achieves a value of G which is $\Delta G \sim 40$
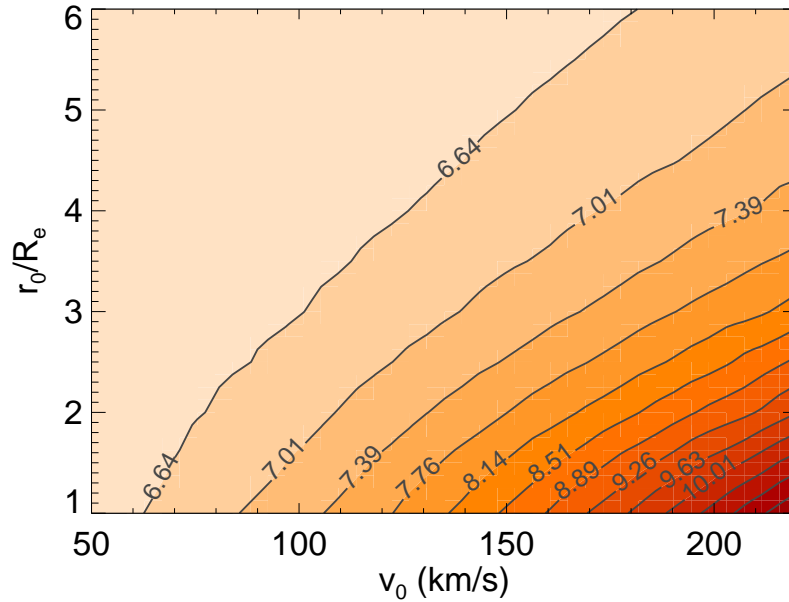
Figure 3.10: Total enclosed mass (stars plus dark matter) within $2R_\mathrm{e}$ for different values of the halo parameters r_0 and v_0. Contour values are in units of $10^{10} M_\odot$.

$(\Delta\chi^2 \sim 40)$ away from the best-fitting model. Applying the classical χ^2 statistics for two degrees of freedom, the true parameters of the dark matter halo would be discarded at the 99.99% level. We investigate this issue in Section 3.4.4

Note that the contours of ΔG remain open to the top-right edge of the plot (see also *e.g.* Gerhard et al., 1998; Thomas et al., 2005b; Murphy et al., 2011), showing that it is not possible to put robust constraints on both halo parameters simultaneously in this case. Similar values of G, and hence similarly good models are achieved for halo models located along a large band extending from low r_0 and low v_0 to high r_0 and high v_0. Such diagonal band shrinks when modeling target galaxies embedded in more massive halos, as the models that do not contain enough mass are ruled out. Models inside this band share a similar total enclosed mass within the radial region constrained by the observational data, as shown in Fig. 3.10 by means of contours of total mass within $2R_\mathrm{e}$ in the same (r_0, v_0) parameter space. Evidently, the total enclosed mass inside a certain radius is what the dynamical models constrain best with the data at hand.

Indeed, when plotting the values of ΔG of the final NMAGIC models against enclosed mass (see Fig. 3.11) the shape of a parabola is evident, despite the scatter in the values of ΔG.
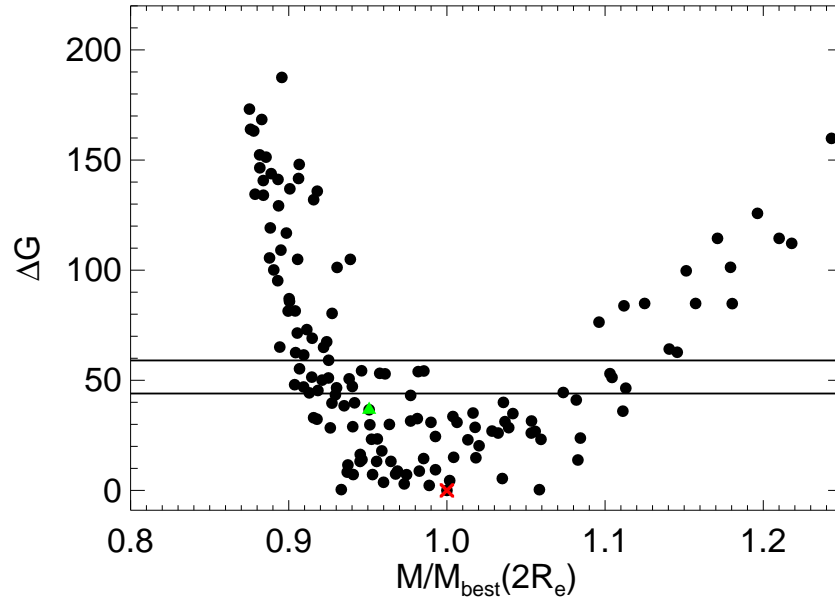
Figure 3.11: ΔG of the final NMAGIC models fitting the data of the NGC 4494-like galaxy, as a function of the total mass inside $2R_{\mathrm{e}}$ divided by the corresponding quantity for the best-fitting model. The *red cross* shows the best-fitting model, the *green triangle* the model with the true dark halo parameters. The black lines correspond to 70% and 90% confidence regions derived from the simulations of Section 3.4.4.

Finally, how well the NMAGIC models are able to recover the mass-to-light ratio and the dark matter fraction of the NGC 4494-like galaxy from these data can be appreciated in Figs. 3.12-3.13. These are both important quantities which we are interested in measuring with accuracy for real galaxies.

At this stage, two obvious questions are: what is the typical ΔG difference between the best-fitting NMAGIC model and the model with the true halo parameters? And related to this, within what errors can we trust the dark halo parameters of the best-fitting model? The following analysis is designed to answer these questions.

3.4.4   Parameter estimation for the dark matter halo: confidence levels

We now use Monte Carlo simulations to estimate the values of ΔG which represent a specific confidence level, given the observational data of NGC 4494 and our NMAGIC modelling technique (see *e.g.* Press et al., 1992).

In practice, given constraints on computer time, we construct a sequence of NGC 4494-like galaxies embedded in 10 different dark halos, and model each one of them with a range of dark halo parameters. Then, for each target galaxy we compute the ΔG between the
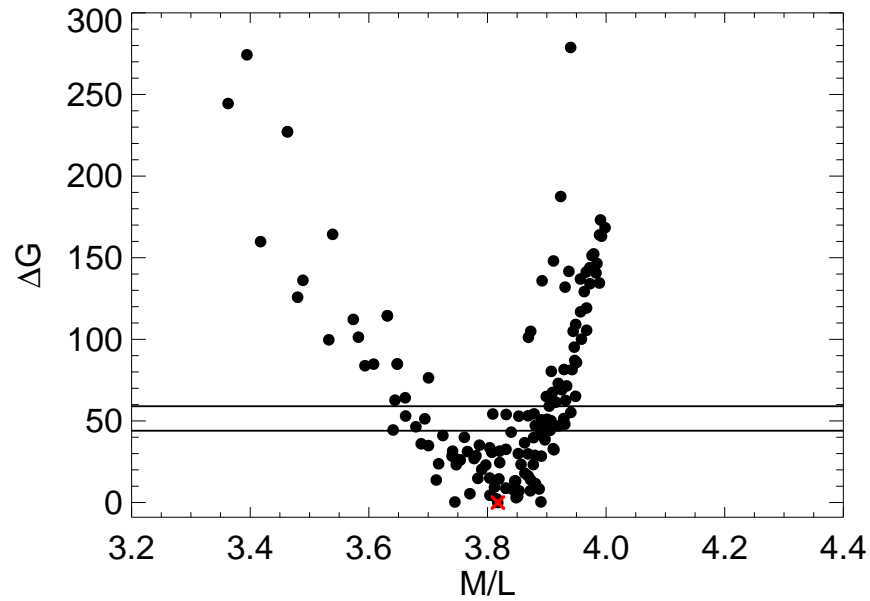
Figure 3.12: As Fig. 3.11, but ΔG of the final NMAGIC models as a function of stellar mass-to-light. The galaxy has (known) $M/L = 3.8$.
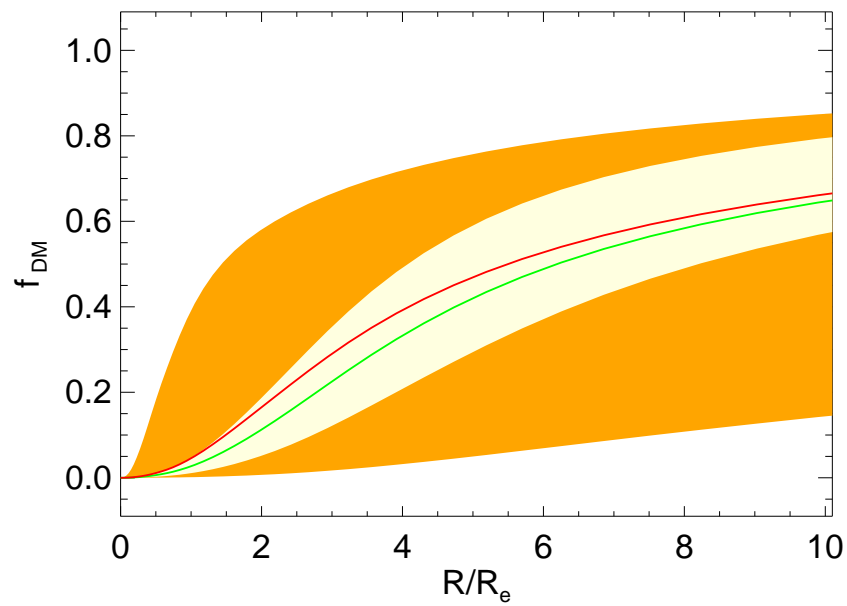

Figure 3.13: Recovery of the dark matter fraction $f_{DM} = M_{DM}/M$ as a function of radius for the range of explored NMAGIC models of the NGC 4494-like data (*orange shaded region*). The *green line* represents the known target, and the *red line* the best-fitting model. The *yellow shaded region* shows the 70% confidence region (see Section 3.4.4).
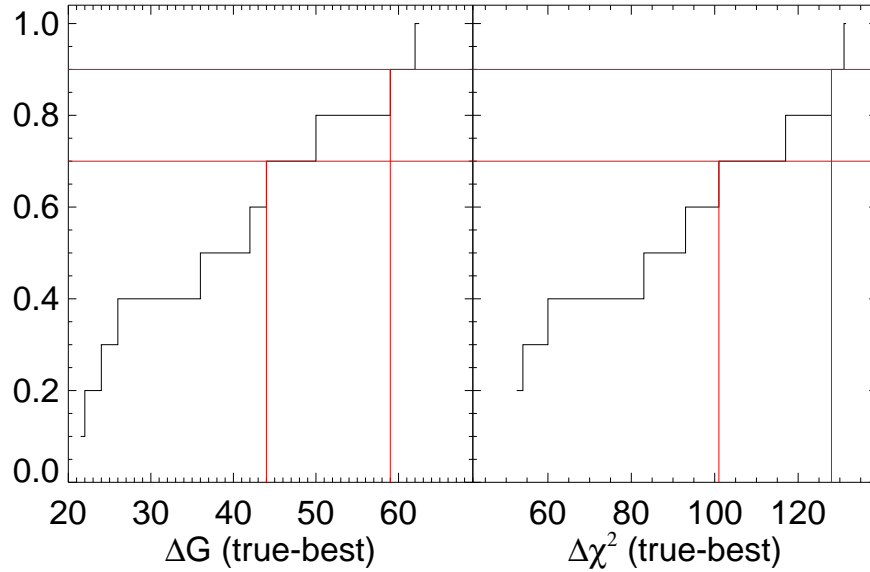
Figure 3.14: Normalized cumulative distribution of ΔG (*left*) and $\Delta \chi^2$ (*right*) between the true dark halo and the best fitting model, for the NGC 4494-like galaxy embedded in 10 different dark halos and modelled with NMAGIC. The best fitting model is defined as that with the minimum G (χ^2). The *red lines* correspond to 70% and 90% confidence levels.

best-fitting model and the model obtained for the true parameters. In this way, we can estimate the proper ΔG within which the true parameters are found in 70% or 90% of our experiments.

The main results from these experiments are summarized in Fig. 3.14, which shows the cumulative distribution of ΔG and $\Delta \chi^2$ between the true dark halo model and the best fitting model, for the 10 different experiments. It is seen that the NMAGIC models recover the true potential of the dark matter halo within $\Delta G \lesssim 44$ about 70% of the time, and within $\Delta G \lesssim 59$ about 90% of the time. Corresponding values are $\Delta \chi^2 \lesssim 101$ and $\Delta \chi^2 \lesssim 108$ for 70% and 90% confidence bands, respectively, not including the log likelihood.

The magnitude of these differences is quite surprising. Therefore we perform several additional tests to understand them better. First, we verify that the measured differences ΔG are actually significant with respect to fluctuations caused by modelling noise or measurements uncertainties. Indeed, it is natural to speculate that the numerical noise in the procedure of the weight-adjustment may cause fluctuations of G over time. However, these fluctuations are comparatively small, as on average they are ~ 14 in G (~ 30 in
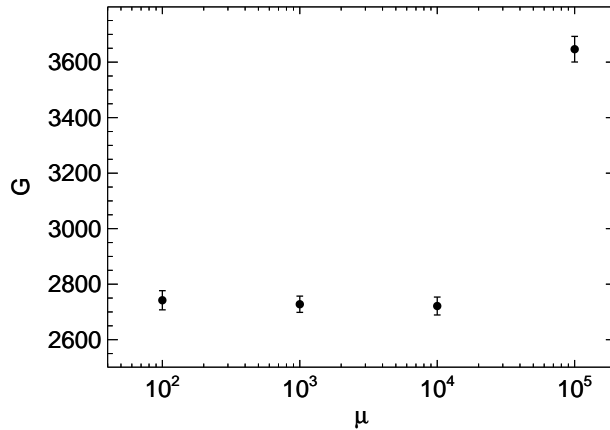
Figure 3.15: The merit function $G = \chi^2/2 + \mathcal{L}$ for increasing values of the regularization parameter μ. *Dots* represent the mean over 100 models fits to Monte Carlo realizations of the kinematic data of the NGC 4494-like galaxy; *error bars* represent the RMS deviations from the mean.

χ^2), i.e. a factor of three smaller than the typical values of ΔG (and $\Delta\chi^2$).

Then, in order to quantify the relevance of the observational measurement uncertainties, we generate a Monte Carlo chain of one hundred realizations of the data of the NGC 4494-like mock galaxy of Section 3.4.1. Every realization is constructed by drawing random Gaussian-distributed values for all kinematic data points, such that the mean is as predicted for the mock galaxy, and the variance corresponds to the observational errors (see *e.g.* van der Marel et al., 1998; Cretton et al., 2000; Thomas et al., 2005b). Then, we model each realization with NMAGIC, assuming the true gravitational potential of the target galaxy. Computing the dispersion of the values of G obtained modeling $N_{\mathrm{mock}} = 100$ realizations of the observational data, we conclude that random variations in the data according to the observational errors correspond to fluctuations in the merit function $G \sim 25$ (and in $\chi^2 \sim 50$) within 1σ. Instead, the experiments above showed that if the potential is not known in advance, NMAGIC models match the true potential of the dark matter halo within $\Delta G \lesssim 44$ at 1σ level. Hence, the $\Delta\chi^2$ difference computed by only fitting the true model to N_{mock} data sets (*e.g.* Thomas et al., 2005b) may be slightly underestimated.

As a further check, we verify whether the minimum value of G and/or the magnitude of ΔG are influenced by the degree of regularization employed in the NMAGIC fits. In the framework of Schwarzschild modelling, Verolme et al. (2002) showed that smoothing

constraints do not affect the shape of χ^2-contours significantly, and leave the overall best-fitting parameters unchanged. Thomas et al. (2005b) constructed Schwarzschild models for different values of the smoothing parameter, and computed the $\Delta\chi^2$ due to $N_{\mathrm{mock}} = 60$ different realizations of the data sets as a function of the smoothing parameter. They found that the magnitude of $\Delta\chi^2$ increases for increasing regularization (see their Fig. 6). We repeat their experiment modelling $N_{\mathrm{mock}} = 100$ realizations of the data of the NGC 4494-like mock galaxy for different values of the regularization parameter μ, and show our results in Fig. 3.15. The error bars represent the 1σ-variation ΔG as a function of μ, and show no indication that such ΔG is influenced by the regularization, up until and including the optimal regularization parameter used in our modeling ($\mu = 10^4$). An increase of the fluctuations of G due to regularization is only seen for oversmoothed models ($\mu = 10^5$, see Section 3.4.2).

The Monte Carlo experiments also reveal some slight biases which are intrinsic to our diagnostics of the best-fitting model. In particular, we find that the minimum χ^2 values are achieved on average for more massive halos than that of the target galaxy, as previously noted in Gerhard et al. (1998), while the maximum $\mathcal{L}$ values are typically achieved for halos which are more diffuse than the true (known) halo. The combination of χ^2 and $\mathcal{L}$ in the merit function G in equation (3.7) is less biased, since it strikes a compromise between these two opposite trends.

3.4.5   Summary

To summarize, we investigated how well the dark halo parameters can be constrained from data which have the spatial coverage and error bars of the current observational data for NGC 4494. These data do not suffice to determine both the scale radius and the circular velocity of the halo in equation (3.5), and different combinations of (r_0, v_0, Υ) that provide similar values of the total enclosed mass are allowed. The enclosed mass within $2R_{\mathrm{e}}$ can be determined to within 10%, and the dark matter fraction $f_{\mathrm{DM}}(3R_{\mathrm{e}})$ to within ± 0.1. For the family of logarithmic dark matter halos, the total circular velocity can be determined to ± 20 km/s.

Via Monte Carlo experiments, we computed confidence levels for parameter estimation. We conclude that, for NMAGIC models of the observational data at hand, the usual 1σ (70%) level corresponds to a value of $\Delta G \sim 44$, and of $\Delta\chi^2 \sim 101$ (and $\Delta G \sim 59$,

$\Delta\chi^2 \sim 108$ at 90% confidence level). Using these statistical results, we can now derive the uncertainties on the determination of the halo parameters for NGC 4494.

3.5 Dynamical models of NGC 4494

We now use NMAGIC to construct axisymmetric dynamical models for NGC 4494 fitting all the photometric and kinematic data described in Section 3.2. Three different inclinations for the stellar distribution are considered, $i = 90°, 70°, 45°$, for which we carried out the deprojections of the photometric data (see Section 3.2.1). In particular, the latter value is close to the minimum inclination allowed by the observed flattening of NGC 4494 (N09; F11). For each inclination, we explore a sequence of gravitational potentials including the self-consistent case with constant M/L, and various quasi-isothermal dark matter halos.
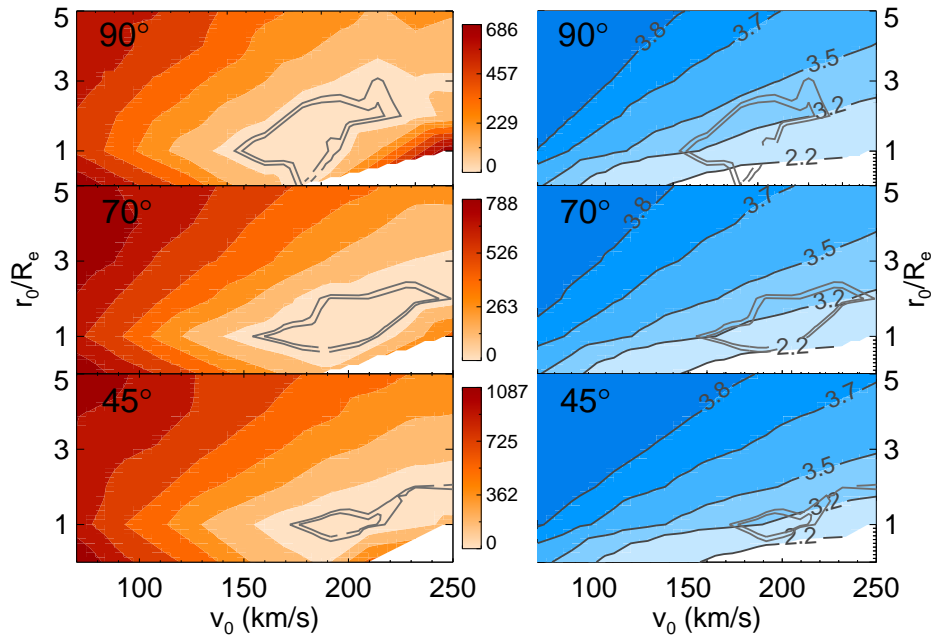

Figure 3.16: Results of the NMAGIC dynamical models of NGC 4494 for the range of explored halo parameters (r_0,v_0). *From top to bottom*: $i = 90°, 70°, 45°$. The *grey contours* correspond to 70% and 90% confidence levels, as determined in Section 3.4.4. *Left column*: ΔG of NMAGIC models relative to the best-fitting model (separate colour bar for each inclination). The bottom-right corner is a region in which no good models for the data could be found. *Right column*: V-band mass-to-light Υ_V of the final models.

The main results of our suite of dynamical models are presented in Fig. 3.16. In analogy with the analysis of the previous Section, we plot the ΔG of each NMAGIC model

relative to the best-fitting model, defined as that with minimum G, for each inclination $i = 90°, 70°, 45°$. In the same figure, we also overplot the 70% and 90% confidence levels determined from the Monte Carlo experiments of Section 3.4.4. In the right panel, we show the final mass-to-light ratios of our dynamical models.

The shape of the ΔG-contours is regular, and the range of dark matter halos consistent with the data within the confidence levels has circular velocity in the range $[160 - 240]$ km/s and scale radius $\sim 1 - 2R_e$. The stellar mass-to-light ratio is $\Upsilon_V \sim 3.2$. The main characteristics of the mass distribution of the explored models, and of the preferred models, are plotted in Fig. 3.17. The total circular velocity curve of the good models is approximately flat ("isothermal") outside $1R_e$, with $v_c(3R_e) \sim 220$ km/s. Less massive halos, as well as models with constant M/L, are not consistent with the data. It is apparent from Fig. 3.16 that these results, and the topology of the contours of G, are independent on the adopted inclination of the stellar distribution. Accordingly, the allowed range for the dark halo parameters is not sensitive to our ignorance of the true inclination of NGC 4494.
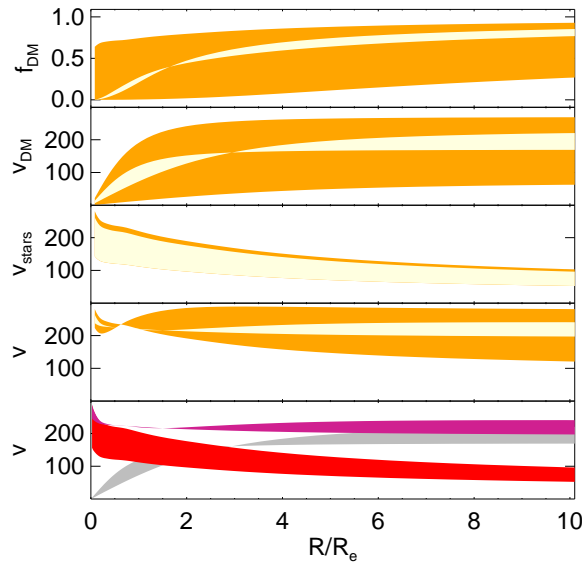
Figure 3.17: *Top four panels*: as a function of radius, the dark matter fraction $f_{DM} = M_{DM}/M$ within R, and the circular velocity curves corresponding to dark matter, stars, and total potential for the NMAGIC edge-on models (*orange shaded region*). The *yellow shaded region* shows the 70% confidence region (see Section 3.4.4). *Lowest panel*: the contributions of stars (*red*) and dark matter (*grey*) to the total circular velocity curve (*violet*) for the edge-on models in the 70% confidence band.

In general, we find that edge-on models ($i = 90°$) are preferred, in the sense of a lower

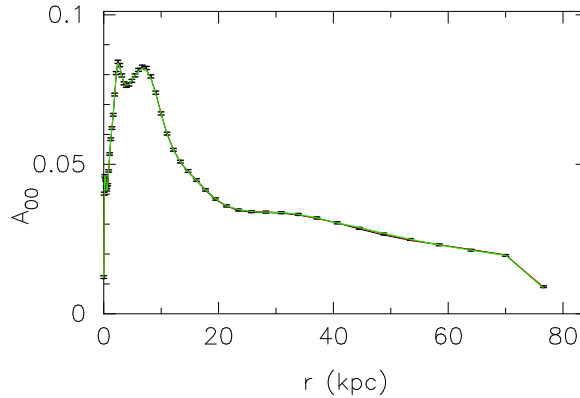Figure 3.18: NMAGIC fits to the differential stellar mass distribution (A_{00} coefficient) for an inclination of 90°. The *black* line is for the best-fitting model ($r_0 = 1R_{\rm e}$, $v_0 = 170$ km/s), the *red* line is for the model residing in a diffuser halo ($r_0 = 5R_{\rm e}$, $v_0 = 90$ km/s), and the *green* line represents the model obtained for a massive halo ($r_0 = 1R_{\rm e}$, $v_0 = 250$ km/s). The three model curves are nearly identical.

value of G, and of a lower value of χ^2, and a higher value of $\mathcal{L}$, respectively. A discussion of this issue is deferred to Section 3.5.3, whereas we now describe the model fits to the data, and the orbital structure of the dynamical models.

3.5.1   Model fits to the observational data

For a wide range of dark halos, NMAGIC finds very good fits to the observational data in terms of χ^2 values. In particular, for an assumed inclination of 90° all the models that we tried converged to χ^2 values per data point less than 1 (unless extreme values of the parameters, corresponding to the bottom-right corner of Fig. 3.16 are considered). For an inclination $i = 70°$, the model with constant M/L achieves the poorest fit with a value of reduced $\chi^2 = 1.14$. Similar values of χ^2 are also found for a few models obtained with the more extreme value of the inclination $i = 45°$.

The fits to the photometric constraints are generally excellent, and they are indistinguishable visually for most potentials, and for the different inclinations. Models compatible with the data at the 90% level achieve these fits with a maximum value of $\chi^2 = 0.43, 0.48, 0.88$ per data point, for $i = 90°, 70°, 45°$, respectively. Fig. 3.18 shows the very good fit to the first moment of the A_{lm}, i.e. the differential stellar mass distribution, for the preferred inclination of 90°. Three fiducial halo models are shown: the best-fitting model, and two models which fit the data with $\chi^2 < 1$, but lie outside the 90% confidence band, having a more massive and a more diffuse dark halo than the best-fitting models. The fits to the long-slit kinematics are also generally good. Models within the 90%

confidence range achieve a maximum value of $\chi^2 = 0.36, 0.41, 0.35$ per point, for $i = 90°, 70°, 45°$, respectively. For the fiducial models, these fits are shown in Fig. 3.19, where it is apparent that the central feature of the kinematically decoupled core in v and in h_3 is reproduced well by our particle models, and that the models have some difficulty in matching the detailed long-slit kinematics along the outer major axis. In particular, the best-fitting models have slightly lower values of v and slightly higher values of σ. To a great extent, these systematic deviations can be credited to the compromise (see below) that the models must find between the long-slit and the slitlets kinematic data, which extend to larger radii. The fiducial models show that more massive/diffuse halos result in higher/lower values of σ and h_4 along both axes. Finally, the shaded regions in Fig. 3.19 show the range of models allowed by the different inclinations (for the more massive and the more diffuse fiducial models), and by the 90% confidence region (for the best-fitting model).

The fits to the newer slitlets kinematics are achieved with maximum $\chi^2 = 1., 1.18, 1.27$ per data point within the 90% confidence level, for the three inclinations of $90°, 70°, 45°$, respectively. Fig. 3.20 shows the fits of the preferred edge-on particle models to the slitlets kinematics for the fiducial potentials. The trends with halo mass described before are still clearly visible. Moreover, it can be seen that the best-fitting edge-on model, corresponding to the black line, has to find a compromise between the kinematic data in slit and slitlets in the outer region. This results in a lower magnitude for the velocity, and in a higher velocity dispersion, which explains the deviations from the long-slit kinematics in the outermost data points.

Finally, Fig. 3.21 shows a comparison of the final NMAGIC models with the PN kinematic data, for all the inclinations and for the fiducial potentials. The velocity, velocity dispersion, and LOSVD are plotted in the angular segments in which the PNe velocities are binned for the modelling (see Section 3.2.2). The axisymmetric nature of our models is apparent in the reflection symmetry of the kinematics in diagonally opposite segments. While the mean velocity profiles are well fit by all models shown, the low (high) dark matter models are systematically low (high) in the PN dispersion plot, and show systematic deviations from the data histograms. The best-fitting models, instead, provide a good match to all the observed PN data.
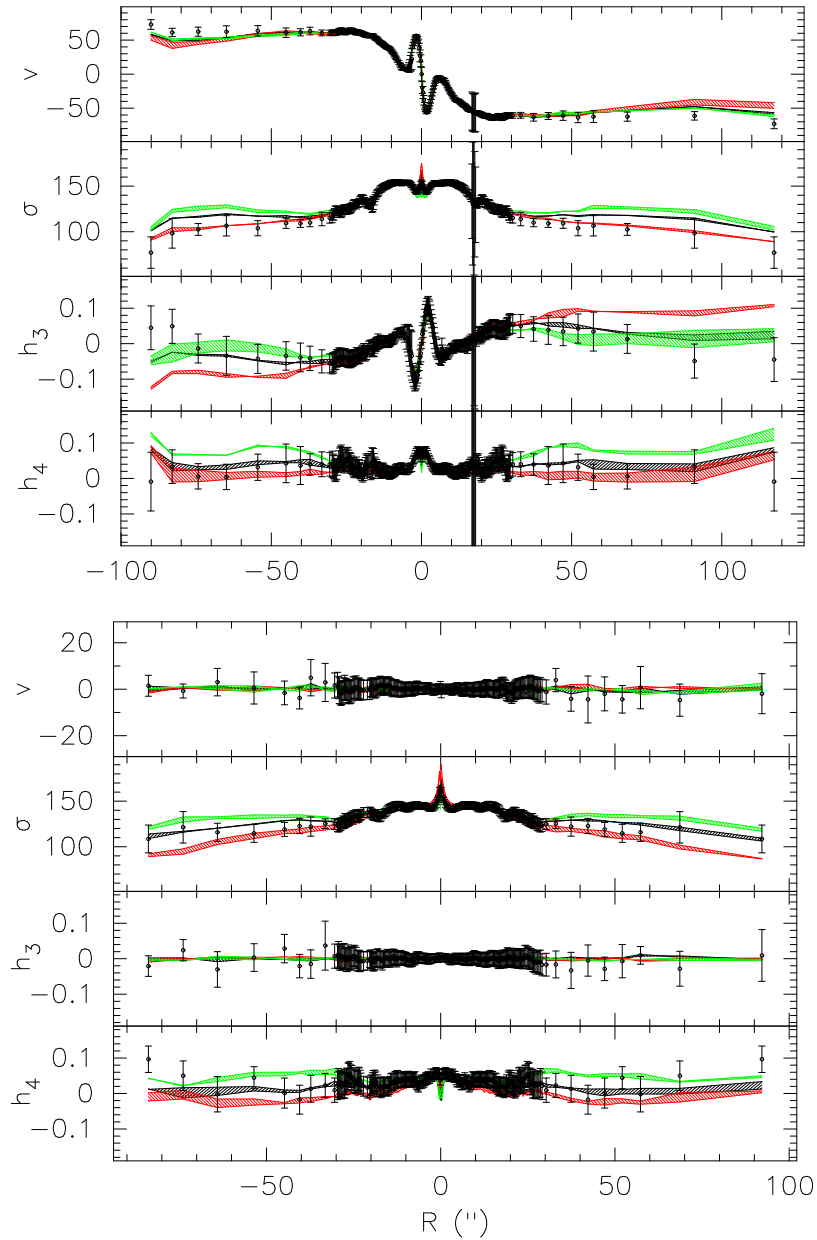
Figure 3.19: NMAGIC fits to the long-slit kinematic data (*black dots*) of NGC 4494 along the major (*top*) and minor (*bottom*) axis. The *black shaded region* shows the best-fitting edge-on models within the 90% confidence range. The *red and green shaded regions* show the spread of the fiducial models for the explored inclinations; *red* is for the model residing in a lighter halo ($r_0 = 5R_e$, $v_0 = 90$ km/s), and *green* is for the model obtained for a massive halo ($r_0 = 1R_e$, $v_0 = 250$ km/s).

Figure 3.20: NMAGIC fits to the slitlets kinematics near the major axis of NGC 4494 (*black dots* with error bars). For comparison, *light-green dots* represent the major-axis slit data. The model points are averages over the same slit cells as the data, and are connected by straight line segments. Different colours represent the fiducial models: *black* is for the best-fitting model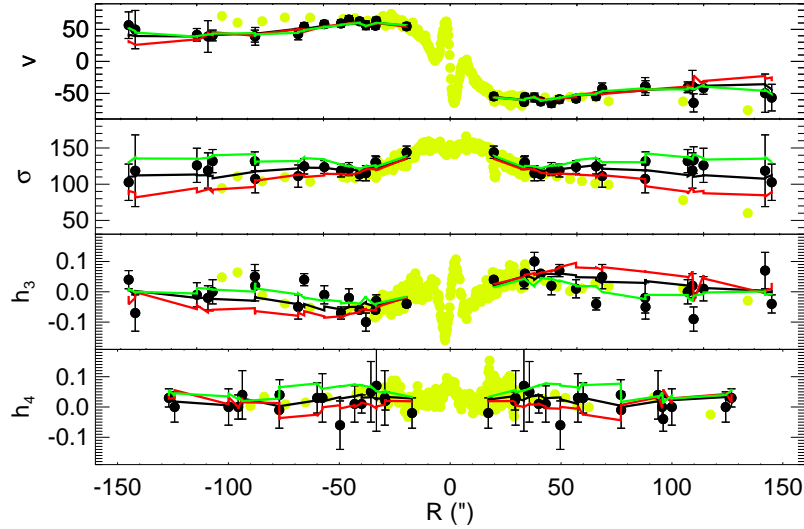 ($r_0 = 1R_{\rm e}$, $v_0 = 170$ km/s), *red* is for the model residing in a lighter halo ($r_0 = 5R_{\rm e}$, $v_0 = 90$ km/s), and *green* is for the model obtained for a massive halo ($r_0 = 1R_{\rm e}$, $v_0 = 250$ km/s). For simplicity, only the preferred edge-on models are shown.

3.5.2   The internal kinematics of NGC 4494

We now look at the intrinsic kinematics of NGC 4494 models, in order to learn about the orbital anisotropy of this galaxy. Fig. 3.22 shows the internal kinematics for the range of explored inclinations.

As expected, in the radial region well constrained by the kinematic data the ratio of the radial to tangential velocity dispersions is larger for models embedded in a massive halo than for low dark matter models (see *e.g.* Binney and Mamon, 1982).

On average, the ratio of the radial to tangential velocity dispersions along R in the best-fitting models is ~ 1.2, i.e. the underlying orbital distribution is slightly radially biased. As discussed further in Section 3.6, the degree of radial anisotropy of NGC 4494 is milder than what was previously found for the two other intermediate-luminosity ellipticals NGC 4697 (de Lorenzi et al., 2008) and NGC 3379 (de Lorenzi et al., 2009).

For all the explored potentials, the two components of the tangential velocity dispersion are similar along the minor axis, as required for an axisymmetric system, whereas the azimuthal dispersions are higher in the equatorial plane, suggesting that this (rotating) elliptical may be flattened by meridional anisotropy (*e.g.* Dehnen and Gerhard, 1993;
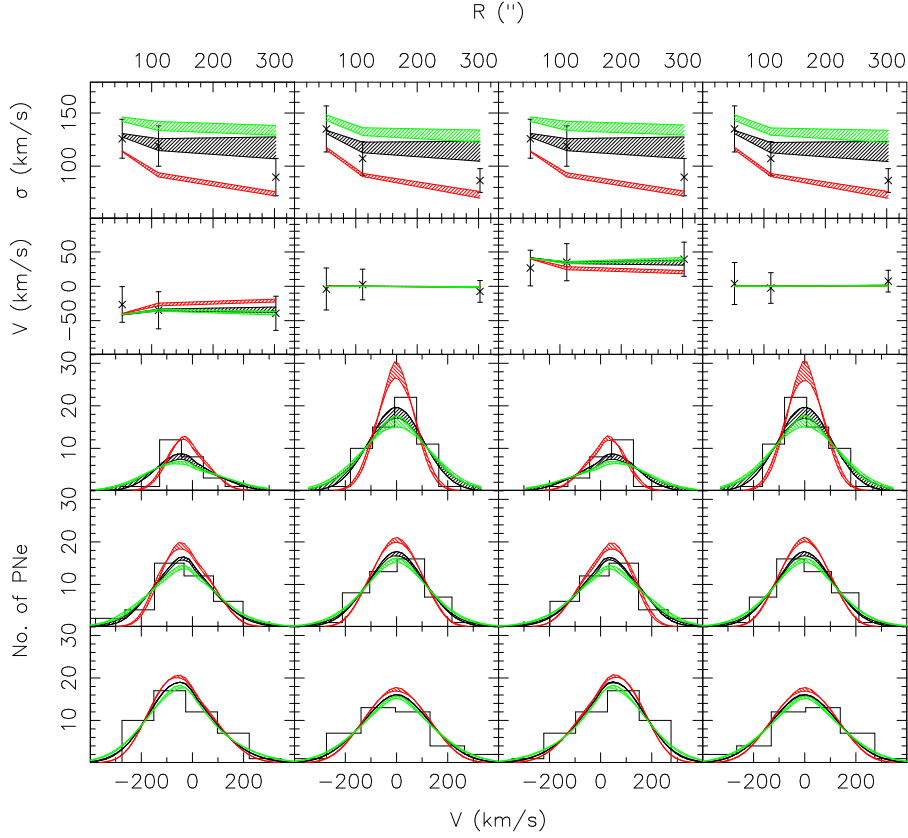
Figure 3.21: NMAGIC fits to the PNe velocities for all the considered inclinations. *Top two rows*: mean velocity dispersion and velocity profiles in the angular segments centered on 0° (major axis), 90°, 180°, 270°, from left to right. *Bottom three rows*: LOSVD in the same angular segments at radii of 52″, 110″, and 300″, going upwards. Colours of the *shaded regions* are as in Fig. 3.19.
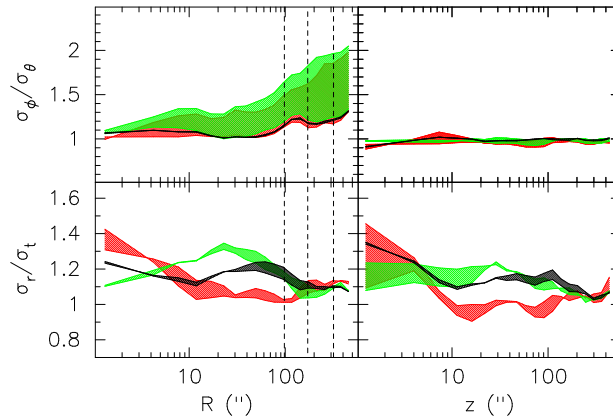
Figure 3.22: Internal kinematics of the final NMAGIC models for NGC 4494. The ratio of the azimuthal to meridional velocity dispersion (*top*) and of the radial to tangential velocity dispersion $\sigma_{\rm t} = \sqrt{(\sigma_\vartheta^2 + \sigma_\phi^2)/2}$ (*bottom*) are plotted as a function of the major axis R in the equatorial plane (*left column*), and of the minor axis z in the meridional plane (*right column*). Colours of the *shaded regions* are as for Figs. 3.19, 3.21. The *vertical dashed lines* show the extent of the kinematic data (long-slit, slitlets, and PNe, going outwards).

Thomas et al., 2009a; Das et al., 2010a). Variations due to the assumed inclination are always larger in the ratio between the azimuthal and meridional velocity dispersions along R.

Finally, at larger radii, and close to the outermost data points (marked by the vertical dashed lines), the orbital structure is nearly isotropic along both R and z. As we have shown in the previous Chapter 2, in those external regions, which are unconstrained by the observational data, a bias towards the dynamical structure of the initial (isotropic, in this case) particle model cannot be avoided.

3.5.3   The inclination of NGC 4494

From our NMAGIC models of NGC 4494, we would conclude that the observational data prefer an inclination of 90° out of the three inclinations that we explored. Indeed, edge-on models provide better fits to the data than models with lower inclinations, in terms of the merit function G, and of χ^2, and $\mathcal{L}$ in turn. In particular, we find a $\Delta G \sim 140$ (270) between the best-fitting edge-on model and the best-fitting model obtained for 70° (45°), which is highly significant when compared to the typical differences ΔG among different potentials for a given inclination. Visually, it is hard to distinguish the fit to the observables provided by the 90° and the 70° inclinations, whereas the more face-on 45° models are characterized by a systematically low velocity and velocity dispersion with respect to the observational data.

Should this preference for edge-on inclinations really be believed? Up to now, we have assumed a spherical dark halo for all the considered inclinations, and only the stellar distribution was axisymmetric and varied according to the inclination. We can relax the assumption of sphericity of the dark matter halo, and investigate dark matter halos with similar flattening as for the stars. To this end, we consider the more general parametrization for the logarithmic potential

$$\phi_D(R, z) = \frac{v_0^2}{2} \ln \left(r_0^2 + R^2 + \frac{z^2}{q_\phi^2} \right) \tag{3.8}$$

(Binney and Tremaine, 2008). Then, we use the approximate relation $1 - q_\phi \sim (1 - q_\rho)/3$ to derive the flattening of the potential q_ϕ from that of the density distribution q_ρ, which we infer from the apparent flattening q of the isophotes via

$$q^2 = \cos^2 i + q_\rho^2 \sin^2 i. \tag{3.9}$$

For an average flattening of the isophotes $q = 0.82$, the intrinsic flattening of the density distribution $q_\rho = 0.82, 0.79, 0.59$ for $i = 90°, 70°, 45°$, respectively, and the corresponding $q_\phi = 0.94, 0.93, 0.86$.

We have explored a few flattened dark halos having the same spherically-averaged mass distribution of the best-fitting models at $i = 70°$ and $45°$. Although some of them provide slightly better fits to the observational data, our main result does not change, and edge-on models are still preferred by far.

The obvious next question is whether there could be some bias in the modelling technique. This explanation was proposed by Thomas et al. (2007a), who found that all their best-fitting Schwarzschild models of N-body merger remnants have $i = 90°$, and argued that edge-on models necessarily have a smaller χ^2 than face-on models, due to their greater freedom in the adjustment of prograde and retrograde orbits to fit rotation and axisymmetric deviations from a Gaussian LOSVD.

We used our NGC 4494-like galaxy (see Section 3.4.1) to test whether particle models exhibit a bias analogous to that of orbit-based models. First, we constructed a series of NGC 4494-like galaxies assuming different inclinations $i = 90°, 70°, 45°$ for the stellar distribution. Then, we modelled the observational data of these mock galaxy with NMAGIC for different inclinations. The results of these experiments are summarized in Table 3.1, and confirm the findings and the argument of Thomas et al. (2007a): on average, the values of χ^2, and of the merit function G, increase for lower values of the inclination. An inspection of Table 3.1 reveals that edge-on models generally provide better fits. This is true both in the case in which the model has the true known inclination of the target galaxy, and in the case in which the model assumes a wrong value of the inclination. For reasons that are currently unclear to us, the likelihood favours instead more face-on models.

This test does not only confirm the existence of some sort of bias (*e.g.* Thomas et al., 2007a), but also enables us to quantify its effect on the dynamical models of NGC 4494. The experiments show that, when modelling a NGC 4494-like galaxy which has a true inclination $i = 70°(45°)$, a $\Delta G \sim 60(180)$ between the edge-on model and the more inclined models could be associated with the "edge-on bias". However, our runs display much larger differences in ΔG between the edge-on and the $i = 70°, 45°$ models. Thus, combining all these results suggests that NGC 4494 is truly close to edge-on. If so, this

i_{G}	i_{M}	χ^2	$\chi^2_{\mathrm{A_{1m}}}$	χ^2_{Sl}	χ^2_{Lets}	$-\mathcal{L}$	G
90°	90°	0.34	0.40	0.14	0.67	1539.87	2256.25
70°	70°	0.37	0.48	0.17	0.67	1535.97	2315.56
45°	45°	0.44	0.92	0.19	0.73	1509.86	2436.94
90°	70°	0.36	0.45	0.16	0.66	1539.69	2298.21
90°	45°	0.49	0.96	0.20	0.84	1541.79	2574.22
45°	70°	0.40	0.49	0.20	0.73	1513.12	2355.92
45°	90°	0.41	0.43	0.20	0.76	1513.71	2377.58

Table 3.1: Results of the NMAGIC fit to an NGC 4494-like galaxy whose stellar distribution has a known inclination i_{G}, assuming an inclination i_{M} in the modelling. χ^2 values are normalized by the respective number of observables $J_{\mathrm{Tot}} = 4214$, $J_{\mathrm{A_{1m}}} = 450$, $J_{\mathrm{Sl}} = 2390$, $J_{\mathrm{Lets}} = 1374$.

might provide also a simple explanation for the slightly larger rotation velocities measured in the major axis slit compared to the surrounding slitlets (see Fig. 3.20). This could be the kinematic signature of a faint disk.

3.6   Discussion

In this Section we discuss (*i*) the results on parameter estimation of dark matter halos with NMAGIC, (*ii*) our dynamical models for NGC 4494 in comparison with previous work, and (*iii*) the dark matter distribution and orbital structure of NGC 4494 in the wider context of the intermediate-luminosity elliptical galaxies with steeply falling velocity dispersion profiles.

3.6.1   Confidence levels for parameter estimation with NMAGIC

In Section 3.4 we used Monte Carlo simulations of an NGC 4494-like mock galaxy, to assess the range of dark halo parameters that provide statistically valid fits to the observational data for the real NGC 4494. The data set for the mock galaxy closely resembled that used for the dynamical modelling of NGC 4494. We measured the differences in the merit function ΔG which specify confidence levels enclosing a certain probability of finding the true values of the parameters (*e.g.* Press et al., 1992; Thomas et al., 2005b). Specifically, we constructed and modelled $N_{\mathrm{mock}} = 10$ NGC 4494-like galaxies in different dark matter halos, and estimated the distribution of values ΔG between the best-fitting model and the model with the true halo parameters for our data and modelling set-up.

These experiments showed that NMAGIC dynamical models match the true potential of the dark matter halo within $\Delta G \lesssim 44$ ($\Delta \chi^2 \lesssim 101$) about 70% of the time, and within $\Delta G \lesssim 59$ ($\Delta \chi^2 \lesssim 108$) about 90% of the time. These values also correspond

approximately to the fluctuations found within the confidence boundaries. The numerical noise in G or χ^2 caused by the adjustment of particle weights explains only a minor fraction of these ΔG or $\Delta \chi^2$ fluctuations. Fluctuations induced by varying the data within their error bars are much more significant compared to the measured ΔG or $\Delta \chi^2$ values, as already noted by Thomas et al. (2005b) in the related context of Schwarzschild method. Our experiments show, however, that some additional uncertainty must be related to the freedom associated with comparing different trial potentials. They also indicate that these results are unaffected by the strength of regularization as long as the model is not oversmoothed.

The relative differences ΔG (and $\Delta \chi^2$) found in our experiments are substantially larger than what is often assumed, and reveal that *e.g.* the $\Delta \chi^2 = 1$ criterion for one free parameter used in many dynamical studies in the literature (*e.g.* van der Marel et al., 1998; Cretton et al., 1999; Barth et al., 2001; Verolme et al., 2002; Cappellari et al., 2002; Gebhardt et al., 2003; Valluri et al., 2004; Shapiro et al., 2006; Chanamé et al., 2008; Cappellari et al., 2009b; van den Bosch and de Zeeuw, 2010; Murphy et al., 2011; Adams et al., 2012) is inappropriate for our NMAGIC particle models.

The $\Delta \chi^2 = 1$ approach is based on χ^2-statistics and assumes that the number of degrees of freedom is known and the number of free parameters is, in this case, one; this assumes that all the freedom in the fitted weights (or orbits) is used to constrain the distribution function from the data in the given trial potential, and the trial potential parameter(s) are then constrained from the remaining data degrees of freedom. Given that the number of weights is much larger than the number of data points, this assumption does not appear very likely, and it is not supported by the experiments in our case.

The experience in dynamical modelling with made-to-measure particle models is still limited, and it is possible that there are some issues with these methods that influence parameter estimation in different ways than, *e.g.*, Schwarzschild models. In fact, the $\Delta \chi^2$ values found in our experiments appear to be large compared to typical Schwarzschild applications. However, given the wide-spread use of dynamical modelling for measuring, *e.g.*, black hole masses in galaxies, it is important to test the statistical premises of this work more thoroughly. We believe that Monte Carlo simulations like those we have performed may be the best way to tackle these issues, and determine the appropriate $\Delta \chi^2$ values for estimating confidence limits for a given observational and modelling set-up.

3.6.2   Dynamical models for NGC 4494: comparison with the literature

The elliptical NGC 4494 has previously attracted the attention of several dynamical studies (*e.g.* van der Marel, 1991; Kronawitter et al., 2000; Magorrian and Ballantyne, 2001; Romanowsky et al., 2003; Rodionov et al., 2009; Napolitano et al., 2009; Lackner and Ostriker, 2010).

Our NMAGIC models improve on the models explored so far in some important aspects. First, we considered as many observational data as currently available, i.e. at large radii we had available both PNe velocities (N09) and galaxy spectra in slitlets (F11). The newer slitlets data show a milder drop of the velocity dispersion than what it is suggested by the long-slit data (F11), and this is likely to account for the larger enclosed mass beyond $\sim 2R_{\mathrm{e}}$ in our results compared to the Jeans models of N09. Second, because of the greater constraining power of the new data compared to the PNe, we sampled the dark halo parameter space much finely than before, for three different values of the inclination $i = 45°, 70°, 90°$. Thirdly, we performed a thorough analysis of the confidence levels at which these parameters can be estimated with our models, given the data at hand. Finally, contrary to most previous studies that considered spherical models (but see Rodionov et al., 2009), our NMAGIC models are axisymmetric, and we also explored the possibility of flattened dark halos. While it is true that the most robust results should eventually be derived using triaxial models, it has been shown that relaxing the spherical assumption hardly influences the recovered halo mass (see *e.g.* DL09).

While NGC 4494 was among the three galaxies described as "naked" in Romanowsky et al. (2003), and has an unusually low dark matter fraction in the analysis of Deason et al. (2012), our dynamical models show that a dark matter halo is required. In this respect, they agree with Rodionov and Athanassoula (2011), although the small sequence of explored models did not allow them to put robust constraints on the halo mass, and also with N09. N09 investigated a family of multi-component kurtosis-based Jeans models, and found the best-fitting logarithmic dark halo for $r_0 = 4R_{\mathrm{e}}$ and $v_0 = 150$ km/s. These parameters describe a diffuser halo than what we obtained (see Section 3.5), even if our best-fitting models are probably consistent with their errors. Whereas at large radii the differences are mostly owing to the additional slitlets constraints that we included in the modelling, at small radii we used the surface brightness data of Lauer et al. (2005) that,

at variance with the Sersic fit modelled by N09, show a strong concentration of light in the center of NGC 4494 (despite the dust).

The dark matter fraction of our best-fitting NMAGIC models $f_{\mathrm{DM}}(< 5R_{\mathrm{e}}) = 0.6 \pm 0.1$ is slightly higher than what reported by N09. Interestingly, this value agrees very well with the model predictions computed by Deason et al. (2012) assuming a Chabrier initial mass function (see their Fig. 7). Their spherical distribution function models of the PNe velocities indicated instead a surprisingly low dark matter fraction $f_{\mathrm{DM}}(< 5R_{\mathrm{e}}) = 0.32 \pm 0.12$.

Of course, alternative estimates of the mass of NGC 4494, *e.g.* from the X-ray emission of hot gas, would be highly desirable. From the compact X-ray gas emission, Fukazawa et al. (2006) estimated $\Upsilon_B = 6.2 \pm 1.9$ inside $1R_{\mathrm{e}}$, consistent with the Jeans modelling of N09 but higher than our NMAGIC results. However, the existence of an X-ray emitting gas around this galaxy has been questioned (O'Sullivan and Ponman, 2004; Diehl and Statler, 2007), and the validity of hydrostatic equilibrium may also be dubious (Ciotti and Pellegrini, 1996).

Additional kinematic constraints at large radii could be obtained from different tracers of the mass distribution, such as GCs. However, from the analysis of the spatial and kinematic distribution of blue and red GCs around NGC 4494, which does not follow that of the stars (F11), it is likely that PNe and GCs are in distinct dynamical equilibria in the same gravitational potential (see *e.g.* Das et al., 2011).

Compared to the Jeans models of N09, our best-fitting NMAGIC models have a lower mass-to-light $\Upsilon_B = 3.71 \pm 0.15$, obtained converting to Υ_V using the de-reddened colour from Goudfrooij et al. (1994). This value of the stellar mass-to-light ratio is easier to reconcile with independent measurements from stellar population models, which gave $\Upsilon_B = 4.3 \pm 0.7$ for a Kroupa initial mass function (see N09). In this respect, Lackner and Ostriker (2010) fitted galaxy formation model to the PNe velocities of NGC 4494, and found that the best-fit dissipational and dissipationless models give $\Upsilon_B = 2.97$ and $\Upsilon_B = 3.96$, respectively, so that a purely dissipational formation scenario for NGC 4494 seemed to be ruled out (Lackner and Ostriker, 2010).

Finally, the edge-on NMAGIC models that best reproduce the observational data of NGC 4494 are mildly radially anisotropic, i.e. $\beta \sim 0.4$ for the 90% confidence range. More inclined NMAGIC models ($i = 45°$) within the same confidence range are more

radially anisotropic, i.e. $\beta \sim 0.6$. The degree of orbital anisotropy is consistent with the previous analysis of N09 and Deason et al. (2012).

3.6.3   The wider context: intermediate-luminosity ellipticals

NGC 4494 belongs to the group of intermediate-luminosity elliptical galaxies with rapidly falling velocity dispersion profile (NGC 821,NGC 3379, NGC 4494, NGC 4697), dubbed "naked" galaxies because of the unusually low dark matter content revealed by the original (simplified) dynamical models (Romanowsky et al., 2003). The analysis of Coccato et al. (2009) identified a larger group of early-type galaxies (NGC 821, NGC 3377, NGC 3379, NGC 4494, NGC 4564, NGC 4697) with strongly decreasing $v_{\rm rms} = \sqrt{\sigma^2 + v^2}$ profiles. Currently, dynamical models have been obtained for all of the galaxies in the original sample of Romanowsky et al. (2003), including observational constraints from the higher order moments of the LOSVD, as summarized in N09 (see Weijmans et al. (2009); Forestell and Gebhardt (2010) for the Schwarzschild models of NGC 821). On the whole, these dynamical models suggest that most intermediate-luminosity galaxies are inconsistent with previous claims of little to no dark matter halo.

We now compare the results that we derived for NGC 4494 in this work, with the findings previously obtained by DL08 and DL09 for NGC 4697 and NGC 3379 using the same modelling technique (see also the previous Chapter).

Indeed, the photometry and kinematics of these three galaxies are not very different. They all have intermediate values of luminosity and stellar mass, similarly low values of the central velocity dispersion $\sim 150 - 210$ km/s, and similarly falling $v_{\rm rms}$ profiles (Coccato et al., 2009).

Fig. 3.23 shows the comparison of the NMAGIC models obtained for NGC 4697, NGC 3379, and NGC 4494. For NGC 4494, we plot the range of best-fitting edge-on models as determined in Section 3.5. For the other intermediate-luminosity ellipticals, no rigorous $\Delta\chi^2$ analysis was performed, but a range of valid models was determined based on the likelihood of PNe.

As can be seen in the bottom panel of Fig. 3.23, the orbital structure of the three intermediate luminosity ellipticals is radially biased, in agreement with dynamical models of elliptical galaxies in the literature (*e.g.* Merritt and Oh, 1997; Rix et al., 1997; Gerhard et al., 1998; van der Marel et al., 1998; Matthias and Gerhard, 1999; Gebhardt et al., 2000;
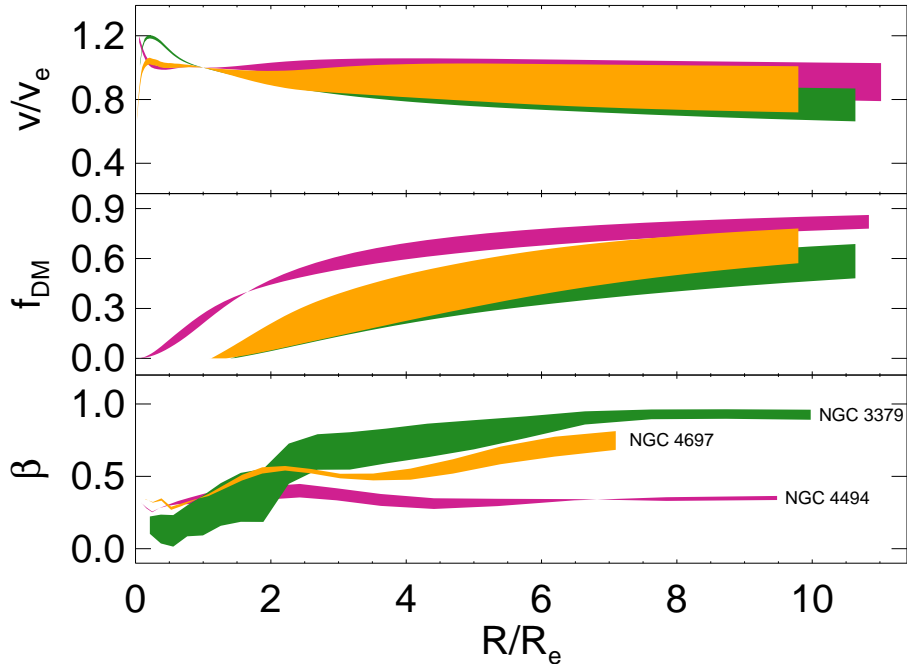
Figure 3.23: *From top to bottom*: as a function of radius, circular velocity normalized by its value at $1R_e$, dark matter fraction, and anisotropy parameter of the range of valid NMAGIC models obtained fitting the data of NGC 4494 (this work, *violet*), NGC 4697 (DL08, *orange*), and NGC 3379 (DL09, *green*).

Saglia et al., 2000), with predictions of the monolithic collapse scenario (van Albada, 1982), and with simulations of both binary-mergers (*e.g.* Gerhard, 1981; Abadi et al., 2006; Thomas et al., 2009a) and cosmological mergers (*e.g.* Abadi et al., 2006), though the remnants of binary mergers can exhibit a variety of orbital distributions (Naab et al., 2006). NGC 4494, by its side, is characterized by a milder level of radial anisotropy than the other two galaxies, consistent with the fact that its projected velocity dispersion is higher (see Fig. 15 of Coccato et al. (2009)) and its surface density profile steeper. Recent simulations have shown that dissipational processes in wet mergers may decrease the level of radial anisotropy (*e.g.* Naab et al., 2006; Thomas et al., 2009b), and also explain many observed features such as counter-rotating disks, kinematically decoupled components, and extra light at small radii (*e.g.* Mihos and Hernquist, 1994; Springel et al., 2005a; Cox et al., 2006; Jesseit et al., 2007; Hopkins et al., 2008; Hoffman et al., 2010).

The top panel of Fig. 3.23 shows the circular velocity curves normalized at $1R_e$. At large radii, the behaviour of the circular velocity is not so different, whereas the greatest discrepancies can be seen in the central regions, and they are probably due to different imprints left by baryonic processes during galaxy formation.

That different baryonic processes were at work in individual galaxies is also suggested by the fact that the dark matter fraction of these three galaxies is remarkably different (middle panel of Fig. 3.23), while their global circular velocity curves are more similar. In particular, the dark matter fraction of NCG 4494 has much higher values, particularly inside $3R_e$, than those of NGC 4697 and NGC 3379.

Indications have been reported that the dark matter fractions are lower for fast rotators than for slow rotators (Cappellari et al., 2006), and indeed it is not immediate to classify NGC 4494 as a fast rotator, given its central kinematically decoupled core (Krajnović et al., 2011), and the small value of λ_R at large radii (Coccato et al., 2009). Transitions between slow and fast rotators at large distances from the galactic center are not unusual (Proctor et al., 2009; Coccato et al., 2009) and may be a signature of merger events (*e.g.* Hoffman et al., 2010).

At variance with the findings for NGC 3379 and NGC 4697, the larger dark matter fraction of NGC 4494 is consistent with studies of strong gravitational lensing (*e.g.* Gavazzi et al., 2007; Auger et al., 2010a; Barnabè et al., 2011), and with the theoretical results of disk-galaxy mergers (Dekel et al., 2005) or cosmological smoothed particle hydrodynamics simulations (*e.g.* Naab et al., 2007; Oñorbe et al., 2007). Such high dark matter fraction could be a consequence of some merger event (like those advocated by Proctor et al. (2009) or F11), able to scatter dark matter particles inside the inner regions of the galaxy (*e.g.* Oser et al., 2012; Hilz et al., 2012).

3.7   Conclusions

We presented dynamical models for the intermediate luminosity elliptical galaxy NGC 4494, fitting photometric and kinematic observational data to investigate its mass distribution and orbital structure. Our extended kinematic data included the recently available integrated light spectra in slitlets (Foster et al., 2011) and hundreds of planetary nebulae velocities reaching out to $\simeq 7R_e$ (Napolitano et al., 2009). We used the χ^2-made-to-measure particle code NMAGIC to construct axisymmetric models for various inclinations exploring a large sequence of gravitational potentials.

In parallel, we carried out a parameter estimation study, investigating how well the characteristic parameters of dark matter halos can be recovered via NMAGIC modelling of

the available observational data. For this, we used Monte Carlo simulations of NGC 4494-like mock galaxies to determine the confidence regions around the best-fitting model. These confidence bands were then used to discriminate the range of valid models for NGC 4494.

Our main results can be summarized as follows:

- Given the observational data of NGC 4494 and our NMAGIC modelling set-up, Monte Carlo simulations showed that the usual 1σ (70%) confidence level corresponds to a value of the relative difference $\Delta G = 44$ ($\Delta\chi^2 = 101$). At 90% confidence level, $\Delta G = 59$ and $\Delta\chi^2 \sim 108$. These differences are much larger than the usual $\Delta\chi^2 = 1$ criterion, which implicitly assumes that the number of degrees of freedom involved in the problem is known.

- The best-fitting models for NGC 4494 determined within these confidence levels have an approximately flat total circular velocity curve outside $1R_{\mathrm{e}}$, with $v_{\mathrm{c}}(3R_{\mathrm{e}}) \sim 220$ km/s. The larger variation is in the dark matter velocity curve, rather than in the stellar one. The dark matter fraction of the models within 70% confidence level is about 0.6 ± 0.1 at $5R_{\mathrm{e}}$, and they are embedded in a concentrated dark halo ($r_0 \sim 1 - 2R_{\mathrm{e}}$) with circular velocity $\sim [160 - 230]$ km/s. With this large dark matter fraction, the stellar mass-to-light ratio is consistent with the value predicted by Deason et al. (2012) from the models for a Chabrier IMF. The discrepancy with the diffuser halo found by the Jeans models of Napolitano et al. (2009) is likely due to the additional slitlets constraints, which suggest a milder drop of the velocity dispersion than what predicted from the long-slit kinematics.

- The edge-on models provide the best fits to the available observational data, but the inferred dark halo parameters (r_0,v_0) do not depend sensitively on the assumed inclination. We explored a sequence of flattened dark matter halos, which however did not change our main result: edge-on models provide better fits to the data than models with lower inclinations.

- The orbital anisotropy of the stars is increasingly radial from the center outwards, but the amount of radial anisotropy is smaller than what found in similar previous works for the two other intermediate luminosity ellipticals with rapidly falling velocity dispersion profiles NGC 3379 and NGC 4697.

- Comparing the halos of the intermediate-luminosity ellipticals with rapidly decreasing dispersion profile modelled so far with the same made-to-measure particle technique (NGC 3379, NGC 4697 and NGC 4494), we conclude that they have similar global circular velocity curves. NGC 4494 shows a particularly high dark matter fraction, and a strong central concentration of baryons. These differences are probably related to the detailed baryonic processes which shaped these galaxies.

4

Conclusions

The study of galaxy formation and evolution has nowadays become an observational science, and dynamical models are key tools to infer the intrinsic properties of galaxies from a vast amount of diverse data, with the ultimate goal of learning about their build-up over cosmic time.

Although largely outnumbered by spiral galaxies, ellipticals contain a significant fraction of the stars in the Universe, and they are the most massive galaxies known. Therefore, they provide valuable insight into those processes which govern the assembly of galaxies. Among ellipticals, a particularly interesting family is represented by the less massive, X-ray faint, intermediate-luminosity galaxies with rapidly falling velocity dispersion profiles, which may be surrounded by unusually diffuse dark matter halos, in some tension with predictions of galaxy formation models. The evidence of dark matter in these galaxies is particularly challenging, and relies on accurate dynamical models.

This thesis presents advancements in both the methodological respect, regarding made-to-measure dynamical models of galaxies, and the astrophysical respect, regarding the intermediate-luminosity ellipticals with strongly decreasing velocity dispersion profiles.

On one hand we have addressed some relevant issues concerning the dynamical modeling of galaxies with made-to-measure particle methods that reproduce the observational data. In particular, we have improved the made-to-measure technique by developing a new regularization scheme, and we have investigated the uniqueness of the solution,

the accuracy of the method, and the dark halo parameter estimation with the particle modeling approach.

On the other hand, we have studied the enigmatic case of the intermediate-luminosity elliptical NGC 4494, which might be surrounded by a surprisingly diffuse dark matter halo. In particular, we have constructed axisymmetric made-to-measure particle models of NGC 4494 for various inclinations, fitting a variety of observational data in luminous and dark potentials, with the aim of constraining the orbital structure of the stars, and the dark matter content deep into the halo. Our detailed analysis expands the sample of currently modelled intermediate-luminosity ellipticals with rapidly falling velocity dispersion profiles, and allows us to compare with previous results based on made-to-measure models.

In the following we will summarize the main improvements to the modeling technique (Section 4.1), the astronomical analysis and findings (Section 4.2), and some future perspectives (Section 4.3).

4.1   Made-to-measure dynamical models of galaxies: technical improvements

Galaxies can be modelled with particles using made-to-measure (M2M) methods such as the parallel code NMAGIC, which adapt the particle weights in an N-body system until a good match to the observational data is achieved. Because of their geometric flexibility and high versatility in modeling observational data of various kind, these are very powerful modeling tools. However, they have not been explored as extensively as *e.g.* Schwarzschild methods.

Among the issues which are worth considering in order to draw robust conclusions from M2M particle models of galaxies, there are: the reliability, uniqueness, and accuracy of the final solution, the effects of imperfect data on the recovery of the intrinsic properties of an observed target galaxy, the impact of regularization, and the confidence levels for parameter estimation.

All these topics are relevant for Schwarzschild models as well, and indeed have been investigated to some extent with the Schwarzschild technique (*e.g.* Verolme et al., 2002; Valluri et al., 2004; Cretton and Emsellem, 2004; Thomas et al., 2004, 2005b; van de Ven et al., 2008; Chanamé et al., 2008).

In the first, methodological part of this work, our efforts have been devoted to explore these issues in detail with M2M particle models, obtaining the results that we will now concisely summarize. For this analysis we made an extensive use of *mock target galaxies* of known intrinsic properties, which we constructed, together with their mock observational data, using NMAGIC itself. Such reference galaxies are precious tools to elucidate the reliability and potential problems of dynamical models.

A new Moving Prior Regularization method   An accurate and unbiased reconstruction of the intrinsic properties of an observed galaxy with M2M methods is deeply connected to the concept of regularization.

In order to avoid arbitrarily large changes in the particle weights driven by the noise in the data, the traditional M2M practice makes use of a Global Weight entropy Regularization, i.e. all the weights are biased towards a smooth distribution of predefined flat priors through an entropy function (Syer and Tremaine, 1996). These flat priors are specified together with the initial particle model, and therefore contain implicit assumptions about the (unknown) dynamical structure of the modelled galaxy. A large contribution of the entropy to the correction of particle weights is needed to obtain a smooth model. However, this typically reduces not only local, but also global phase-space gradients. Hence, unless the (unknown) phase-space structures of the target galaxy are already in place in the initial conditions, the Global Weight entropy Regularization has hard times reconciling smoothness and orbital anisotropies in the final particle model.

Instead, we devised and implemented in NMAGIC an alternative Moving Prior Regularization method for particle models, which allows to smooth the particle weights *locally* without washing out the global phase-space gradients. This new technique is based on determining from the particles a distribution of priors in phase-space, which are updated during the weight adaptation, and mirror the phase-space structures of the evolving weight distribution. In practice, these moving priors are the same for particles that share the same value of the isolating integrals of motion, and vary smoothly between neighbouring tori. Used in a weight entropy function, the moving priors allow a correct recovery of the orbital structure of the target galaxy without introducing any overfitting of the observational data. The dependence of the final particle model on the adopted initial one is efficiently minimized, and the recovery of a smoother and more accurate

distribution function from noisy observational data is facilitated.

We have tested this method in the simpler spherical case, binning particles in energy and angular momentum (more precisely, circularity function), and we have generalized it to axisymmetric systems, using energy, angular momentum component along the symmetry axis, and angular momentum. We have used the new Moving Prior Regularization method throughout this work, and the main improvements achieved with respect to the traditional smoothing scheme are reported in the following.

Recovery of the intrinsic properties of galaxies   It is a natural question whether the M2M particle methods can recover the dynamical structure of an observed galaxy if the data uniquely specify it. Also, it is natural to wonder what happens when only imperfect observational data are available, as in typical astronomical applications.

In the case in which a unique inversion of the data to recover the distribution function of the target galaxy exists (Dejonghe and Merritt, 1992), we have found that NMAGIC empowered with the new Moving Prior Regularization method converges to the true solution independently of the choice of the initial particle model. Typical fluctuations in the mass-weighted relative RMS difference between the (mass) distribution function of the model galaxy and that of the known target galaxy are of order 12%, while the intrinsic kinematics of the target galaxy is recovered almost perfectly.

Our sequence of tests shows that the new Moving Prior Regularization represents a clear improvement over the traditional Global Weight entropy Regularization, since it removes biases in the dynamical structure, and reduces local fluctuations in the intrinsic distribution function. Moreover, it allows the use of a larger degree of smoothing without spoiling the fit to the data.

Inevitably, realistic data, which are spatially limited and possess large error bars, introduce degeneracies that limit the reliability of the models well inside those regions in which good data constraints exist. This is true even using the new Moving Prior Regularization, though the bias towards the initial conditions is reduced, and the properties of the target galaxy are better recovered. As soon as there is a lack of data to constrain the particle models, severe uncertainties in the inferred dynamical structure, together with an increased dependence on the initial particle model, cannot be avoided. Our analysis shows that the uncertainties in the recovery of *e.g.* the anisotropy parameter of the target galaxy

can be seen down to 1/3 of the limiting radius of the data. It is very important to be aware of such intrinsic, and somehow hidden, limitations, and it is likely that overlooking these issues may lead to *e.g.* the kind of discrepancies between M2M and Schwarzschild models which have been recently reported by Long and Mao (2012) without a satisfactory explanation.

Of course, these results also stress the need for high quality data with extended spatial coverage for constructing accurate dynamical models of galaxies.

Parameter estimation Among the questions that are commonly addressed via dynamical models, a special place is occupied by the recovery of the mass distribution, and especially of the dark matter content of galaxies.

Until now, very little was known about the uncertainties associated with dark halo parameter estimates carried out with M2M particle models.

In the literature, the $\Delta\chi^2 = 1$ (or 2.3,3.5) criterion is commonly adopted to determine the 68%-confidence level for one (or two, three) free parameter(s), and to assess which combinations of the parameters are as good as the one that achieves the minimum χ^2 (*e.g.* Cappellari et al., 2002; Gebhardt et al., 2003; Murphy et al., 2011; Adams et al., 2012). However, this procedure assumes that the number of degrees of freedom involved in the modeling is known, and that the number of free parameters is only one (or two, three). In practice, this neglects the large uncertainty associated with the determination of the number of degrees of freedom (*e.g.* van der Marel et al., 1998; Cretton et al., 2000; Gebhardt et al., 2000), and it does not seem a very likely assumption, since the number of fitted weights is typically much larger than the number of data points. In this respect, M2M and Schwarzschild models are in principle similar, as they both adapt many (particle/orbit) weights to match a smaller number of data constraints. However, it is possible that there are some issues which affect parameter estimation in different ways for the two different techniques.

In Section 3.4 we have studied how well the dark halo parameters can be determined via M2M particle modeling of realistic data, and we have computed confidence levels for parameter estimation using Monte Carlo simulations (*e.g.* Press et al., 1992).

For the analysis, we used mock NGC 4494-like galaxies embedded in known dark matter halos, together with the photometric and kinematic data set-up of the elliptical galaxy

NGC 4494.

Firstly, we found that the currently available observational data are not enough to determine the scale radius and the circular velocity of the dark halo simultaneously, and different combinations of the dark halo parameters that provide similar values of the total enclosed mass are allowed. For these (realistic) observational data, the enclosed mass within $2R_{\mathrm{e}}$ can be determined to within 10%, the dark matter fraction $f_{\mathrm{DM}}(3R_{\mathrm{e}})$ to within ± 0.1, and the total circular velocity to ± 20 km/s. Again, these findings stress the importance of the quality of the observational data: better data would likely narrow down the range of admitted potentials (*e.g.* Gerhard, 1993; Merritt, 1993; Chanamé et al., 2008).

Secondly, we found via Monte Carlo experiments that the true potential of the dark matter halo is recovered within $\Delta G(\text{merit function}) \lesssim 44$ ($\Delta \chi^2 \lesssim 101$) at 70% confidence level, and within $\Delta G \lesssim 59$ ($\Delta \chi^2 \lesssim 108$) at 90% confidence level. Interestingly, these relative differences are much larger than the common criterion $\Delta \chi^2 = 1$. Numerical errors caused by noise in the M2M weight adaptation cannot explain the magnitude of these differences, and also regularization plays a weak role. Instead, as already noted by Thomas et al. (2005b) in the context of Schwarzschild models, these differences are of the same order as the fluctuations caused by variations of the data within errors. Our experiments suggest, however, that some additional uncertainty (freedom) must be associated with comparing different trial potentials.

These surprising results may be case-specific, since we used the specific observational set-up of NGC 4494. However, a larger $\Delta \chi^2$ "threshold" than that usually assumed might as well be general for M2M particle models. Given its relevance for halo (and black hole mass) determinations, this issue would be clearly worth investigating further. In this work we showed that a promising way to tackle the problem is via Monte Carlo simulations, which allow to determine the appropriate $\Delta \chi^2$ for parameter estimation in a robust way for a given observational and modelling set-up.

4.2   Intermediate-luminosity elliptical galaxies with rapidly falling velocity dispersion profiles

Having tested and improved the accuracy of the M2M particle approach, we have then used it to reconstruct dynamical models of the intermediate-luminosity elliptical galaxies

NGC 4697 and NGC 3379, obtaining smoother fits than de Lorenzi et al. (2008) and de Lorenzi et al. (2009), and to study NGC 4494. These galaxies belong to the family of ellipticals with curiously low projected velocity dispersion (Romanowsky et al., 2003), and strongly declining velocity dispersion profile (Coccato et al., 2009).

Unfortunately, the diffuse gas envelopes of these intermediate-luminosity ellipticals do not allow an independent estimate of their mass distribution via hydrostatic equilibrium of the X-ray emitting gas, and the evidence of dark matter relies on dynamical models, which have now and again questioned it (*e.g.* Romanowsky et al., 2003; Douglas et al., 2007), indicating possible tensions with the current paradigm of galaxy formation.

As shown by the merger simulations of Dekel et al. (2005), a lower projected velocity dispersion does not necessarily imply low or no dark matter, and can also result from a larger radial anisotropy of the stars, or even an intrinsic triaxial geometry. Indeed, when modelled with more sophisticated techniques, as *e.g.* NMAGIC, under more general assumptions, it has been found that the observational data of NGC 4697 and NGC 3379 could be fitted well by models embedded in dark matter halos and characterized by radially-biased orbital distributions (de Lorenzi et al., 2008, 2009).

In order to expand the sample of intermediate-luminosity ellipticals modelled so far with NMAGIC, in the second part of this work we have focused on NGC 4494, for which a particularly diffuse dark matter halo has been found via Jeans modeling (Napolitano et al., 2009), and a puzzlingly low dark matter fraction has been recently reported by Deason et al. (2012).

Also, a short while ago the measurements of absorption-line kinematics in multiple slitlets out to large radii (Foster et al., 2011) became available for this galaxy, in addition to the radial velocities of PNe (Napolitano et al., 2009).

NMAGIC models of NGC 4494   We have generated NMAGIC models of NGC 4494 for three different inclinations of the stellar distribution ($i = 90°, 70°, 45°$) in a variety of luminous and dark potentials. In contrast to earlier studies using spherical models, we have constructed axisymmetric models, so to take into account inclination effects and rotation. Furthermore, we have explored the possibility of flattened, non-spherical dark matter halos.

The spatial coverage of our kinematic constraints was boosted by hundreds of PNe radial

velocities reaching out to $\simeq 7R_{\mathrm{e}}$ (Napolitano et al., 2009), and - for the very first time - by the absorption line kinematics (V, σ, h_3, h_4) in slitlets placed all around the galaxy, out to $\simeq 3.5R_{\mathrm{e}}$ (Foster et al., 2011). According to our previous tests, pushing the limiting radius of the data farther is essential to improve the accuracy of the recovery of the intrinsic properties of the target galaxy at those radii at which the dark matter is expected to be important. Being the newest, these slitlets data are very interesting, though attention must be paid to deal with them, and *e.g.* devise an objective procedure to identify possible outliers.

The confidence regions determined with the parameter estimation study described above were used to discriminate among dynamical models obtained for different dark halo-parameters, and allowed us to ascertain that the observational data do require some dark matter, and not even in small amount.

The best-fitting models for NGC 4494 have a dark matter fraction of about 0.6 ± 0.1 at $5R_{\mathrm{e}}$, and are embedded in a concentrated dark halo with circular velocity $\sim [160 - 240]$ km/s. The total circular velocity curve of the models within 90% confidence level is approximately flat outside $1R_{\mathrm{e}}$, with $v_{\mathrm{c}}(3R_{\mathrm{e}}) \sim 220$ km/s. More diffuse dark matter halos, as well as models with constant M/L, are not consistent with the data. The discrepancy with the diffuser halo preferred by the spherical Jeans models of Napolitano et al. (2009) is likely due to the additional slitlets constraints, which predict a milder drop of the velocity dispersion than that suggested by the long-slit kinematics.

The best-fitting NMAGIC models of NGC 4494 are characterized by a moderately radial orbital anisotropy of the stars, which increases slightly from the center outwards.

Edge-on models provide the best fits to the available observational data. However, the best-fitting dark halo parameters are hardly affected by the assumptions on inclination or flattening of the dark halo, and this strengthen the results. Using the related Schwarzschild approach, Thomas et al. (2007a) noted a bias that led to smaller χ^2 values for edge-on models, due to their greater freedom in the adjustment of the orbits to fit rotation and axisymmetric deviations from a Gaussian LOSVD. By modelling a sequence of mock galaxies of known inclinations with the M2M method, we have confirmed the findings and the argument of Thomas et al. (2007a). Nonetheless, we believe that NGC 4494 is truly close to edge-on, since the "edge-on bias" alone cannot account for the large χ^2-differences found between edge-on models and models with lower inclinations.

Implications   As a final step, we have compared the halos of the intermediate-luminosity ellipticals which have been modelled so far with the M2M method, i.e. NGC 4697 (de Lorenzi et al., 2008), NGC 3379 (de Lorenzi et al., 2009), and NGC 4494 (this work).

The photometry and kinematics of these three galaxies are similar: they all have intermediate values of luminosity and stellar mass, similarly low values of the central velocity dispersion, and falling v_{rms} profiles (Coccato et al., 2009), though the projected velocity dispersion of NGC 4494 is higher (see Fig. 1.5).

M2M dynamical models reveal that the orbital structure of the three galaxies is radially biased, in agreement with dynamical models of elliptical galaxies in the literature (*e.g.* Merritt and Oh, 1997; Rix et al., 1997; Gerhard et al., 1998; van der Marel et al., 1998; Matthias and Gerhard, 1999; Gebhardt et al., 2000; Saglia et al., 2000). As discussed in the Introduction of this thesis, the way in which an elliptical galaxy assembled its stars is reflected in its present-day orbital distribution, due to the collisionless nature of these stellar systems. In particular, radial anisotropy is consistent with theoretical predictions of the monolithic collapse scenario (van Albada, 1982), and with the simulations of both binary mergers (*e.g.* Abadi et al., 2006; Thomas et al., 2009a) and cosmological mergers (*e.g.* Abadi et al., 2006).

NGC 4494 is characterized by a milder level of radial anisotropy than the other two galaxies, consistent with its higher projected velocity dispersion combined with a steeper surface density profile. Simulations show that dissipational processes in gas-rich mergers are able to decrease the level of radial anisotropy (*e.g.* Naab et al., 2006; Thomas et al., 2009b). Gas dissipation might also explain features such as kinematically decoupled components and extra light at small radii (*e.g.* Mihos and Hernquist, 1994; Springel et al., 2005a; Cox et al., 2006; Jesseit et al., 2007; Hopkins et al., 2008; Hoffman et al., 2010). The core of the elliptical NGC 4494 is indeed very concentrated, presumably due to baryonic concentration during the last merger.

At large radii, the best-fitting circular velocity curves of the three intermediate-luminosity ellipticals NGC 4697, NGC 3379, and NGC 4494 are similar, whereas this is not true in the central regions, probably owing to the detailed interplay between luminous and dark matter during galaxy formation. Indeed, the dark matter fraction of these three galaxies is also remarkably different, and NGC 4494 has the highest values of f_{DM}, particularly inside $4R_{\mathrm{e}}$. In contrast with the results for NGC 4696 and NGC 3379, which led to speculate

that the intermediate-luminosity ellipticals could be different from the more massive ones, such large dark matter fraction is consistent with the findings of strong gravitational lensing (*e.g.* Gavazzi et al., 2007; Auger et al., 2010a; Barnabè et al., 2011), and with the predictions of disk-galaxy mergers (Dekel et al., 2005) and cosmological simulations (*e.g.* Naab et al., 2007; Oñorbe et al., 2007). In particular, the high central values of f_{DM} in NGC 4494 might be a consequence of merger events, as shown by several cosmological simulations of the formation of elliptical galaxies (*e.g.* Boylan-Kolchin et al., 2005; Nipoti et al., 2009; Hilz et al., 2012; Oser et al., 2012). In the two-phase formation scenario outlined in Section 1.2, mergers, and in particular minor mergers, may be responsible for increasing the central dark matter fractions of ellipticals. The increase of f_{DM} within the observable R_e in major mergers is driven by violent relaxation, which scatters dark matter particles in energy space (Oser et al., 2012; Hilz et al., 2012). In minor mergers, instead, the increase of f_{DM}, which is higher and roughly proportional to the mass growth (Hilz et al., 2012), can be explained with the size-growth caused by the assembly of a halo of "ex-situ" stars, which pushes the effective radius farther out, at those radii where the host galaxy was previously dominated by dark matter.

Interestingly, while NGC 4697 and NGC 3379 are both classified as fast rotators, a similar classification for NGC 4494 is more dubious, due to the presence of a central kinematically decoupled core, which is a characteristic feature of slow rotators (Krajnović et al., 2011), and to the small value of λ_R at large radii (Coccato et al., 2009). Transitions between slow and fast rotators at large radii are pretty common (Proctor et al., 2009; Coccato et al., 2009), and may be a signature of merger events (*e.g.* Hoffman et al., 2010). Consistent with our findings on the dark matter fraction, Cappellari et al. (2006) found indications that the dark matter fractions may be larger for slow rotators than for fast rotators. Indeed, as suggested by our favoured edge-on inclination for NGC 4494, rotation might really be of minor importance in this galaxy.

At present, dynamical models have been obtained for all the "naked" galaxies in the sample of Romanowsky et al. (2003), including observational constraints from the higher order moments of the LOSVD. On the whole, these dynamical models suggest that most intermediate-luminosity ellipticals with rapidly falling velocity dispersion profiles are not consistent with the previous claims of little to no dark matter, and agree with theoretical predictions in the current scenario of structure formation.

4.3   Outlook

Based on what we have learnt with this work, we conclude that further progress in the field could be made in the following ways.

From the *methodological* point of view, we showed that there are ways to actually improve the accuracy of dynamical modeling, by understanding the limitations and validity of the method, and devising more efficient techniques, like the Moving Prior Regularization. Of course, the version of the Moving Prior Regularization described here could be generalized also to systems of lower symmetry, assigning moving priors in phase-space based on the invariants associated with orbits, *e.g.* the turning points. Alternatively, a cumulative, grid-less variants of the method could be implemented (*e.g.* Dehnen, 2009).

Additional and desirable improvements of the made-to-measure modelling techniques include arbitrary (not constant) stellar mass-to-light profiles, and cosmologically rooted parametrizations for the dark matter halos. Also, the effect of triaxial geometry could be explored with made-to-measure particle models (*e.g.* de Lorenzi et al., 2009). Instead of performing full triaxial models fitting the observational data, some useful insights could be more easily obtained with a forward approach, i.e. constructing mock galaxies of various orientation, angular momentum, and shape, computing their observational data with NMAGIC, and finally comparing them against realistic data.

Our study has made it clear that the construction of such mock galaxies with mock observables is of the greatest help to understand and improve the status of dynamical modeling. It would be interesting to further exploit these mock galaxies to *e.g.* predict the amount and quality of observational data needed to construct more accurate dynamical models, or put more robust constraints on the dark halo parameters. Moreover, our surprising findings on the large magnitude of the $\Delta\chi^2$ within which the true dark halo parameters can be recovered with made-to-measure models also deserve further study. Given the relevance and the wide-spread use of dynamical models to infer dark halo masses (but also *e.g.* black hole masses or galaxy inclinations) from observational data, it would be important to check the generality of our results for made-to-measure models, and to understand the reasons behind them.

Finally, mock galaxies could be used in a comprehensive comparison project of the various modeling techniques available nowadays, to elucidate the performances and limitations of

each method.

From the *astrophysical* point of view, it would be interesting to construct dynamical models for a much larger sample of ellipticals, belonging to any regime of mass and environment, so as to strengthen the current results, and improve our understanding of galaxy formation and evolution.

Of course, it is highly desirable that the amount and quality of the observational constraints improve, in order to narrow down model degeneracies.

Similarities between the orbital structures and dark matter distributions of the dynamical models and of the outcomes of cosmological simulations of galaxy formation should be searched, and then used to connect real galaxies to the corresponding assembly history (Sáiz et al., 2004; Jesseit et al., 2005; Burkert and Naab, 2005; Burkert et al., 2008; Thomas et al., 2009a). In particular, the remnants of simulated collisionless mergers have properties similar to the ellipticals in the intermediate-mass regime (*e.g.* Naab and Trujillo, 2006). So far, however, the simulated galaxies do not predict the strongly falling velocity dispersion profiles observed by Coccato et al. (2009), and this suggests that more refinements in the numerical simulations of galaxies are necessary before they can match the full spectrum of observed ellipticals.

Recently, cosmological simulations, in particular those of massive galaxies, have been challenged by several claims that the stellar mass-to-light ratio rises as a function of the stellar mass of galaxies (van Dokkum and Conroy, 2010; Auger et al., 2010b; Treu et al., 2010; Cappellari et al., 2012; Conroy and van Dokkum, 2012; Ferreras et al., 2012). If true, such systematic variation of the stellar Initial Mass Function of elliptical galaxies could leave little room for the presence of dark matter at the center of massive galaxies, with important implications for galaxy formation theories. Clearly, these also represent interesting issues to be explored in the future.

5

Bibliography

Abadi, M. G., Navarro, J. F., and Steinmetz, M. (2006). Stars beyond galaxies: the origin of extended luminous haloes around galaxies. *MNRAS*, 365:747–758.

Adams, J. J., Gebhardt, K., Blanc, G. A., Fabricius, M. H., Hill, G. J., Murphy, J. D., van den Bosch, R. C. E., and van de Ven, G. (2012). The Central Dark Matter Distribution of NGC 2976. *ApJ*, 745:92.

Amorisco, N. C. and Evans, N. W. (2012). Line Profiles from Discrete Kinematic Data. *ArXiv e-prints*.

An, J. H. and Evans, N. W. (2006). A Cusp Slope-Central Anisotropy Theorem. *ApJ*, 642:752–758.

Arnaboldi, M., Freeman, K. C., Mendez, R. H., Capaccioli, M., Ciardullo, R., Ford, H., Gerhard, O., Hui, X., Jacoby, G. H., Kudritzki, R. P., and Quinn, P. J. (1996). The Kinematics of the Planetary Nebulae in the Outer Regions of NGC 4406. *ApJ*, 472:145.

Arnold, J. A., Romanowsky, A. J., Brodie, J. P., Chomiuk, L., Spitler, L. R., Strader, J., Benson, A. J., and Forbes, D. A. (2011). The Fossil Record of Two-phase Galaxy Assembly: Kinematics and Metallicities in the Nearest S0 Galaxy. *ApJL*, 736:L26.

Auger, M. W., Treu, T., Bolton, A. S., Gavazzi, R., Koopmans, L. V. E., Marshall, P. J., Moustakas, L. A., and Burles, S. (2010a). The Sloan Lens ACS Survey. X. Stellar, Dynamical, and Total Mass Correlations of Massive Early-type Galaxies. *ApJ*, 724:511–525.

Auger, M. W., Treu, T., Gavazzi, R., Bolton, A. S., Koopmans, L. V. E., and Marshall, P. J. (2010b). Dark Matter Contraction and the Stellar Content of Massive Early-type Galaxies: Disfavoring "Light" Initial Mass Functions. *ApJL*, 721:L163–L167.

Avila-Reese, V., Colín, P., Valenzuela, O., D'Onghia, E., and Firmani, C. (2001). Formation and Structure of Halos in a Warm Dark Matter Cosmology. *ApJ*, 559:516–530.

Bacon, R., Copin, Y., Monnet, G., Miller, B. W., Allington-Smith, J. R., Bureau, M., Carollo, C. M., Davies, R. L., Emsellem, E., Kuntschner, H., Peletier, R. F., Verolme, E. K., and de Zeeuw, P. T. (2001). The SAURON project - I. The panoramic integral-field spectrograph. *MNRAS*, 326:23–35.

Baldry, I. K., Balogh, M. L., Bower, R. G., Glazebrook, K., Nichol, R. C., Bamford, S. P., and Budavari, T. (2006). Galaxy bimodality versus stellar mass and environment. *MNRAS*, 373:469–483.

Baldry, I. K., Glazebrook, K., Brinkmann, J., Ivezić, Ž., Lupton, R. H., Nichol, R. C., and Szalay, A. S. (2004). Quantifying the Bimodal Color-Magnitude Distribution of Galaxies. *ApJ*, 600:681–694.

Barnabè, M., Czoske, O., Koopmans, L. V. E., Treu, T., and Bolton, A. S. (2011). Two-dimensional kinematics of SLACS lenses - III. Mass structure and dynamics of early-type lens galaxies beyond z 0.1. *MNRAS*, 415:2215–2232.

Barnes, J. E. and Hernquist, L. (1992). Dynamics of interacting galaxies. *ARA&A*, 30:705–742.

Barnes, J. E. and Hernquist, L. (1996). Transformations of Galaxies. II. Gasdynamics in Merging Disk Galaxies. *ApJ*, 471:115.

Barth, A. J., Sarzi, M., Rix, H.-W., Ho, L. C., Filippenko, A. V., and Sargent, W. L. W. (2001). Evidence for a Supermassive Black Hole in the S0 Galaxy NGC 3245. *ApJ*, 555:685–708.

Baum, W. A. (1959). Population Inferences from Star Counts, Surface Brightness and Colors. *Publications of the Astronomical Society of the Pacific*, 71:106–117.

Begelman, M. C., Blandford, R. D., and Rees, M. J. (1980). Massive black hole binaries in active galactic nuclei. *Nature*, 287:307–309.

Bekki, K. and Shioya, Y. (1997). Formation of Boxy and Disky Elliptical Galaxies in Early Dissipative Mergers. *ApJL*, 478:L17.

Bell, E. F., McIntosh, D. H., Katz, N., and Weinberg, M. D. (2003). The Optical and Near-Infrared Properties of Galaxies. I. Luminosity and Stellar Mass Functions. *ApJS*, 149:289–312.

Bell, E. F., Naab, T., McIntosh, D. H., Somerville, R. S., Caldwell, J. A. R., Barden, M., Wolf, C., Rix, H.-W., Beckwith, S. V., Borch, A., Häussler, B., Heymans, C., Jahnke, K., Jogee, S., Koposov, S., Meisenheimer, K., Peng, C. Y., Sanchez, S. F., and Wisotzki, L. (2006). Dry Mergers in GEMS: The Dynamical Evolution of Massive Early-Type Galaxies. *ApJ*, 640:241–251.

Bender, R. (1988a). Rotating and counter-rotating cores in elliptical galaxies. *A&A*, 202:L5–L8.

Bender, R. (1988b). Velocity anisotropies and isophote shapes in elliptical galaxies. *A&A*, 193:L7–L10.

Bender, R. (1990). Unraveling the kinematics of early-type galaxies - Presentation of a new method and its application to NGC4621. *A&A*, 229:441–451.

Bender, R., Burstein, D., and Faber, S. M. (1992). Dynamically hot galaxies. I - Structural properties. *ApJ*, 399:462–477.

Bender, R., Doebereiner, S., and Moellenhoff, C. (1988). Isophote shapes of elliptical galaxies. I - The data. *A&A Supp.*, 74:385–426.

Bender, R. and Moellenhoff, C. (1987). Morphological analysis of massive early-type galaxies in the Virgo cluster. *A&A*, 177:71–83.

Bender, R., Saglia, R. P., and Gerhard, O. E. (1994). Line-of-Sight Velocity Distributions of Elliptical Galaxies. *MNRAS*, 269:785–+.

Berger, M. and Colella, P. (1989). Local adaptive mesh refinement for shock hydrodynamics. *Journal of Computational Physics*, 82(1):64 – 84.

Bernardi, M., Shankar, F., Hyde, J. B., Mei, S., Marulli, F., and Sheth, R. K. (2010). Galaxy luminosities, stellar masses, sizes, velocity dispersions as a function of morphological type. *MNRAS*, 404:2087–2122.

Bernardi, M., Sheth, R. K., Annis, J., Burles, S., Eisenstein, D. J., Finkbeiner, D. P., Hogg, D. W., Lupton, R. H., Schlegel, D. J., SubbaRao, M., Bahcall, N. A., Blakeslee, J. P., Brinkmann, J., Castander, F. J., Connolly, A. J., Csabai, I., Doi, M., Fukugita, M., Frieman, J., Heckman, T., Hennessy, G. S., Ivezić, Ž., Knapp, G. R., Lamb, D. Q., McKay, T., Munn, J. A., Nichol, R., Okamura, S., Schneider, D. P., Thakar, A. R., and York, D. G. (2003). Early-Type Galaxies in the Sloan Digital Sky Survey. III. The Fundamental Plane. *AJ*, 125:1866–1881.

Bertin, G. (2000). *Dynamics of Galaxies*.

Bertola, F. and Capaccioli, M. (1975). Dynamics of early type galaxies. I - The rotation curve of the elliptical galaxy NGC 4697. *ApJ*, 200:439–445.

Bertola, F., Pizzella, A., Persic, M., and Salucci, P. (1993). Dark Matter Halos in Elliptical Galaxies. *ApJL*, 416:L45.

Binney, J. (1977). The physics of dissipational galaxy formation. *ApJ*, 215:483–491.

Binney, J. (1978). On the rotation of elliptical galaxies. *MNRAS*, 183:501–514.

Binney, J. (2010). Distribution functions for the Milky Way. *MNRAS*, 401:2318–2330.

Binney, J. and de Vaucouleurs, G. (1981). The apparent and true ellipticities of galaxies of different Hubble types in the Second Reference Catalogue. *MNRAS*, 194:679–691.

Binney, J. and Mamon, G. A. (1982). M/L and velocity anisotropy from observations of spherical galaxies, or must M87 have a massive black hole. *MNRAS*, 200:361–375.

Binney, J. and Tremaine, S., editors (2008). *Galactic Dynamics: Second Edition*. Princeton University Press.

Binney, J. J., Davies, R. L., and Illingworth, G. D. (1990). Velocity mapping and models of the elliptical galaxies NGC 720, NGC 1052, and NGC 4697. *ApJ*, 361:78–97.

Bissantz, N., Debattista, V. P., and Gerhard, O. (2004). Large-Scale Model of the Milky Way: Stellar Kinematics and the Microlensing Event Timescale Distribution in the Galactic Bulge. *ApJL*, 601:L155–L158.

Blakeslee, J. P., Franx, M., Postman, M., Rosati, P., Holden, B. P., Illingworth, G. D., Ford, H. C., Cross, N. J. G., Gronwall, C., Benítez, N., Bouwens, R. J., Broadhurst, T. J., Clampin, M., Demarco, R., Golimowski, D. A., Hartig, G. F., Infante, L., Martel, A. R., Miley, G. K., Menanteau, F., Meurer, G. R., Sirianni, M., and White, R. L. (2003). Advanced Camera for Surveys Photometry of the Cluster RDCS 1252.9-2927: The Color-Magnitude Relation at z = 1.24. *ApJL*, 596:L143–L146.

Blumenthal, G. R., Faber, S. M., Primack, J. R., and Rees, M. J. (1984). Formation of galaxies and large-scale structure with cold dark matter. *Nature*, 311:517–525.

Bode, P., Ostriker, J. P., and Turok, N. (2001). Halo Formation in Warm Dark Matter Models. *ApJ*, 556:93–107.

Bois, M., Emsellem, E., Bournaud, F., Alatalo, K., Blitz, L., Bureau, M., Cappellari, M., Davies, R. L., Davis, T. A., de Zeeuw, P. T., Duc, P.-A., Khochfar, S., Krajnović, D., Kuntschner, H., Lablanche, P.-Y., McDermid, R. M., Morganti, R., Naab, T., Oosterloo, T., Sarzi, M., Scott, N., Serra, P., Weijmans, A.-M., and Young, L. M. (2011). The ATLAS^{3D} project - VI. Simulations of binary galaxy mergers and the link with fast rotators, slow rotators and kinematically distinct cores. *MNRAS*, 416:1654–1679.

Bolton, A. S., Burles, S., Treu, T., Koopmans, L. V. E., and Moustakas, L. A. (2007). A More Fundamental Plane. *ApJL*, 665:L105–L108.

Bolton, A. S., Treu, T., Koopmans, L. V. E., Gavazzi, R., Moustakas, L. A., Burles, S., Schlegel, D. J., and Wayth, R. (2008). The Sloan Lens ACS Survey. VII. Elliptical Galaxy Scaling Laws from Direct Observational Mass Measurements. *ApJ*, 684:248–259.

Bournaud, F., Jog, C. J., and Combes, F. (2005). Galaxy mergers with various mass ratios: Properties of remnants. *A&A*, 437:69–85.

Bower, R. G., Lucey, J. R., and Ellis, R. S. (1992). Precision Photometry of Early Type Galaxies in the Coma and Virgo Clusters - a Test of the Universality of the Colour / Magnitude Relation - Part Two - Analysis. *MNRAS*, 254:601.

Boylan-Kolchin, M., Ma, C.-P., and Quataert, E. (2005). Dissipationless mergers of elliptical galaxies and the evolution of the fundamental plane. *MNRAS*, 362:184–196.

Brodie, J. P. and Strader, J. (2006). Extragalactic Globular Clusters and Galaxy Formation. *ARA&A*, 44:193–267.

Buote, D. A. and Humphrey, P. J. (2012). Dark Matter in Elliptical Galaxies. In Kim, D.-W. and Pellegrini, S., editors, *Astrophysics and Space Science Library*, volume 378 of *Astrophysics and Space Science Library*, page 235.

Burkert, A. and Naab, T. (2005). The surprising anisotropy of fast rotating, discy elliptical galaxies. *MNRAS*, 363:597–602.

Burkert, A., Naab, T., Johansson, P. H., and Jesseit, R. (2008). SAURON's Challenge for the Major Merger Scenario of Elliptical Galaxy Formation. *ApJ*, 685:897–903.

Busarello, G., Capaccioli, M., Capozziello, S., Longo, G., and Puddu, E. (1997). The relation between the virial theorem and the fundamental plane of elliptical galaxies. *A&A*, 320:415–420.

Cappellari, M. (2008). Measuring the inclination and mass-to-light ratio of axisymmetric galaxies via anisotropic Jeans models of stellar kinematics. *MNRAS*, 390:71–86.

Cappellari, M., Bacon, R., Bureau, M., Damen, M. C., Davies, R. L., de Zeeuw, P. T., Emsellem, E., Falcón-Barroso, J., Krajnović, D., Kuntschner, H., McDermid, R. M., Peletier, R. F., Sarzi, M., van den Bosch, R. C. E., and van de Ven, G. (2006). The SAURON project - IV. The mass-to-light ratio, the virial mass estimator and the Fundamental Plane of elliptical and lenticular galaxies. *MNRAS*, 366:1126–1150.

Cappellari, M., di Serego Alighieri, S., Cimatti, A., Daddi, E., Renzini, A., Kurk, J. D., Cassata, P., Dickinson, M., Franceschini, A., Mignoli, M., Pozzetti, L., Rodighiero, G., Rosati, P., and Zamorani, G. (2009a). Dynamical Masses of Early-Type Galaxies at z ~ 2: Are they Truly Superdense? *ApJL*, 704:L34–L39.

Cappellari, M., Emsellem, E., Krajnović, D., McDermid, R. M., Serra, P., Alatalo, K., Blitz, L., Bois, M., Bournaud, F., Bureau, M., Davies, R. L., Davis, T. A., de Zeeuw, P. T., Khochfar, S., Kuntschner, H., Lablanche, P.-Y., Morganti, R., Naab, T., Oosterloo, T., Sarzi, M., Scott, N., Weijmans, A.-M., and Young, L. M. (2011). The ATLAS^{3D} project - VII. A new look at the morphology of nearby galaxies: the kinematic morphology-density relation. *MNRAS*, 416:1680–1696.

Cappellari, M., McDermid, R. M., Alatalo, K., Blitz, L., Bois, M., Bournaud, F., Bureau, M., Crocker, A. F., Davies, R. L., Davis, T. A., de Zeeuw, P. T., Duc, P.-A., Emsellem, E., Khochfar, S., Krajnović, D., Kuntschner, H., Lablanche, P.-Y., Morganti, R., Naab, T., Oosterloo, T., Sarzi, M., Scott, N., Serra, P., Weijmans, A.-M., and Young, L. M. (2012). Systematic variation of the stellar initial mass function in early-type galaxies. *Nature*, 484:485–488.

Cappellari, M., Neumayer, N., Reunanen, J., van der Werf, P. P., de Zeeuw, P. T., and Rix, H.-W. (2009b). The mass of the black hole in Centaurus A from SINFONI AO-assisted integral-field observations of stellar kinematics. *MNRAS*, 394:660–674.

Cappellari, M., Verolme, E. K., van der Marel, R. P., Kleijn, G. A. V., Illingworth, G. D., Franx, M., Carollo, C. M., and de Zeeuw, P. T. (2002). The Counterrotating Core and the Black Hole Mass of IC 1459. *ApJ*, 578:787–805.

Carignan, C. and Beaulieu, S. (1989). Optical and H I studies of the 'gas-rich' dwarf irregular galaxy DDO 154. *ApJ*, 347:760–770.

Carlberg, R. G. (1986). The phase space density in elliptical galaxies. *ApJ*, 310:593–596.

Carollo, C. M., de Zeeuw, P. T., and van der Marel, R. P. (1995). Velocity profiles of Osipkov-Merritt models. *MNRAS*, 276:1131–+.

Carter, D. (1978). The structure of the isophotes of elliptical galaxies. *MNRAS*, 182:797.

Chaisson, E. and McMillan, S. (2004). *Astronomy: A Beginner's Guide to the Universe*.

Chanamé, J., Kleyna, J., and van der Marel, R. (2008). Constraining the Mass Profiles of Stellar Systems: Schwarzschild Modeling of Discrete Velocity Data Sets. *ApJ*, 682:841–860.

Churazov, E., Tremaine, S., Forman, W., Gerhard, O., Das, P., Vikhlinin, A., Jones, C., Böhringer, H., and Gebhardt, K. (2010). Comparison of approximately isothermal gravitational potentials of elliptical galaxies based on X-ray and optical data. *MNRAS*, 404:1165–1185.

Ciardullo, R., Jacoby, G. H., and Dejonghe, H. B. (1993). The radial velocities of planetary nebulae in NGC 3379. *ApJ*, 414:454–462.

Ciotti, L. (2009). Co-evolution of elliptical galaxies and their central black holes. Clues from their scaling laws. *Nuovo Cimento Rivista Serie*, 32:1–69.

Ciotti, L. and Bertin, G. (1999). Analytical properties of the R$^{1/m}$ law. *A&A*, 352:447–451.

Ciotti, L., Lanzoni, B., and Renzini, A. (1996). The tilt of the fundamental plane of elliptical galaxies - I. Exploring dynamical and structural effects. *MNRAS*, 282:1–12.

Ciotti, L., Lanzoni, B., and Volonteri, M. (2007). The Importance of Dry and Wet Merging on the Formation and Evolution of Elliptical Galaxies. *ApJ*, 658:65–77.

Ciotti, L. and Morganti, L. (2009). Two-component galaxy models: the effect of density profile at large radii on the phase-space consistency. *MNRAS*, 393:179–191.

Ciotti, L. and Morganti, L. (2010a). Consistency criteria for generalized Cuddeford systems. *MNRAS*, 401:1091–1098.

Ciotti, L. and Morganti, L. (2010b). How general is the global density slope-anisotropy inequality? *MNRAS*, 408:1070–1074.

Ciotti, L., Morganti, L., and de Zeeuw, P. T. (2009). Two-component galaxies with flat rotation curve. *MNRAS*, 393:491–500.

Ciotti, L. and Pellegrini, S. (1996). The energetics of flat and rotating early-type galaxies and their X-ray luminosity. *MNRAS*, 279:240.

Ciotti, L. and van Albada, T. S. (2001). The M_{BH}-σ_c Relation as a Constraint on the Formation of Elliptical Galaxies. *ApJL*, 552:L13–L16.

Coccato, L., Arnaboldi, M., Gerhard, O., Freeman, K. C., Ventimiglia, G., and Yasuda, N. (2010). Kinematics and line strength indices in the halos of the Coma brightest cluster galaxies NGC 4874 and NGC 4889. *A&A*, 519:A95.

Coccato, L., Gerhard, O., Arnaboldi, M., Das, P., Douglas, N. G., Kuijken, K., Merrifield, M. R., Napolitano, N. R., Noordermeer, E., Romanowsky, A. J., Capaccioli, M., Cortesi, A., de Lorenzi, F., and Freeman, K. C. (2009). Kinematic properties of early-type galaxy haloes using planetary nebulae. *MNRAS*, 394:1249–1283.

Coccato, L., Gerhard, O., Arnaboldi, M., and Ventimiglia, G. (2011). Stellar population and the origin of intra-cluster stars around brightest cluster galaxies: the case of NGC 3311. *A&A*, 533:A138.

Cole, S., Percival, W. J., Peacock, J. A., Norberg, P., Baugh, C. M., Frenk, C. S., Baldry, I., Bland-Hawthorn, J., Bridges, T., Cannon, R., Colless, M., Collins, C., Couch, W., Cross, N. J. G., Dalton, G., Eke, V. R., De Propris, R., Driver, S. P., Efstathiou, G., Ellis, R. S., Glazebrook, K., Jackson, C., Jenkins, A., Lahav, O., Lewis, I., Lumsden, S., Maddox, S., Madgwick, D., Peterson, B. A., Sutherland, W., and Taylor, K. (2005). The 2dF Galaxy Redshift Survey: power-spectrum analysis of the final data set and cosmological implications. *MNRAS*, 362:505–534.

Colín, P., Klypin, A. A., and Kravtsov, A. V. (2000). Velocity Bias in a Λ Cold Dark Matter Model. *ApJ*, 539:561–569.

Conroy, C. and van Dokkum, P. (2012). The Stellar Initial Mass Function in Early-Type Galaxies From Absorption Line Spectroscopy. II. Results. *ArXiv e-prints*.

Contopoulos, G. (1963). On the existence of a third integral of motion. *AJ*, 68:1.

Cooper, M. C., Griffith, R. L., Newman, J. A., Coil, A. L., Davis, M., Dutton, A. A., Faber, S. M., Guhathakurta, P., Koo, D. C., Lotz, J. M., Weiner, B. J., Willmer, C. N. A., and Yan, R. (2012). The DEEP3 Galaxy Redshift Survey: the impact of environment on the size evolution of massive early-type galaxies at intermediate redshift. *MNRAS*, 419:3018–3027.

Copin, Y., Cretton, N., and Emsellem, E. (2004). Axisymmetric dynamical models for SAURON and OASIS observations of NGC3377. *A&A*, 415:889–903.

Côté, P., McLaughlin, D. E., Cohen, J. G., and Blakeslee, J. P. (2003). Dynamics of the Globular Cluster System Associated with M49 (NGC 4472): Cluster Orbital Properties and the Distribution of Dark Matter. *ApJ*, 591:850–877.

Cowie, L. L., Songaila, A., Hu, E. M., and Cohen, J. G. (1996). New Insight on Galaxy Formation and Evolution From Keck Spectroscopy of the Hawaii Deep Fields. *AJ*, 112:839.

Cox, T. J., Dutta, S. N., Di Matteo, T., Hernquist, L., Hopkins, P. F., Robertson, B., and Springel, V. (2006). The Kinematic Structure of Merger Remnants. *ApJ*, 650:791–811.

Cretton, N., de Zeeuw, P. T., van der Marel, R. P., and Rix, H. (1999). Axisymmetric Three-Integral Models for Galaxies. *ApJS*, 124:383–401.

Cretton, N. and Emsellem, E. (2004). On the reliability of the black hole mass and mass-to-light ratio determinations with Schwarzschild models. *MNRAS*, 347:L31–L35.

Cretton, N., Rix, H.-W., and de Zeeuw, P. T. (2000). The Distribution of Stellar Orbits in the Giant Elliptical Galaxy NGC 2320. *ApJ*, 536:319–330.

Daddi, E., Cimatti, A., Renzini, A., Vernet, J., Conselice, C., Pozzetti, L., Mignoli, M., Tozzi, P., Broadhurst, T., di Serego Alighieri, S., Fontana, A., Nonino, M., Rosati, P., and Zamorani, G. (2004). Near-Infrared Bright Galaxies at z~=2. Entering the Spheroid Formation Epoch? *ApJL*, 600:L127–L130.

Das, P., Gerhard, O., Churazov, E., and Zhuravleva, I. (2010a). Steepening mass profiles, dark matter and environment of X-ray bright elliptical galaxies. *MNRAS*, 409:1362–1378.

Das, P., Gerhard, O., Churazov, E., and Zhuravleva, I. (2010b). Steepening mass profiles, dark matter and environment of X-ray bright elliptical galaxies. *MNRAS*, 409:1362–1378.

Das, P., Gerhard, O., Mendez, R. H., Teodorescu, A. M., and de Lorenzi, F. (2011). Using NMAGIC to probe the dark matter halo and orbital structure of the X-ray bright, massive elliptical galaxy, NGC 4649. *MNRAS*, 415:1244–1258.

Davies, R. L. (1981). Observations of the dynamics of eight early-type galaxies. *MNRAS*, 194:879–902.

de Blok, W. J. G., McGaugh, S. S., Bosma, A., and Rubin, V. C. (2001). Mass Density Profiles of Low Surface Brightness Galaxies. *ApJL*, 552:L23–L26.

de Blok, W. J. G., Walter, F., Brinks, E., Trachternach, C., Oh, S.-H., and Kennicutt, Jr., R. C. (2008). High-Resolution Rotation Curves and Galaxy Mass Models from THINGS. *AJ*, 136:2648–2719.

de Lorenzi, F., Debattista, V. P., Gerhard, O., and Sambhus, N. (2007). NMAGIC: a fast parallel implementation of a made-to-measure algorithm for modelling observational data. *MNRAS*, 376:71–88.

de Lorenzi, F., Gerhard, O., Coccato, L., Arnaboldi, M., Capaccioli, M., Douglas, N. G., Freeman, K. C., Kuijken, K., Merrifield, M. R., Napolitano, N. R., Noordermeer, E., Romanowsky, A. J., and Debattista, V. P. (2009). Dearth of dark matter or massive dark halo? Mass-shape-anisotropy degeneracies revealed by NMAGIC dynamical models of the elliptical galaxy NGC 3379. *MNRAS*, 395:76–96.

de Lorenzi, F., Gerhard, O., Saglia, R. P., Sambhus, N., Debattista, V. P., Pannella, M., and Méndez, R. H. (2008). Dark matter content and internal dynamics of NGC 4697: NMAGIC particle models from slit data and planetary nebula velocities. *MNRAS*, 385:1729–1748.

De Lucia, G., Springel, V., White, S. D. M., Croton, D., and Kauffmann, G. (2006). The formation history of elliptical galaxies. *MNRAS*, 366:499–509.

de Vaucouleurs, G. (1948). Recherches sur les Nebuleuses Extragalactiques. *Annales d'Astrophysique*, 11:247.

de Vaucouleurs, G., de Vaucouleurs, A., Corwin, Jr., H. G., Buta, R. J., Paturel, G., and Fouque, P. (1991). Book-Review - Third Reference Catalogue of Bright Galaxies. *Sky and Telescope*, 82:621–+.

de Zeeuw, T. (1985). Elliptical galaxies with separable potentials. *MNRAS*, 216:273–334.

de Zeeuw, T. and Franx, M. (1991). Structure and dynamics of elliptical galaxies. *ARA&A*, 29:239–274.

Deason, A. J., Belokurov, V., Evans, N. W., and McCarthy, I. G. (2012). Elliptical Galaxy Masses Out to Five Effective Radii: The Realm of Dark Matter. *ApJ*, 748:2.

Debattista, V. P. and Sellwood, J. A. (2000). Constraints from Dynamical Friction on the Dark Matter Content of Barred Galaxies. *ApJ*, 543:704–721.

Dehnen, W. (2009). Tailoring triaxial N-body models via a novel made-to-measure method. *MNRAS*, 395:1079–1086.

Dehnen, W. and Gerhard, O. E. (1993). Three-integral models of oblate elliptical galaxies. *MNRAS*, 261:311–336.

Dehnen, W. and Gerhard, O. E. (1994). Two-Integral Models for Oblate Elliptical Galaxies with Cusps. *MNRAS*, 268:1019–+.

Dejonghe, H. (1986). Stellar dynamics and the description of stellar systems. *Phys. Rep.*, 133:217–313.

Dejonghe, H., de Bruyne, V., Vauterin, P., and Zeilinger, W. W. (1996). The internal dynamics of very flattened normal galaxies. Stellar distribution functions for NGC 4697. *A&A*, 306:363.

Dejonghe, H. and de Zeeuw, T. (1988). Analytic axisymmetric galaxy models with three integrals of motion. *ApJ*, 333:90–129.

Dejonghe, H. and Merritt, D. (1992). Inferring the mass of spherical stellar systems from velocity moments. *ApJ*, 391:531–549.

Dekel, A., Stoehr, F., Mamon, G. A., Cox, T. J., Novak, G. S., and Primack, J. R. (2005). Lost and found dark matter in elliptical galaxies. *Nature*, 437:707–710.

Diehl, S. and Statler, T. S. (2007). The Hot Interstellar Medium of Normal Elliptical Galaxies. I. A Chandra Gas Gallery and Comparison of X-Ray and Optical Morphology. *ApJ*, 668:150–167.

Djorgovski, S. and Davis, M. (1987). Fundamental properties of elliptical galaxies. *ApJ*, 313:59–68.

Dopita, M. A., Jacoby, G. H., and Vassiliadis, E. (1992). A theoretical calibration of the planetary nebular cosmic distance scale. *ApJ*, 389:27–38.

Doroshkevich, A. G. and Zeldovich, I. B. (1975). Formation of galaxies in the expanding universe. *Ap&SS*, 35:55–65.

Douglas, N. G., Arnaboldi, M., Freeman, K. C., Kuijken, K., Merrifield, M. R., Romanowsky, A. J., Taylor, K., Capaccioli, M., Axelrod, T., Gilmozzi, R., Hart, J., Bloxham, G., and Jones, D. (2002). The Planetary Nebula Spectrograph: The Green Light for Galaxy Kinematics. *Publ. Astr. Soc. Pac.*, 114:1234–1251.

Douglas, N. G., Napolitano, N. R., Romanowsky, A. J., Coccato, L., Kuijken, K., Merrifield, M. R., Arnaboldi, M., Gerhard, O., Freeman, K. C., Merrett, H. R., Noordermeer, E., and Capaccioli, M. (2007). The PN.S Elliptical Galaxy Survey: Data Reduction, Planetary Nebula Catalog, and Basic Dynamics for NGC 3379. *ApJ*, 664:257–276.

Doyon, R., Wells, M., Wright, G. S., Joseph, R. D., Nadeau, D., and James, P. A. (1994). Stellar velocity dispersion in ARP 220 and NGC 6240: Elliptical galaxies in formation. *ApJL*, 437:L23–L26.

Dressler, A. (1980). Galaxy morphology in rich clusters - Implications for the formation and evolution of galaxies. *ApJ*, 236:351–365.

Dressler, A., Lynden-Bell, D., Burstein, D., Davies, R. L., Faber, S. M., Terlevich, R., and Wegner, G. (1987). Spectroscopy and photometry of elliptical galaxies. I - A new distance estimator. *ApJ*, 313:42–58.

Dubinski, J. (1998). The Origin of the Brightest Cluster Galaxies. *ApJ*, 502:141.

Dunlop, J. S., Guiderdoni, B., Rocca-Volmerange, B., Peacock, J. A., and Longair, M. S. (1989). The colour evolution of high-redshift radio galaxies. *MNRAS*, 240:257–284.

Efstathiou, G., Sutherland, W. J., and Maddox, S. J. (1990). The cosmological constant and cold dark matter. *Nature*, 348:705–707.

Eggen, O. J., Lynden-Bell, D., and Sandage, A. R. (1962). Evidence from the motions of old stars that the Galaxy collapsed. *ApJ*, 136:748.

Einasto, J., Kaasik, A., and Saar, E. (1974). Dynamic evidence on massive coronas of galaxies. *Nature*, 250:309–310.

Emsellem, E., Cappellari, M., Krajnović, D., Alatalo, K., Blitz, L., Bois, M., Bournaud, F., Bureau, M., Davies, R. L., Davis, T. A., de Zeeuw, P. T., Khochfar, S., Kuntschner, H., Lablanche, P.-Y., McDermid, R. M., Morganti, R., Naab, T., Oosterloo, T., Sarzi, M., Scott, N., Serra, P., van de Ven, G., Weijmans, A.-M., and Young, L. M. (2011). The ATLAS^{3D} project - III. A census of the stellar angular momentum within the effective radius of early-type galaxies: unveiling the distribution of fast and slow rotators. *MNRAS*, 414:888–912.

Emsellem, E., Cappellari, M., Krajnović, D., van de Ven, G., Bacon, R., Bureau, M., Davies, R. L., de Zeeuw, P. T., Falcón-Barroso, J., Kuntschner, H., McDermid, R., Peletier, R. F., and Sarzi, M. (2007). The SAURON project - IX. A kinematic classification for early-type galaxies. *MNRAS*, 379:401–417.

Emsellem, E., Cappellari, M., Peletier, R. F., McDermid, R. M., Bacon, R., Bureau, M., Copin, Y., Davies, R. L., Krajnović, D., Kuntschner, H., Miller, B. W., and de Zeeuw, P. T. (2004). The SAURON project - III. Integral-field absorption-line kinematics of 48 elliptical and lenticular galaxies. *MNRAS*, 352:721–743.

Emsellem, E., Dejonghe, H., and Bacon, R. (1999). Dynamical models of NGC 3115. *MNRAS*, 303:495–514.

Faber, S. M. (1973). Variations in Spectral-Energy Distributions and Absorption-Line Strengths among Elliptical Galaxies. *ApJ*, 179:731–754.

Faber, S. M. and Jackson, R. E. (1976). Velocity dispersions and mass-to-light ratios for elliptical galaxies. *ApJ*, 204:668–683.

Faber, S. M. and Lin, D. N. C. (1983). Is there nonluminous matter in dwarf spheroidal galaxies. *ApJL*, 266:L17–L20.

Faber, S. M., Tremaine, S., Ajhar, E. A., Byun, Y.-I., Dressler, A., Gebhardt, K., Grillmair, C., Kormendy, J., Lauer, T. R., and Richstone, D. (1997). The Centers of Early-Type Galaxies with HST. IV. Central Parameter Relations. *AJ*, 114:1771.

Faber, S. M., Willmer, C. N. A., Wolf, C., Koo, D. C., Weiner, B. J., Newman, J. A., Im, M., Coil, A. L., Conroy, C., Cooper, M. C., Davis, M., Finkbeiner, D. P., Gerke, B. F., Gebhardt, K., Groth, E. J., Guhathakurta, P., Harker, J., Kaiser, N., Kassin, S., Kleinheinrich, M., Konidaris, N. P., Kron, R. G., Lin, L., Luppino, G., Madgwick, D. S., Meisenheimer, K., Noeske, K. G., Phillips, A. C., Sarajedini, V. L., Schiavon, R. P., Simard, L., Szalay, A. S., Vogt, N. P., and Yan, R. (2007). Galaxy Luminosity Functions to z~1 from DEEP2 and COMBO-17: Implications for Red Galaxy Formation. *ApJ*, 665:265–294.

Fall, S. M. (1979). Dissipation, merging and the rotation of galaxies. *Nature*, 281:200–202.

Fall, S. M. and Efstathiou, G. (1980). Formation and rotation of disc galaxies with haloes. *MNRAS*, 193:189–206.

Ferrarese, L. and Merritt, D. (2000). A Fundamental Relation between Supermassive Black Holes and Their Host Galaxies. *ApJL*, 539:L9–L12.

Ferreras, I., La Barbera, F., de Carvalho, R. R., de la Rosa, I. G., Vazdekis, A., Falcon-Barroso, J., and Ricciardelli, E. (2012). Systematic variation of the stellar Initial Mass Function with velocity dispersion in early-type galaxies. *ArXiv e-prints*.

Fish, R. A. (1964). A Mass-Potential Relationship in Elliptical Galaxies and Some Inferences Concerning the Formation and Evolution of Galaxies. *ApJ*, 139:284.

Forbes, D. A., Franx, M., and Illingworth, G. D. (1995). Ellipticals with Kinematically Distinct Cores: WFPC1 Imaging of Nearby Ellipticals. *AJ*, 109:1988.

Forbes, D. A., Franx, M., Illingworth, G. D., and Carollo, C. M. (1996). Ellipticals with Kinematically Distinct Cores: WFPC2 Imaging of Globular Clusters. *ApJ*, 467:126.

Forbes, D. A., Spitler, L. R., Strader, J., Romanowsky, A. J., Brodie, J. P., and Foster, C. (2011). Evidence for two phases of galaxy formation from radial trends in the globular cluster system of NGC 1407. *MNRAS*, 413:2943–2949.

Forestell, A. D. and Gebhardt, K. (2010). Hobby-Eberly Telescope Observations of the Dark Halo in NGC 821. *ApJ*, 716:370–383.

Forman, W., Schwarz, J., Jones, C., Liller, W., and Fabian, A. C. (1979). X-ray observations of galaxies in the Virgo cluster. *ApJL*, 234:L27–L31.

Foster, C., Spitler, L. R., Romanowsky, A. J., Forbes, D. A., Pota, V., Bekki, K., Strader, J., Proctor, R. N., Arnold, J. A., and Brodie, J. P. (2011). Global properties of 'ordinary' early-type galaxies: photometry and spectroscopy of stars and globular clusters in NGC 4494. *MNRAS*, pages 906–+.

Franx, M. and Illingworth, G. D. (1988). A counterrotating core in IC 1459. *ApJL*, 327:L55–L59.

Franx, M., Labbé, I., Rudnick, G., van Dokkum, P. G., Daddi, E., Förster Schreiber, N. M., Moorwood, A., Rix, H.-W., Röttgering, H., van der Wel, A., van der Werf, P., and van Starkenburg, L. (2003). A Significant Population of Red, Near-Infrared-selected High-Redshift Galaxies. *ApJL*, 587:L79–L82.

Franx, M., van Gorkom, J. H., and de Zeeuw, T. (1994). Evidence for axisymmetric halos: The case of IC 2006. *ApJ*, 436:642–653.

Fridman, A. M. and Poliachenko, V. L. (1984). *Physics of gravitating systems. II - Nonlinear collective processes: Nonlinear waves, solitons, collisionless shocks, turbulence. Astrophysical applications.*

Fukazawa, Y., Botoya-Nonesa, J. G., Pu, J., Ohto, A., and Kawano, N. (2006). Scaling Mass Profiles around Elliptical Galaxies Observed with Chandra and XMM-Newton. *ApJ*, 636:698–711.

G. Wahba, editor (1990). *Spline models for observational data.*

Gabor, J. M. and Davé, R. (2012). The Growth of Red Sequence Galaxies in a Cosmological Hydrodynamic Simulation. *ArXiv e-prints*.

Gaitskell, R. J. (2004). Direct Detection of Dark Matter. *Annual Review of Nuclear and Particle Science*, 54:315–359.

Gallazzi, A., Charlot, S., Brinchmann, J., and White, S. D. M. (2006). Ages and metallicities of early-type galaxies in the Sloan Digital Sky Survey: new insight into the physical origin of the colour-magnitude and the Mg_2-σ_V relations. *MNRAS*, 370:1106–1124.

Gargiulo, A., Haines, C. P., Merluzzi, P., Smith, R. J., Barbera, F. L., Busarello, G., Lucey, J. R., Mercurio, A., and Capaccioli, M. (2009). On the origin of the scatter around the Fundamental Plane: correlations with stellar population parameters. *MNRAS*, 397:75–89.

Gavazzi, R., Treu, T., Rhodes, J. D., Koopmans, L. V. E., Bolton, A. S., Burles, S., Massey, R. J., and Moustakas, L. A. (2007). The Sloan Lens ACS Survey. IV. The Mass Density Profile of Early-Type Galaxies out to 100 Effective Radii. *ApJ*, 667:176–190.

Gebhardt, K., Bender, R., Bower, G., Dressler, A., Faber, S. M., Filippenko, A. V., Green, R., Grillmair, C., Ho, L. C., Kormendy, J., Lauer, T. R., Magorrian, J., Pinkney, J., Richstone, D., and Tremaine, S. (2000). A Relationship between Nuclear Black Hole Mass and Galaxy Velocity Dispersion. *ApJL*, 539:L13–L16.

Gebhardt, K., Richstone, D., Tremaine, S., Lauer, T. R., Bender, R., Bower, G., Dressler, A., Faber, S. M., Filippenko, A. V., Green, R., Grillmair, C., Ho, L. C., Kormendy, J., Magorrian, J., and Pinkney, J. (2003). Axisymmetric Dynamical Models of the Central Regions of Galaxies. *ApJ*, 583:92–115.

Genel, S., Genzel, R., Bouché, N., Sternberg, A., Naab, T., Schreiber, N. M. F., Shapiro, K. L., Tacconi, L. J., Lutz, D., Cresci, G., Buschkamp, P., Davies, R. I., and Hicks, E. K. S. (2008). Mergers and Mass Accretion Rates in Galaxy Assembly: The Millennium Simulation Compared to Observations of z ˜ 2 Galaxies. *ApJ*, 688:789–793.

Genzel, R., Tacconi, L. J., Rigopoulou, D., Lutz, D., and Tecza, M. (2001). Ultraluminous Infrared Mergers: Elliptical Galaxies in Formation? *ApJ*, 563:527–545.

Gerhard, O. (2006). Modelling Kinematics and Dark Matter: The Halos of Elliptical Galaxies. In Stanghellini, L., Walsh, J. R., and Douglas, N. G., editors, *Planetary Nebulae Beyond the Milky Way*, page 299.

Gerhard, O., Jeske, G., Saglia, R. P., and Bender, R. (1998). Breaking the degeneracy between anisotropy and mass - The dark halo of the E0 galaxy NGC 6703. *MNRAS*, 295:197–+.

Gerhard, O., Kronawitter, A., Saglia, R. P., and Bender, R. (2001). Dynamical Family Properties and Dark Halo Scaling Relations of Giant Elliptical Galaxies. *AJ*, 121:1936–1951.

Gerhard, O. E. (1981). N-body simulations of disc-halo galaxies - Isolated systems, tidal interactions and merging. *MNRAS*, 197:179–208.

Gerhard, O. E. (1983a). A quasi-stable stellar system with prolate inner and oblate outer parts. *MNRAS*, 202:1159–1167.

Gerhard, O. E. (1983b). Intrinsic principal axes twists in N-body models of elliptical galaxies. *MNRAS*, 203:19P–23P.

Gerhard, O. E. (1991). A new family of distribution functions for spherical galaxies. *MNRAS*, 250:812–830.

Gerhard, O. E. (1993). Line-of-sight velocity profiles in spherical galaxies: breaking the degeneracy between anisotropy and mass. *MNRAS*, 265:213–+.

Gerhard, O. E. and Binney, J. J. (1996). On the deprojection of axisymmetric bodies. *MNRAS*, 279:993.

Gerhard, O. E., Jeske, G., Saglia, R. P., and Bender, R. (1999). Mass Distribution of the E0 Galaxy NGC 6703 From Absorption Line Profile Kinematics. In J. E. Barnes & D. B. Sanders, editor, *Galaxy Interactions at Low and High Redshift*, volume 186 of *IAU Symposium*, page 189.

Gerhard, O. E. and Saha, P. (1991). Recovering galactic orbits by perturbation theory. *MNRAS*, 251:449–467.

Giannantonio, T., Scranton, R., Crittenden, R. G., Nichol, R. C., Boughn, S. P., Myers, A. D., and Richards, G. T. (2008). Combined analysis of the integrated Sachs-Wolfe effect and cosmological implications. *Phys. Rev. D*, 77(12):123520.

Glazebrook, K., Abraham, R. G., McCarthy, P. J., Savaglio, S., Chen, H.-W., Crampton, D., Murowinski, R., Jørgensen, I., Roth, K., Hook, I., Marzke, R. O., and Carlberg, R. G. (2004). A high abundance of massive galaxies 3-6 billion years after the Big Bang. *Nature*, 430:181–184.

Goad, J. W. and Roberts, M. S. (1981). Spectroscopic observations of superthin galaxies. *ApJ*, 250:79–86.

Gondolo, P. (2004). Introduction to Non-Baryonic Dark Matter. *ArXiv Astrophysics e-prints*.

Goudfrooij, P., de Jong, T., Hansen, L., and Norgaard-Nielsen, H. U. (1994). Interstellar Matter in Elliptical Galaxies - Part Three - Properties of Dust Extinction. *MNRAS*, 271:833.

Graves, G. J. and Faber, S. M. (2010). Dissecting the Red sequence. III. Mass-to-Light Variations in Three-dimensional Fundamental Plane Space. *ApJ*, 717:803–824.

Greene, J. E., Murphy, J. D., Comerford, J. M., Gebhardt, K., and Adams, J. J. (2012). The Stellar Halos of Massive Elliptical Galaxies. *ArXiv e-prints*.

Greggio, L. and Renzini, A. (1983). The binary model for type I supernovae - Theoretical rates. *A&A*, 118:217–222.

Grillo, C. (2012). On the Average Density Profile of Dark-matter Halos in the Inner Regions of Massive Early-type Galaxies. *ApJL*, 747:L15.

Guo, Q. and White, S. D. M. (2008). Galaxy growth in the concordance ΛCDM cosmology. *MNRAS*, 384:2–10.

Guth, A. H. (1981). Inflationary universe: A possible solution to the horizon and flatness problems. *Phys. Rev. D*, 23:347–356.

Harris, W. E. (1991). Globular cluster systems in galaxies beyond the Local Group. *ARA&A*, 29:543–579.

Henon, M. (1982). Vlasov equation. *A&A*, 114:211.

Hernquist, L. (1990). An analytical model for spherical galaxies and bulges. *ApJ*, 356:359–364.

Hernquist, L. (1992). Structure of merger remnants. I - Bulgeless progenitors. *ApJ*, 400:460–475.

Hernquist, L. and Ostriker, J. P. (1992). A self-consistent field method for galactic dynamics. *ApJ*, 386:375–397.

Hernquist, L., Spergel, D. N., and Heyl, J. S. (1993). Structure of Merger Remnants. III. Phase-Space Constraints. *ApJ*, 416:415.

Hill, G. J., MacQueen, P. J., Smith, M. P., Tufts, J. R., Roth, M. M., Kelz, A., Adams, J. J., Drory, N., Grupp, F., Barnes, S. I., Blanc, G. A., Murphy, J. D., Altmann, W., Wesley, G. L., Segura, P. R., Good, J. M., Booth, J. A., Bauer, S.-M., Popow, E., Goertz, J. A., Edmonston, R. D., and Wilkinson, C. P. (2008). Design, construction, and performance of VIRUS-P: the prototype of a highly replicated integral-field spectrograph for HET. In *Society of Photo-Optical Instrumentation Engineers (SPIE) Conference Series*, volume 7014 of *Society of Photo-Optical Instrumentation Engineers (SPIE) Conference Series*.

Hilz, M., Naab, T., Ostriker, J. P., Thomas, J., Burkert, A., and Jesseit, R. (2012). Relaxation and Stripping: The Evolution of Sizes, Dispersions and Dark Matter Fractions in Major and Minor Mergers of Elliptical Galaxies. *ArXiv e-prints*.

Hirschmann, M., Naab, T., Somerville, R. S., Burkert, A., and Oser, L. (2012). Galaxy formation in semi-analytic models and cosmological hydrodynamic zoom simulations. *MNRAS*, 419:3200–3222.

Hoffman, L., Cox, T. J., Dutta, S., and Hernquist, L. (2010). Orbital Structure of Merger Remnants. I. Effect of Gas Fraction in Pure Disk Mergers. *ApJ*, 723:818–844.

Hopkins, P. F., Cox, T. J., Dutta, S. N., Hernquist, L., Kormendy, J., and Lauer, T. R. (2009). Dissipation and Extra Light in Galactic Nuclei. II. "Cusp" Ellipticals. *ApJS*, 181:135–182.

Hopkins, P. F., Hernquist, L., Cox, T. J., Dutta, S. N., and Rothberg, B. (2008). Dissipation and Extra Light in Galactic Nuclei. I. Gas-Rich Merger Remnants. *ApJ*, 679:156–181.

Houghton, R. C. W., Magorrian, J., Sarzi, M., Thatte, N., Davies, R. L., and Krajnović, D. (2006). The central kinematics of NGC 1399 measured with 14 pc resolution. *MNRAS*, 367:2–18.

Hubble, E. P. (1936). *Realm of the Nebulae.*

Hui, X., Ford, H. C., Freeman, K. C., and Dopita, M. A. (1995). The Planetary Nebula System and Dynamics of NGC 5128. III. Kinematics and Halo Mass Distributions. *ApJ*, 449:592.

Humphrey, P. J., Buote, D. A., Gastaldello, F., Zappacosta, L., Bullock, J. S., Brighenti, F., and Mathews, W. G. (2006). A Chandra View of Dark Matter in Early-Type Galaxies. *ApJ*, 646:899–918.

Hunter, C. and de Zeeuw, P. T. (1992). Triaxial galaxy models with thin tube orbits. *ApJ*, 389:79–117.

Hunter, C. and Qian, E. (1993). Two-integral distribution functions for axisymmetric galaxies. *MNRAS*, 262:401–428.

Hyde, J. B. and Bernardi, M. (2009). The luminosity and stellar mass Fundamental Plane of early-type galaxies. *MNRAS*, 396:1171–1185.

Illingworth, G. (1977). Rotation in 13 elliptical galaxies. *ApJL*, 218:L43–L47.

Jarrett, T. H. (2000). Near-Infrared Galaxy Morphology Atlas. *Publ. Astr. Soc. Pac.*, 112:1008–1080.

Jeans, J. H. (1902). The Stability of a Spherical Nebula. *Royal Society of London Philosophical Transactions Series A*, 199:1–53.

Jedrzejewski, R. I. (1987). CCD surface photometry of elliptical galaxies. I - Observations, reduction and results. *MNRAS*, 226:747–768.

Jesseit, R., Naab, T., and Burkert, A. (2005). Orbital structure of collisionless merger remnants: on the origin of photometric and kinematic properties of elliptical and S0 galaxies. *MNRAS*, 360:1185–1200.

Jesseit, R., Naab, T., Peletier, R. F., and Burkert, A. (2007). 2D kinematics of simulated disc merger remnants. *MNRAS*, 376:997–1020.

Jimenez, R., Friaca, A. C. S., Dunlop, J. S., Terlevich, R. J., Peacock, J. A., and Nolan, L. A. (1999). Premature dismissal of high-redshift elliptical galaxies. *MNRAS*, 305:L16–L20.

Johansson, P. H., Naab, T., and Ostriker, J. P. (2012). Forming Early-Type Galaxies in LambdaCDM Simulations -I. Assembly histories. *ArXiv e-prints*.

Kalnajs, A. J. (1977). Dynamics of flat galaxies. IV - The integral equation for normal modes in matrix form. *ApJ*, 212:637–644.

Kauffmann, G., Heckman, T. M., White, S. D. M., Charlot, S., Tremonti, C., Brinchmann, J., Bruzual, G., Peng, E. W., Seibert, M., Bernardi, M., Blanton, M., Brinkmann, J., Castander, F., Csábai, I., Fukugita, M., Ivezic, Z., Munn, J. A., Nichol, R. C., Padmanabhan, N., Thakar, A. R., Weinberg, D. H., and York, D. (2003). Stellar masses and star formation histories for 10^5 galaxies from the Sloan Digital Sky Survey. *MNRAS*, 341:33–53.

Kauffmann, G., White, S. D. M., and Guiderdoni, B. (1993). The Formation and Evolution of Galaxies Within Merging Dark Matter Haloes. *MNRAS*, 264:201.

Keeton, C. R. (2001). Cold Dark Matter and Strong Gravitational Lensing: Concord or Conflict? *ApJ*, 561:46–60.

Kent, S. M. (1984). CCD surface photometry of field galaxies. I - Observations. *ApJS*, 56:105–141.

Khochfar, S. and Burkert, A. (2005). On the origin of isophotal shapes in elliptical galaxies. *MNRAS*, 359:1379–1385.

Khochfar, S., Emsellem, E., Serra, P., Bois, M., Alatalo, K., Bacon, R., Blitz, L., Bournaud, F., Bureau, M., Cappellari, M., Davies, R. L., Davis, T. A., de Zeeuw, P. T., Duc, P.-A., Krajnović, D., Kuntschner, H., Lablanche, P.-Y., McDermid, R. M., Morganti, R., Naab, T., Oosterloo, T., Sarzi, M., Scott, N., Weijmans, A.-M., and Young, L. M. (2011). The ATLAS^{3D} project - VIII. Modelling the formation and evolution of fast and slow rotator early-type galaxies within ΛCDM. *MNRAS*, 417:845–862.

Khochfar, S. and Silk, J. (2006). A Simple Model for the Size Evolution of Elliptical Galaxies. *ApJL*, 648:L21–L24.

King, I. R. (1978). Surface photometry of elliptical galaxies. *ApJ*, 222:1–13.

Koch, A., Wilkinson, M. I., Kleyna, J. T., Gilmore, G. F., Grebel, E. K., Mackey, A. D., Evans, N. W., and Wyse, R. F. G. (2007). Stellar Kinematics and Metallicities in the Leo I Dwarf Spheroidal Galaxy-Wide-Field Implications for Galactic Evolution. *ApJ*, 657:241–261.

Kodama, T. and Arimoto, N. (1997). Origin of the colour-magnitude relation of elliptical galaxies. *A&A*, 320:41–53.

Komatsu, E., Smith, K. M., Dunkley, J., Bennett, C. L., Gold, B., Hinshaw, G., Jarosik, N., Larson, D., Nolta, M. R., Page, L., Spergel, D. N., Halpern, M., Hill, R. S., Kogut, A., Limon, M., Meyer, S. S., Odegard, N., Tucker, G. S., Weiland, J. L., Wollack, E., and Wright, E. L. (2011). Seven-year Wilkinson Microwave Anisotropy Probe (WMAP) Observations: Cosmological Interpretation. *ApJS*, 192:18.

Koopmans, L. V. E., Bolton, A., Treu, T., Czoske, O., Auger, M. W., Barnabè, M., Vegetti, S., Gavazzi, R., Moustakas, L. A., and Burles, S. (2009). The Structure and Dynamics of Massive Early-Type Galaxies: On Homology, Isothermality, and Isotropy Inside One Effective Radius. *ApJL*, 703:L51–L54.

Kormendy, J. (1977). Brightness distributions in compact and normal galaxies. II - Structure parameters of the spheroidal component. *ApJ*, 218:333–346.

Kormendy, J. (1982). Observations of galaxy structure and dynamics. In L. Martinet & M. Mayor, editor, *Saas-Fee Advanced Course 12: Morphology and Dynamics of Galaxies*, pages 113–288.

Kormendy, J. (1989). Did elliptical galaxies form by mergers or by dissipative collapse? *ApJL*, 342:L63–L66.

Kormendy, J. (1993). Kinematics of extragalactic bulges: evidence that some bulges are really disks. In Dejonghe, H. and Habing, H. J., editors, *Galactic Bulges*, volume 153 of *IAU Symposium*, page 209.

Kormendy, J. (1999). The Central Structure of Elliptical Galaxies and the Stellar-Dynamical Search for Supermassive Black Holes. In Merritt, D. R., Valluri, M., and Sellwood, J. A., editors, *Galaxy Dynamics - A Rutgers Symposium*, volume 182 of *Astronomical Society of the Pacific Conference Series*, page 124.

Kormendy, J. and Bender, R. (1996). A Proposed Revision of the Hubble Sequence for Elliptical Galaxies. *ApJL*, 464:L119.

Kormendy, J. and Bender, R. (2012). A Revised Parallel-sequence Morphological Classification of Galaxies: Structure and Formation of S0 and Spheroidal Galaxies. *ApJS*, 198:2.

Kormendy, J. and Djorgovski, S. (1989). Surface photometry and the structure of elliptical galaxies. *ARA&A*, 27:235–277.

Kormendy, J., Drory, N., Bender, R., and Cornell, M. E. (2010). Bulgeless Giant Galaxies Challenge Our Picture of Galaxy Formation by Hierarchical Clustering. *ApJ*, 723:54–80.

Kormendy, J., Fisher, D. B., Cornell, M. E., and Bender, R. (2009). Structure and Formation of Elliptical and Spheroidal Galaxies. *ApJS*, 182:216–309.

Kormendy, J. and Kennicutt, Jr., R. C. (2004). Secular Evolution and the Formation of Pseudobulges in Disk Galaxies. *ARA&A*, 42:603–683.

Krajnović, D., Emsellem, E., Cappellari, M., Alatalo, K., Blitz, L., Bois, M., Bournaud, F., Bureau, M., Davies, R. L., Davis, T. A., de Zeeuw, P. T., Khochfar, S., Kuntschner, H., Lablanche, P.-Y., McDermid, R. M., Morganti, R., Naab, T., Oosterloo, T., Sarzi, M., Scott, N., Serra, P., Weijmans, A.-M., and Young, L. M. (2011). The ATLAS^{3D} project - II. Morphologies, kinemetric features and alignment between photometric and kinematic axes of early-type galaxies. *MNRAS*, 414:2923–2949.

Kronawitter, A., Saglia, R. P., Gerhard, O., and Bender, R. (2000). Orbital structure and mass distribution in elliptical galaxies. *A&A Supp.*, 144:53–84.

Kuijken, K. (1995). An Axisymmetric Distribution Function for the Galactic Bulge. *ApJ*, 446:194–+.

La Barbera, F., Lopes, P. A. A., de Carvalho, R. R., de La Rosa, I. G., and Berlind, A. A. (2010). SPIDER - III. Environmental dependence of the Fundamental Plane of early-type galaxies. *MNRAS*, 408:1361–1386.

Lackner, C. N., Cen, R., Ostriker, J. P., and Joung, M. R. (2012). Building galaxies by accretion and in-situ star formation. *ArXiv e-prints*.

Lackner, C. N. and Ostriker, J. P. (2010). Dissipational Versus Dissipationless Galaxy Formation and the Dark Matter Content of Galaxies. *ApJ*, 712:88–100.

Lake, G. and Dressler, A. (1986). A dynamical study of merger remnants. *ApJ*, 310:605–612.

Larson, R. B. (1975). Models for the formation of elliptical galaxies. *MNRAS*, 173:671–699.

Lauer, T. R. (1985). Boxy isophotes, discs and dust lanes in elliptical galaxies. *MNRAS*, 216:429–438.

Lauer, T. R., Faber, S. M., Gebhardt, K., Richstone, D., Tremaine, S., Ajhar, E. A., Aller, M. C., Bender, R., Dressler, A., Filippenko, A. V., Green, R., Grillmair, C. J., Ho, L. C., Kormendy, J., Magorrian, J., Pinkney, J., and Siopis, C. (2005). The Centers of Early-Type Galaxies with Hubble Space Telescope. V. New WFPC2 Photometry. *AJ*, 129:2138–2185.

Liller, M. H. (1960). The Distribution of Intensity in Elliptical Galaxies of the Virgo Cluster. *ApJ*, 132:306.

Loewenstein, M. and White, III, R. E. (1999). Prevalence and Properties of Dark Matter in Elliptical Galaxies. *ApJ*, 518:50–63.

Lokas, E. L. (2002). Dark matter distribution in dwarf spheroidal galaxies. *MNRAS*, 333:697–708.

Lokas, E. L. and Mamon, G. A. (2003). Dark matter distribution in the Coma cluster from galaxy kinematics: breaking the mass-anisotropy degeneracy. *MNRAS*, 343:401–412.

Long, R. J. and Mao, S. (2010). Made-to-measure galaxy models - I. Methodology. *MNRAS*, 405:301–317.

Long, R. J. and Mao, S. (2012). Made-to-measure galaxy models - II. Elliptical and lenticular galaxies. *MNRAS*, 421:2580–2592.

Lotz, J. M., Jonsson, P., Cox, T. J., Croton, D., Primack, J. R., Somerville, R. S., and Stewart, K. (2011). The Major and Minor Galaxy Merger Rates at z 1.5. *ApJ*, 742:103.

Lynden-Bell, D. (1962). Stellar dynamics. Potentials with isolating integrals. *MNRAS*, 124:95.

Lynden-Bell, D. (1967). Statistical mechanics of violent relaxation in stellar systems. *MNRAS*, 136:101.

Maddox, S. J., Efstathiou, G., Sutherland, W. J., and Loveday, J. (1990). Galaxy correlations on large scales. *MNRAS*, 242:43P–47P.

Magorrian, J. (1995). Reconstructing Two-Integral Distribution Functions from Moments. *MNRAS*, 277:1185–+.

Magorrian, J. (1999). Kinematical signatures of hidden stellar discs. *MNRAS*, 302:530–536.

Magorrian, J. and Ballantyne, D. (2001). Mass profiles and anisotropies of early-type galaxies. *MNRAS*, 322:702–714.

Magorrian, J. and Binney, J. (1994). Predicting line-of-sight velocity distributions of elliptical galaxies. *MNRAS*, 271:949–+.

Magorrian, J., Tremaine, S., Richstone, D., Bender, R., Bower, G., Dressler, A., Faber, S. M., Gebhardt, K., Green, R., Grillmair, C., Kormendy, J., and Lauer, T. (1998). The Demography of Massive Dark Objects in Galaxy Centers. *AJ*, 115:2285–2305.

Malin, D. F. and Carter, D. (1983). A catalog of elliptical galaxies with shells. *ApJ*, 274:534–540.

Mamon, G. A. and Lokas, E. L. (2005). Dark matter in elliptical galaxies - II. Estimating the mass within the virial radius. *MNRAS*, 363:705–722.

Maoz, D. and Rix, H.-W. (1993). Early-Type Galaxies, Dark Halos, and Gravitational Lensing Statistics. *ApJ*, 416:425.

Mateo, M., Olszewski, E. W., and Walker, M. G. (2008). The Velocity Dispersion Profile of the Remote Dwarf Spheroidal Galaxy Leo I: A Tidal Hit and Run? *ApJ*, 675:201–233.

Mathews, W. G. and Brighenti, F. (2003). Hot Gas in and around Elliptical Galaxies. *ARA&A*, 41:191–239.

Matteucci, F. and Greggio, L. (1986). Relative roles of type I and II supernovae in the chemical enrichment of the interstellar gas. *A&A*, 154:279–287.

Matthews, L. D., Gallagher, III, J. S., and van Driel, W. (1999). The Extraordinary "Superthin" Spiral Galaxy UGC 7321. I. Disk Color Gradients and Global Properties from Multiwavelength Observations. *AJ*, 118:2751–2766.

Matthias, M. and Gerhard, O. (1999). Dynamics of the boxy elliptical galaxy NGC 1600. *MNRAS*, 310:879–891.

Mehlert, D., Saglia, R. P., Bender, R., and Wegner, G. (2000). Spatially resolved spectroscopy of Coma cluster early-type galaxies. I. The database. *A&A Supp.*, 141:449–468.

Mehlert, D., Thomas, D., Saglia, R. P., Bender, R., and Wegner, G. (2003). Spatially resolved spectroscopy of Coma cluster early-type galaxies. III. The stellar population gradients. *A&A*, 407:423–435.

Mellier, Y., Fort, B., and Kneib, J.-P. (1993). The dark matter distribution in MS 2137-23 from the modeling of the multiple arc systems. *ApJ*, 407:33–45.

Méndez, R. H., Riffeser, A., Kudritzki, R.-P., Matthias, M., Freeman, K. C., Arnaboldi, M., Capaccioli, M., and Gerhard, O. E. (2001). Detection, Photometry, and Slitless Radial Velocities of 535 Planetary Nebulae in the Flattened Elliptical Galaxy NGC 4697. *ApJ*, 563:135–150.

Merrett, H. R., Kuijken, K., Merrifield, M. R., Romanowsky, A. J., Douglas, N. G., Napolitano, N. R., Arnaboldi, M., Capaccioli, M., Freeman, K. C., Gerhard, O., Evans, N. W., Wilkinson, M. I., Halliday, C., Bridges, T. J., and Carter, D. (2003). Tracing the star stream through M31 using planetary nebula kinematics. *MNRAS*, 346:L62–L66.

Merritt, D. (1985). Spherical stellar systems with spheroidal velocity distributions. *AJ*, 90:1027–1037.

Merritt, D. (1993). Dynamical mapping of hot stellar systems. *ApJ*, 413:79–94.

Merritt, D. (1996). The Dynamical Inverse Problem for Axisymmetric Stellar Systems. *AJ*, 112:1085–+.

Merritt, D. (2006). Mass Deficits, Stalling Radii, and the Merger Histories of Elliptical Galaxies. *ApJ*, 648:976–986.

Merritt, D. and Fridman, T. (1996). Triaxial Galaxies with Cusps. *ApJ*, 460:136.

Merritt, D. and Hernquist, L. (1991). Stability of nonrotating stellar systems. II - Prolate shell-orbit models. *ApJ*, 376:439–457.

Merritt, D. and Oh, S. P. (1997). The Stellar Dynamics of M87. *AJ*, 113:1279–1285.

Merritt, D. and Saha, P. (1993). Mapping spherical potentials with discrete radial velocities. *ApJ*, 409:75–90.

Merritt, D. and Sellwood, J. A. (1994). Bending instabilities in stellar systems. *ApJ*, 425:551–567.

Mihos, J. C. and Hernquist, L. (1994). Dense stellar cores in merger remnants. *ApJL*, 437:L47–L50.

Milgrom, M. (1983). A modification of the Newtonian dynamics as a possible alternative to the hidden mass hypothesis. *ApJ*, 270:365–370.

Milosavljević, M. and Merritt, D. (2003). Long-Term Evolution of Massive Black Hole Binaries. *ApJ*, 596:860–878.

Monaghan, J. J. (1992). Smoothed particle hydrodynamics. *ARA&A*, 30:543–574.

Moore, B. (1994). Evidence against dissipation-less dark matter from observations of galaxy haloes. *Nature*, 370:629–631.

Morganti, L. and Gerhard, O. (2012). Regularizing made-to-measure particle models of galaxies. *MNRAS*, 422:1571–1585.

Murphy, J., Gebhardt, K., and Adams, J. J. (2011). Galaxy Kinematics with VIRUS-P: The Dark Matter Halo of M87. In *American Astronomical Society Meeting Abstracts 217*, volume 43 of *Bulletin of the American Astronomical Society*, page 151.02.

Naab, T. and Burkert, A. (2003). Statistical Properties of Collisionless Equal- and Unequal-Mass Merger Remnants of Disk Galaxies. *ApJ*, 597:893–906.

Naab, T., Jesseit, R., and Burkert, A. (2006). The influence of gas on the structure of merger remnants. *MNRAS*, 372:839–852.

Naab, T., Johansson, P. H., and Ostriker, J. P. (2009). Minor Mergers and the Size Evolution of Elliptical Galaxies. *ApJL*, 699:L178–L182.

Naab, T., Johansson, P. H., Ostriker, J. P., and Efstathiou, G. (2007). Formation of Early-Type Galaxies from Cosmological Initial Conditions. *ApJ*, 658:710–720.

Naab, T. and Trujillo, I. (2006). Surface density profiles of collisionless disc merger remnants. *MNRAS*, 369:625–644.

Nagino, R. and Matsushita, K. (2009). Gravitational potential and X-ray luminosities of early-type galaxies observed with XMM-Newton and Chandra. *A&A*, 501:157–169.

Napolitano, N. R., Romanowsky, A. J., Capaccioli, M., Douglas, N. G., Arnaboldi, M., Coccato, L., Gerhard, O., Kuijken, K., Merrifield, M. R., Bamford, S. P., Cortesi, A., Das, P., and Freeman, K. C. (2011). The PN.S Elliptical Galaxy Survey: a standard ΛCDM halo around NGC 4374? *MNRAS*, 411:2035–2053.

Napolitano, N. R., Romanowsky, A. J., Coccato, L., Capaccioli, M., Douglas, N. G., Noordermeer, E., Gerhard, O., Arnaboldi, M., de Lorenzi, F., Kuijken, K., Merrifield, M. R., O'Sullivan, E., Cortesi, A., Das, P., and Freeman, K. C. (2009). The Planetary Nebula Spectrograph elliptical galaxy survey: the dark matter in NGC 4494. *MNRAS*, 393:329–353.

Navarro, J. F., Frenk, C. S., and White, S. D. M. (1996). The Structure of Cold Dark Matter Halos. *ApJ*, 462:563.

Navarro, J. F., Ludlow, A., Springel, V., Wang, J., Vogelsberger, M., White, S. D. M., Jenkins, A., Frenk, C. S., and Helmi, A. (2010). The diversity and similarity of simulated cold dark matter haloes. *MNRAS*, 402:21–34.

Negroponte, J. and White, S. D. M. (1983). Simulations of mergers between disc-halo galaxies. *MNRAS*, 205:1009–1029.

Nieto, J.-L. and Bender, R. (1989). Boxiness in elliptical galaxies. *A&A*, 215:266–271.

Nieto, J.-L., Bender, R., and Surma, P. (1991). Central brightness profiles and isophotal shapes in elliptical galaxies. *A&A*, 244:L37–L40.

Nipoti, C., Londrillo, P., and Ciotti, L. (2003). Galaxy merging, the fundamental plane of elliptical galaxies and the M_{BH}-σ_0 relation. *MNRAS*, 342:501–512.

Nipoti, C., Treu, T., and Bolton, A. S. (2009). Dry Mergers and the Formation of Early-Type Galaxies: Constraints from Lensing and Dynamics. *ApJ*, 703:1531–1544.

Norman, M. L., Bryan, G. L., Harkness, R., Bordner, J., Reynolds, D., O'Shea, B., and Wagner, R. (2007). Simulating Cosmological Evolution with Enzo. *ArXiv e-prints*.

Oñorbe, J., Domínguez-Tenreiro, R., Sáiz, A., and Serna, A. (2007). Bright and dark matter in elliptical galaxies: mass and velocity distributions from self-consistent hydrodynamical simulations. *MNRAS*, 376:39–60.

Oosterloo, T. A., Morganti, R., Sadler, E. M., Vergani, D., and Caldwell, N. (2002). Extended H I Disks in Dust Lane Elliptical Galaxies. *AJ*, 123:729–744.

Oser, L., Naab, T., Ostriker, J. P., and Johansson, P. H. (2012). The Cosmological Size and Velocity Dispersion Evolution of Massive Early-type Galaxies. *ApJ*, 744:63.

Oser, L., Ostriker, J. P., Naab, T., Johansson, P. H., and Burkert, A. (2010). The Two Phases of Galaxy Formation. *ApJ*, 725:2312–2323.

Osipkov, L. P. (1979). Spherical systems of gravitating bodies with an ellipsoidal velocity distribution. *Pis ma Astronomicheskii Zhurnal*, 5:77–80.

O'Sullivan, E. and Ponman, T. J. (2004). XMM-Newton and Chandra observations of three X-ray-faint early-type galaxies. *MNRAS*, 349:535–546.

Peacock, J. A. (1999). *Cosmological Physics*.

Peebles, P. J. E. (1984). The origin of galaxies and clusters of galaxies. *Science*, 224:1385–1391.

Peletier, R. F., Davies, R. L., Illingworth, G. D., Davis, L. E., and Cawson, M. (1990). CCD surface photometry of galaxies with dynamical data. II - UBR photometry of 39 elliptical galaxies. *AJ*, 100:1091–1142.

Pellegrini, S., Baldi, A., Kim, D. W., Fabbiano, G., Soria, R., Siemiginowska, A., and Elvis, M. (2007). A Deep Chandra Look at the Low-L_B Elliptical NGC 821: X-Ray Binaries, a Galactic Wind, and Emission at the Nucleus. *ApJ*, 667:731–748.

Peng, E. W., Ford, H. C., and Freeman, K. C. (2004). The Globular Cluster System of NGC 5128. II. Ages, Metallicities, Kinematics, and Formation. *ApJ*, 602:705–722.

Percival, W. J. et al. (2010). Baryon Acoustic Oscillations in the Sloan Digital Sky Survey Data Release 7 Galaxy Sample. *Mon. Not. Roy. Astron. Soc.*, 401:2148–2168.

Perlmutter, S., Aldering, G., Goldhaber, G., Knop, R. A., Nugent, P., Castro, P. G., Deustua, S., Fabbro, S., Goobar, A., Groom, D. E., Hook, I. M., Kim, A. G., Kim, M. Y., Lee, J. C., Nunes, N. J., Pain, R., Pennypacker, C. R., Quimby, R., Lidman, C., Ellis, R. S., Irwin, M., McMahon, R. G., Ruiz-Lapuente, P., Walton, N., Schaefer, B., Boyle, B. J., Filippenko, A. V., Matheson, T., Fruchter, A. S., Panagia, N., Newberg, H. J. M., Couch, W. J., and The Supernova Cosmology Project (1999). Measurements of Omega and Lambda from 42 High-Redshift Supernovae. *ApJ*, 517:565–586.

Persic, M., Salucci, P., and Stel, F. (1996). The universal rotation curve of spiral galaxies - I. The dark matter connection. *MNRAS*, 281:27–47.

Postman, M. and Geller, M. J. (1984). The morphology-density relation - The group connection. *ApJ*, 281:95–99.

Press, W. H., Teukolsky, S. A., Vetterling, W. T., and Flannery, B. P. (1992). *Numerical recipes in FORTRAN. The art of scientific computing*.

Proctor, R. N., Forbes, D. A., Romanowsky, A. J., Brodie, J. P., Strader, J., Spolaor, M., Mendel, J. T., and Spitler, L. (2009). Probing the 2D kinematic structure of early-type galaxies out to three effective radii. *MNRAS*, 398:91–108.

Pu, S. B., Saglia, R. P., Fabricius, M. H., Thomas, J., Bender, R., and Han, Z. (2010). Radially extended kinematics and stellar populations of the massive ellipticals NGC 1600, NGC 4125, and NGC 7619 . Constraints on the outer dark halo density profile. *A&A*, 516:A4.

Rasia, E., Tormen, G., and Moscardini, L. (2004). A dynamical model for the distribution of dark matter and gas in galaxy clusters. *MNRAS*, 351:237–252.

Rees, M. J. and Ostriker, J. P. (1977). Cooling, dynamics and fragmentation of massive gas clouds - Clues to the masses and radii of galaxies and clusters. *MNRAS*, 179:541–559.

Reid, B. A., Percival, W. J., Eisenstein, D. J., Verde, L., Spergel, D. N., Skibba, R. A., Bahcall, N. A., Budavari, T., Frieman, J. A., Fukugita, M., Gott, J. R., Gunn, J. E., Ivezić, Ž., Knapp, G. R., Kron, R. G., Lupton, R. H., McKay, T. A., Meiksin, A., Nichol, R. C., Pope, A. C., Schlegel, D. J., Schneider, D. P., Stoughton, C., Strauss, M. A., Szalay, A. S., Tegmark, M., Vogeley, M. S., Weinberg, D. H., York, D. G., and Zehavi, I. (2010). Cosmological constraints from the clustering of the Sloan Digital Sky Survey DR7 luminous red galaxies. *MNRAS*, 404:60–85.

Renzini, A. (2006). Stellar Population Diagnostics of Elliptical Galaxy Formation. *ARA&A*, 44:141–192.

Richstone, D. O. and Tremaine, S. (1985). Dynamical models of M87 without a central black hole. *ApJ*, 296:370–378.

Richstone, D. O. and Tremaine, S. (1988). Maximum-entropy models of galaxies. *ApJ*, 327:82–88.

Riess, A. G., Filippenko, A. V., Challis, P., Clocchiatti, A., Diercks, A., Garnavich, P. M., Gilliland, R. L., Hogan, C. J., Jha, S., Kirshner, R. P., Leibundgut, B., Phillips, M. M., Reiss, D., Schmidt, B. P., Schommer, R. A., Smith, R. C., Spyromilio, J., Stubbs, C., Suntzeff, N. B., and Tonry, J. (1998). Observational Evidence from Supernovae for an Accelerating Universe and a Cosmological Constant. *AJ*, 116:1009–1038.

Rix, H.-W., Carollo, C. M., and Freeman, K. (1999). Large Stellar Disks in Small Elliptical Galaxies. *ApJL*, 513:L25–L28.

Rix, H.-W., de Zeeuw, P. T., Cretton, N., van der Marel, R. P., and Carollo, C. M. (1997). Dynamical Modeling of Velocity Profiles: The Dark Halo around the Elliptical Galaxy NGC 2434. *ApJ*, 488:702.

Rix, H.-W. and White, S. D. M. (1992). Optimal estimates of line-of-sight velocity distributions from absorption line spectra of galaxies - Nuclear discs in elliptical galaxies. *MNRAS*, 254:389–403.

Roberts, M. S. and Haynes, M. P. (1994). Physical Parameters along the Hubble Sequence. *ARA&A*, 32:115–152.

Robertson, B., Cox, T. J., Hernquist, L., Franx, M., Hopkins, P. F., Martini, P., and Springel, V. (2006). The Fundamental Scaling Relations of Elliptical Galaxies. *ApJ*, 641:21–40.

Rodionov, S. A. and Athanassoula, E. (2011). Dynamical models of the elliptical galaxy NGC 4494. *MNRAS*, 410:111–126.

Rodionov, S. A., Athanassoula, E., and Sotnikova, N. Y. (2009). An iterative method for constructing equilibrium phase models of stellar systems. *MNRAS*, 392:904–916.

Romanowsky, A. J., Douglas, N. G., Arnaboldi, M., Kuijken, K., Merrifield, M. R., Napolitano, N. R., Capaccioli, M., and Freeman, K. C. (2003). A Dearth of Dark Matter in Ordinary Elliptical Galaxies. *Science*, 301:1696–1698.

Romanowsky, A. J. and Kochanek, C. S. (2001). Dynamics of Stars and Globular Clusters in M87. *ApJ*, 553:722–732.

Romanowsky, A. J., Strader, J., Spitler, L. R., Johnson, R., Brodie, J. P., Forbes, D. A., and Ponman, T. (2009). Mapping The Dark Side with DEIMOS: Globular Clusters, X-Ray Gas, and Dark Matter in the NGC 1407 Group. *AJ*, 137:4956–4987.

Rothberg, B. and Joseph, R. D. (2004). A Deep K-Band Photometric Survey of Merger Remnants. *AJ*, 128:2098–2143.

Rybicki, G. B. (1987). Deprojection of Galaxies - how much can BE Learned. In de Zeeuw, P. T. and Tremaine, S. D., editors, *Structure and Dynamics of Elliptical Galaxies*, volume 127 of *IAU Symposium*, page 397.

Saglia, R. P., Bertin, G., Bertola, F., Danziger, J., Dejonghe, H., Sadler, E. M., Stiavelli, M., de Zeeuw, P. T., and Zeilinger, W. W. (1993). Stellar dynamical evidence for dark halos in elliptical galaxies - The case of NGC 4472, IC 4296, and NGC 7144. *ApJ*, 403:567–572.

Saglia, R. P., Kronawitter, A., Gerhard, O., and Bender, R. (2000). The Orbital Structure and Potential of NGC 1399. *AJ*, 119:153–161.

Saglia, R. P., Sánchez-Blázquez, P., Bender, R., Simard, L., Desai, V., Aragón-Salamanca, A., Milvang-Jensen, B., Halliday, C., Jablonka, P., Noll, S., Poggianti, B., Clowe, D. I., De Lucia, G., Pelló, R., Rudnick, G., Valentinuzzi, T., White, S. D. M., and Zaritsky, D. (2010a). The fundamental plane of EDisCS galaxies. The effect of size evolution. *A&A*, 524:A6.

Saglia, R. P., Sánchez-Blázquez, P., Bender, R., Simard, L., Desai, V., Aragón-Salamanca, A., Milvang-Jensen, B., Halliday, C., Jablonka, P., Noll, S., Poggianti, B., Clowe, D. I., De Lucia, G., Pelló, R., Rudnick, G., Valentinuzzi, T., White, S. D. M., and Zaritsky, D. (2010b). The fundamental plane of EDisCS galaxies. The effect of size evolution. *A&A*, 524:A6.

Sáiz, A., Domínguez-Tenreiro, R., and Serna, A. (2004). Elliptical Galaxies at z=0 from Self-consistent Hydrodynamical Simulations: Comparison with Sloan Digital Sky Survey Structural and Kinematical Data. *ApJL*, 601:L131–L134.

Sanchez, A. G., Scoccola, C. G., Ross, A. J., Percival, W., Manera, M., Montesano, F., Mazzalay, X., Cuesta, A. J., Eisenstein, D. J., Kazin, E., McBride, C. K., Mehta, K., Montero-Dorta, A. D., Padmanabhan, N., Prada, F., Rubino-Martin, J. A., Tojeiro, R., Xu, X., Vargas Magana, M., Aubourg, E., Bahcall, N. A., Bailey, S., Bizyaev, D., Bolton, A. S., Brewington, H., Brinkmann, J., Brownstein, J. R., Gott, III, J. R., Hamilton, J. C., Ho, S., Honscheid, K., Labatie, A., Malanushenko, E., Malanushenko, V., Maraston, C., Muna, D., Nichol, R. C., Oravetz, D., Pan, K., Ross, N. P., Roe, N. A., Reid, B. A., Schlegel, D. J., Shelden, A., Schneider, D. P., Simmons, A., Skibba, R., Snedden, S., Thomas, D., Tinker, J., Wake, D. A., Weaver, B. A., Weinberg, D. H., White, M., Zehavi, I., and Zhao, G. (2012). The clustering of galaxies in the SDSS-III Baryon Oscillation Spectroscopic Survey: cosmological implications of the large-scale two-point correlation function. *ArXiv e-prints*.

Sandage, A. (1972). Absolute Magnitudes of E and so Galaxies in the Virgo and Coma Clusters as a Function of U - B Color. *ApJ*, 176:21.

Sandage, A., Freeman, K. C., and Stokes, N. R. (1970). The Intrinsic Flattening of e, so, and Spiral Galaxies as Related to Galaxy Formation and Evolution. *ApJ*, 160:831.

Sarazin, C. L. (1988). *X-ray emission from clusters of galaxies*.

Sarazin, C. L. (1990). Cooling flows and X-ray emission in early-type galaxies. In H. A. Thronson Jr. & J. M. Shull, editor, *The Interstellar Medium in Galaxies*, volume 161 of *Astrophysics and Space Science Library*, pages 201–238.

Scannapieco, C., Tissera, P. B., White, S. D. M., and Springel, V. (2005). Feedback and metal enrichment in cosmological smoothed particle hydrodynamics simulations - I. A model for chemical enrichment. *MNRAS*, 364:552–564.

Scarlata, C., Carollo, C. M., Lilly, S. J., Feldmann, R., Kampczyk, P., Renzini, A., Cimatti, A., Halliday, C., Daddi, E., Sargent, M. T., Koekemoer, A., Scoville, N., Kneib, J.-P., Leauthaud, A., Massey, R., Rhodes, J., Tasca, L., Capak, P., McCracken, H. J., Mobasher, B., Taniguchi, Y., Thompson, D., Ajiki, M., Aussel, H., Murayama, T., Sanders, D. B., Sasaki, S., Shioya, Y., and Takahashi, M. (2007). The Redshift Evolution of Early-Type Galaxies in COSMOS: Do Massive Early-Type Galaxies Form by Dry Mergers? *ApJS*, 172:494–510.

Schindler, S., Guzzo, L., Ebeling, H., Boehringer, H., Chincarini, G., Collins, C. A., de Grandi, S., Neumann, D. M., Briel, U. G., Shaver, P., and Vettolani, G. (1995). Discovery of an arc system in the brightest ROSAT cluster of galaxies. *A&A*, 299:L9.

Schmidt, B. P. et al. (1998). The High Z supernova search: Measuring cosmic deceleration and global curvature of the universe using type Ia supernovae. *Astrophys.J.*, 507:46–63.

Schrabback, T., Hartlap, J., Joachimi, B., Kilbinger, M., Simon, P., Benabed, K., Bradač, M., Eifler, T., Erben, T., Fassnacht, C. D., High, F. W., Hilbert, S., Hildebrandt, H., Hoekstra, H., Kuijken, K., Marshall, P. J., Mellier, Y., Morganson, E., Schneider, P., Semboloni, E., van Waerbeke, L., and Velander, M. (2010). Evidence of the accelerated expansion of the Universe from weak lensing tomography with COSMOS. *A&A*, 516:A63.

Schwarzschild, M. (1979). A numerical model for a triaxial stellar system in dynamical equilibrium. *ApJ*, 232:236–247.

Schwarzschild, M. (1993). Self-consistent models for galactic halos. *ApJ*, 409:563–577.

Schweizer, F. (1982). Colliding and merging galaxies. I - Evidence for the recent merging of two disk galaxies in NGC 7252. *ApJ*, 252:455–460.

Scorza, C., Bender, R., Winkelmann, C., Capaccioli, M., and Macchetto, D. F. (1998). Stellar disks and embedded bars in early-type galaxies. I. 2-D photometric decomposition of 28 southern early-type galaxies. *A&A Supp.*, 131:265–286.

Seljak, U., Slosar, A., and McDonald, P. (2006). Cosmological parameters from combining the Lyman-α forest with CMB, galaxy clustering and SN constraints. *Journal of Cosmology and Astroparticle Physics*, 10:14.

Sellwood, J. A. (2003). Bars and Dark Matter Halo Cores. *ApJ*, 587:638–648.

Sersic, J. L. (1968). *Atlas de galaxias australes.*

Shapiro, K. L., Cappellari, M., de Zeeuw, T., McDermid, R. M., Gebhardt, K., van den Bosch, R. C. E., and Statler, T. S. (2006). The black hole in NGC 3379: a comparison of gas and stellar dynamical mass measurements with HST and integral-field data. *MNRAS*, 370:559–579.

Silk, J. (1977). On the fragmentation of cosmic gas clouds. I - The formation of galaxies and the first generation of stars. *ApJ*, 211:638–648.

Spergel, D. N. and Hernquist, L. (1992). Statistical mechanics of violent relaxation. *ApJL*, 397:L75–L78.

Spolaor, M., Hau, G. K. T., Forbes, D. A., and Couch, W. J. (2010). Early-type galaxies at large galactocentric radii - I. Stellar kinematics and photometric properties. *MNRAS*, 408:254–271.

Springel, V. (2000). Modelling star formation and feedback in simulations of interacting galaxies. *MNRAS*, 312:859–879.

Springel, V. (2010). E pur si muove: Galilean-invariant cosmological hydrodynamical simulations on a moving mesh. *MNRAS*, 401:791–851.

Springel, V., Di Matteo, T., and Hernquist, L. (2005a). Modelling feedback from stars and black holes in galaxy mergers. *MNRAS*, 361:776–794.

Springel, V., Wang, J., Vogelsberger, M., Ludlow, A., Jenkins, A., Helmi, A., Navarro, J. F., Frenk, C. S., and White, S. D. M. (2008). The Aquarius Project: the subhaloes of galactic haloes. *MNRAS*, 391:1685–1711.

Springel, V., White, S. D. M., Jenkins, A., Frenk, C. S., Yoshida, N., Gao, L., Navarro, J., Thacker, R., Croton, D., Helly, J., Peacock, J. A., Cole, S., Thomas, P., Couchman, H., Evrard, A., Colberg, J., and Pearce, F. (2005b). Simulations of the formation, evolution and clustering of galaxies and quasars. *Nature*, 435:629–636.

Springel, V., Yoshida, N., and White, S. D. M. (2001). GADGET: a code for collisionless and gasdynamical cosmological simulations. *Nature*, 6:79–117.

Stark, A. A. (1977). Triaxial Models of the Bulge of M31. *ApJ*, 213:368–373.

Statler, T. S. (1987). Self-consistent models of perfect triaxial galaxies. *ApJ*, 321:113–152.

Strader, J., Caldwell, N., and Seth, A. C. (2011). Star Clusters in M31. V. Internal Dynamical Trends: Some Troublesome, Some Reassuring. *AJ*, 142:8.

Syer, D. and Tremaine, S. (1996). Made-to-measure N-body systems. *MNRAS*, 282:223–233.

Szomoru, D., Franx, M., and van Dokkum, P. G. (2012). Sizes and Surface Brightness Profiles of Quiescent Galaxies at z ˜ 2. *ApJ*, 749:121.

Tegmark, M., Strauss, M. A., Blanton, M. R., Abazajian, K., Dodelson, S., Sandvik, H., Wang, X., Weinberg, D. H., Zehavi, I., Bahcall, N. A., Hoyle, F., Schlegel, D., Scoccimarro, R., Vogeley, M. S., Berlind, A., Budavari, T., Connolly, A., Eisenstein, D. J., Finkbeiner, D., Frieman, J. A., Gunn, J. E., Hui, L., Jain, B., Johnston, D., Kent, S., Lin, H., Nakajima, R., Nichol, R. C., Ostriker, J. P., Pope, A., Scranton, R., Seljak, U., Sheth, R. K., Stebbins, A., Szalay, A. S., Szapudi, I., Xu, Y., Annis, J., Brinkmann, J., Burles, S., Castander, F. J., Csabai, I., Loveday, J., Doi, M., Fukugita, M., Gillespie, B., Hennessy, G., Hogg, D. W., Ivezić, Ž., Knapp, G. R., Lamb, D. Q., Lee, B. C., Lupton, R. H., McKay, T. A., Kunszt, P., Munn, J. A., O'Connell, L., Peoples, J., Pier, J. R., Richmond, M., Rockosi, C., Schneider, D. P., Stoughton, C., Tucker, D. L., vanden Berk, D. E., Yanny, B., and York, D. G. (2004). Cosmological parameters from SDSS and WMAP. *Phys. Rev. D*, 69(10):103501.

Teodorescu, A. M., Méndez, R. H., Saglia, R. P., Riffeser, A., Kudritzki, R.-P., Gerhard, O. E., and Kleyna, J. (2005). Planetary Nebulae and Stellar Kinematics in the Flattened Elliptical Galaxy NGC 1344. *ApJ*, 635:290–304.

Thomas, D., Maraston, C., Bender, R., and Mendes de Oliveira, C. (2005a). The Epochs of Early-Type Galaxy Formation as a Function of Environment. *ApJ*, 621:673–694.

Thomas, J., Jesseit, R., Naab, T., Saglia, R. P., Burkert, A., and Bender, R. (2007a). Axisymmetric orbit models of N-body merger remnants: a dependency of reconstructed mass on viewing angle. *MNRAS*, 381:1672–1696.

Thomas, J., Jesseit, R., Saglia, R. P., Bender, R., Burkert, A., Corsini, E. M., Gebhardt, K., Magorrian, J., Naab, T., Thomas, D., and Wegner, G. (2009a). The flattening and the orbital structure of early-type galaxies and collisionless N-body binary disc mergers. *MNRAS*, 393:641–652.

Thomas, J., Saglia, R. P., Bender, R., Thomas, D., Gebhardt, K., Magorrian, J., Corsini, E. M., and Wegner, G. (2005b). Regularized orbit models unveiling the stellar structure and dark matter halo of the Coma elliptical NGC 4807. *MNRAS*, 360:1355–1372.

Thomas, J., Saglia, R. P., Bender, R., Thomas, D., Gebhardt, K., Magorrian, J., Corsini, E. M., and Wegner, G. (2007b). Dynamical modelling of luminous and dark matter in 17 Coma early-type galaxies. *MNRAS*, 382:657–684.

Thomas, J., Saglia, R. P., Bender, R., Thomas, D., Gebhardt, K., Magorrian, J., Corsini, E. M., and Wegner, G. (2009b). Dark Matter Scaling Relations and the Assembly Epoch of Coma Early-Type Galaxies. *ApJ*, 691:770–782.

Thomas, J., Saglia, R. P., Bender, R., Thomas, D., Gebhardt, K., Magorrian, J., and Richstone, D. (2004). Mapping stationary axisymmetric phase-space distribution functions by orbit libraries. *MNRAS*, 353:391–404.

Tonry, J. L., Dressler, A., Blakeslee, J. P., Ajhar, E. A., Fletcher, A. B., Luppino, G. A., Metzger, M. R., and Moore, C. B. (2001). The SBF Survey of Galaxy Distances. IV. SBF Magnitudes, Colors, and Distances. *ApJ*, 546:681–693.

Toomre, A. (1977). Mergers and Some Consequences. In Tinsley, B. M. and Larson, D. Campbell, R. B. G., editors, *Evolution of Galaxies and Stellar Populations*, page 401.

Tortora, C., Napolitano, N. R., Romanowsky, A. J., Capaccioli, M., and Covone, G. (2009). Central mass-to-light ratios and dark matter fractions in early-type galaxies. *MNRAS*, 396:1132–1150.

Tremaine, S. D. (1987). Summary - Structure and Dynamics of Elliptical Galaxies. In P. T. de Zeeuw & S. D. Tremaine, editor, *Structure and Dynamics of Elliptical Galaxies*, volume 127 of *IAU Symposium*, page 367.

Treu, T., Auger, M. W., Koopmans, L. V. E., Gavazzi, R., Marshall, P. J., and Bolton, A. S. (2010). The Initial Mass Function of Early-Type Galaxies. *ApJ*, 709:1195–1202.

Treu, T. and Koopmans, L. V. E. (2004). Massive Dark Matter Halos and Evolution of Early-Type Galaxies to z ˜ 1. *ApJ*, 611:739–760.

Trimble, V. (1995). The 1920 Shapley-Curtis Discussion: Background, Issues, and Aftermath. *Publ. Astr. Soc. Pac.*, 107:1133.

Trujillo, I., Burkert, A., and Bell, E. F. (2004a). The Tilt of the Fundamental Plane: Three-Quarters Structural Nonhomology, One-Quarter Stellar Population. *ApJL*, 600:L39–L42.

Trujillo, I., Erwin, P., Asensio Ramos, A., and Graham, A. W. (2004b). Evidence for a New Elliptical-Galaxy Paradigm: Sérsic and Core Galaxies. *AJ*, 127:1917–1942.

Trujillo, I., Förster Schreiber, N. M., Rudnick, G., Barden, M., Franx, M., Rix, H.-W., Caldwell, J. A. R., McIntosh, D. H., Toft, S., Häussler, B., Zirm, A., van Dokkum, P. G., Labbé, I., Moorwood, A., Röttgering, H., van der Wel, A., van der Werf, P., and van Starkenburg, L. (2006). The Size Evolution of Galaxies since z˜3: Combining SDSS, GEMS, and FIRES. *ApJ*, 650:18–41.

Tully, R. B. and Fisher, J. R. (1977). A new method of determining distances to galaxies. *A&A*, 54:661–673.

Valluri, M., Merritt, D., and Emsellem, E. (2004). Difficulties with Recovering the Masses of Supermassive Black Holes from Stellar Kinematical Data. *ApJ*, 602:66–92.

van Albada, T. S. (1982). Dissipationless galaxy formation and the R to the 1/4-power law. *MNRAS*, 201:939–955.

van Albada, T. S. and Sancisi, R. (1986). Dark matter in spiral galaxies. *Royal Society of London Philosophical Transactions Series A*, 320:447–464.

van de Ven, G., de Zeeuw, P. T., and van den Bosch, R. C. E. (2008). Recovery of the internal orbital structure of galaxies. *MNRAS*, 385:614–646.

van de Ven, G., Hunter, C., Verolme, E. K., and de Zeeuw, P. T. (2003). General solution of the Jeans equations for triaxial galaxies with separable potentials. *MNRAS*, 342:1056–1082.

van den Bergh, S. (1976). A new classification system for galaxies. *ApJ*, 206:883–887.

van den Bosch, R. C. E. and de Zeeuw, P. T. (2010). Estimating black hole masses in triaxial galaxies. *MNRAS*, 401:1770–1780.

van den Bosch, R. C. E., van de Ven, G., Verolme, E. K., Cappellari, M., and de Zeeuw, P. T. (2008). Triaxial orbit based galaxy models with an application to the (apparent) decoupled core galaxy NGC 4365. *MNRAS*, 385:647–666.

van der Marel, R. P. (1991). The velocity dispersion anisotropy and mass-to-light ratio of elliptical galaxies. *MNRAS*, 253:710–726.

van der Marel, R. P., Cretton, N., de Zeeuw, P. T., and Rix, H. (1998). Improved Evidence for a Black Hole in M32 from HST/FOS Spectra. II. Axisymmetric Dynamical Models. *ApJ*, 493:613–+.

van der Marel, R. P. and Franx, M. (1993). A new method for the identification of non-Gaussian line profiles in elliptical galaxies. *ApJ*, 407:525–539.

van der Marel, R. P., Magorrian, J., Carlberg, R. G., Yee, H. K. C., and Ellingson, E. (2000). The Velocity and Mass Distribution of Clusters of Galaxies from the CNOC1 Cluster Redshift Survey. *AJ*, 119:2038–2052.

van Dokkum, P. G. (2005). The Recent and Continuing Assembly of Field Elliptical Galaxies by Red Mergers. *AJ*, 130:2647–2665.

van Dokkum, P. G. and Conroy, C. (2010). A substantial population of low-mass stars in luminous elliptical galaxies. *Nature*, 468:940–942.

van Dokkum, P. G., Franx, M., Fabricant, D., Illingworth, G. D., and Kelson, D. D. (2000). Hubble Space Telescope Photometry and Keck Spectroscopy of the Rich Cluster MS 1054-03: Morphologies, Butcher-Oemler Effect, and the Color-Magnitude Relation at Z = 0.83. *ApJ*, 541:95–111.

van Dokkum, P. G., Whitaker, K. E., Brammer, G., Franx, M., Kriek, M., Labbé, I., Marchesini, D., Quadri, R., Bezanson, R., Illingworth, G. D., Muzzin, A., Rudnick, G., Tal, T., and Wake, D. (2010). The Growth of Massive Galaxies Since z = 2. *ApJ*, 709:1018–1041.

Verolme, E. K., Cappellari, M., Copin, Y., van der Marel, R. P., Bacon, R., Bureau, M., Davies, R. L., Miller, B. M., and de Zeeuw, P. T. (2002). A SAURON study of M32: measuring the intrinsic flattening and the central black hole mass. *MNRAS*, 335:517–525.

Visvanathan, N. and Sandage, A. (1977). The color-absolute magnitude relation for E and S0 galaxies. I - Calibration and tests for universality using Virgo and eight other nearby clusters. *ApJ*, 216:214–226.

Walker, M. G. and Peñarrubia, J. (2011). A Method for Measuring (Slopes of) the Mass Profiles of Dwarf Spheroidal Galaxies. *ApJ*, 742:20.

Wechsler, R. H., Bullock, J. S., Primack, J. R., Kravtsov, A. V., and Dekel, A. (2002). Concentrations of Dark Halos from Their Assembly Histories. *ApJ*, 568:52–70.

Weijmans, A.-M., Cappellari, M., Bacon, R., de Zeeuw, P. T., Emsellem, E., Falcón-Barroso, J., Kuntschner, H., McDermid, R. M., van den Bosch, R. C. E., and van de Ven, G. (2009). Stellar velocity profiles and line strengths out to four effective radii in the early-type galaxies NGC3379 and 821. *MNRAS*, 398:561–574.

Weijmans, A.-M., Krajnović, D., van de Ven, G., Oosterloo, T. A., Morganti, R., and de Zeeuw, P. T. (2008). The shape of the dark matter halo in the early-type galaxy NGC 2974. *MNRAS*, 383:1343–1358.

Weil, M. L. and Hernquist, L. (1996). Global Properties of Multiple Merger Remnants. *ApJ*, 460:101.

Weinberg, S. (1972). *Gravitation and Cosmology: Principles and Applications of the General Theory of Relativity.*

White, S. D. M. and Frenk, C. S. (1991). Galaxy formation through hierarchical clustering. *ApJ*, 379:52–79.

White, S. D. M., Frenk, C. S., Davis, M., and Efstathiou, G. (1987). Clusters, filaments, and voids in a universe dominated by cold dark matter. *ApJ*, 313:505–516.

White, S. D. M. and Rees, M. J. (1978). Core condensation in heavy halos - A two-stage theory for galaxy formation and clustering. *MNRAS*, 183:341–358.

Williams, M. J., Bureau, M., and Cappellari, M. (2009). Kinematic constraints on the stellar and dark matter content of spiral and S0 galaxies. *MNRAS*, 400:1665–1689.

Willman, B. and Strader, J. (2012). "Galaxy," Defined. *ArXiv e-prints*.

Wojtak, R., Lokas, E. L., Gottlöber, S., and Mamon, G. A. (2005). Radial velocity moments of dark matter haloes. *MNRAS*, 361:L1–L5.

Young, P. (1980). Numerical models of star clusters with a central black hole. I - Adiabatic models. *ApJ*, 242:1232–1237.

Zwicky, F. (1937). On the Masses of Nebulae and of Clusters of Nebulae. *ApJ*, 86:217.

6

Acknowledgments

Finally, it is pleasure to thank those friends who came and visited me in Munich, bringing *stracchino*, cheerfulness, and sense of belonging to a special place, back in Monte Amiata: Laura, Valentina, Giulia, Federico, Francesco, Raffaele, Viola, Azzurra, Erika, Carlo, Marco, Linda, Alessio.

And in that place far away, where the nights are still full of fireflies and stars, I thank my family and in particular my grandparents whom I have missed a lot. A special acknowledgment to my parents, who have been supportive and trustful throughout these years, and to my brother Simone.

Last but not least, I thank Marco, the amazing *uomo camion* who made me hold on, and enjoy.

WHEN I HEARD THE LEARN'D ASTRONOMER,
WHEN THE PROOFS, THE FIGURE, WERE RANGED IN COLUMNS BEFORE ME,
WHEN I WAS SHOWN THE CHARTS AND THE DIAGRAMS, TO ADD, DIVIDE, AND MEASURE THEM,
WHEN I, SITTING, HEARD THE ASTRONOMER
WHERE HE LECTURED WITH MUCH APPLAUSE IN THE LECTURE-ROOM,
HOW SOON, UNACCOUNTABLE, I BECAME TIRED AND SICK,
TILL RISING AND GLIDING OUT, I WANDER'D OFF BY MYSELF,
IN THE MYSTICAL MOIST NIGHT-AIR, AND FROM TIME TO TIME,
LOOK'D UP IN PERFECT SILENCE AT THE STARS.
Walt Whitman